

Cardiff University



**Magnetotransport Measurements of NiFe Thin
Films and Nanostructures**

Doctor of Philosophy

Kane Esien

September 2016

Abstract

A custom built thermal evaporator equipped with *in situ* electrical transport probes and an electromagnet, designed to investigate magnetic thin films and nanostructures, was constructed and calibrated. Magnetoresistance measurements were used to characterise a 20 nm thick film grown in 2 nm steps and measured *in situ* as a function of film thickness. It was found that the thin film had a smaller than expected anisotropic magnetoresistance (AMR) signal of 0.024%. It was suggested that an oxide formed at each 2nm thick layers during the growth phase altered the conductivity of the film and caused the measured AMR to be anomalously small.

Lateral spin valves fabricated from a range of ferromagnetic and normal metal components were investigated. NiFe/Au/NiFe lateral spin valves were the most thoroughly investigated to determine the spin diffusion length in the Au, the spin polarisation of NiFe and the injection efficiency at the NiFe/Au interface. Lateral spin valves fabricated from NiFe/Al/NiFe and utilising tunnelling contacts were also investigated and a pure spin current detected. Other devices, including a non-local lateral spin valve dual spin injection structure, were fabricated and measured.

Nanomachining using diamond coated silicon nitride atomic force microscope (AFM) tips was employed to modify nickel iron (NiFe) nanowires. The modifications to nanowires in this way subsequently altered the observed domain wall motion in the wires. AFM nanomachining was found mostly to increase the coercive field of the nanowires owing to the formation of a pinning site for domain walls.

Magnetoresistance measurements were used to study the effect of machining nanowires of varying widths and thickness. Theoretical predictions regarding the change in coercive field due to machining were larger than those experimentally measured. Domain wall anisotropic magnetoresistance (DW AMR) was also studied as a function of width for two thicknesses of nanowire (10nm and 20nm). Deviation from existing theoretical models was observed consistently for both wire thicknesses. A dependence of the DW AMR on the proximity to the phase boundary between different domain wall types was observed for each thickness of nanowire studied.

Acknowledgments

I would like would like to thank Cardiff University for providing me with a safe haven to study, grow, learn and prosper. My life has been truly enhanced by my experiences and time spent at Cardiff University, I am forever grateful.

I would like to give thanks to Mr. Josh Jones and his supervisor Dr. Dr Emmanuel Brousseau for assistance with the AFM nanomachining project.

I would like to give thanks to my mother and farther, my mother for me showing how to be kind and resilient and my farther for showing me how to be courageous and wise (among the many, many, many other things parents do...).

I would like to thank my supervisor, Dr. Dan Read, you educated me in the elusive ways of experimental physics and I will be forever grateful.

I would like to give thanks to the funding agency ESPRC and Cardiff University for giving me this opportunity, particularly financially. I only hope I may go out there and make the world a better place in your honour.

I would like to give thanks to my Partner (Bianca) and my son (Elijah), you inspire me to be better me. Your support is all I will ever need.

I would like to give thanks and praise to the countless hours and countless scientists who have made science a reality and a powerful tool in our society.

Contents

Abstract	III
Acknowledgments	IV
Contents.....	V
List of Figures.....	X
List of Symbols.....	XXII
1. Introduction.....	1
2. Magnetism: A Brief Introduction to Modern Magnetism	2
2.1. An Introduction to Magnetism: The Origin of The Magnetic Moment, Different Material Classifications and Basic Definitions.	2
2.2. Origin of Magnetic Moment – In Terms of Spin and Angular Momentum.....	3
2.3. Magnetic Permeability and Susceptibility and the Classification of Magnetic Materials	5
2.3.1. Diamagnetism.....	7
2.3.2. Paramagnetism	7
2.3.3. Ferromagnetism	8
2.4. Micromagnetism.....	10
2.4.1. The Exchange Interaction.....	11
2.4.2. Magnetocrystalline Anisotropy.....	12
2.4.3. Zeeman Energy	13
2.4.4. Magnetostatic Energy, The Formation of Domains And Shape Anisotropy.....	13
2.5. Domain wall types	15
2.6. Domain Wall Anisotropic Magnetoresistance (DW AMR) in NiFe Nanowires. 16	
2.6.1. 1D Model for Doman Wall AMR in Planar nanowires	16
2.6.2. Conduction Channel Model	17

2.7.	Spin Transport in Lateral Spin Valves Theory	18
2.7.1.	Introduction.....	18
2.7.2.	Two Current Model – Motts Discovery.....	19
2.7.3.	Spin Asymmetry – The Final Ingredient to Make Spintronics a Reality	20
2.7.4.	Spin Accumulation.....	21
2.7.5.	Estimation of the Spin Diffusion Length.....	21
2.7.6.	A Simple Two Terminal Device – A Spin Valve	22
2.7.7.	Theory of Spin Injection and Accumulation.....	23
2.7.8.	Literature Review.....	26
3.	Sample Fabrication.....	34
3.1.	Introduction	34
3.2.	Electron Beam Lithography.....	34
3.3.	Thermal Evaporation.....	41
3.1.	A Custom Built Thermal Evaporator – With Optical and Electrical <i>In Situ</i> Probes	42
3.2.	Sample Production.....	45
4.	SAMPLE CHARACTERISATION	47
4.1.	Introduction	47
4.2.	Scanning Electron Microscopy.....	47
4.3.	Anisotropic Magnetoresistance (AMR).....	49
4.3.1.	Introduction.....	49
4.3.2.	Practical Use of AMR.....	51
4.4.	Atomic Force Microscopy (AFM).....	56
4.4.1.	AFM for Thickness and Roughness Measurements	56
4.4.2.	AFM Nanomachining	59
4.5.	Experimental Setup for Low Noise Magnetotransport Measurements as A Function of Temperature.....	61
4.5.1.	Introduction.....	61

4.5.2.	Experimental Setup	61
4.5.3.	Calibration Measurements.....	62
5.	USING AFM TO MODIFY PERMALLOY NANOWIRES	68
5.1.	Introduction	68
5.2.	Literature Review of AFM Machining	69
5.3.	Experimental Data Prior to Machining a 10nm Thick, 10um Long, 674nm Wide Nanowire.....	74
5.4.	Experimental Data Post-Machining (1 st Scratch).....	77
5.5.	Experimental Data Post-Machining (2 nd Scratch).....	81
5.6.	Destruction of <i>Nanowire 1 (10nm thick)</i>	84
5.7.	20nm Thick Permalloy nanowires of Various Widths Machined Using AFM	86
5.7.1.	Experimental Data: Prior to Machining a 20nm Thick, 2μm Long, 211nm Wide Nanowire	87
5.7.2.	Experimental Data: Post Machining of a 20nm Thick, 2um Long, 211nm Wide Nanowire (1 st Scratch).....	89
5.7.1.	Experimental Data: Prior to Machining a 20nm Thick, 2μm Long, 403nm Wide Nanowire	93
5.7.1.	Experimental Data: Post Machining of a 20nm Thick, 2μm Long and 403nm Wide Permalloy Nanowire.....	96
5.7.2.	Experimental Data: Post Machining of a 20nm Thick, 2μm Long and 403nm Wide Permalloy Nanowire second scratch.....	99
5.7.1.	Data Prior to Machining a 20nm Thick, 2μm Long and 323nm Wide Permalloy Nanowire.....	105
5.7.2.	Experimental Data: Post Machining of a 20nm Thick, 2μm Long and 323nm Wide Permalloy Nanowire.....	107
5.8.	Discussion of AFM Machined NiFe Nanowires	112
5.8.1.	10 nm Chip Discussion: Coercive field analysis.	112
5.8.2.	Discussion: Domain Wall Resistance Compared With 1D Model	118

5.8.3.	Discussion: Domain Wall Resistance Compared With Conduction Channel Model.....	120
5.8.4.	DW AMR as a Function of Scratch depth	122
5.9.	20nm Thick Chip Discussion	123
5.9.1.	20nm Thick Chip Discussion: Experimentally Determined Change in Coercive Field Compared With Theoretical Predications.....	125
5.9.2.	20nm Thick Chip Discussion: DW AMR Compared with the 1D model and the conduction channel model.	130
5.9.3.	20nm Thick Chip Discussion : DW AMR reduction due to machining / reduced thickness.....	132
5.9.4.	Conclusion.....	134
6.	<i>In-situ</i> AMR Measurements of a Thin Film of NiFe as a Function of Thickness	135
6.1.	Introduction	135
6.2.	Literature Review	135
6.1.	<i>In-situ</i> Experiments	138
6.2.	Discussion.....	150
6.3.	Conclusion	152
7.	EXPERIMENTS WITH METAL SPIN VALVES.....	154
7.1.	Introduction	154
7.2.	Spin injection From Nickel Electrodes into A Gold Spin Channel.....	154
7.3.	Spin Injection from NiFe Electrodes into A Gold Spin Channel.....	159
7.4.	Spin Injection from NiFe into Au as a Function of the Injection Length	164
7.5.	Spin Injection from NiFe Electrodes into An Aluminium Spin Channel Through an Aluminium Oxide Tunnel Barrier	166
7.6.	Discussion.....	170
7.6.1.	Spin Injection from Nickel Electrodes	170
7.6.2.	Spin Injection In NiFe/Gold/NiFe Lateral Spin Valves.....	170

7.6.3. Spin Injection Using AlO _x Tunnel barriers.....	172
7.6.4. Spin Injection Using AlO _x Tunnel barriers And a Dual Injection Scheme 173	
7.7. Conclusion	175
8. Further Experiments and Outlook.....	176
9. Conclusion.....	177
10. References	179

List of Figures

Figure 2-1. a) shows a schematic of an electron orbiting the nucleus, it shows the magnetic moment which is a due to the orbital motion of the electron and the associated angular momentum (L). b) Shows the magnetic moment and angular momentum associated with the intrinsic spin of the electron and associated angular momentum (S).	4
Figure 2-2 Showing example responses to a magnetic field, curve a) shows the response of diamagnetic material, b) shows the response of a paramagnet and c) shows the response of a ferromagnet. Image adapted from reference [3].	6
Figure 2-3 Showing a typical 'M-H' plot for a ferromagnetic sample. Image adapted from reference [94].	10
Figure 2-4 Showing how the formation of domains reduces the magnetostatic energy by reducing the stray field.	14
Figure 2-5 Showing the relevant domain wall types studied in this thesis. Top images in a) and b) correspond to a transverse domain wall. The bottom image of a) and b) corresponds to a vortex domain wall type. Image adapted from [8]	15
Figure 2-6 Showing how a nanowire can be deconstructed as a resistor network and using the OOMMF software this model can be used to evaluate the DW AMR.	18
Figure 2-7 Showing the spin splits density of states of a typical ferromagnet (a), the exchange splitting of the band structure presents different sections of the band structure to the Fermi level, for each spin state, thus resulting in different mobility's for the spin up and spin down carriers. Image adapted from [16].....	20
Figure 2-8 Showing a simple two terminal device whose output resistance depends directly on spin dependent transport. This known as either a spin valve or giant magnetoresistance head.	22
Figure 2-9 Showing the experimental setup used by Johnson and Silsbee in their pioneering research paper. Note the micrometre dimensions. Images adapted from reference [21]	26
Figure 2-10 Showing the development of spintronics post 1985. The image is taken from reference [22] A few developments most relevant to this thesis have been highlighted.	27

Figure 2-11 Showing the results obtained for super-lattices of Fe(0,0,1) and Cr(0,0,1) with a simple schematic to aid understanding. There is a clearly defined two states of resistance corresponding. Image adapted from [23] 28

Figure 2-12 Showing the device (left image) used by Jedema et al to show pure spin current injection, The right image shows the measuring configuration used to achieve pure spin current injection. Images adapted form reference [26] 30

Figure 2-13 showing a standard lateral spin valve with only one injecting electrode (top image) and a dual lateral spin valve with two electrodes for injecting the spin current and a reduced volume for spin relaxation. Image adapted from reference [31] 31

Figure 2-14 showing the two different designs used to prove that geometrical confinement of the spin relaxation volume is one way to increase the spin signal. Image a) is a standard spin valve, image b) is a spin valve with reduced volume for spin relaxation. Images adapted from reference [47] 32

Figure 2-15 showing a geometrical ratchet design used for increasing the spin signal, by preferentially allowing spin current to flow in one direction easier than the other. Image adapted from reference [48] 33

Figure 3-1 Showing the principle of electron beam lithography. Electrons penetrate the resist and can be elastically forward scattered forward. They can also ionise secondary electrons which have a longer mean free path. Some electrons will travel straight through the resist and interact with the substrate, backscatterd electrons return from the substrate as a consequence of increased scattering in the higher density substrate. 36

Figure 3-2 Showing the effect of secondary electrons with respect to the incident beam energy in the resist and substrate. Top images correspond to the resist and bottom images correspond to the substrate. A larger beam energy corresponds to more secondary electrons being generated in the resist and the depth and width of the exposed resist increases. In the substrate the opposite happens. Image adapted from [55]. 39

Figure 3-3 Showing optical micrographs presenting a second layer exposure of a spin channel. Left image is in the resist and the right image shows after metal deposition. The material which is already deposited and is visible through the resist is the ferromagnetic material Ni. The spin channel is Au with a Cr buffer layer (right

image only). All materials were thermally evaporated. This serves to demonstrate both EBL and thermal deposition. 42

Figure 3-4 Showing a schematic of a thermal evaporation setup. The main components are a vacuum system (turbo and rotary pumps), a crucible and a power supply, crystal monitor to track thickness and a shutter to begin and end the deposition..... 43

Figure 3-5 Image a) showing a real image of the in-situ setup prior to being loaded into the vacuum chamber. The foil is used as a mask to isolate the contacts and wires from the deposited thin film. The sample cannot rotate in the chamber therefore the wires are changed to make transverse and longitudinal anisotropic magnetoresistance measurements. Image b) shows the sample holder without the magnet for clarity..... 44

Figure 3-6. A series of images summarising the various steps involved in sample fabrication. See the text for full detail of the individual processes. 46

Figure 4-1 Showing SEM micrographs of a fabricated spin valve device. The spin channel (vertical conduit) is Au and the magnetic electrodes (Horizontal conduits) are made of NiFe..... 48

Figure 4-2 High magnification SEM image of a spin valve device, as presented in figure 4-1 49

Figure 4-3 AMR curves for the typical measurement orientations in a NiFe thin film. The lowest resistance change is when the current and magnetisation are perpendicular. 51

Figure 4-4 Presenting a typical AMR dataset as measured for the nanowire presented in Figure 4-10. The blue data corresponds to a positive to negative field sweep and the opposite applies to the red data A clear abrupt change in the resistance occurs at the coercive field of the nanowire, as shown for both field directions..... 53

Figure 4-5 Showing an SEM micrograph of a NiFe nanowire with two sets of contacts, two for current and two for voltage. AMR data from this nanowire is presented in Figure 4-4. The dimensions of the nanowire are 20nm thick, 200nm wide and 20µm in length. Sample 20152004_AuSV. 53

Figure 4-6 Showing an AMR curve for a NiFe nanowire of 300nm width, 16nm thickness and 20µm in length. Measurement configuration is current and field parallel. In short there are two features: an essentially zero field feature

corresponding to magnetisation large pads connected to the nanowire and included in the measurement. The second feature is an abrupt change to the resistance at 40 Oe corresponding to the nanowire reversing its magnetisation via a domain wall reversal mechanism. Images adapted from [70] 55

Figure 4-7 Showing a schematic of an AFM. The deflection of the cantilever tip due to the interaction with the surface is measured by a laser reflecting from the cantilever to a photodiode. 56

Figure 4-8 Showing a single line scan generated by using an AFM on a Au thin film. The sudden increase in height is attributed to the edge of a Au film and is used to determine the height of the thin film. 58

Figure 4-9 Shows a Histogram constructed from an entire high magnification AFM image used for analysing roughness..... 59

Figure 4-10 Top images showing a Diamond coated Silicon tip. Side (top left image) and Top View (top right image). Bottom images showing the before (left image) and after (right image) of using the Diamond tip to modify a Permalloy nanowire. Images adapted from [80] 60

Figure 4-11 Showing the experimental setup that was designed and implemented to measure the anisotropic magnetoresistance of samples used in this thesis. It consists of a magnet connected to a power supply connected to a computer, this is all that is needed for field control. To make electrical measurements a resistance bridge connects to the sample and is in turn connected to the computer for remote control. All Equipment is interfaced through LabView. 62

Figure 4-12 Showing the magnetic field distribution for three orthogonal directions. There is a region of uniformity in the centre of the poles of approximately a cm^3 . The measurement axes are defined as shown (z is into the page). Therefore the largest chip size fabricated is 1 cm x 1 cm to ensure it experiences a uniform field. 63

Figure 4-13 Showing the magnetic field as a function of the magnet voltage. A linear trend is observed with a gradient of 7.4 mT/V for the curve taken in the centre of the poles..... 64

Figure 4-14 Showing the calibration measurements for the homemade magnetoresistance setup. Measurements were performed on a GaAs hall bar the two shown configurations corresponding to magnetoresistance (top and bottom left images) and a hall measurement (top and bottom right images) 65

Figure 5-1 Showing a scratch in a NiFe thin film (middle image). AFM profile of the scratch (right image) and the correlation between force and depth/width. The graph shows the threshold force and the logarithmic trend after overcoming the threshold force for scratching. Images adapted from [80] 69

Figure 5-2 Showing multiple line scans taken at random locations along a groove. The four line scans correspond to four different scratching directions. Image (a) is an upward direction, (b) is a forward direction, (c) is a downward direction (d) is a backward direction. All grooves were scratched with a load force of 9uN and at a tip speed of 100nm/s on a30nm thick NiFe thin film. The small image to right defines the different directions. Images adapted from[79] 70

Figure 5-3 Showing vertical modification of a nanostructure (a), Simulations of a transverse (b) and vortex (c) domain wall propagating though such a vertical modification[66]. 72

Figure 5-4 Showing the results of the micromagnetic simulations performed. Considering a transverse wall image (a) shows the depth dependence at a fixed length, Image (b) shows the length dependence for a fixed depth. Considering the vortex wall image (c) shows the depth dependence at a fixed length, image (d) shows the length dependence for a fixed depth. 73

Figure 5-5 Showing the energy profiles with respect to the domain wall position for a transverse wall (a) and a vortex wall (b). Images (c) and (d) show the energy profile for a range of nanotrench lengths for transverse and vortex walls respectively. The change in energy profile as a function of the length of the nanotrench is shown as inset..... 73

Figure 5-6 Showing different magnification SEM images to show the two different designs employed. The bottom image shows a high magnification image of a fabricated 10nm thick, 400nm wide Permalloy nanowire used for AFM nanomachining 75

Figure 5-7 Showing a typical AMR curve for a 673.5nm wide, 10nm thick, 2um in length nanowire. The image to the right shows both field sweep directions. In both cases a discontinuous jump in the resistance is associated with the depinning of a domain wall and rapid reversal via domain wall propagation. 76

Figure 5-8 Image a) shows the results of the linescan which is shown in the 2D AFM image (image b)). Image b) shows the a 2D AFM image. Image c) shows a 3D AFM image. The results of the linescan show the depth (3.9nm) and width (524nm) and

the debris to one side of the nanotrench. Image c) shows the scratch can clearly be seen along with debris at one side (due to the cutting direction used) 79

Figure 5-9 Shows a comparison of the data taken before and after the first machining session. Image a) shows the positive to negative field sweep direction. Image b) shows the negative to positive field sweep. Both sets of data taken after the machining, show a small increase in depinning field, the pinning field remaining similar to the non-scratched data. Un-scratched data is offset to overlay with the scratch data..... 80

Figure 5-10 Image a) showing the results of a linescan (the linescan is shown in the 2D plot, image b)). The results of the linescan show the depth (4.5nm) and width (400nm) and the debris to one side of the nanotrench. Image c) shows a 3D image produced from AFM, the scratch can clearly be seen along with debris at one side (due to the cutting direction used). The second scratch served to marginally increase the depth of the scratch..... 82

Figure 5-11 Showing a comparison of data taken before and after the second machining session. Image a) compares the positive to negative field data and image b) compares the negative to positive field data. 83

Figure 5-12 Showing an SEM image of nanowire 1 (10nm thick), after the final machining attempt which destroyed the wire..... 85

Figure 5-13 Showing a SEM image of a 20nm thick, 211nm wide nanowire, prior to being machined. It shows the clean edge profiles and overall good quality of the fabricated nanowire. 87

Figure 5-14 Showing a typical AMR curve as measured for a 211nm wide 20nm thick and 2µm long nanowire of Permalloy (SEM shown in figure 5.13). The magnetic field applied along the easy axis of the nanowire. In both sweep directions there is a clear abrupt change in the resistance around 11mT corresponding to the rapid reversal of the nanowire facilitated by domain wall motion. 88

Figure 5-15 Showing the modification to nanowire 2 (20nm thick, 211nm wide), there is no clear indication that the machining has happened here although it was decided to measure the AMR response of the nanowire as that would be another independent way to investigate if any changes have occurred. Most likely position of the scratch is show with an arrow..... 90

Figure 5-16 Showing a comparison of the data taken before and after scratching nanowire 2. At a glance it is clear the coercive field has increased and it looks like

the size of the effect has reduced. The resistance has increased also due to the scratch. This is evidence to suggest a scratch took place and has formed a pinning site for domain walls in nanowire 2. 91

Figure 5-17 A comparison of data taken before and after the scratching of nanowire 2. It is clear that the coercive field has increased and the size of the effect has reduced. The dataset taken after the scratch was offset to overlay the datasets. 92

Figure 5-18 High magnification SEM image of nanowire 3 (20nm thick, 403nm wide). Showing clean edge profiles and overall good integrity of the fabricated nanowire. 93

Figure 5-19 Image a) Showing a typical trend measured in the transverse AMR configuration for nanowire 3. This nanowire was fabricated and utilised a device design that allowed simultaneous measurement of the nanowire and other larger sections of magnetic material that the nanowire is connected to. See figure 5.6 for clarity (shows and SEM of both designs employed). The highest field effects correspond to pinning and depinning of a domain wall corresponding to reversal of the nanostructure. The inset image shows the AMR curve plotted to higher magnetic fields to show the full trend measured for this nanowire. Image b) showing the design used for nanowire 3, it has been added to aid description of the data presented in image a). 95

Figure 5-20 Showing a 2D AFM image of the nanowire 3 (20nm thick, 403nm wide) after being scratched. The red box denotes a line scan. Depth of scratch is approximately 1nm. 96

Figure 5-21 Results of the linescan shown in figure 5.20. It shows a depth of 1nm and a small pile up of debris, at one side, due to the cutting direction used. 97

Figure 5-22 Showing a typical AMR response from nanowire 4 (20nm thick, 403nm wide). The red data points show a feature corresponding to reversal of the nanowire via domain wall reversal at around 8mT. The blue data points contain a feature associated with the nanowire reversal at around 5mT. Such a large difference between the two depinning fields implies that it may be two different domain wall types for each field direction shown in the above graph. 98

Figure 5-23 Showing a comparison between datasets taken before and after the first scratching session for a single field sweep, the data corresponding to no scratch was offset to allow for a visual comparison. Immediately obvious is the reduction in the size of the effect. In the above figures it is difficult to see the effect in the scratched

dataset, it is easier to view in figure 5.23 without the superimposed unscratched datasets..... 99

Figure 5-24 Showing a 2D AFM image of the second scratch made on the surface of nanowire 3 (20nm thick, 403nm wide).The red box shows a linescan. There is a clear scratch now in this nanowire. There is also debris shown by the white spots. 100

Figure 5-25 Showing the results of the linescan shown in figure 5.25. There is clear modification of the nanowire, maximum depth being 6nm. There is debris pile up at one side as a result of the cutting direction used. The length of the scratch is now approximately 400nm. 101

Figure 5-26 Showing a 3D AFM image taken after nanowire 3 was machined for a second time. A clear scratch is visible in the 3D image..... 101

Figure 5-27 Showing the AMR transverse response measured after the 2nd scratch. The resistance has increased due to material being removed. Coercive field associated with the reversal of the nanowire are similar and all trends needs to be analysed to assign an average value and error. The size of the effect looks to have decreased further also..... 102

Figure 5-28 Showing the domain wall depinning field as a function of the depth of the scratch for nanowire 3. A clear linear decrease in the depinning field is observed for this nanowire. 104

Figure 5-29 Showing the change in domain wall depinning field as a function of the length of the scratch. A clear linear decrease is observed. It is not clear what produce a decrease in the depinning field..... 105

Figure 5-30 High magnification image of nanowire 4 (20nm thick, 323nm wide), this nanowire had a rougher edge profile than all other 20nm thick nanowires, it is not known why, as all 20nm thick nanowires were fabricated in the exact same conditions. 106

Figure 5-31 Showing the transverse AMR response of nanowire 4 (20nm thick, 323nm wide). The blue dataset shows an abrupt change in the resistance at a single field value corresponding to the nanowire being reversed via domain wall propagation. The red dataset has more than one feature attributed to the domain wall getting pinned at defects within the nanowire due to its rougher edges. 107

Figure 5-32 Showing a 2D AFM image and a linescan. The scratch not clearly visible in this image and the linescan needs to be reviewed to assess the scratch further. 108

Figure 5-33 Showing the results of the linescan shown in Figure 5-32. This is an unclear linescan, the scratch is nearly obstructed entirely by the material littering the nanowire surface. 109

Figure 5-34 Showing a typical AMR curve taken after nanowire 4 was machined. The red dataset shows a abrupt change at a single field value corresponding to a domain wall reversing the nanostructures magnetisation. The blue dataset has a more fine structure in the curve than in the red dataset, this is believed to be due to a domain wall being pinned at different points throughout the nanowire during reversal. 110

Figure 5-35 Comparing data taken before and after nanowire 4 was machined, the scratched datasets have coercive fields at a value higher than the unscratched data. 111

Figure 5-36 Showing the phase diagram for domain walls in Permalloy. Two extra points are added corresponding to the thickness of the nanowire before and after scratching. Image adapted from [95]. 113

Figure 5-37 Showing how a domain wall is nucleated in the pad before propagating and being pinned at the notch. Wire dimensions are 50nm thick, 450nm wide and a few microns long. The term nucleation pad is widely used in the literature. Images adapted from [115] 114

Figure 5-38 Showing the change in depinning field as a function of the depth of the nanotrench/notch. Left image shows both theory and experiment. Right image shows only the experimental data with the theoretical linear gradient taken from fitting the theory dataset. Theoretical data taken and adapted from [66] 116

Figure 5-39 Showing the dependence on the depinning field as a function of the length of the nanotrench. Left image shows both experimental data and theory both with fitted with a linear fit. The right image shows only the experimental data and the linear fit (included for clarity). Theoretical data adapted from reference [66]. 117

Figure 5-40 Showing the variation in domain wall resistance as a function of the width for a 10nm thick nanowire only the widest device underwent successful machining. Two straight lines have been added to the plot to showing the theoretical prediction by the 1D model for vortex and transverse domain walls. 118

Figure 5-41 Showing the experimentally determined domain wall anisotropic magnetoresistance for 10nm thick nanowires, as a function of width, along with the theoretical prediction made by the conduction model. 121

Figure 5-42 Showing the coercive fields obtained, for each device and scratch iteration, as a function of width. This image allows a clear way of visualising all the results.....	124
Figure 5-43 Showing the depinning field as a function of the depth of the scratch, for the cases where the coercive decreased. Linear fits were made to the experimental datasets. Theoretical data was adapted from [66].....	127
Figure 5-44 Showing the depinning field as a function of depth of the scratch, for all nanowires that showed an increase in coercive field due to machining. Linear Fits were created from theoretical data presented in reference [66]	128
Figure 5-45 Showing the experimentally measured DW AMR as a function of width from 20nm thick nanowires along with the predictions of the DW AMR for vortex and transverse walls using the 1D model.....	130
Figure 5-46 Comparing the experimentally measured DW AMR with the theoretical predications of the conduction channel model. Theory is shown for 10nm and 20nm thick nanowires for both domain wall types (vortex and transverse) and a line has been added to show the expected phase boundary for transverse and vortex wall for both thicknesses.	132
Figure 5-47 Showing the DW AMR for 20nm thick Permalloy nanowires of various widths. The data suggests a decrease in DW AMR after machining.	133
Figure 6-1 Showing how different magnetic fields applied during the deposition directly affect the microstructure of the film. The different microstructures are distinguishable by their sheet resistance as a function of thickness in the low thickness regime, images adapted from [98].....	137
Figure 6-2 Showing the sheet resistance as a function of thickness from reference [98], of particular interest is the difference in trends in the low thickness limit for different applied fields i.e. each different applied field is resulting in microstructure changes that are measureable. There is a sharp increase in resistance during the initial stages of the deposition and then a tending to the bulk value for all traces beyond 100nm thick.	138
Figure 6-3 Showing how the resistance varies with increasing thickness, measured in situ. For comparison data has been taken from a relevant dataset [94]. The trends are in agreement.	139
Figure 6-4 Showing the AMR data obtained for in situ run 3, the current and magnetic field are in the same direction (transverse configuration). To be compared	

and contrasted with measurements made ex situ in the same configuration, Figure 6-5).	140
Figure 6-5 Presenting ex-situ measurements made for the sample in-situ run 3) in the transverse configuration. There is agreement between the in situ data (Figure 6-4) and the ex-situ data (above figure) apart from the sample undergoing oxidisation upon exposure to air.	140
Figure 6-6 Presenting the AMR data for sample in situ run 3 with the magnetic field and current perpendicular to one another (longitudinal configuration). This image is to be compared and contrasted with data measured ex-situ for the same sample and configuration shown in Figure 6-7.	141
Figure 6-7 Presenting the ex-situ data for sample in situ run 3, measured in the low noise AMR setup (ex-situ) with the current and applied magnetic field perpendicular to one another. There is agreement between the in situ (Figure 6-6) and the ex situ data (above image) although the ex-situ data has undergone oxidisation.....	142
Figure 6-8 Showing the AMR for both field and current configurations for the sample used to investigate oxidisation. Upper graph corresponds to the transverse configuration measurement and the lower graph corresponds to the longitudinal configuration measurement.	145
Figure 6-9 Showing the change in resistance upon exposing the sample to air. The inset shows the chamber closed and pumped removing the air the increase in resistance attributed to oxidisation was absent in the vacuum.	146
Figure 6-10 Comparing an ideal thin film (right image) with a thin film grown in 2nm steps (left image). Both films are 20nm thick and measured ex-situ. Clearly the right has a lower resistance and larger effect.	147
Figure 6-11 Showing a comparison between and ideal thin film (right image) and a thin film grown in 2nm steps (left image). Both are 20nm thick and measured in the transverse configuration.	149
Figure 7-1 Showing a schematic of a fabricated spin valve device (a) for highlighting how different measurements are carried to ensure the device is performing as expected prior to measuring the spin valve effect. Image b) shows example resistances obtained using two terminal electrical measurements.	155
Figure 7-2 Showing AMR curves for the injecting and detecting Ni electrodes shown in Figure 7-3. Allows evaluation of coercive fields.	156

Figure 7-3 Showing a high magnification SEM image of a fabricated Nickel/Gold/Nickel lateral spin valve structure with a 200nm separation between injecting and detecting electrodes.	157
Figure 7-4 Presenting the non-local spin valve effect measured for a Nickel/Gold/Nickel lateral spin valve with an injector –detector separation of 200nm. The spin valve effect was not observed for this device.	158
Figure 7-5 Presenting an SEM image of a measured NiFe/Gold/NiFe lateral spin valve. SEM was employed to determine the widths of fabricated nanowires and injector-detector spacing's.....	161
Figure 7-6 Showing two distinct coercive fields measured with the AMR effect. Two distinct coercive fields are shown at approximately 5mT and 3mT for the 300nm wide and 400nm wide nanowires respectively.....	162
Figure 7-7 Presenting the local spin valve effect measured at room temperature using a NiFe/Gold/NiFe lateral spin valve.	163
Figure 7-8 Showing the non-local spin valve effect in a NiFe/Au/NiFe lateral spin valve. No effect was observed and only an upper limit was placed on the effect ($<0.1 \text{ m}\Omega$).....	164
Figure 7-9 Presenting the local spin valve effect as a function of the injector-detector separation. The data was fitted with a 1D model describing spin transport.	165
Figure 7-10 Presenting an AMR measurement of a magnetic electrode used in the spin valve measurement for a NiFe/ AlO_x /Al/ AlO_x /NiFe lateral spin valve, coercive field is close to 5mT for both field directions. Image b) presents the local spin valve effect measured for a NiFe/ AlO_x /Al/ AlO_x /NiFe lateral spin valve, the coercive field of the measured magnetic electrode is also plotted to aid interpretation.....	168
Figure 7-11 Presents the non-local signal in a NiFe/ AlO_x /Al/ AlO_x /NiFe dual injection lateral spin valve, measured in the dual injection configuration. The datasets are not typical of a non-local spin valve effect in a dual injection lateral spin valve, but were repeatable. In this configuration the measured voltage is only sensitive to spin dependent effects.....	169
Figure 8-1 Showing an interesting 3D structure produced as a side product of machining a thin film.....	176

List of Symbols

A list of all symbols used within this thesis for ease of access. Symbols are presented first in order of appearance in the thesis. In the text parameters shown in bold represent vector quantities otherwise it is a scalar quantity.

$\boldsymbol{\mu}_m$	Total magnetic moment
\boldsymbol{J}	Total angular momentum
g	Lande g-factor
μ_B	Bohr magnetron
\hbar	Reduced Planck's constant
χ	Magnetic susceptibility
H	Magnetic field strength
M	Magnetisation
μ	Magnetic permeability
μ_r	Relative magnetic permeability
μ_0	Magnetic permeability of free space
C	Curie constant
T	Temperature
H	Heisenberg Hamiltonian
J	Exchange Constant
S	Spin
ϵ_{ex}	Exchange Energy

A	Exchange Stiffness
M	Magnetisation (Vector Field)
Φ	Magnetic Anisotropy
K_1, K_2	Magnetic anisotropy constants
$\alpha_{1,2,3}$	Direction Cosines relative to crystal edges
ε_z	Zeeman Energy
ε_s	Magnetostatic Energy
H_s	Stray Field
R_{TW}	Resistance associated with transvers domain wall
R_{VW}	Resistance associated with vortex domain wall
ρ	Resistivity
t	Thickness
λ_{sd}	Spin Diffusion Length
λ	Electron Mean Free Path
v_f	Fermi Velocity
$\tau_{\uparrow\downarrow}$	Spin Flip Time
μ_E	Electrochemical potential
μ_{ch}	Chemical Potential
e	Fundamental Electronic Charge
V	Electric Potential
n	Electron Density

$N(E_f)$	Density of States at Fermi Level
σ	Conductivity
D	Diffusion Constant
j	Current Density
α_F	Spin Polarisation
∂R	Change in Resistance
$\partial \rho$	Change in Resistivity
t	Thickness
π	The Fundamental Constant Pi
$\rho(\theta)$	Resistivity As a Function of Angle
ρ_{para}	Resistivity With Current Density and Magnetisation Vectors Parallel At Magnetic Saturation
$\delta \rho$	Change in Resistivity
Δd_x	Major gap length between adjacent lines/grains
δd_x	Minor gap length between adjacent lines/grains

1. Introduction

Magnetic nanostructures and thin films are of technical importance in industry and commerce, used as magnetic recording media and read heads mostly. The study of nanoscale magnetic elements is interesting from an applied physics point of view as well as from a fundamental physics point of view. Regarding magnetic nanowires and the domain walls that are typically responsible for magnetisation reversal in these structures, a great deal of interesting devices can be fabricated, such as race track memory [1], and domain wall logic circuits [2]. Magnetic nanowires have been fabricated and studied in this thesis, in both an applied sense and in a fundamental way. A new and novel way of modifying nanowires has been explored using an atomic force microscope (AFM), a diamond coated SiN tip was used to machine the surface of nanowires and in the case of magnetic nanowires a pinning site was thus formed for domain walls. Domain wall anisotropic magnetoresistance was also studied in terms of magnetic nanowires as a function of width and thickness. A custom built thermal evaporator was assembled with the capability to probe magnetic material *in situ*. Lateral spin valve devices were fabricated to study pure spin current.

2. Magnetism: A Brief Introduction to Modern Magnetism

2.1. An Introduction to Magnetism: The Origin of The Magnetic Moment, Different Material Classifications and Basic Definitions.

Magnetism is a varied and broad subject which arguably covers most areas of scientific research in some way, from astrophysics and models of the universe as a whole, right down to sub atomic particles and their interactions with one another. Electromagnetism is one of the four fundamental forces of nature and as such it is studied in every respect imaginable. In this section of the thesis, the groundwork is laid down for a theoretical understanding of the behaviour discussed in the later chapters. Beginning with why materials are potentially magnetic and ending with a theoretical description of the physics relevant to this thesis.

In this chapter, the relevant theory for the results chapters are expounded. The origin of the magnetic moment is first described, showing how the electron gives the largest contribution to the magnetic moment of an atom. Bulk magnetism is then introduced, extending the idea of an isolated magnetic atom to the collective behaviour of magnetic atoms in bulk materials, diamagnetism, paramagnetism and ferromagnetism are introduced as examples of different manifestations of magnetism in bulk matter. The concept of a magnetic domain is introduced here to aid the explanation of ferromagnetic materials. Basic magnetic parameters such as susceptibility and permeability are defined and related to different magnetic materials.

Next micromagnetism is introduced and the energy terms governing magnetic behaviour are introduced and discussed formally. The concept of the domain is explained in detail, in terms of competing energy terms and minimisation of such energy terms to reach an equilibrium distribution of magnetisation. How micromagnetism is used as a tool for modelling magnetic systems in the micrometre and nanometre regimes is also discussed.

The effect of reducing dimensions on magnetic behaviour is next introduced specifically for Permalloy, a magnetic material used extensively in this thesis and the

magnetic community at large. Firstly bulk Permalloy is discussed, then a thin film and finally a nanowire. The end result is a detailed description of the nanowires used within this thesis for spin injection and for AFM nanomachining studies.

Next domain wall motion is discussed in terms of the existing literature. Showing how domain wall motion is an active field of research with applications in commercial technology. Literature directly relevant to this thesis is discussed in detail such as domain wall motion, the pinning of domain walls using artificial pinning sites, how anisotropic magnetoresistance (AMR) can be used to detect and distinguish domain walls and finally models for identifying domain walls using AMR are introduced and discussed.

The theory relevant to AFM nanomachining is introduced next with an associated literature review. An experimental perspective is taken here as little theoretical models exist to describe AFM nanomachining.

Finally the theory relevant for metallic lateral spin valves is laid down. Spin injection, propagation and detection are all formally discussed. A review of the literature is also presented relevant to work undertaken within this thesis.

2.2. Origin of Magnetic Moment – In Terms of Spin and Angular Momentum

The origin of the magnetic moment of a bulk sample can be related back to the atoms that compose a bulk sample. Considering a single atom it is possible to calculate the magnetic moment which has three components. The first component comes from the moving of the electron in an orbit around the nucleus, any accelerating charge will produce a magnetic field and associated magnetic moment **Figure 2-1 a)**. Circular motion implies constant acceleration and thus an orbiting electron will create a magnetic field and associated magnetic moment. The second contribution to the total magnetic moment of an atom comes from the intrinsic magnetic moment of an electron due to its spin (**Figure 2-1 b)**. Electron spin being an entirely quantum mechanical phenomena, it is not possible to describe the

magnetic moment due to spin classically, quantum mechanical arguments must be used. Owing to the quantum mechanical nature of an electrons spin, it is quantised in two defined states known as spin up or spin down. The third component which contributes to the total magnetic moment of an atom is the nucleus, again it has an intrinsic spin although it is roughly three orders of magnitude smaller than that contributed by the electron, it is often neglected in the calculation of the total magnetic moment of an atom. The total magnetic moment of an atom may be represented as:

$$\mu_m = - \frac{g\mu_B}{\hbar} \mathbf{J} \quad \text{Equation 1}$$

Where μ_m is the total magnetic moment, g is the Lande g factor, μ_B is the Bohr magneton (the Bohr magneton is equal to the magnetic moment of an orbiting electron in its ground state) and \hbar is the reduced Planck constant and \mathbf{J} is the total angular momentum.

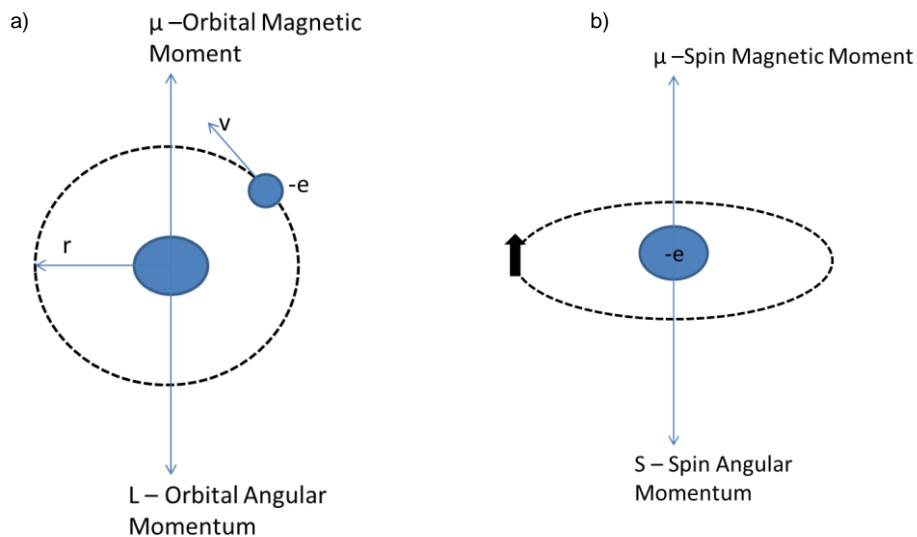


Figure 2-1. a) shows a schematic of an electron orbiting the nucleus, it shows the magnetic moment which is a due to the orbital motion of the electron and the associated angular momentum (L). b) Shows the magnetic moment and angular momentum associated with the intrinsic spin of the electron and associated angular momentum (S).

This discussion shows how the magnetic moment of an atom is generated and what it is comprised of, the main contribution coming from the electron. It is no small step

to extend the description of an isolated atom to that of bulk materials, especially whilst maintaining a microscopic picture. Before a micromagnetic picture is described the magnetic materials are described in terms of macroscopic parameters to gain a general understanding of magnetism in the bulk sense as opposed to a single isolated atom.

2.3. Magnetic Permeability and Susceptibility and the Classification of Magnetic Materials

Magnetic materials are generally classified by their response to a magnetic field, historically it was simply this response which empirically defined different magnetic materials. It is possible to characterise the response of a material to a magnetic field by using two parameters, susceptibility and the relative permeability. The susceptibility of a magnetic material is defined as the ratio between the induced magnetisation (due to the applied field) and the applied field, expressed mathematically as follows:

$$\chi = \frac{M}{H} \quad \text{Equation 2}$$

Where χ is the susceptibility, M is the magnetisation induced in the applied field (H) measured in Amperes per meter, H is the applied field again measured in Amperes per meter thus making χ unit less. Susceptibility can be used to describe all classes of magnetic material, differentiating the classes in terms of magnitude and direction. Another way of defining the magnetic response of a material is the use of the parameter magnetic permeability. The magnetic permeability is defined as:-

$$\mu = \mu_r \mu_0 \quad \text{Equation 3}$$

Where μ is the magnetic permeability, μ_r is the relative magnetic permeability, and μ_0 is the permeability of free space. The relative permeability is defined by the following equation:-

$$\mu_r = 1 + \chi \quad \text{Equation 4}$$

Where the susceptibility (χ) was defined earlier.

Materials are classified corresponding to their response to a magnetic field and the above parameters. As our understanding of magnetism grew, and our repertoire of techniques to probe materials also grew, it was possible to relate these empirical responses to the microscopic behaviour of the magnetic materials under consideration. Eventually more magnetic phases were identified as our tools and theories developed, more parameters were also created to constrain these phases.

A relatively straight-forward way to probe and classify materials in practice is measuring a magnetisation curve whereby one is directly measuring the induced response of a magnetic material to an applied field. A typical experiment sees the material under question placed inside of at least two coils, one of which is used to magnetise the material by setting up a solenoidal field, the other coil is used to probe the response of the material, by measuring the induced current due to the sample becoming magnetised, by virtue of electromagnetic induction. The use of some simple equations and applied theory allow one to plot out the magnetisation curve of a sample which can be used to classify a material. Example magnetisation curves are shown in **Figure 2-2** for highlighting the different classes of magnetic material.

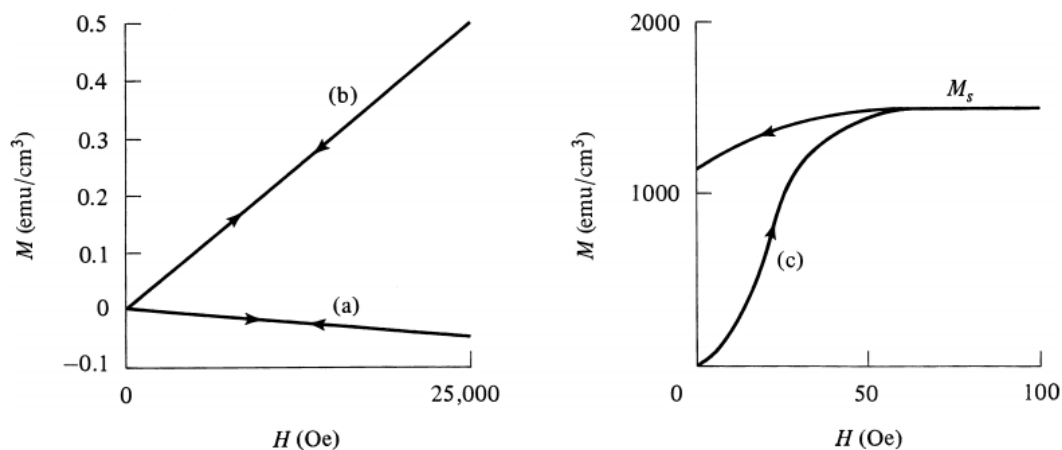


Figure 2-2 Showing example magnetisation curves, curve a) shows the response of diamagnetic material, b) shows the response of a paramagnet and c) shows the response of a ferromagnet. Image adapted from reference [3].

Figure 2-2 shows typical magnetisation curves for three different types of magnetic materials. The different magnetic types are known as diamagnetic (a), paramagnetic (b) and ferromagnetic (c) and will be discussed one by one in the next few sections.

2.3.1. Diamagnetism.

In **Figure 2-2** the plot labelled (a) corresponds to a diamagnetic material. All materials are inherently diamagnetic, although often the diamagnetic effects are overwhelmed by other magnetic ordering responses of a greater extent. The response of a diamagnetic material to a magnetic field is a small induced magnetic field in opposition to the applied field (**Figure 2-2** (a)). In other words, it acts to reduce and minimise the applied field similar to how Lenz's law works in electromagnetic induction. Microscopically electrons are orbiting the nucleus in fixed orbits i.e. within any material there are little current loops that produce small magnetic fields, in the presence of an externally applied field these internal small magnetic fields orientate themselves in such a way as to minimise any change in magnetic field, similar to Lenz's law, the effect is enhanced in conductors due to the free electrons that can flow and produce larger magnetic fields to also oppose any change in magnetic field. The effect is typically linear in response to the applied field and it is sufficient to describe a diamagnetic material using its susceptibility alone, the susceptibility of a typical diamagnetic material is the order of -10^{-6} i.e. it is a small effect in opposition to the applied field.

2.3.2. Paramagnetism

Paramagnetism is another magnetic phase. It is distinguished in the magnetisation curves by an induced magnetisation that serves to increase an externally applied field, it is typically linear in response to an applied field (**Figure 2-2** (b)). The susceptibility is small although larger than that of a diamagnetic material and the susceptibility is positive (typical effects are of the $+10^{-5}$). Paramagnetism stems from unpaired electrons, which possess a magnetic moment (see section 2.2), it is the alignment of these magnetic moments with an applied field that create an induced magnetisation (in the same direction of the applied field) and the paramagnetic effect. In the absence of an applied field the atomic moments are randomly oriented by thermal energy and no net magnetisation results. This hints to a temperature dependent susceptibility for paramagnets, and this was investigated by Pierre Curie

in 1895 [4], a simple relationship was found between the susceptibility of a paramagnet and temperature as shown in **Equation 5**.

$$\chi = \frac{C}{T} \text{ Equation 5}$$

Where χ is the susceptibility defined earlier, T is the temperature and C is the Curie constant. The Curie constant may be thought of as a measure of how well a material can align with a magnetic field given its sensitivity to thermal fluctuations, this constant will be material dependent.

2.3.3. Ferromagnetism

Ferromagnetism is another state of magnetic ordering, in this case a magnetisation can exist without a field being applied. The magnitude of the magnetisation of a ferromagnet can be several orders larger than the magnetisation induced by an applied field in paramagnetism (**Figure 2-2 (c)**). The behaviour of a ferromagnet is more complex than diamagnetism or paramagnetism, being non-linear in its response to an applied magnetic field. In the case of ferromagnetism, the concept of a domain is needed to understand what happens to this type of magnetic phase upon application an external magnetic field. Domains and their boundaries will be formally introduced in a later section of this chapter (section 2.5) but a simple definition severing as an introduction will suffice here.

A domain in magnetism is a collection of magnetic moments coupled together due to the exchange interaction i.e. they are all pointing in the same direction, and due to energy considerations it is not energy efficient to have a large sample with a single domain composed of the whole sample. Therefore the samples magnetisation will typically break up into domains that are energetically more favourable, typical domain sizes are of the order (10^{-4} to 10^{-6}) m and depend on the competing energetic terms for a given sample. A ferromagnetic sample possessing a null magnetisation at zero applied field implies the domains are oriented in such a way as to produce no net effect. A ferromagnetic sample possessing a finite magnetisation in the absence of an applied field implies the domain are arranged in such a way as to produce a net magnetisation effect.

Figure 2-3 show a typical magnetisation curve for a ferromagnetic sample, the curve beginning at the origin of the graph corresponds to what is often referred to as the virgin curve. It shows a ferromagnet having zero magnetisation at zero applied field corresponding physically to all the domains randomly oriented and producing no net magnetisation. If a ferromagnetic material is deposited/grown with no applied field to magnetise the sample during its growth stage, the domains would be randomly oriented and not necessarily sum to a significant magnetisation. Upon application of a magnetic field however the domains would begin to align with the applied field and would do so until they are all aligned. Saturation of the magnetisation would result when there are no more domains to align with the field, this is shown in **Figure 2-3** at high field. When increasing the applied field produces no extra induced magnetisation, saturation has been reached. Let us now assume the ferromagnetic sample has just undergone the virgin curve up to saturation and then the field is decreased until zero. **Figure 2-3** shows a complete hysteresis loop for a ferromagnetic material, let us follow the curve from positive saturation according to the arrow. The plot will follow the curve down to remanence, where it will then retain a significant magnetisation with no applied field (M_r). To remove this magnetisation an external field will need to be applied but now in the negative direction, again shown by **Figure 2-3**, at some value the magnetisation will reduce to zero and this is known as the coercive field of a ferromagnet (H_c). Further increasing of the magnetic field after the coercive field serves to align the domains in the opposite direction up to negative saturation of the magnetisation. After the sample has been magnetised, subsequent field cycles will trace the same magnetisation curve denoted by the line or minor cycles if saturation is not reached.

The area enclosed within in a loop of **Figure 2-3** is related to the energy lost per cycle. The coercive field of a ferromagnet determines whether it is a magnetically soft (low coercive field) or hard (high coercive field) material. There are only a few natural elemental ferromagnets, namely the 3d transition metals Nickel, Iron and Cobalt and the rare earth element Gadolinium. A particular ratio of Nickel and Iron is used extensively throughout this thesis and will be discussed in detail in later sections of this theory chapter.

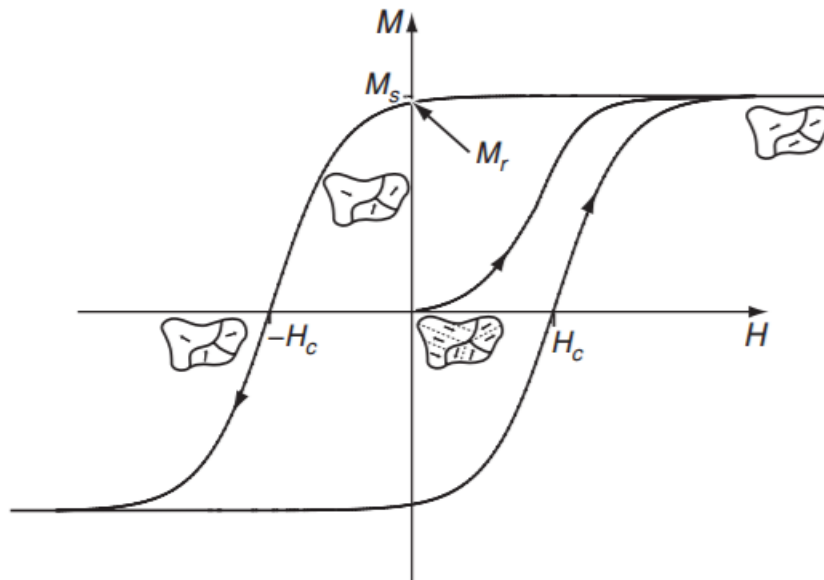


Figure 2-3 Showing a typical 'M-H' plot for a ferromagnetic sample. Image adapted from reference [4].

2.4. Micromagnetism

Micromagnetism is a description of ferromagnetic behaviour in the sub-micrometre regime. As introduced earlier the scale at which individual magnetic moments are generated is atomic, therefore this allows a semi-classical approximation of the variations in local magnetic moment by a continuous vector field \mathbf{M} . This approximation requires variations from atomic moment to atomic moment (nearest neighbours) to be small and this is enforced by the exchange interaction that will be introduced in this section. This approximation serves to greatly simplify calculations relating to magnetic materials in the sub-micrometre regime, rendering the problem a matter of minimising competing energy terms as opposed to a complete quantum mechanical model of $\sim 10^{15}$ interacting spins. The technique was pioneered by Landau and Lifshitz in 1935 [5] and further developed by Brown in 1963 [6]. The different energetic terms involved in solving for energy minima are all defined in terms of the approximated magnetisation vector field and are as follows:

1. The Exchange Interaction
2. Magnetocrystalline Anisotropy
3. Zeeman Energy
4. Magnetostatic Energy and Shape Anisotropy

2.4.1. The Exchange Interaction

As discussed earlier the origin of the magnetic moment lies with the electron. Also discussed was how different materials can have different responses to an applied field, of particular interest was the ferromagnetic phase of magnetism which required the use of domains (small collections of atomic moments coupled together) to explain their behaviour in an applied field. The driving force to couple regions of a magnetic material together is known as the exchange interaction. The exchange interaction is quantum mechanical phenomena existing between nearest neighbour electrons that overlap in wavefunction, giving a difference in energy for whether the electrons magnetic moments are aligned in parallel or anti-parallel. This interaction can be described using the Heisenberg Hamiltonian expressed in **Equation 6**:

$$H = \sum_{i \neq j} J_{i,j} \mathbf{S}_i \cdot \mathbf{S}_j \quad \text{Equation 6}$$

Where H is the Heisenberg Hamiltonian, $J_{i,j}$ is the exchange constant and S_i is the spin of the i^{th} electron. This interaction is named direct exchange if only nearest neighbours interacting with each other are included in the calculation, other forms of exchange interaction exist that involve more interactions than just nearest neighbours. For ferromagnetic behaviour $J > 0$ favouring regions of continuous magnetisation, for anti-ferromagnetic ordering $J < 0$ and spins tend to align in an anti-parallel manner. Utilising the micromagnetic approximation of the atomic moments replaced by a varying vector field, it is possible to re-write **Equation 6** in terms of a vector field as opposed to a sum over all atoms.

$$\epsilon_{\text{ex}} = \int A (\text{div } \mathbf{M})^2 dV \quad \text{Equation 7}$$

Where ϵ_{ex} is the exchange energy, A is the exchange stiffness with units of Joules per metre and $\text{div } \mathbf{M}$ is the divergence of the vector field \mathbf{M} , \mathbf{M} was defined earlier as an approximation of the atomic moments. The integral is to be evaluated over a volume (dV). The exchange constant for Permalloy is equal to 1.3×10^{11} J/m showing how strong a driving force exchange is for forming continuous regions of magnetisation in a ferromagnet.

2.4.2. Magnetocrystalline Anisotropy

Magnetocrystalline anisotropy describes how the energy required to magnetise a sample has a dependence on its crystal structure. It has its origins in the spin-orbit interaction, the electron orbitals and coupled to the lattice and hence the overall crystallographic structure. For the simple cubic lattice structures (Ni, and Fe) an easy and hard axis is well defined, where it is easy to magnetise the sample along the easy axis and the sample requires more energy to magnetise along its hard axis. The extra energy required to magnetise the sample along its hard axis is the magnetocrystalline anisotropy energy. The effect is most pronounced in single crystals with well-defined easy and hard axes. In this thesis Permalloy is used mostly as the magnetic material of choice and due to its ratio of Nickel to Iron it has an intrinsic very low magnetocrystalline anisotropy even in the single crystal state. Permalloy used in this thesis is polycrystalline, meaning there are many grains within the sample, for such a sample the different grain directions will often cancel out leaving little to no magnetocrystalline anisotropy. Magnetocrystalline anisotropy plays little role in the competing energetic terms when considering polycrystalline Permalloy. For cubic structures such as Ni, Fe and NiFe the equation governing magnetocrystalline anisotropy is shown in **Equation 8**.

$$\Phi = K_1(\alpha_1^2 \alpha_2^2 + \alpha_2^2 \alpha_3^2 + \alpha_3^2 \alpha_1^2) + K_2(\alpha_1^2 \alpha_2^2 \alpha_3^2)$$

Equation 8

Where Φ represents the magnetic anisotropy, K_1 and K_2 are material dependent magnetic anisotropy constants and $\alpha_{1,2,3}$ represent the direction cosines relative to the crystal edges. Values for the magnetic anisotropy constants are shown in **Table 1**.

Material	K_1 (J/m ³)	K_2 (J/m ³)
Ni	-4.5×10^3	2.5×10^3
Fe	4.8×10^4	1×10^4
NiFe	$\sim 10^{-3}$	$\sim 10^{-3}$

Table 1 Showing the magnetic anisotropy constants for Nickel, Iron and Nickel-Iron (Permalloy). Values taken from reference [7] for Ni and Fe and for NiFe from reference [8].

2.4.3. Zeeman Energy

The Zeeman energy is the energy of interaction between the magnetisation vector and an externally applied field and may be expressed as:

$$\epsilon_z = -\mu_0 \int \mathbf{M} \cdot \mathbf{H}_{ext} dV \quad \text{Equation 9}$$

Where ϵ_z is the Zeeman energy, μ_0 the permeability of free space, \mathbf{M} is the continuously varying magnetisation vector field introduced at the beginning of this section and \mathbf{H}_{ext} is the externally applied magnetic field. The energy of interaction is minimised when the applied field and magnetisation are parallel to one another.

2.4.4. Magnetostatic Energy, The Formation of Domains And Shape Anisotropy

Magnetostatic energy is the energy associated with the creation of stray fields outside of a magnetised body, it is generated by the dipole-dipole interactions of the individual magnetic moments and depends critically on the distribution of magnetisation. The magnetostatic energy may be expressed as:

$$\epsilon_s = \frac{\mu_0}{2} \int H_s^2 dV \quad \text{Equation 10}$$

Where ϵ_s is the magnetostatic energy, μ_0 is the permeability of free space and H_s is the stray field. The factor of one half is included so that magnetic moments are not accounted for twice. The magnetostatic energy works over larger scales than the exchange interaction (nearest neighbour), encompassing the whole material. To lower the magnetostatic energy and avoid producing stray fields, a magnetic sample will arrange itself such that the stray field is minimised by forming domains.

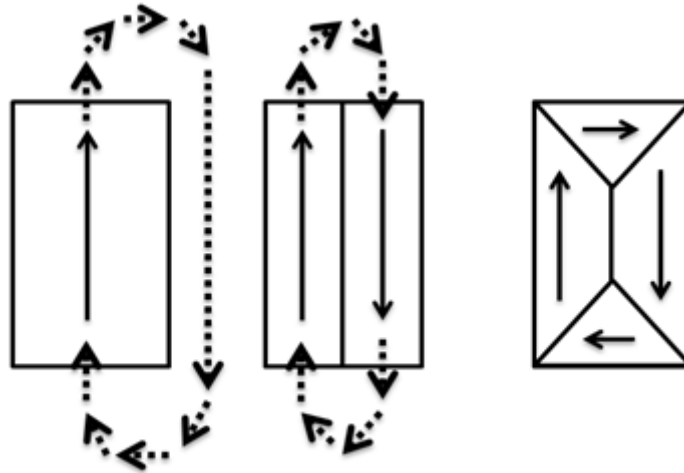


Figure 2-4 Showing how the formation of domains reduces the magnetostatic energy by reducing the stray field [9].

Figure 2-4 shows a series of images to aid understanding the formation of domains and how they reduce the magnetostatic energy [9]. If there is magnetic charge that is not cancelled out by magnetic charge of the opposite polarity, a magnetic field will be created. The left image shows a sample in a single domain state, a large stray field is generated by the charges at the ends of the magnet. The middle image shows that splitting the magnetisation in two domains reducing the stray field drastically, by approximately one half. The formation of the smaller domains shown in the right image are known as flux closure domains as they completely remove the stray field. Division of the magnetisations into domains occurs up to the point where the energy required to create another domain is greater than the reduction in magnetostatic energy. The region separating domains from one another are known as domain walls and are of technological importance as many proposed data storage and logic systems are based upon the domain wall in nanoscale magnetic structures.

For magnetic samples of reduced dimensions the shape of a sample can induce shape anisotropy due to the magnetostatic energy. The magnetisation will prefer certain directions due to its shape and will exhibit increased magnetostatic energy for certain magnetisation configurations. In a thin film (<20nm) of Permalloy (used in this thesis extensively) which is a soft ferromagnetic material, there are little to no intrinsic anisotropic effects in the Permalloy. In the absence of an applied field this leaves only the exchange interaction and the magnetostatic energy (which can be influenced by shape for micrometre and nanometre sized magnets). The

magnetostatic energy is minimised by the formation of domains to reduce any stray fields as discussed previously and is thus minimised in the plane of the film. For a thin film only perpendicular magnetostatic anisotropy exists with it costing more energy to magnetise a thin film in the direction of its smallest dimension (thickness). The exchange interaction thus dominates in a thin film and application of a magnetic field causes the magnetisation to rotate coherently, always maintaining small angles between adjacent magnetic moments. The same theory is applicable to a nanowire although the reduction in width to nanometre dimensions forces the magnetisation to lay along the long axis of the wire driven by exchange and shape anisotropy.

2.5. Domain wall types

There are various domain wall structures that form based on the competing energetic terms described above. The nanowire dimensions investigated in this thesis and the material used ensure that either transverse or vortex domain walls are formed [10] [11], the spin structure of both domain wall types is displayed in **Figure 2-5**. The vortex wall type corresponds to the bottom images of a) and b). The transverse wall corresponds to the top images in a) and b). Both domain wall types behave differently and can be distinguished experimentally in various ways.

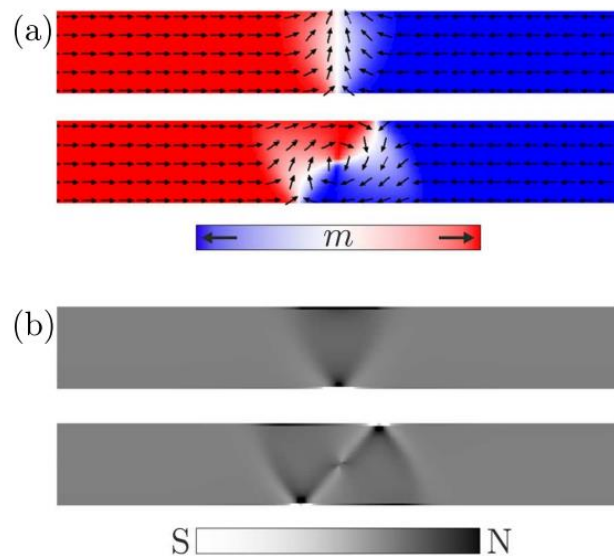


Figure 2-5 Showing the relevant domain wall types studied in this thesis. Top images in a) and b) correspond to a transverse domain wall and are generated using OOMMF. The bottom image of a) and b) corresponds to a vortex domain wall type, these images show the divergence of the magnetisation in magnetic nanowires. Image adapted from [11].

2.6. Domain Wall Anisotropic Magnetoresistance (DW AMR) in NiFe Nanowires.

The formation of domains was discussed in terms of an energy minimisation process in section 2.4.4. Here the models that are used to compare domain wall anisotropic magnetoresistance (DW AMR) data within chapter 5 are developed, namely the 1D model for DW AMR in planar nanowires and the conduction channel model [12]. The DW AMR is the change in a nanowires resistance due to the presence of a domain wall. The change in resistance stems from the resistivity depending on the angle between the current density vector and the magnetisation vector. A domain wall in a nanowire presents a deviation to the magnetisation of a nanowire typically aligned along the long axis of a nanowire giving rise to characteristic DW AMR signal for each domain wall type based on the exact spin structure of the considered domain wall. It has been shown experimentally that DW AMR measurements can be used to identify the domain wall type and chirality in reference [13], where AMR measurements were combined with magnetic force microscopy to show a unique AMR signature for each domain wall type. This research paper demonstrates the power of identifying domain wall types using AMR solely. However this research paper only considers a single width and thickness and a theoretical description of the AMR signature for different domain wall types as a function of both width and thickness is highly desirable.

2.6.1. 1D Model for Doman Wall AMR in Planar nanowires

A simple expression for the DW AMR is obtained using the 1D model for planar nanowires that was developed by Nakatani *et al.* [14]. The model using the theoretical framework of Bloch walls applied to nanowire dimensions in 1D, A key simplification in this model is the estimation of the domain wall width parameter which is known to underestimate the domain wall width. The estimation of the domain wall with parameters are obtained by fitting the domain wall magnetisation profile to the magnetisation profile of a 1D Bloch wall. The DW AMR predicted by the 1D model is width independent and only depends on the thickness of the nanowire and the AMR. The full width over which a domain wall magnetisation rotates is at

least three times larger than what is obtained through the fitting procedure described in reference [14]. The equations governing the DW AMR are **Equation 11** and **Equation 12** for transverse and vortex domain wall types respectively.

$$\partial R_{TW} = \frac{2 \partial \rho}{\pi t} \quad \text{Equation 11}$$

$$\partial R_{VW} = \frac{3 \partial \rho}{2t} \quad \text{Equation 12}$$

Where ∂R corresponds to a change in resistance, $\partial \rho$ a change in resistivity (how to evaluate this was defined earlier), t is the thickness. The vortex domain wall type is seen to have a larger contribution to DW AMR than the transverse domain wall type and this is assumed due to the larger wall width, which makes sense when one compares the micromagnetic images for both domain wall types.

2.6.2. Conduction Channel Model

The conduction channel model is another model used to predict the DW AMR [12]. It is based on taking the full spin structure of the domain wall into account as opposed to an under estimation of the domain wall width as in the 1D model presented in the previous section. The micromagnetic software (OOMMF) is used utilising a 2D solver to simulate the DW AMR in a nanowire, the nanowire is thus deconstructed into cells (typically 5nm) and these cells will also be used to form a resistor network (See **Figure 2-6**) and calculate a resistance. In the framework of OOMMF the magnetic saturation of Permalloy is set to be 860×10^3 A/m, the exchange energy constant is set at 13×10^{-12} J/m and the damping parameter is set to 0.5 to speed up the simulation time. The nanowire is modelled with no domain wall initially and the resistivity of each cell is calculated according to **Equation 24** where the resistivity depends on the angle between the magnetisation and current density vector (the current density is presumed to be parallel to the long axis of the nanowire). Another simulation is then performed (same dimensions) where a domain wall of a specific type is introduced into the nanowire and allowed to relax, the same process is then followed to obtain the resistivity with a domain wall present in the nanowire. The difference is taken between the nanowire with a domain wall and the nanowire

without a domain wall to obtain the resistivity associated with a specific domain wall type for a specific thickness and width. Using the standard equation for resistivity and the dimensions of the nanowire it is possible to convert the resistivity to a resistance, thus the DW AMR of a domain wall type is obtained. The simulations are carried out for a variety of thicknesses and widths. The end result is a width dependent domain wall resistance that directly depends on the detailed spin structure of a domain wall.

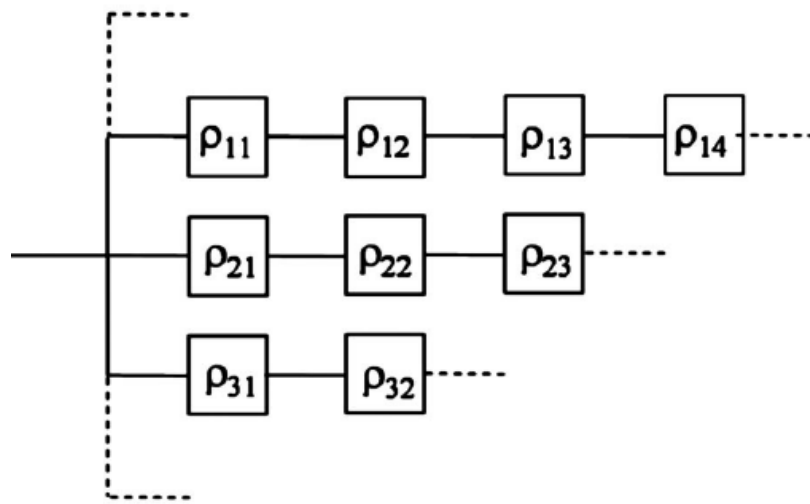


Figure 2-6 Showing how a nanowire can be deconstructed as a resistor network and using the OOMMF software this model can be used to evaluate the DW AMR. Image adapted from reference [12]

2.7. Spin Transport in Lateral Spin Valves Theory

2.7.1. Introduction

Spintronics is concerned with utilising the spin degree of freedom for technological applications and fundamental physics. The word spintronics itself is a portmanteau of the words spin and electronics, highlighting that spintronics is a merging of modern charge based electronics with the electrons spin degree of freedom. The idea is to create a generation of devices that incorporate and utilise both spin and charge as opposed to just charge. As devices get smaller and smaller the inclusion and understanding of how spin affects electronic transport is essential. The motivation behind modern day spintronics research is well summarised by Coey's lemma [4], it states "Conventional electronics has ignored the spin of the electron".

The electron is historically known to have two technologically important physical properties charge and spin [15], [16], although modern electronics has focused solely on the charge aspect of the electron in most devices. For example, complementary metal-oxide semiconductor logic (CMOS) technology which is used in modern computers to encode information, stores binary information by the presence or absence of charge on the gates of a CMOS transistor. These devices consume significant power only whilst being switched between the 0 and 1 states and are a scalable technology [4]. All modern electronics pre 1990 only incorporate charge in a functional manner and neglect spin, microscopically the electrons in any device obviously have spin but there is not net polarisation, spin being an un-conserved quantity unlike charge. For the development of spintronics then, the generation of a spin current was first needed. Spintronics is now heavily researched within the condensed matter physics community due to the promise of low power non-volatile data storage, novel device physics based on spin rather than charge, the need to understand the effect of spin which cannot be ignored as devices get smaller and smaller and from a fundamental point of view, with respect to furthering our understanding of the spin degree of freedom.

2.7.2. Two Current Model – Mott's Discovery

The first step towards creating spin transport based components was the discovery of the two current model applicable to ferromagnets developed by Mott [17] in the 1930s. He was investigating anomalous resistivity behaviour upon doping ferromagnets and postulated that the anomalous behaviour could be explained if the ferromagnets electrical transport was comprised of two independent charge carrier families i.e. spin up and spin down. Mott suggested that the two families of charge carriers were independent in the sense that a spin up electron would rarely undergo a scattering event which would change its spin direction when considering the timescales of all other scattering processes for the given problem.

2.7.3. Spin Asymmetry – The Final Ingredient to Make Spintronics a Reality

The same interaction that drives ferromagnetic ordering (the exchange interaction) discussed earlier in section 2.4.1 enables spin transport to be a possibility. The introduction of the two current model states that charge carriers within a ferromagnet are of two independent families. If the two families conduct equally well then no net spin polarisation in a ferromagnet would result, as an additional caveat the two independent families must contribute to the overall conduction differently. The exchange interaction creates an asymmetry in the band structure of a ferromagnet as shown in **Figure 2-7**.

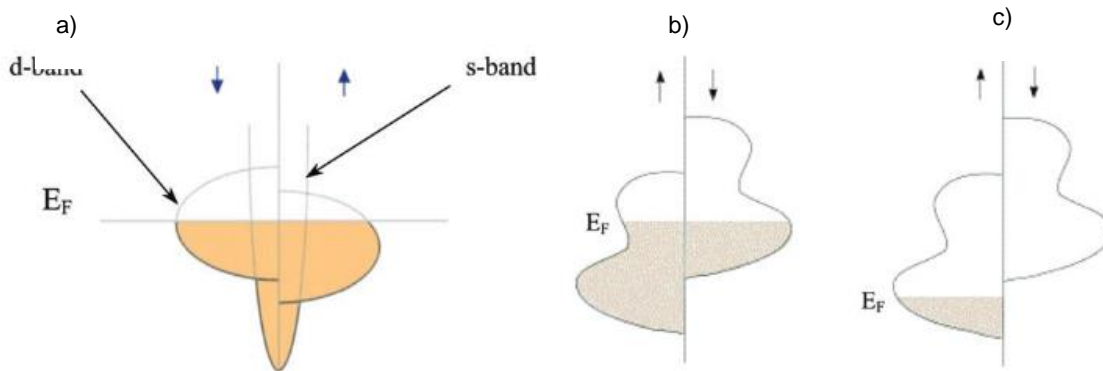


Figure 2-7 Showing the spin splits density of states of a typical ferromagnet (a), the exchange splitting of the band structure presents different sections of the band structure to the Fermi level, for each spin state, thus resulting in different mobility's for the spin up and spin down carriers. Image adapted from [18]

This implies that for a current passing through a ferromagnetic metal the conduction is primarily mediated by charge carriers with the largest mobility. If current is then passed from a ferromagnet into a non-magnetic material, the injected current will be spin polarised by virtue of the differing mobility's of the charge carriers. Image b) and c) of **Figure 2-7** show the band diagrams of a spin split ferromagnet and a half metal respectively. The physical importance of a half metal is that it only has one type of carrier available for conduction at the Fermi level. Thus it is possible to achieve 100% spin polarised spin injection if there is only one type of carrier (spin up or spin down) available at the Fermi level as is the case with a half metals. Successful spin injection from half metals has been hampered mostly by interface issues [19].

2.7.4. Spin Accumulation

If a ferromagnet is used to inject spins into a non-magnetic metal, a dynamic equilibrium will be setup between how fast spins are being injected versus the rate spins lose their polarisation, this defines a characteristic length scale known as the spin diffusion length. The previously ignored spin flip processes discussed in section 2.7.1 now have to be considered in the non-magnetic metal. The spatial dependence of the injected spin decays exponentially with respect to distance away from the injecting interface. It is possible to make a simple estimate of the spin diffusion length which highlights the underlying physics and gives a remarkable accurate answer as compared to more in depth calculations, such as a full treatment in 1D using the diffusion equation presented later.

2.7.5. Estimation of the Spin Diffusion Length

Consider an injected spin, it undergoes N momentum collision altering events until its spin is finally flipped (defining an average spin flip time $\tau_{\uparrow\downarrow}$). The average distance between momentum scattering events is known as the electron mean free path λ . Using the random walk model it can be said that the injected spin penetrates to an average depth of $\lambda\sqrt{\frac{N}{3}}$ (where a factor of three is included to account for the three dimensions an electron can move in). This derived distance is known as the spin diffusion length. The total distance travelled by an injected spin is $N\lambda = v_f \tau_{\uparrow\downarrow}$, using this relation it is possible to eliminate N from the average distance to obtain the spin diffusion length as a function of the mean free path, Fermi velocity and spin scattering time.

$$\lambda_{sd} = \sqrt{\frac{\lambda v_f \tau_{\uparrow\downarrow}}{3}} \quad \text{Equation 13}$$

This equation highlights the effects impurities have on the spin diffusion length, for increased impurity levels not only does the mean free path of the electrons reduce but also it reduces the spin flip time by virtue of introducing more spin-orbit scattering into the system. The above equation allows estimation of the spin diffusion length,

taking silver as an example it is possible to obtain spin diffusion lengths of micrometres for very pure silver and 10nm for a 1% gold doping [20].

2.7.6. A Simple Two Terminal Device – A Spin Valve

The simplest possible device utilising spin transport in a functional manner is shown in **Figure 2-8**. It is possible to construct a simple two terminal device known as a spin valve, where the resistance of the device is spin dependent.

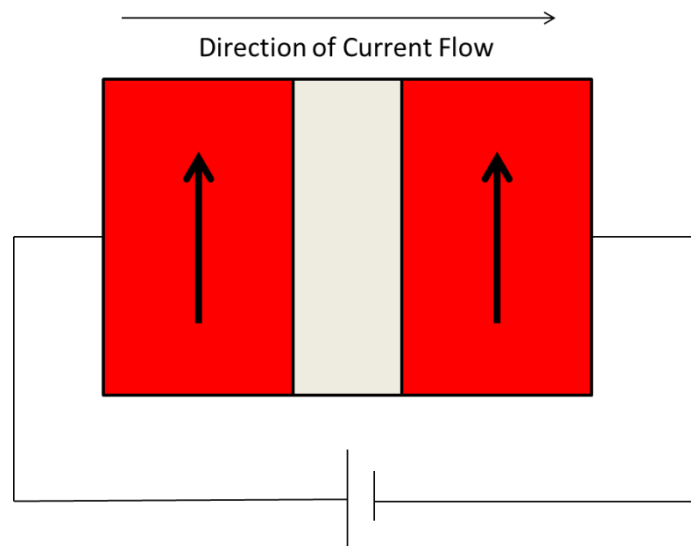


Figure 2-8 Showing a simple two terminal device whose output resistance depends directly on spin dependent transport. This known as either a spin valve or giant magnetoresistance head. Image adapted from reference [18]

Error! Reference source not found. **Figure 2-8** is a two terminal device, the bright red outer section of the device corresponds to ferromagnetic electrodes and the light grey area corresponds to a non-magnetic metal. If spin is injected from the ferromagnetic (on the left) into the non-magnetic medium, provided the length of the non-magnetic medium is no more than a few diffusion lengths, injected spins will reach the second magnetic electrode and will be scattered more or less depending on the orientation of the second ferromagnetic (right electrode) with respect to the first. For parallel alignment of the magnetic electrodes (Shown in **Figure 2-8**) the device is in a low resistance state and for anti-parallel alignment the device is in a high resistance

state. This effect has been termed giant magnetoresistance due to the change in resistance being as large as 100%. These simple two terminal devices were quickly optimised and used to replace an older technology in hard disk drive read heads. Anisotropic magnetoresistance sensors were the replaced older technology which showed changes in resistance in response to a magnetic field on the order a few percent.

2.7.7. Theory of Spin Injection and Accumulation

The following derivation follows the lines presented in reference [21]. The electrochemical potential is used to describe spin transport in the diffusive regime. Using the electrochemical potential it is possible to write down the potential energy for an electron as:

$$\mu_E = \mu_{ch} - eV \quad \text{Equation 14}$$

Where μ_E is the electrochemical potential, μ_{ch} is the chemical potential (defined as the excess electron density n , divided by the density of states at the fermi level $\left[\mu_{ch} = \frac{n}{N(E_f)}\right]$ equation 14 shows it is possible to consider electron transport as a consequence of a spatially varying electron density (diffusion) or application of an electric field (drift). The term eV (electron volts) is a measure of energy, in particular it is the energy transferred to an electron in an electric potential of a single Volt. The diffusive picture is used to build up the model of spin transport as it physically relates to the lateral spin valve systems which are setup by spatially varying electron densities. The two pictures (drift and diffusion) are equivalent and related via the Einstein relation:

$$\sigma = e^2 N(E_f) D \quad \text{Equation 15}$$

σ is the conductivity, $N(E_f)$ is the density of states at the fermi level, e is the fundamental electronic charge and D is the diffusion constant.

Valet and Fert [22] used the Boltzmann transport formalism to derive expressions that related the parameters of the a spin transport system to the measureable quantities i.e. spin diffusion length, injection efficiency etc. as a function of the

voltage induced by spin accumulation. This formalism has been adapted to describe spin transport in lateral structures in reference [21] .

Stemming from the two current model discussed in section 2.7.2, electronic transport in a ferromagnet may be represented by two independent channels, each with a distinct conductivity.

$$\sigma_{\uparrow} = N_{\uparrow} e^2 D_{\uparrow} \quad , \quad D_{\uparrow} = \frac{1}{3} v_{f\uparrow} \tau_{e\uparrow} \quad \text{Equation 16}$$

$$\sigma_{\downarrow} = N_{\downarrow} e^2 D_{\downarrow} \quad , \quad D_{\downarrow} = \frac{1}{3} v_{f\downarrow} \tau_{e\downarrow} \quad \text{Equation 17}$$

Where $N_{\uparrow\downarrow}$ denotes the spin dependent density of states at the fermi energy and $D_{\uparrow\downarrow}$ is the spin dependent diffusion constants defined in terms of the spin dependent fermi velocities $v_{f\uparrow\downarrow}$ and electron mean free path $\tau_{e\uparrow\downarrow}$. The notation for spin up is assumed to be the majority carriers in the following derivation. It is worth noting that both spin dependent conductivities play a role in producing a net spin polarisation, for a magnetic tunnel junction however it is defined by the spin dependent density of states directly. For the use of single defined spin dependent conductivities to be used the electronic scattering times and inter-band scattering times need to be smaller than the timescale at which spins flip, this is generally the case. Due to the difference in conductivities the current in a ferromagnet is distributed over two channels:

$$j_{\downarrow} = \frac{\sigma_{\downarrow}}{e} \frac{\partial \mu_{E\downarrow}}{\partial x} \quad \text{Equation 18}$$

$$j_{\uparrow} = \frac{\sigma_{\uparrow}}{e} \frac{\partial \mu_{E\uparrow}}{\partial x} \quad \text{Equation 19}$$

Where $j_{\uparrow\downarrow}$ are the spin up and spin down current densities, other terms were defined earlier. Equations 18 and 19 effectively state that the current in a ferromagnet is spin polarised. The polarisation being given by:

$$\alpha_F = \frac{\sigma_{\uparrow} - \sigma_{\downarrow}}{\sigma_{\uparrow} + \sigma_{\downarrow}}$$

The model developed thus far required introduction of the spin flip time for both spin states: $\tau_{\uparrow\downarrow}$ being the spin flip time for a spin up to flip to a spin down and the reverse applies for $\tau_{\downarrow\uparrow}$. In equilibrium the number of spins flipping to spin down from a spin up state equals the number of spins flipping to a spin up state from a spin down state, expressed mathematically with the following equation: $\frac{N_{\uparrow}}{\tau_{\uparrow\downarrow}} = \frac{N_{\downarrow}}{\tau_{\downarrow\uparrow}}$, it is now possible to setup a diffusion equation (in 1D only) where the diffusing species is spin and the rate of diffusion is controlled by the spin flip processes.

$$D \frac{\partial^2(\mu_{E\uparrow} - \mu_{E\downarrow})}{\partial x^2} = \frac{(\mu_{E\uparrow} - \mu_{E\downarrow})}{\tau_{sf}} \quad \text{Equation 20}$$

Where $D = D_{\uparrow}D_{\downarrow}(N_{\uparrow}+N_{\downarrow})/(N_{\uparrow}D_{\uparrow} + N_{\downarrow}D_{\downarrow})$ is the average spin diffusion constant. The average spin relation time is defined as: $\frac{1}{\tau_{sf}} = \frac{1}{\tau_{\uparrow\downarrow}} + \frac{1}{\tau_{\downarrow\uparrow}}$. Note the definition of the average spin relation is equivalent to T_1 (magnetisation relaxation in the direction of the applied field) in the Bloch equations. The general solution of **Equation 20** is of the form:

$$\mu_{E\uparrow} = A + Bx + \frac{C}{\sigma_{\uparrow}} \exp(-x/\lambda_{sf}) + \frac{D}{\sigma_{\uparrow}} \exp(x/\lambda_{sf}) \quad \text{Equation 21}$$

$$\mu_{E\downarrow} = A + Bx + \frac{C}{\sigma_{\downarrow}} \exp(-x/\lambda_{sf}) + \frac{D}{\sigma_{\downarrow}} \exp(x/\lambda_{sf}) \quad \text{Equation 22}$$

Where $\lambda_{sf} = \sqrt{D\tau_{sf}}$, the constants A,B,C and D are evaluated from the boundary conditions of the probe at the interfaces. In particular the constant B is used to obtain the resistance change due to spin accumulation. The boundary conditions are (excluding spin flipping at interfaces and any interfacial resistance) as followed.

1. Continuity of μ_{\uparrow} and μ_{\downarrow} at the interface.
2. Conservation of the spin up and spin down currents over the interface.

Applying this formalism to a non-local geometry, details contained in reference [21] the resistance is found to vary according to **Equation 23**.

$$\Delta R = \frac{\eta^2 P^2 \rho \lambda_s}{2A} \exp\left(\frac{-L}{\lambda_s}\right) \quad \text{Equation 23}$$

The solution contains an exponential dependence on the length of the non-magnetic medium, the spin polarisation of the ferromagnetic (P), the injection efficiency of the

interface (η), the cross section area of the non-magnetic medium (A) and the spin diffusion length in the non-magnetic medium (λ_s). This equation is used to extract the stated parameters for lateral spin valve systems discussed later.

2.7.8. Literature Review

The field of spintronics was set in motion by a pivotal paper authored by Johnson and Silsbee [23]. In this research paper they processed a pure single crystalline Aluminium sample and two magnetic contacts— one for injecting spin current and the other for detecting spin current, essentially a spin valve. A schematic is shown in **Figure 2.9**. It shows the device design and the measurement configuration.

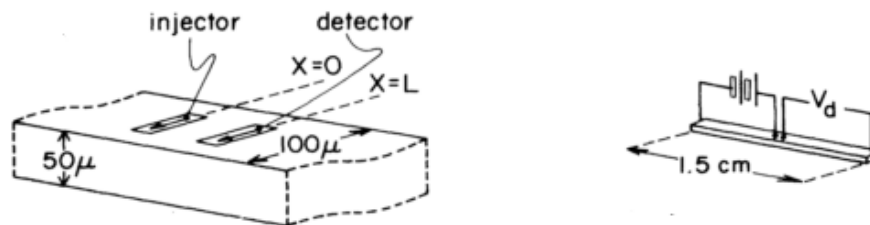


Figure 2-9 Showing the experimental setup used by Johnson and Silsbee in their pioneering research paper. Note the micrometre dimensions. Images adapted from reference [23]

If one considers the injection and detection circuits carefully it is clear that the measurement of the voltage associated with spin accumulation is independent of any charge effects. It is also clear that the smallest dimension processed within their device is in the micrometre range, L being the order of $50\mu\text{m}$ (spin channel length). As a result of the large size of their device they were required to use lower temperatures to increase the spin diffusion length (the spin signal was observed up to 50K). The premise of the experiment was that one could inject spin polarised current simply by driving a current from a ferromagnet to a non-magnetic material as discussed in section 2.7.2. Spins would be injected across the interfacial boundary and then would be able to diffuse. Provided the second (detecting) magnetic electrode was close enough i.e. within a few integer multiples of the spin diffusion length then a voltage would be detected when the injected spin diffused to the second electrode. The voltage measured at the detector electrode decreases exponentially as the spacing between the electrodes increased, due to injected spin losing memory of its spin state by virtue of spin scattering events. In the paper authored by Johnson and

Silsbee Aluminium was used as the non-magnetic medium for spin transport and Permalloy was used as the ferromagnet. Spin current was successfully shown to be injected into the Aluminium and detected at the second magnetic electrode. It was shown that the injected spin maintained the polarisation of the injecting ferromagnet and that the detecting ferromagnet was shown to give either a positive or negative signal depending on its orientation with respect to the injected spins. They also made use of Hanle measurements to measure the T_2 (defined as magnetisation relaxation perpendicular to the applied field) spin relaxation time in a low field limit regime which was also new and novel at this time. They then compared their findings to other existing methods which would allow one to calculate T_2 for similar systems using techniques such as transmission electron spin resonance. This research paper showed that creating spin polarised current was a genuine possibility and also that it could be studied in terms of spin relaxation. The progress after this initial research paper in the area is summarised in **Figure 2-10**.

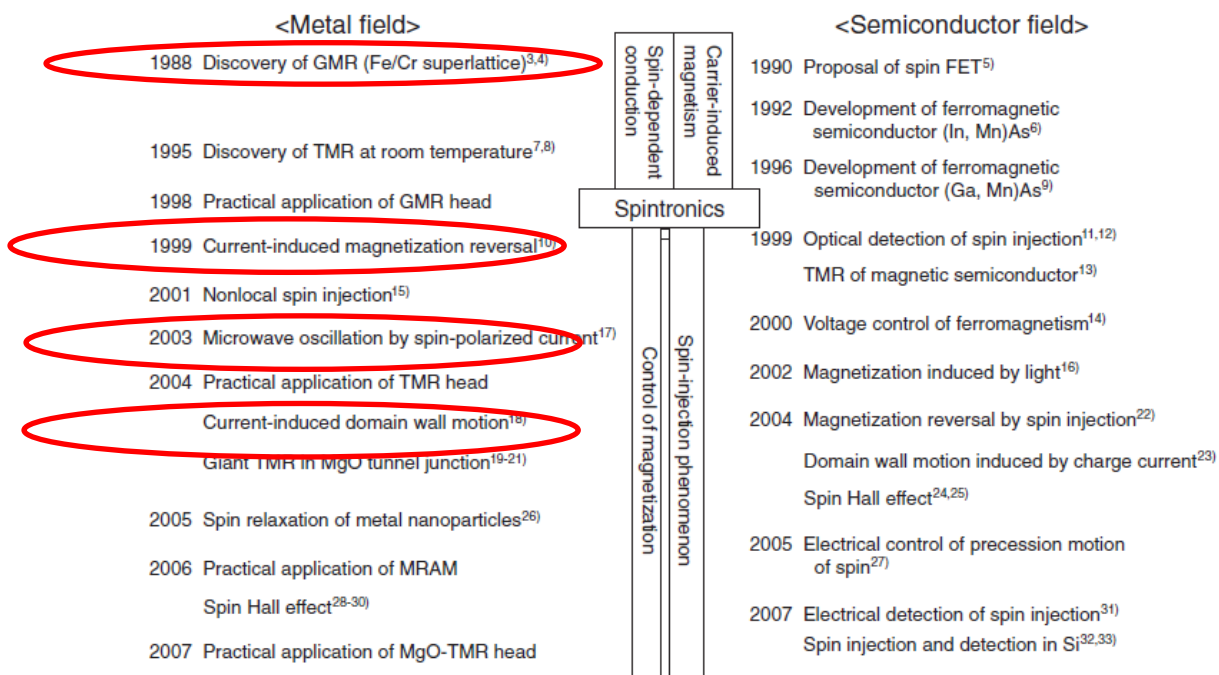


Figure 2-10 Showing the development of spintronics post 1985. The image is adapted from reference [24] A few developments most relevant to this thesis have been highlighted.

Figure 2-10 summarises the progress made after the foundation for spintronics was laid down by Johnson and Silsbee, the image was adapted from reference [24]. Firstly in 1988, which eventually resulted in a Nobel prize, Fert *et al.* [25] showed spin dependent transport at room temperature using super-lattices of Chromium

and Iron fabricated using molecular beam epitaxy. The use of molecular beam epitaxy meant atomic precision and control over the thickness of the layers involved, the effect being crucially related to the Cr layer thickness. Physically a picture was painted by this research paper whereby a spin polarised current was induced via a ferromagnetic layer (Fe) and transmitted through other ferromagnetic (Fe) layers, the Cr interlayer caused the Fe layers to couple anti-ferromagnetically at zero applied field. This meant that the resistance experienced by spin polarised electrons traveling through this structure at zero field was high as shown in **Figure 2-11**. Applying an external magnetic field to the sample had the effect of aligning the ferromagnetic layers after overcoming the anti-ferromagnetic coupling and the sample was then in a low resistance state, again shown in **Figure 2-11**. Essentially, the injected spin maintains the polarisation of the injecting ferromagnet's magnetisation and the injected spin is scattered more so by magnetisation out of alignment with the injected spin, this is summarised in **Figure 2-11** with the schematics, showing that when the magnetisation of each Fe layer are parallel the device is in a low resistance state and when the Fe layers are antiferromagnetically aligned (anti-parallel) a high resistance state is observed for the device.

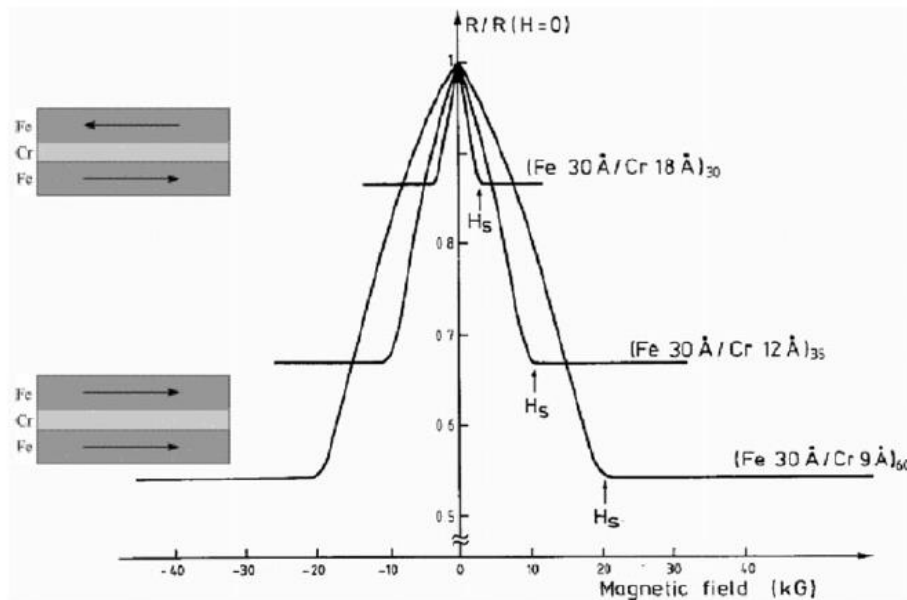


Figure 2-11 Showing the results obtained for super-lattices of Fe(0,0,1) and Cr(0,0,1) with a simple schematic to aid understanding. There is a clearly defined two states of resistance corresponding. Image adapted from [25]

up the door up for making applied devices based on spin dependent effects as opposed to devices designed and based solely on charge effects.

Quite rightfully a Nobel prize was awarded for this work “for the discovery of giant magnetoresistance” [26] and opening the doorway to study and incorporate spin dependent effects in transport phenomena across many different areas of physics.

After the research paper by Fert *et al.* [25] showing the potential for room temperature applications of spin transport, the newly established spintronics community set out to make applied devices based on two terminal spin dependent devices as prototyped by Fert *et al.* In a mere ten years after extensive research into the fundamental and applied aspects of spin transport, a first generation of devices were commercially introduced as magnetic sensors, most prominently in hard disk drive technologies as read and write heads i.e. as tiny highly sensitive magnetoresistive sensors used for reading magnetic bits of information and for re-defining the orientation of said magnetic bits also. This short period from discovery to application is exceptional when compared to other technologies, the speedy application of GMR is owed to the technology it replaces being very similar in design and application (AMR magnetic sensing technology) [27].

It wasn't until 2001 that the next development relating to metallic spintronics was made. Jedema *et al.* [28] fabricated an all metal lateral spin valve and used this device to show successful separation of the charge and spin current and also that the size of the effect was large enough ($1\text{m}\Omega$) to be exploited for device applications. They were able to fabricate a sub micrometre lateral structure by utilising the advances made since 1985 in terms of microfabrication. The increased signal size (pV to mV, associated with spin accumulation is due to the device being in the sub-micrometre range (see **Figure 2-12**) whereas Johnson and Silsbees' device was on the order of micrometres (**Figure 2-9**). Johnson and Silsbee were working in the pV signal size range and Jedema *et al.* were working in the mV signal size range. The separation of spin and charge allows one to study the effects of spin transport solely without the added complication of charge based effects superimposed on top of the spin based effects.

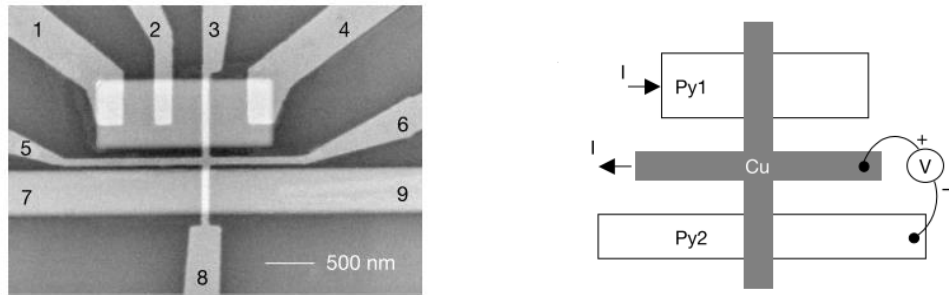


Figure 2-12 Showing the device (left image) used by Jedema *et al.* to show pure spin current injection, The right image shows the measuring configuration used to achieve pure spin current injection. Images adapted form reference [28]

The way in which they achieved pure spin current injection was by using a novel measurement configuration, the measurement configuration is shown in **Figure 2-12** (right image). A conventional electrical circuit is setup between contacts 5 and 1 for example, (see theory section 2.7.7 for a detailed explanation of non-local spin injection) by virtue of the band structure and spin split states of a ferromagnet, the current injected at the Ferromagnet/Non-magnetic interface is spin polarised. No charge will flow outside of the potential difference setup between contacts 5 and 1. Injected spin will diffuse in both directions after being injected at the interface, in one direction it will accompany the charge flow but in the other direction it will diffuse without charge. Placing the voltage contacts say 8 and 9 (**Figure 2-12**) a voltage will be measured relating to the spin accumulation (provided the distance to diffuse is less than a few multiples of the spin diffusion length) devoid of any charge based effects.

This research paper served to reinvigorate the field of metallic spintronics in light of pure spin currents and device applications based on the increased signal size, to attempt to quantify this the number of citations is a reasonable starting point, this research paper being cited over five hundred times [29] the average number of citations per paper being around 10 [30], clearly this was a pivotal paper in the field of spintronics.

The field has grown considerably since the first papers showing successful pure spin current injection [23], topics include but are not limited to the study of how a heat gradient can be used to generate a spin current (spin caloritronics) [31], optimisation

of the spin injection process [32] [33], optimisation of the spin propagation/decoherence processes [34][35], the detection mechanism [32] [36], metallic spintronics [37], [38], semi-conductor spintronics [39], [40], organic spintronics [41], [42], carbon based spintronics [43], [44], tunnel barrier spintronics (magnetic tunnel junctions) [32], [45]–[47], the creation of vertical spin valve structures (pillars) [48] and more.

A review of the literature returned some interesting research papers and corresponding concepts,. In terms of new ideas, dual spin injection involves non-locally injecting current using two closely positioned magnetic electrodes and detecting the spin accumulation using a third electrode. **Figure 2-13** shows a dual and single spin valve.



Figure 2-13 showing a standard lateral spin valve with only one injecting electrode (top image) and a dual lateral spin valve with two electrodes for injecting the spin current and a reduced volume for spin relaxation. Image adapted from reference [33]

A small enhancement was observed for dual spin valves with Ohmic junctions as injected spin at the first electrode is absorbed by the second injecting electrode before ever reaching the detecting electrode. As mentioned previously tunnel barriers reduce the spin absorption effect and so an enhancement by a factor of 2.4 was observed when using dual spin injection for a lateral spin valve that utilised tunnel barriers [33]. Also the volume for spin relaxation has been reduced as no spin will diffuse to the left in the bottom image of **Figure 2-13** but will diffuse in both directions for the single injection electrode case (top image in **Figure 2-13**). Explaining dual injection also serves to explain the enhancing of the spin signal due to geometrical confinement i.e. having less volume for the spin to relax will increase the signal as in the case of a dual lateral spin valve.

This concept was pursued and proven without the need for dual spin injection in another research paper [49]. In this paper the group fabricated a standard spin valve and a spin valve in which they essentially cut off the ends spin channel where the magnetic electrodes ended, see **Figure 2-14**. This experiment demonstrated 100% increase in the spin signal size for the geometrically confined system compared to the standard spin valve design, which makes sense as half of the spin would have been lost to diffusion in the opposite direction to the detecting electrode.

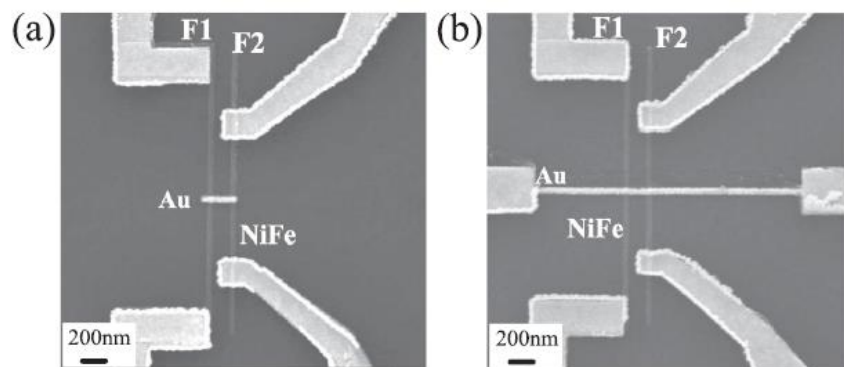


Figure 2-14 showing the two different designs used to prove that geometrical confinement of the spin relaxation volume is one way to increase the spin signal. Image a) is a standard spin valve, image b) is a spin valve with reduced volume for spin relaxation. Images adapted from reference [49]

Finally it was also shown in the literature that the use of geometrical ratchet can increase the signal size by up to a factor of 7 [50], the ratchet reduces a directional effect on the flowing spin current presenting a larger resistance in one direction as opposed to the other, therefore similar to a tunnel barrier, the backflow of injected spin is reduced in this structure due to the ratchets effect. **Figure 2-15** shows a ratchet in a real device taken from the research paper that experimentally verified this effect [49].

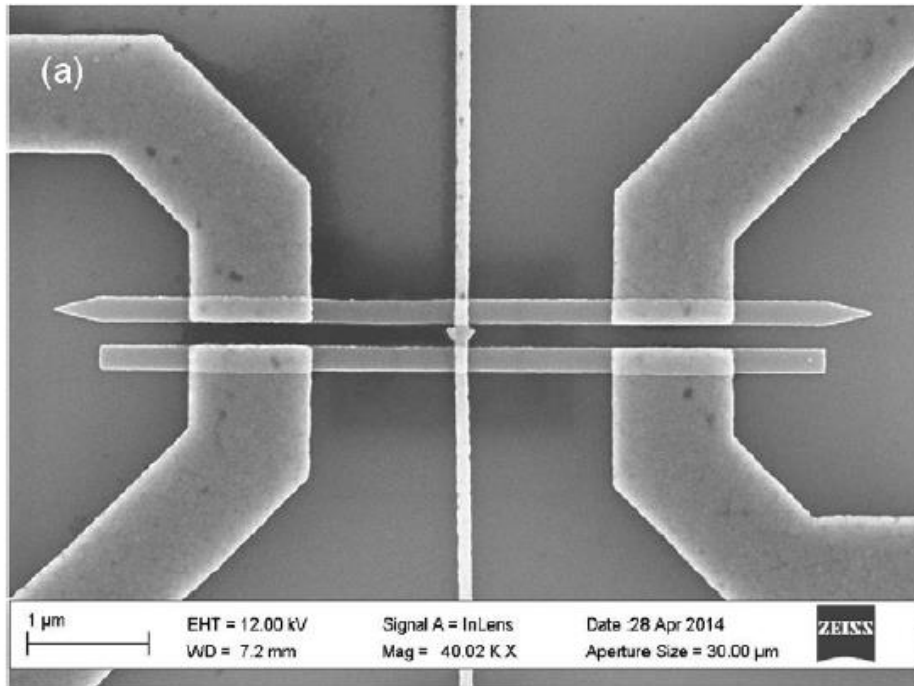


Figure 2-15 showing a geometrical ratchet design used for increasing the spin signal, by preferentially allowing spin current to flow in one direction easier than the other. Image adapted from reference [50]

3. Sample Fabrication

3.1. Introduction

For this thesis samples have been fabricated using standard nanofabrication techniques in the clean room of Cardiff University. Unless otherwise stated I have been responsible for the design and fabrication of all samples studied and reported within this thesis. Electron beam lithography combined with thermal evaporation has been used to produce all samples used in this thesis. An in-housed designed and custom built thermal evaporator was assembled during this PhD for depositing magnetic materials along with non-magnetic metals. In particular, the evaporator was assembled for making in situ electrical transport measurements during the growth of samples. There are few existing systems where magneto-transport measurements can be made *in situ* and during the growth of samples. A low noise magnetoresistance setup was also constructed during my PhD for probing samples *ex-situ*. Both systems will be discussed in more detail in due course.

3.2. Electron Beam Lithography

There are generally two approaches to producing nanostructures for today's applications and research. There is the bottom up approach and the top down approach. The bottom up approach is whereby one looks to forge nanostructures beginning with single atoms and molecules, these single atoms and molecules are the building blocks from which larger more complicated structures are built, utilising techniques such as self-assembly (spontaneous assembling) or STEM /AFM microscopes [51] (systematically placing the molecules where you want them). DNA epitomises the bottom up approach with single strands of the DNA proteins (essentially small building blocks) building larger structures such as various cells (muscular, nerve, blood etc.). The top down approach, that which is used within this

thesis, strives to take a bulk material and fashion it into a nanostructure from the top down using different processing techniques.

There are a variety of ways to implement the “top down” approach, namely electron beam lithography, focused ion beam lithography, photolithography etc.

Photolithography is a technique that uses light and its interaction with a light sensitive resist to produce micro/nanostructures, it is the standard technique for industrial and large scale production of devices but is limited by the wavelength of the light used. In a simple setup using 403nm light and simple optics a resolution of around 1.5µm is possible [51] This can be improved by reducing the wavelength of the light used and improving the optics of the system, with deep UV light and advanced optics it is possible to get line widths down to 32nm [1]. Due to the diffraction limit associated with the wave-like nature of light, there is a limit to how small a photolithographic system can be. Advantages of using photolithography are that it is cheap compared to focussed ion beam and electron beam lithography, both requiring a high vacuum, charged particles sources and a variety of lenses for focussing and controlling the beam. Photolithography can also expose multiple structures in parallel, reducing time and costs. It is possible to use electrons instead of photons to expose multiple structures at once; this is known as electron beam projection printing and is in the early stages of development [52]. It will have all of the advantages of photolithography, high throughput and short exposure times with the potential resolution of electron beam lithography. Focussed ion beam lithography could be used to produce features on the nanometre scale although it is an inherently destructive technique, an ion beam is used to directly write/bombard the surface and remove unwanted areas leaving only the desired structure. It typically results in larger line widths than is possible with electron beam lithography and longer exposure times. Ions can become implanted during milling changing the material's properties [53]. Electron beam lithography can produce very small (<100nm) sized features with minimal damage to the substrate [54]. It is electron beam lithography combined with thermal evaporation that is used to produce nanostructures in this thesis. Thermal evaporation will be discussed in the next section.

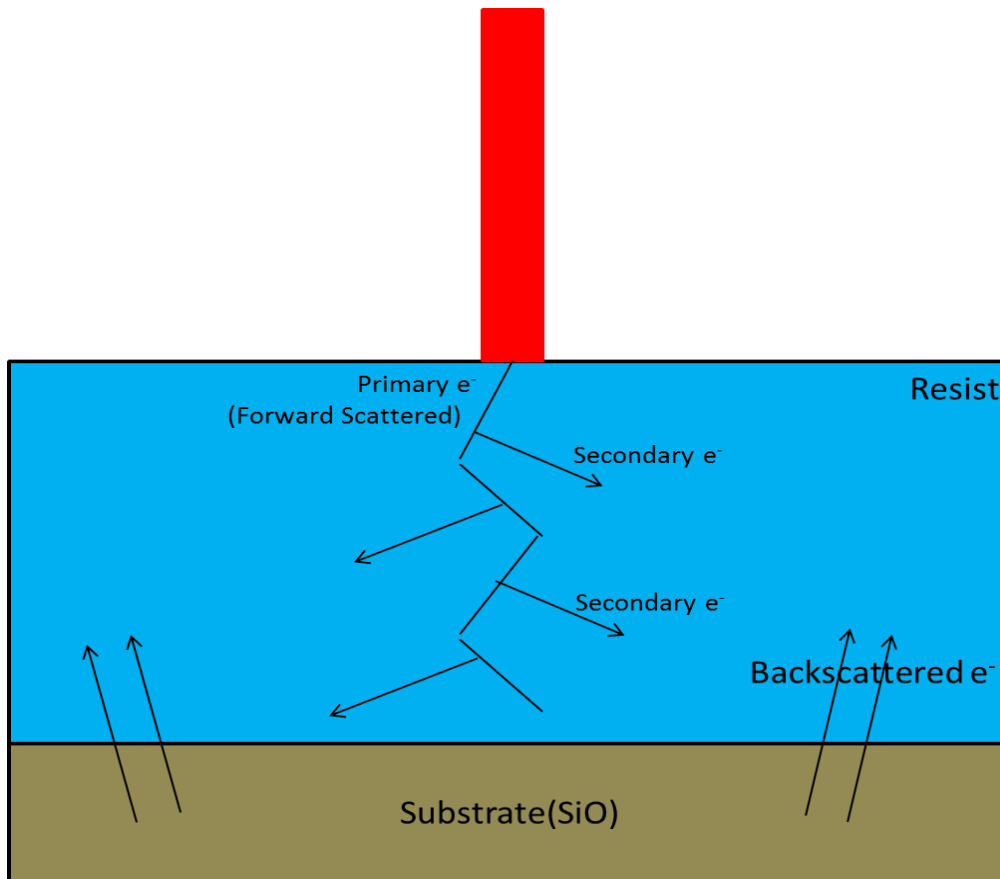


Figure 3-1 Showing the principle of electron beam lithography. Electrons penetrate the resist and can be elastically forward scattered. They can also ionise secondary electrons which have a longer mean free path. Some electrons will travel straight through the resist and interact with the substrate, backscattered electrons return from the substrate as a consequence of increased scattering in the higher density substrate.

Electron beam lithography uses a highly focussed beam of electrons to pattern resist covering a sample. It is shown schematically in **Figure 3-1** and it is conceptually straightforward. A focused beam of electrons penetrates a resist which covers the substrate. The electrons interact with the resist and the area that has been exposed to the electron beam becomes more soluble in a developer. After the desired pattern is exposed, it is then developed and the result is the resist is now a mask of the desired pattern on top of the substrate ready for deposition or some other form of pattern transfer. In other words there is a gap/hole in the resist in shape of the exposed area ready to be filled with a desired material [54] (see **Figure 3-3**).

A field emission electron source is used in the Raith e-line lithographic system to produce nanostructures in this thesis. These types of emission tips have very stable beam currents, are brighter, and have a smaller beam size than that of a thermionic emission tip, decreasing exposure times and increasing resolution. Once a beam of electrons is produced (assuming the chamber is at a low enough pressure so that

the electrons can travel from the tip to the sample with little scattering) it must be focussed to achieve high resolution patterning of the sample. Electrons can be manipulated with both magnetic and electric fields. Electrostatic lenses could be used to focus the beam but the risk of arcing in the chamber would be too high. A series of electromagnetic lenses are used to obtain the required spot size for high resolution pattern generation along with an aperture to further limit the beam diameter in the Raith e-Line system. The Raith e-Line has a beam diameter at 20keV of <2nm with a 10um aperture. The beam diameter can be as small as 1.6nm in practice for new systems [55] .

The electrons being pulled off the tip have a range of energies/velocities and as a result chromatic aberration occurs during focusing. This is because the magnetic force experienced by an electron is dependent on its velocity (similar to a wavelength dependence on refraction for light). Spherical aberration occurs also due to the non-uniformity of the field, focussing the middle and outer section of the electron beam to different extents. A tightly packed beam of electrons will also repel one another according to the coulombic interaction. There are electromagnetic lenses to counteract the effects of aberration, stigmator coils are used to ensure a round beam and alignment coils align the beam with the aperture and system. There are also two sets of coils (scan coils) that are used to raster the electron beam over the imaging area and generate an image. The description presented thus far is no different to a typical scanning electron microscope used for imaging samples with nanometre resolution [56].

For the setup to be used as a lithography setup it is essential that software is added that allows the scanning coils to be controlled and to “draw” out a specific pattern as opposed to just scanning left to right and up and down, a beam blanker is also required for moving the beam over areas that do not correspond to the pattern. In the Raith e-Line system blanking is achieved with an electrostatic lenses and a high speed pattern generator drives the raster coils for high speed beam control.

For electron beam lithography to be possible the sample must be coated with an electron sensitive resist in a controlled manner. This is done by spinning the sample whilst it is covered in an electron resist at a fixed speed for a fixed time, allowing the resist to distribute uniformly. In this thesis Polymethyl methacrylate (PMMA) of

atomic weight 950K has been used with a concentration of 4% in an anisole solution. PMMA is a long chain polymer that can be broken by a specific amount of energy bombarding it, reducing the exposed areas to the monomer chains which are then more soluble in a developer. The specific number of electrons, corresponding to this energy, required to break the polymer down is typically quoted in C/cm^2 (this is also known as the dose). After developing the exposed sample, the pattern has been written into the resist, with the exposed areas dissolving in the solution and the unexposed remaining intact (see **Figure 3-3**).

Clearly it is both, how well focussed the electron beam is and its interaction with the resist which will set the limit on the smallest possible line width. When the electron beam enters the electron sensitive resist it is inelastically scattered through small forward angles by the polymer chains, the extent of which depends on the beam energy. A higher beam energy will produce a smaller spread of forward scattering (see **Figure 3-2**). The forward scattered electrons marginally increase the exposed width with respect to the width of the incident beam. The incident electrons interacting with the resist can ionise secondary electrons that further expose the resist, these secondary electrons have a slightly larger mean free path of around 10nm which serve to further increase the width of the exposed area. Secondary electrons are produced in greater number and have greater energy for increasing beam energy, thus increasing the exposed area with increasing beam energy (see **Figure 3-2**). Many electrons will travel straight through the resist and interact with the substrate, they can undergo multiple large angle scattering events due to the increased density and cross section of the substrate and re-emerge into the resist micrometres away from where the incident beam entered. These backscattered electrons result in a low but constant dose over several micrometres from where the beam entered the resist, it is known as the proximity effect [57].

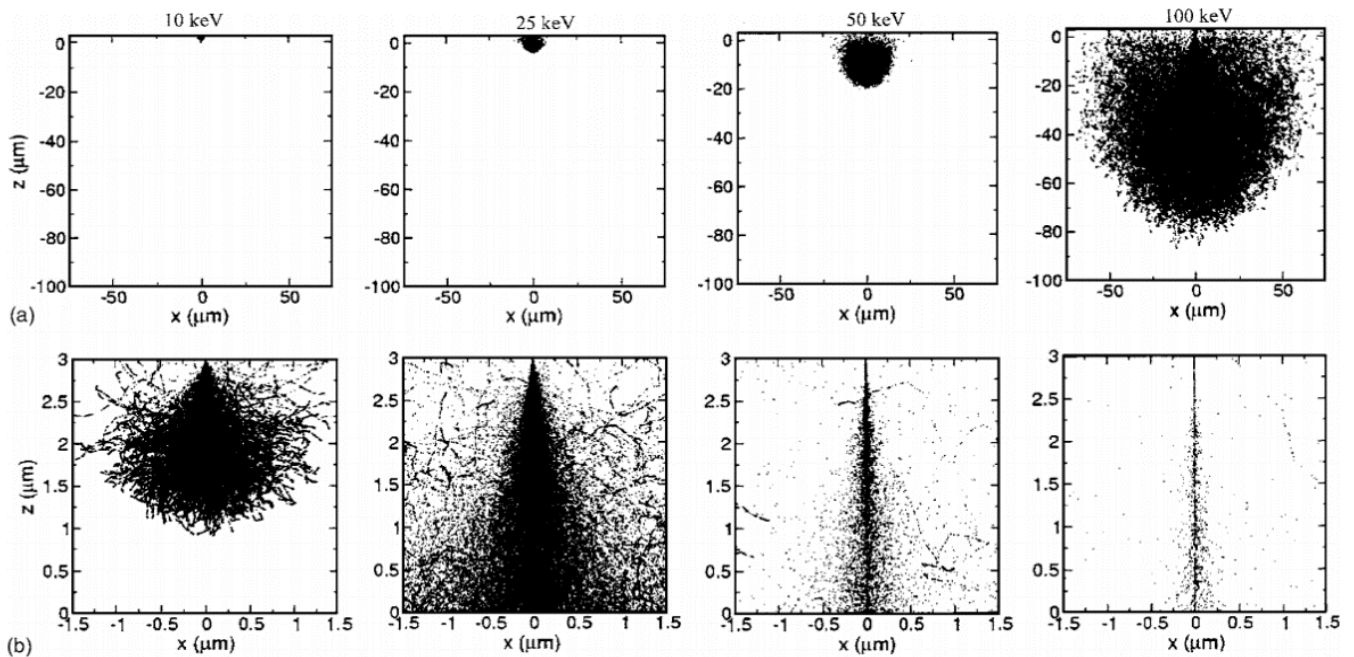


Figure 3-2 Showing the effect of secondary electrons with respect to the incident beam energy in the resist and substrate. Top images correspond to the resist and bottom images correspond to the substrate. A larger beam energy corresponds to more secondary electrons being generated in the resist and the depth and width of the exposed resist increases. In the substrate the opposite happens. Image adapted from [57].

After the resist has been exposed by the electron beam it needs to be removed, this is done by immersing the sample in a mixture of MIBK:IPA in the ratio of 1:3. The microscopic image is that the solvent penetrates the polymer matrix and surrounds fragments that have been exposed and thus chemically changed to be soluble. Developing for longer times will remove larger fragments and thus affect resolution. The final hole/gap in the resist is a product of both the exposure and the development. Different developmental procedures can yield different line widths [57]. After a gap/hole in the resist is formed all that is required now is to fill the gap with some desired material.

Parameter	Process Impact
Exposure Energy	Resolution, Sensitivity, Proximity
Exposure Dose	Pattern Quality, Proximity
Pattern Density	Proximity, Pattern Quality
Resist Material	Resolution, Sensitivity, Contrast
Resist Thickness	Resolution, Sensitivity, Pattern Quality, Proximity
Developer	Resolution, Sensitivity, Pattern Quality
Development Temperature	Resolution, Sensitivity, Pattern Quality
Development Time	Resolution, Sensitivity, Pattern Quality

Table 2 Showing the different parameters involved in EBL and how they relate to different aspects of pattern transfer. Adapted from [57]

The above table attempts to summarise the different processes involved in electron beam lithography and how each affects the overall resolution of the pattern, sensitivity of the resist to the electron beam, prevalence of the proximity effect, the overall quality of a pattern and the pattern contrast. To obtain sub 10nm linewidths understanding and optimisation of the outlined procedures is required.

The parameters used for electron beam lithography in this thesis are summarised in **Table 3:**

Parameter	Numerical Value(s)/Notes
Exposure Energy	20keV
Aperture	10 μ m
Exposure Dose	~ 200 μ C/cm ²
Pattern Density	~100nm smallest spacing b/w structures
Resist Material	950K PMMA 4% in Anisole
Resist Thickness	300nm – 45s spin at 2000rpm
Developer	IPA:MIBK in ratio 3:1
Development Temperature	Room Temp ~ 295K
Development Time	45s develop then 45s IPA rinse

Table 3 Summarising the parameters used in electron beam lithography for fabricating devices for this thesis.

3.3. Thermal Evaporation

Once the resist has been patterned, it needs to be filled with the desired material. There are a variety of deposition techniques available with different advantages and disadvantages. It is not uncommon for the material to be deposited from the vapour phase, as in thermal evaporation, molecular beam epitaxy and electron beam evaporation. It is possible however to have the deposition occur from a solution as in electrochemical deposition. Techniques for making three dimensional structures are available although they are yet to mature being in the process of characterising the technique itself, two photon initiated polymerisation being one example [58]. The different techniques all result in different crystallinity, porosity, adhesion, grain size, composition etc. Deciding what deposition system to use is a matter of cost effectiveness versus the required parameters of the film.

To deposit all materials in this thesis thermal evaporation was used. It is a straightforward technique in which the material of choice is melted in a crucible in a vacuum, the material then begins to evaporate where it condenses on the target substrate suspended about half a metre away. It is depicted in **Figure 3-4**. As simple as the technique is, it does have its limitations. A high vacuum is required to ensure an uncontaminated film is deposited and the mean free path of the evaporated species is great enough that it reaches the sample. It is heavily directional in its deposition resulting in shadowing, often causing complications during lift off as the side walls of the resist are deposited with material also (it can also connect to the metal on the top of the resist forming strong sidewalls). The energy of the particles reaching the substrate is low due to it being an evaporative process and can result in a porous film with low adhesion. Given a low base pressure during the evaporative process and a low deposition rate, good quality films can be deposited [51]. During the evaporation process, a current is used to heat the source material and a quartz crystal monitor microbalance is used to track the film thickness.

A typical evaporation involves loading a sample into the chamber with another unpatterned substrate for thickness calibration, resistivity measurements and possible other measurements (ensuring the same conditions as the fabricated devices). Pumping down the chamber for several hours until a reasonable base

pressure is achieved $\sim 10^{-7}$ mbar. The crucible is resistively heated until the material melts and begins to evaporate. The rate is set by making small changes to the current supplied to the crucible. When a steady rate is obtained the shutter is open and material is allowed to deposit on the sample(s). The material is grown up to the desired thickness and then the shutter is placed back in front of the sample to end the deposition. The chamber is then cooled and allowed up to air so the sample can be removed and further processed. A typical deposition rate is $0.2\text{\AA}/\text{s}$ and growing a 20nm film takes around 20 minutes once the rate has been set.

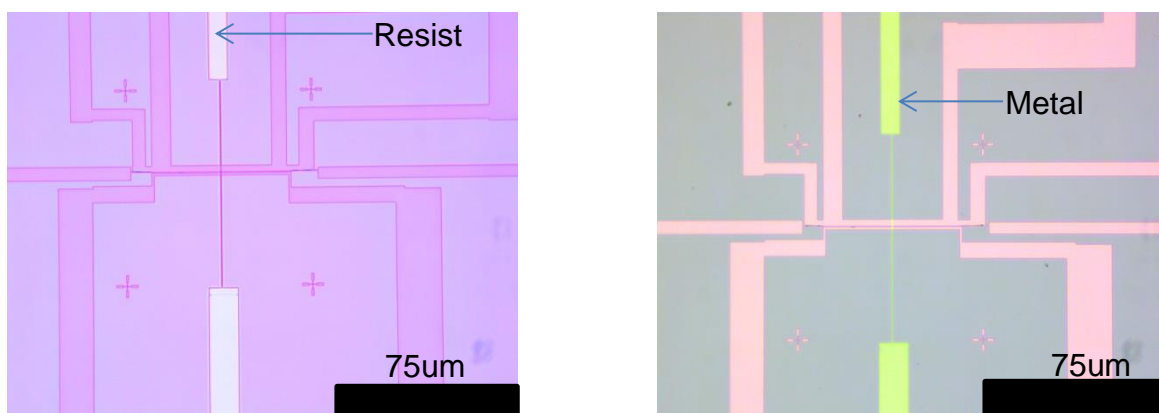


Figure 3-3 Showing optical micrographs presenting a second layer exposure of a spin channel. Left image is in the resist and the right image shows after metal deposition. The material which is already deposited and is visible through the resist is the ferromagnetic material Ni. The spin channel is Au with a Cr buffer layer (right image only). All materials were thermally evaporated. This serves to demonstrate both EBL and thermal deposition.

3.1. A Custom Built Thermal Evaporator – With Optical and Electrical *In Situ* Probes

To carry out evaporations for nanostructures in this thesis a homemade evaporator was constructed. The custom built evaporator was envisioned as a self-contained system for depositing and characterising thin films and nanostructures. It has initially been designed with two probes in mind, electrical and optical, for making magneto-transport (electrical) and MOKE (optical) measurements of samples *in situ* during growth. The vacuum system is a turbo pump backed by a dry rotary pump

with the additional option of using an ion pump for ultra-high vacuum (10^{-10} mbar). The thermal evaporator is designed in-house and custom built, consisting of a power source, a high current supply and the associated wiring along with a crucible for holding/melting the material. The details of thermal evaporation are discussed in section 3.3.

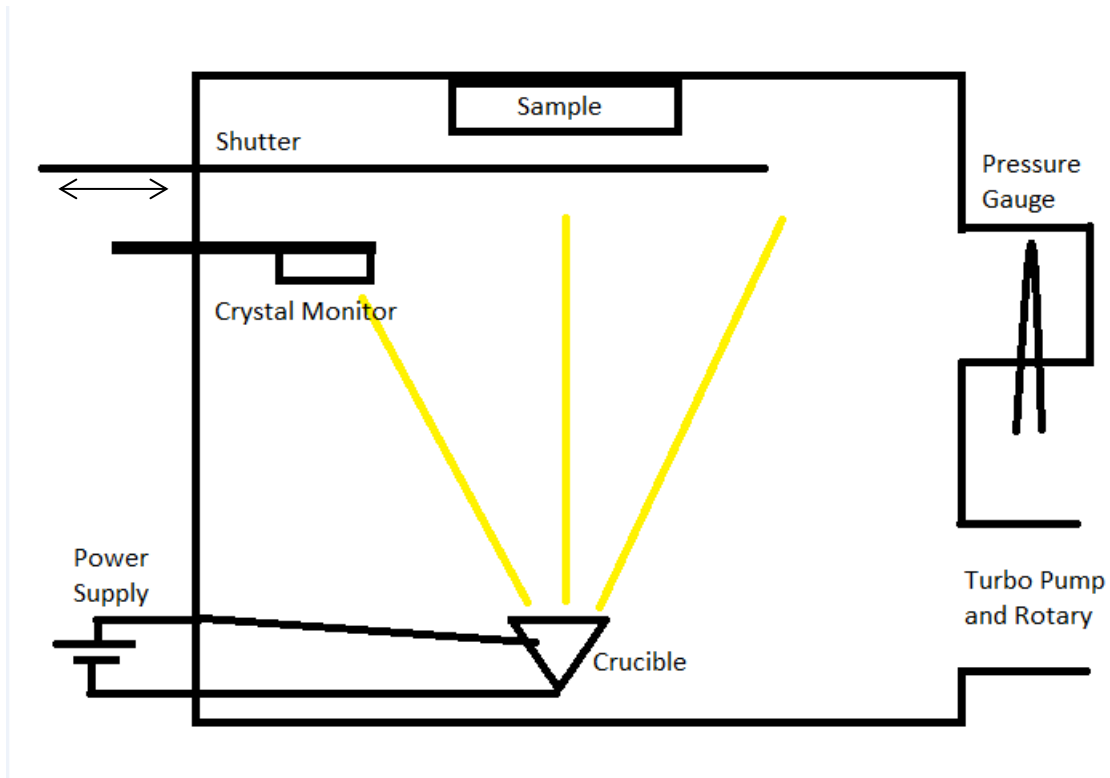


Figure 3-4 Showing a schematic of a thermal evaporation setup. The main components are a vacuum system (turbo and rotary pumps), a crucible and a power supply, crystal monitor to track thickness and a shutter to begin and end the deposition.

In order to be able to characterise magnetic material a magnet was needed inside the chamber. For materials and structures used in this thesis i.e. soft magnetic materials, a field below 30mT is more than enough to magnetise and reverse the magnetisation. A small toroidal magnet was wound and found to have adequate field uniformity and strength (see **Figure 3-5**).

I have concentrated on the electrical characterisation of samples *in situ* for my thesis and will therefore say no more about the optical capabilities of the custom built evaporator. For electrical measurement to be made inside the chamber there needs to be some electrical connection to the exterior of the system. For well resolved data and contact independent measurements four wires will be needed into the chamber to contact the sample at minimum, two for current and two for voltage. It can be

shown that using a four terminal measurement technique can give shape and contact independent resistivity measurements [59]. If the magnet is to be run simultaneously then another two wires will be needed. A vacuum component was selected that had electrical feedthroughs into the vacuum chamber and a nitrogen trap for reducing the pressure.

Eight contacts were fed through into the chamber via the vacuum component, more than enough for running the magnet and measuring a sample simultaneously. The magnet was positioned roughly 0.5m away from the deposition source, an in-house designed and custom built sample holder was used in conjunction with the magnet to enable electrical measurements to be made *in situ* as a function of magnetic field.

Figure 3-5 shows a schematic of the *in-situ* setup used to obtain data for Chapter 6.

Image a) of **Figure 3-5** shows how a foil mask is used to define the thin film area appropriately for the contacts used to carry out measurements. By selecting the pairs of wires used for the 4-terminal resistance measurement transverse and longitudinal AMR configurations can be accessed. Image b) of **Figure 3-5** shows a schematic of the sample holder without the magnet and foil mask for clarity. Silver paint is used to define contacts which the film will then be grown on top of. Care needs to be taken when aligning the mask with the contacts defined for measurements and upon loading the sample into the vacuum chamber.

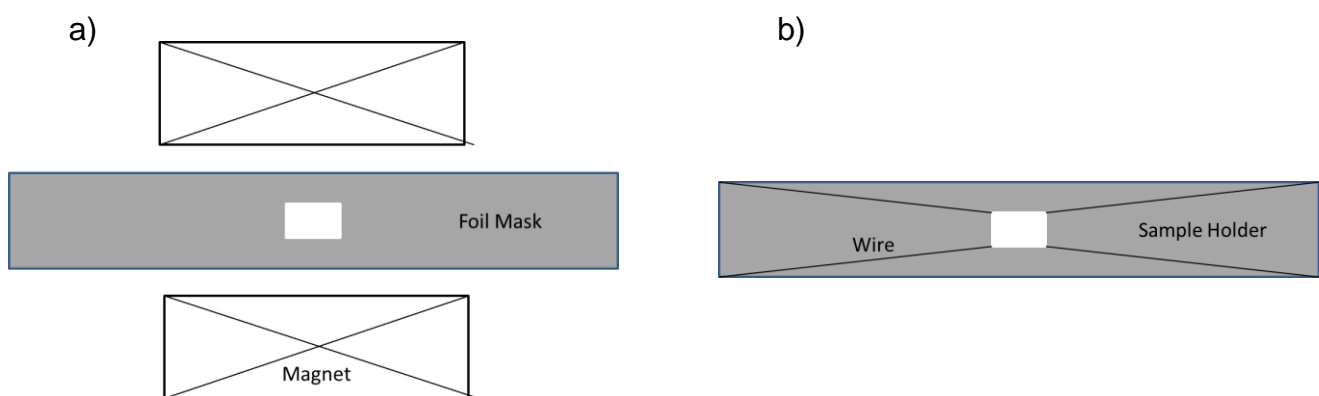


Figure 3-5 Image a) showing a schematic of the *in situ* setup prior to being loaded into the vacuum chamber. The foil is used as a mask to isolate the sample wiring from the deposited thin film. Image b) shows a schematic of the sample holder for clarity.

3.2. Sample Production

Discussed in this section is the general procedure for sample production using electron beam lithography and thermal evaporation. First a 10 x 10 mm polished SiO₂ coated silicon substrate (300nm oxide) chip is cleaned using Acetone in an ultra-sonic bath for 3 minutes, it is then rinsed in Isopropanol and then blown dry with nitrogen gas. It is then heated for 3 minutes at 80°C to aid removal of any remaining solvent via evaporation. Next the substrate is coated with 950K PMMA in a 4% Anisole solution. The resist is applied to a stationary substrate then it is spun to uniformly distribute the resist. It is accelerated to 2000rpm at 7500RPM/sec and the rotation is maintained for 45 seconds. This results in a resist thickness of around 300nm. It is then immediately baked at 180°C on a hot plate where the anisole is evaporated allowing the resist to flow, smoothen and harden. The sample is then loaded into the Raith e-Line system for exposure of the desired pattern. After exposure the sample is developed in a solution of 3:1 of IPA:MIBK respectively for 45 seconds and then rinsed in isopropanol for 45 seconds to remove any remaining exposed resist and developer. The result is that the exposed resist is removed leaving a gap/opening in the resist in the shape of the desired pattern/exposed area. The patterned resist is then further cleaned in a plasma of oxygen in which the O₂ reacts with any leftover organic compounds resulting in water vapour and carbon oxide gases. It is ashed in a plasma of power 10W for 3 minutes at a pressure of 0.6mbar.

The sample is then ready to undergo thermal metal evaporation as described in the previous section. It is loaded into the custom built thermal evaporator and pumped down until the deposition pressure is reached approximately 10⁻⁸mbar. All depositions were carried out with a rate of approximately 0.2 Å/s. After the sample has had a thin film deposited on it, it is removed from the vacuum chamber and is placed in Acetone to wash away the remaining resist, this is done overnight taking approximately 12 hours. An ultra-sonic bath is used for 20 seconds and multiple Acetone rinses are required to remove all the resist and unwanted material. The result is metal features on the SiO₂ substrate. For some devices two electron beam lithography procedures are required. The exact same process is undertaken again, the only difference is the pattern one wishes to expose is aligned with the first layer

features; it is possible to achieve second alignment down to 2nm for the Raith e-Line system [55] used to produce nanostructures in this thesis. **Figure 3-6** shows a schematic of the steps involved in sample production.

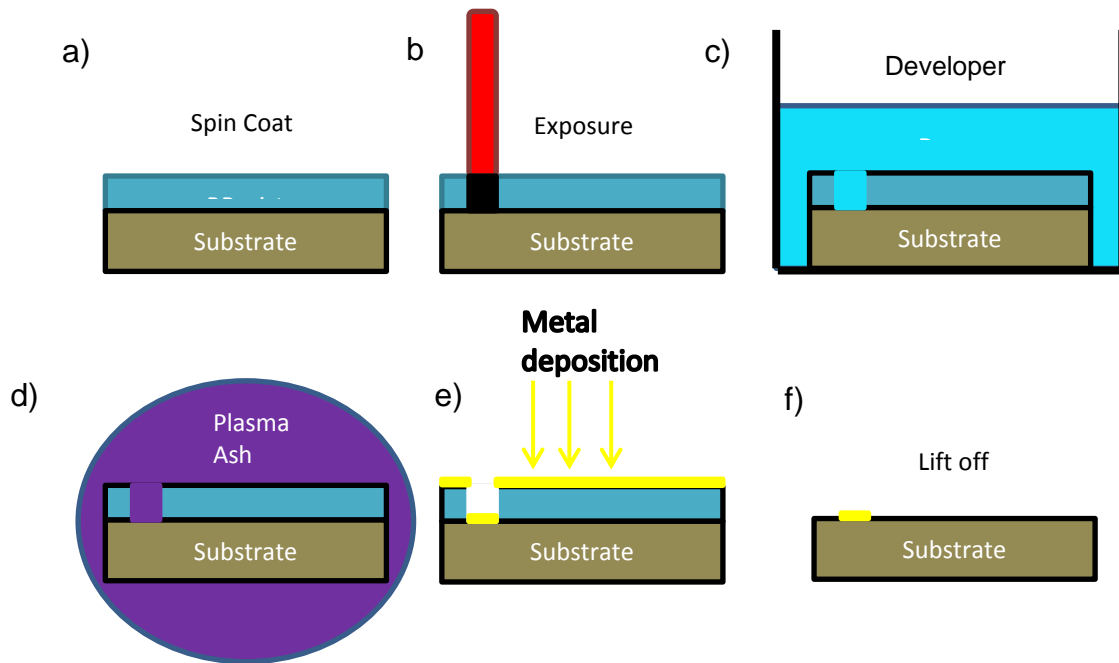


Figure 3-6. A series of images summarising the various steps involved in sample fabrication. See the text for full detail of the individual processes.

4. SAMPLE CHARACTERISATION

4.1. Introduction

There are a variety of techniques available today to characterise a sample. A first point of call in the fabrication of a nanostructure device is to use the optical microscope to judge the overall integrity of the resist after cleaning and spin coating the sample. It is then used in between every other processing step to image and monitor the fabrication process. Further instruments are required to gain further information on the sample. Thickness, roughness and film uniformity are measured using an atomic force microscope, magnetic information is probed with anisotropic magnetoresistance measurements and the magneto-optical Kerr effect. Dimensions and distances are measured in the nanoscale regime using a scanning electron microscope.

4.2. Scanning Electron Microscopy

Scanning electron microscopy is a high resolution imaging technique used to image surfaces and structures in the nanometre regime, it is used throughout most areas of sciences as a tool for research and can be used to image a variety of different types of samples/materials and also can be used to image in a variety of different modes [60]. A focussed beam of electrons is impacted on the surface and it can interact with the sample in different ways giving rise to the different imaging techniques. The electrons can scatter elastically giving rise to back scattered electrons of high energy or inelastically giving rise to low energy secondary electrons[60]. It is the secondary electrons that are collected and processed to produce an image of the sample in the Raith e-Line system using an inLens detector, the secondary electrons obtain topographical information and are surface sensitive owing to their low energy and small volume they are emitted from. The contrast shown in an in-lens SEM micrograph is related to the electronic work functions of the sample [61]. This imaging mode is ideal for imaging thin nanostructures (10's of nm's). The back scattered electrons due to their higher energy can penetrate deeper into the sample and are emitted from a greater volume. They contain information relating to the

atomic density of sample, as they penetrate much deeper. The Raith e-Line system does not have a back scattered electron detector although due to how thin the nanostructures being fabricated for this thesis are, the image would be dominated by electrons emitted from the substrate and show little contrast relating to any thin film nanostructure. The electron beam hitting the surface can also ionise the surface atoms of the sample which relax to produce characteristic x-rays which contain elemental and compositional information[61]

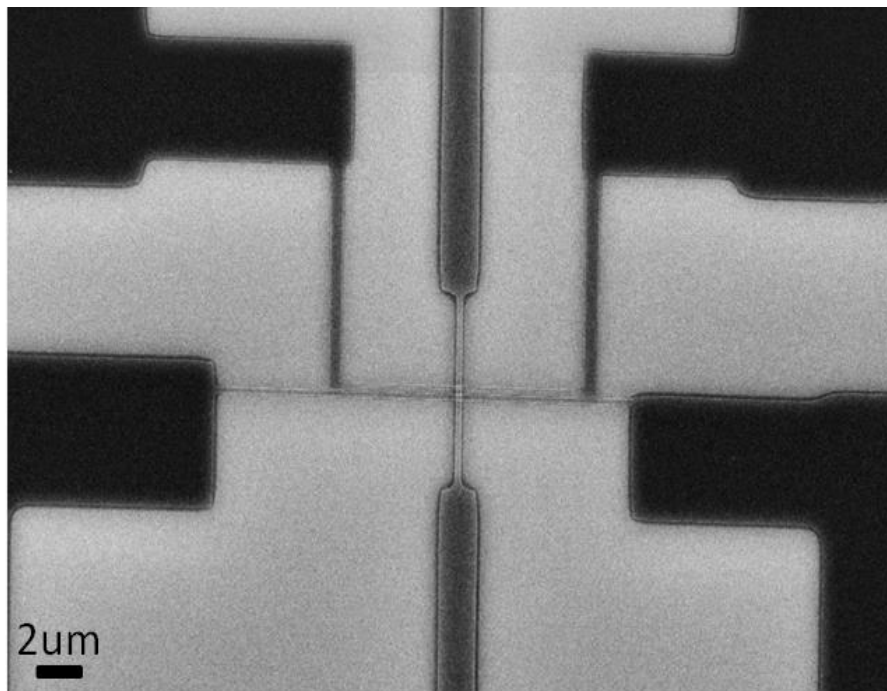


Figure 4-1 Showing SEM micrographs of a fabricated spin valve device. The spin channel (vertical conduit) is Au and the magnetic electrodes (Horizontal conduits) are made of NiFe.

Figures 4-1 and **4-2** show SEM micrographs of a fabricated spin valve device. For this thesis scanning microscopy has been used mostly for visual inspection and measurement of distances in the nanometre regime. **Figure 4-2** is a zoom in of the central section of **Figure 4-1**. The different contrasts of the three different materials are related to their electronic work functions and how easily electrons are liberated from the surface. The image shows how surface sensitive scanning electron microscopy is, the Au is imaged through the Permalloy, the Permalloy only being around 40nm thick

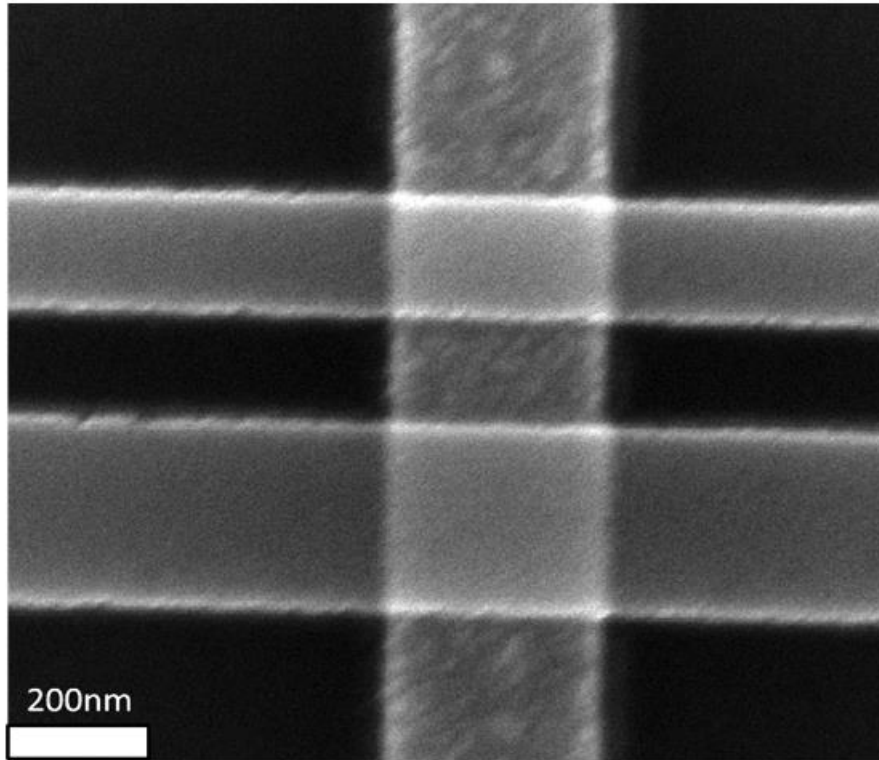


Figure 4-2 High magnification SEM image of a spin valve device, as presented in figure Figure 4-1

It is clear upon inspection of such images that nanoscale measurements are possible with this technique. Distances are easily extractable using simple line scans although care must be taken in assigning errors. When using line scans, two approaches are possible in assigning an error, multiple measurements resulting in standard statistics or detailed analysis of a single/few line scans.

4.3. Anisotropic Magnetoresistance (AMR)

4.3.1. Introduction

Anisotropic magnetoresistance (AMR) is widely used investigative technique for monitoring the magnetisation of a magnetic element using electrical measurements. It has found application within the area of magnetic recording due to its sensitivity to magnetisation direction. In the simplest sense a current is supplied to a magnetic element and an effect is observed depending on the angle between the

magnetisation and current density vectors (see **Figure 4-3**). The effect was discovered by Lord Kelvin and published in 1856 concerning Nickel and Iron [62]. It allows one to monitor the direction of the magnetisation, before, during and after a magnetisation reversal event by measuring the electrical resistance as a function of the magnetic field. Since it was first observed it has been extensively used in both research and applied physics. In applied physics it has found extensive application as a magnetic sensor within magnetic recording technologies [63], other applications including position sensors and biological applications including but not limited to tracking/directing magnetic nanoparticles or delivering drugs attached to said magnetic nanoparticles [64],[65]. As a magnetic read head (the term used to describe a magnetic sensor in a memory unit) it was only out performed with the introduction of a spin based sensor using giant magnetoresistance in 1988 [25]. In research it continues to be used to as a tool to directly monitor the magnetisation of nanoscale magnetic elements[63], [66]–[68] and as devices have been made smaller and smaller and the number of materials investigated increased, AMR has exhibited some new manifestations including but not limited to ballistic AMR (in the active region there will be no scattering of the electrons), antiferromagnetic AMR (using anti-ferromagnets rather than traditional ferromagnets) and Coulomb blockade AMR (involving a Coulomb Blockade in the device architecture), such techniques are reviewed in reference [63].

4.3.2. Practical Use of AMR

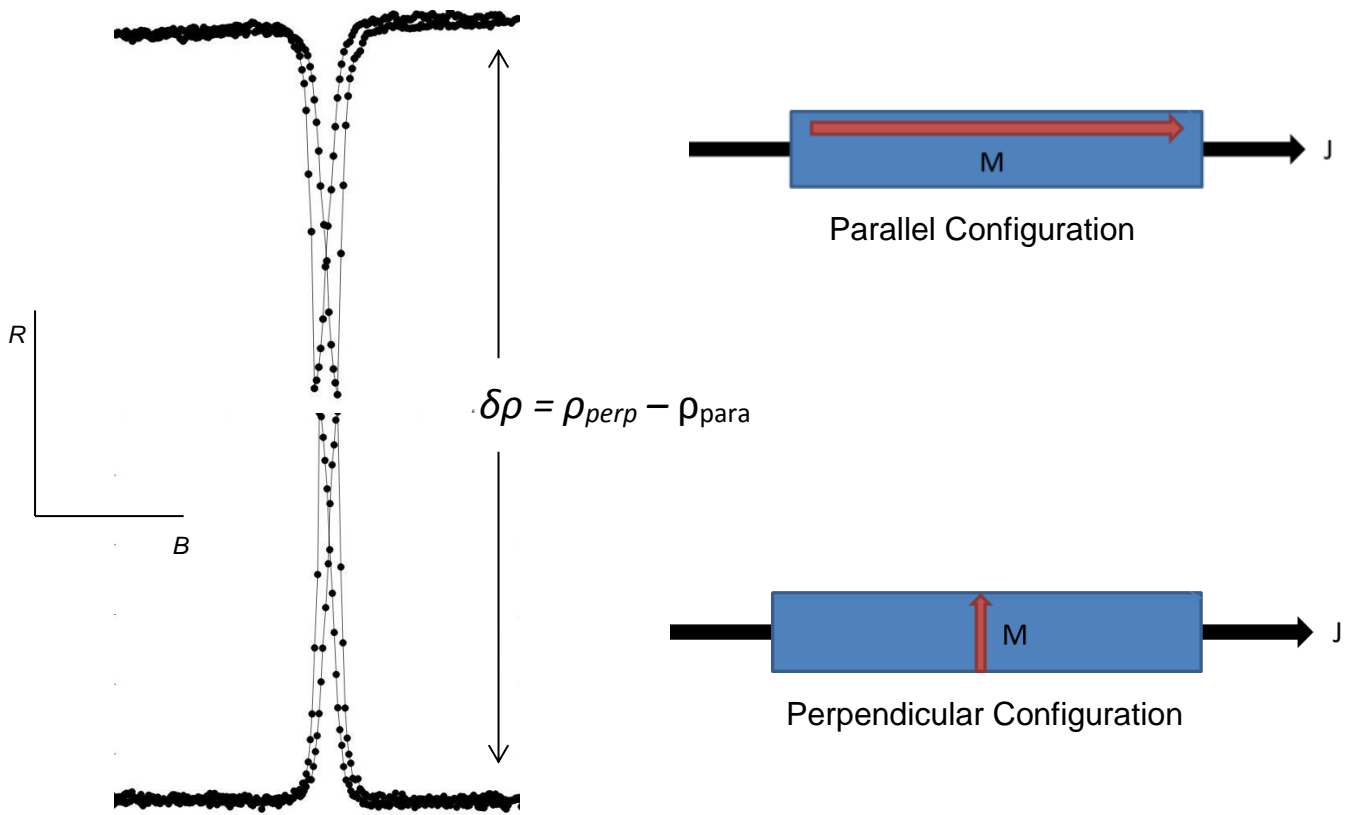


Figure 4-3 AMR curves for the typical measurement orientations in a NiFe thin film. The lowest resistance change is when the current and magnetisation are perpendicular.

To characterise the magnetisation switching of the ferromagnetic elements i.e. to obtain the coercive field of a magnetic element and its reversal mechanism an ‘AMR curve(s)’ is measured. The two measurements configurations are shown in **Figure 4-3**, corresponding to parallel and perpendicular configurations, with respect to the current density and magnetisation vectors. For a thin film of NiFe (20nm thick) the response is as shown in **Figure 4-3**. For the perpendicular case (bottom image **Figure 4-3**) the resistance is the same for both saturated magnetisations states, the same applies to the parallel case. When the magnetisation is reversing direction it begins to deviate from the current direction, this changes the resistance of the sample according to the equation:-

$$\rho(\theta) = \rho_{para} + \delta\rho \cos^2(\theta) \quad \text{Equation 24}$$

Where $\rho(\theta)$ is the resistivity as a function of angle, ρ_{para} is the resistivity in the parallel configuration at magnetic saturation, $\delta\rho$ represents a change in resistivity (shown in **Figure 4-3**). **Figure 4-3** presents the two curves expected for measuring a thin film in the configurations shown. Given the two curves it is now possible to attempt to interpret the two curves for the parameters: coercive field and reversal mechanism (this is for a thin film of NiFe)

The coercive field is the easier of the two to extract from the curves, it is given by the minimum (maximum) value of the resistance for the parallel (perpendicular) case. The largest deviation of the resistance occurs when the current and magnetisation are separated by a 90° angle so for the parallel case at the point where the resistance is lowest corresponds to the magnetisation being midway through reversal (geometrically). For the perpendicular case, the resistance increase is due to the magnetisation being at a 90° angle during the saturated state, therefore the current density and magnetisation vectors are parallel midway during reversal and so an increase in the resistance is measured in this configuration. The coercive field is defined as the amount of energy required to demagnetise a sample, this means at the minimum or maximum point (depending on configuration), the sample has begun demagnetisation and this is taken as the coercive field by convention, at this point the curve becomes irreversible further supporting that it is the coercive field. For a thin film of NiFe the whole process occurs over field ranges of only a few mT. For a NiFe 20nm thick film of 10mm x 10mm lateral dimensions the coercive field is approximately 0.5mT. To extract the reversal mechanism it is more difficult. Further analysis is required, see chapter 6.

For a NiFe nanowire, the same theory is applied (AMR) but due to the change in geometry a change in the reversal mechanism and coercive field results. How and why is due to the different competing energy terms that drive magnetic behaviour discussed in 2.4. In short the relevant energy terms all have a geometrical dependence, resulting in a defined easy axis along the long axis of a nanowire. For a nanowire, given the easy axis, it is possible to extract the coercive field and rotational mechanism from a single AMR measurement, with current and applied magnetic field parallel to one another.

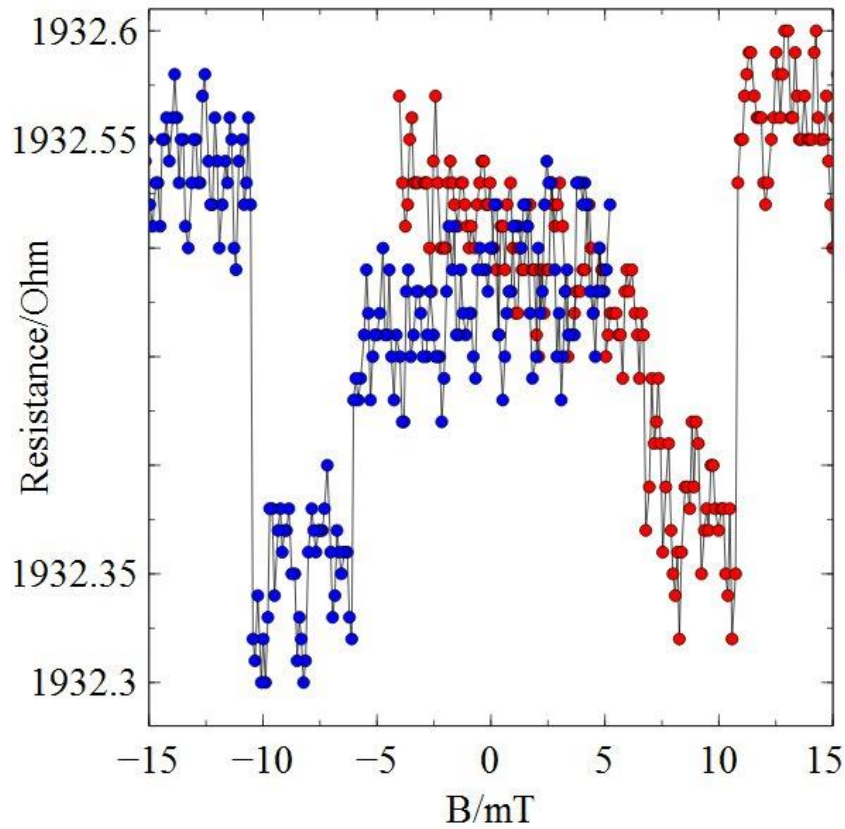


Figure 4-4 Presenting a typical AMR dataset as measured for the nanowire presented in Figure 4-5. The blue data corresponds to a positive to negative field sweep and the opposite applies to the red data. A clear abrupt change in the resistance occurs at the coercive field of the nanowire, as shown for both field directions.

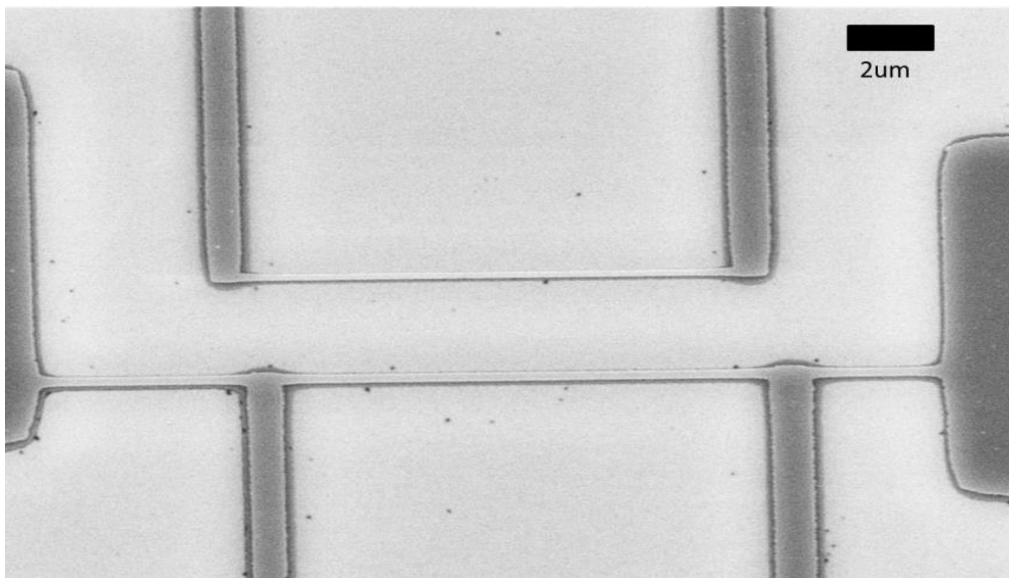


Figure 4-5 Showing an SEM micrograph of a NiFe nanowire with two sets of contacts, two for current and two for voltage. AMR data from this nanowire is presented in Figure 4-4. The dimensions of the nanowire are 20nm thick, 200nm wide and 20μm in length. Sample 20152004_AuSV.

Shown in **Figure 4-4** is the result of making a measurement in the parallel configuration for a 20nm thick NiFe nanowire, for sample 20152004_AuSV (see **Figure 4-5**) of approximately 200nm in width and 20 μ m in length. As in the case of a thin film, the saturated states are of the same resistive value implying the magnetisation and current density vectors point in the same directions (or anti-parallel) at these points. During reversal a bell curve shaped response is not obtained as is the case for a thin film. To have full confidence and assurance that the curve is being interpreted correctly it is possible to model the AMR curve from a micromagnetic point of view. Using software (OOMMF) to simulate the firstly the magnetisation at each simulation cell and then calculate the angle between the current and magnetisation vectors for each simulation cell as described earlier in section 2.6.2. **Equation 24** is then used to calculate the AMR for each cell and using the nanowire dimensions a calculation of the resistance is also possible, this would be done to calculate the AMR response at each field step and create an AMR curve. The curve can be completely and unambiguously reproduced using this method [69].

Reviewing the literature [12], [69]–[74] it is clear that for a single NiFe nanowire of the stated dimensions a domain wall will be nucleated to reverse the magnetisation as opposed to the whole magnetisation coherently rotating. In terms of the ‘AMR curve’ a domain wall reversal corresponds to a sharp switch on the ‘AMR curve’ as shown in **Figure 4-6**.

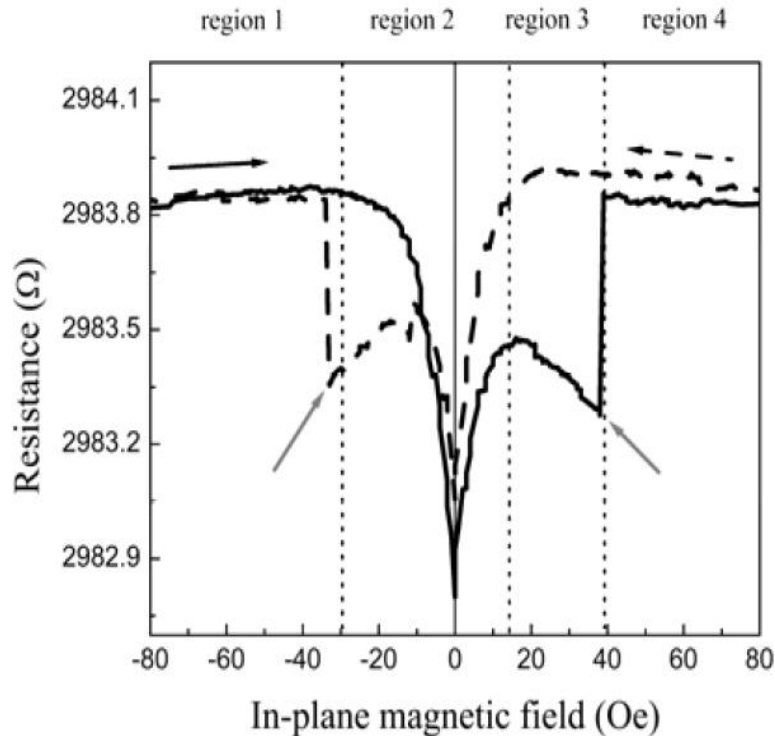


Figure 4-6 Showing an AMR curve for a NiFe nanowire of 300nm width, 16nm thickness and 20 μ m in length. Measurement configuration is current and field parallel. In short there are two features: an essentially zero field feature corresponding to magnetisation large pads connected to the nanowire and included in the measurement. The second feature is an abrupt change to the resistance at 40 Oe corresponding to the nanowire reversing its magnetisation via a domain wall reversal mechanism. Images adapted from [71]

Figure 4-6 shows an AMR curve, measured with the current and magnetic field applied parallel to each other, for a nanowire of similar dimensions to the ones fabricated and used for this thesis (as in **Figure 4-5**). Specifically it is 20 μ m in length, 16nm thick, 300nm wide and made of NiFe in the same method as nanostructures are created for this thesis (i.e. EBL and thermal evaporation). There are two features immediately obvious in the curve, a feature close to zero applied field and another feature close to 40 Oe, this is in both the positive and negative field sweeps. The features close to zero are easily explained as a thin film coherently rotating as in the example of a thin film previously discussed. The thin film that is rotating corresponds to the large pads the nanowire is connected to. Being substantially larger in width this drastically alters the properties of the pads with respect to the nanowire, resulting in an AMR response of the pads akin to a thin film. The feature close to 40 Oe corresponding to the nanowire reversal is more difficult to justify and explain. The argument is as follows:

For a NiFe nanowire the easy axis points along the wires long axis. This means that it's energetically favourable for the nanowire to be in one of two states, corresponding to the magnetisation pointing along the length of the wire, this can take two orientations. Due to the geometry of the nanowire a large energetic barrier exists between these two states and from energetic considerations it costs less energy to create a domain wall to reverse the magnetisation of a nanowire than it does to coherently rotate the magnetisation or by any other mechanism [18] [21].

Referring back to **Figure 4-6**, after the close to zero field features (pad reversal) a domain wall is pinned at the interface between the nanowire and pad. At close to 40 Oe the domain wall is depinned and abruptly, over a very narrow field range the magnetisation reverses direction, returning to the initial value prior to any reversal events i.e. the magnetisation and current are re-aligned anti-parallel. The coercive field of the nanowire is therefore associated with the domain wall depinning event and the domain wall itself is the reversal mechanism for the nanowire [71].

4.4. Atomic Force Microscopy (AFM)

4.4.1. AFM for Thickness and Roughness Measurements

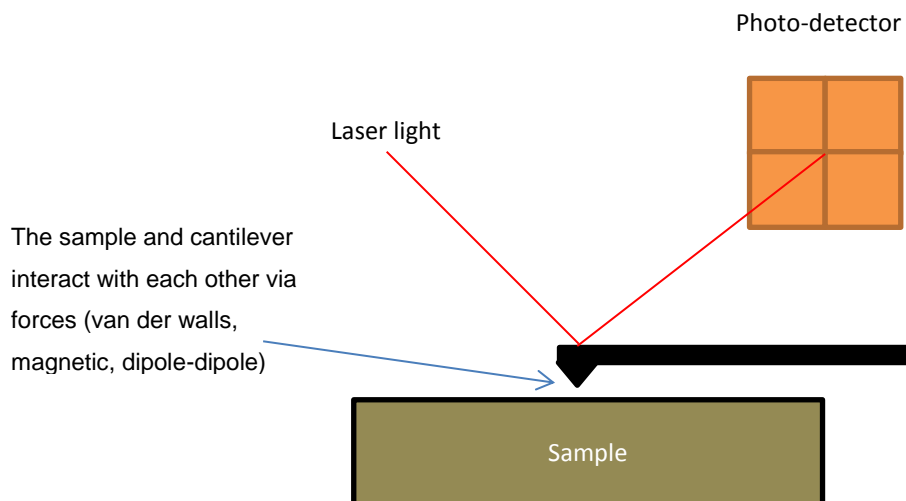


Figure 4-7 Showing a schematic of an AFM. The deflection of the cantilever tip due to the interaction with the surface is measured by a laser reflecting from the cantilever to a photodiode.

This is a technique for probing surface topography with nanometre precision. The technique is an extension of scanning tunnelling microscopy (STM) both of which were pioneered by Binnig et al [25],[26]. Both techniques are based on an extremely fine tip (the order of 20nm) being brought into close proximity of a sample surface. The two techniques probe a surface in different ways. The STM measures electrical tunnelling conduction between the tip and surface and can operate at various biases both positive and negative, obtaining information relating to the electronic orbitals and conduction. The AFM detects/measures the interaction between the surface and tip and this too can be operated in a variety of modes, namely contact or non-contact mode, a topographical image of the surface structure results.

In AFM the deflection of the tip due to the interaction is measured using a laser reflected from the cantilever into a four quadrant photodiode(see **Figure 4-7**), the first AFM used an STM to measure the cantilever deflection [77]. The STM requires a conductive surface to map which is a disadvantage the AFM can overcome. The AFM can also be thought of as a standard profilometer where the contact force has been substantially reduced (10^{-4} N reduced to 10^{-9} N) the increased sensitivity being smaller than inter-atomic interactions [77].

AFM can be used to obtain values for the thickness of a film, roughness and magnetic contrast (MFM, when using a magnetic tip). An AFM can be operated in constant height mode, where the interaction between the sample and tip is mapped at a single height above the sample, this requires a feedback loop that can constantly correct for the forces experienced by the cantilever, recording the z-variation required to maintain a constant height can be used to generate a topographical image of the surface structure. In contact mode the sample and tip are in contact with each other which can affect the sample if it is delicate. The image is a convolution of the tip with the sample surface, applicable to both imaging modes.

The AFM can operate in an alternative mode called non-contact mode where the tip is set into resonant oscillation above the sample and the long range forces between the tip and sample (electrostatic, Van der Waals, Magnetic) are interacting as it is scanned over the surface. As the tip is scanned over the sample and experiences forces, a feedback loop is used to ensure constant oscillation amplitude is

maintained. This is the mode used throughout this thesis for obtaining topographical information because it is not in direct contact with the sample is less invasive. Higher resolution can often be obtained in contact mode.

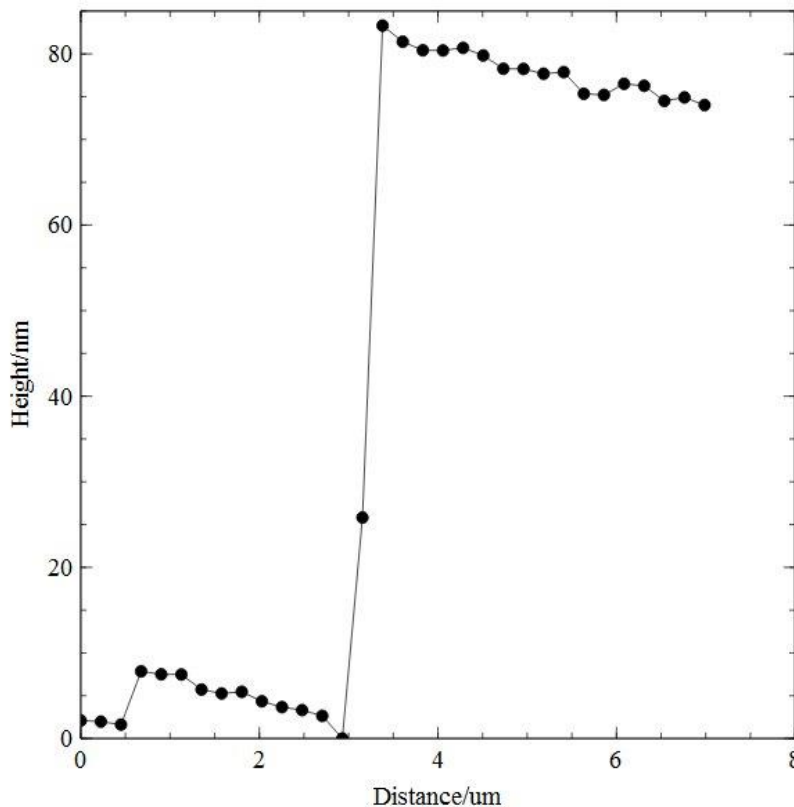


Figure 4-8 Showing a single line scan generated by using an AFM on a Au thin film. The sudden increase in height is attributed to the edge of a Au film and is used to determine the height of the thin film.

Figure 4-8 shows the results of a single line scan measurement made using AFM on an Au thin film. It shows the step height of the Au film, multiple line scans are used to obtain an error. This Au thin film is measured to be (80 ± 5) nm. **Figure 4-9** shows a histogram which is obtained by analysing every pixel of a high resolution AFM image, it essentially groups all the same value of thicknesses together and counts how many are in a given group, this can be used for roughness analysis. The result is often fitted with a Gaussian distribution to extract statistical information, multiple measurements can be used for error analysis. The roughness which is a measure of the local variation in height is given for this film to be approximately 5nm.

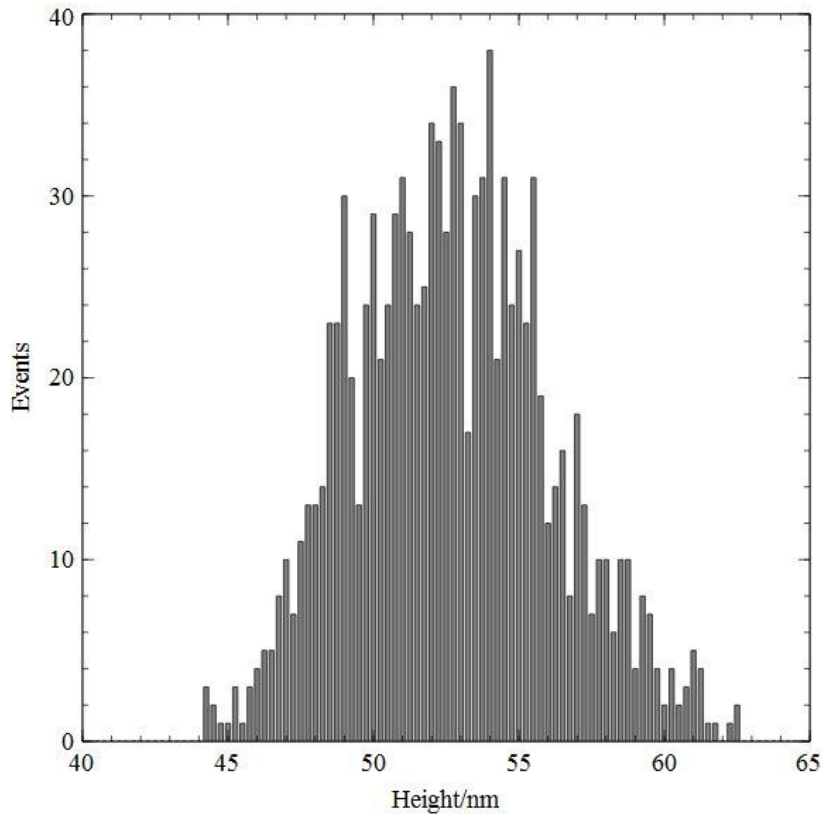


Figure 4-9 Shows a histogram constructed from a high magnification AFM image used for analysing surface roughness.

4.4.2. AFM Nanomachining

As discussed in the preceding section ‘AFM for Thickness and Roughness’ AFM was compared to STM in terms of imaging capability and principle. Here a comparison will be made in terms of sample manipulation and creation. Historically the STM has been used for single atom manipulation and this technique was used to ‘write’ the letters I.B.M using Xenon atoms on a Nickel surface [78]. In 2013 the world’s smallest movie was created by IBM wherein a boy (stick-man made of single atoms) is bouncing a ball (a single atom) [79]. This demonstrates the feasibility of STM as an atomic manipulator, capable of positioning single atoms.

AFM has made its mark modifying structures although in a cruder way than single atom positioning as in STM. In the simplest case a Diamond coated tip replaces the standard tip and the now hardened tip is used to machine the surface of a sample. It is still in the very early stages of development with the only existing publications

being concerned with calibration measurements and the crude breaking of a nanowire [30][31][82][83].

Figure 4-10 shows an SEM image of a Diamond coated Silicon tip for AFM nanomachining and the first attempt to modify a Permalloy nanowire. As is clear from the image and further confirmed in the research paper by taking transport measurements, the nanowire has broken. Clearly for this technique to mature into a nanolithography tool in its own right, demonstration of systematic removal of material is required i.e. the removal of say 5nm thickness on a 30nm thick nanowire in an isolated section of the wire. This has been pursued within this thesis and it has been shown that the technique can be used to modify Permalloy nanowires without breaking them completely, this will be shown in the results Chapter 5.

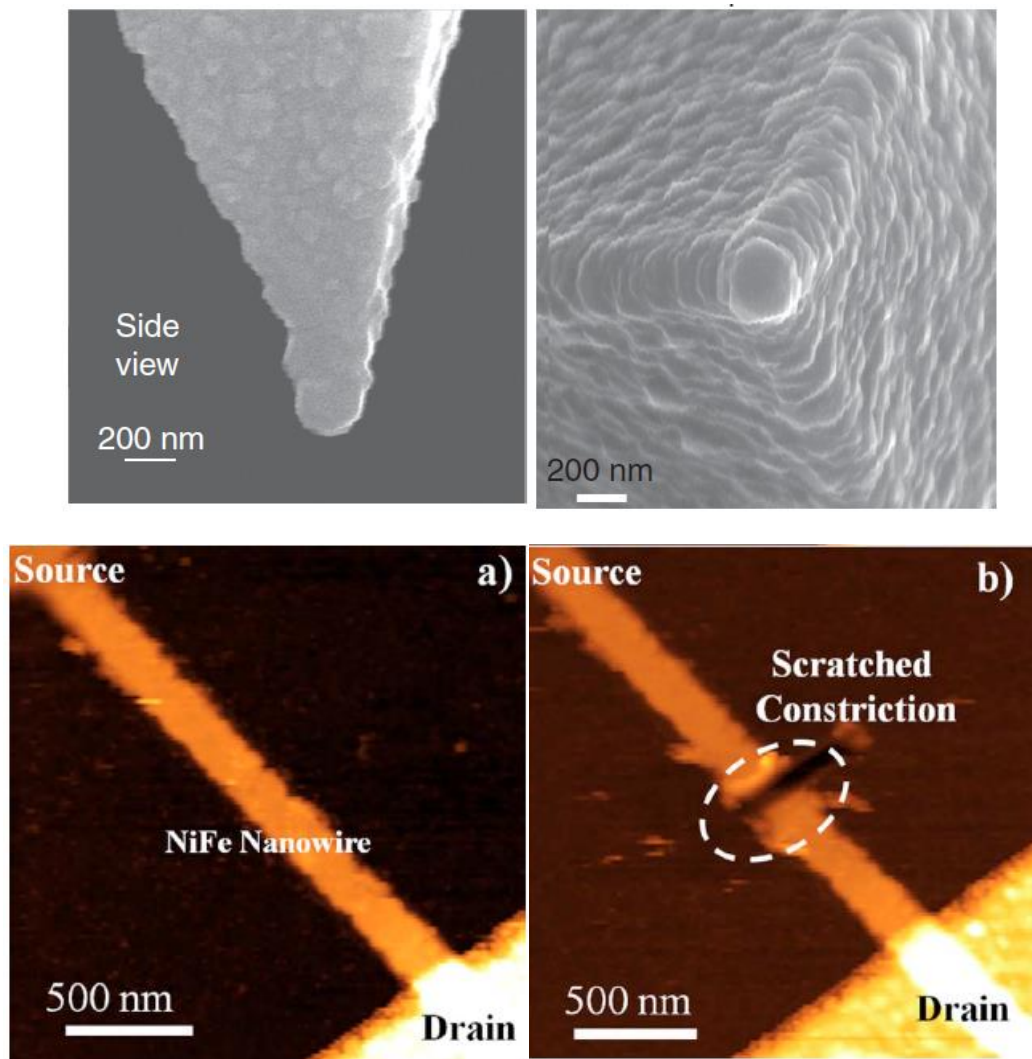


Figure 4-10 Top images showing a Diamond coated Silicon tip. Side (top left image) and Top View (top right image). Bottom images showing the before (left image) and after (right image) of using the Diamond tip to modify a Permalloy nanowire. Images adapted from [81]

4.5. Experimental Setup for Low Noise Magnetotransport Measurements as A Function of Temperature

4.5.1. Introduction

As discussed earlier in section 4.3.2, AMR is a useful technique to gain information relating to the magnetisation of a sample during magnetic reversal. To practically make these measurements a system for varying the magnetic field whilst making low noise electrical measurements is needed.

4.5.2. Experimental Setup

An experimental setup was constructed to allow magnetotransport measurements to be made at room temperature and down to a few K. The field range selected was chosen in order to probe soft magnetic materials (Permalloy) i.e. 0.5T maximum magnetic field. A simple copper wound electromagnet was thus selected to provide the field range necessary. A DC power supply was used in conjunction with the electromagnet for field control. To make sensitive electrical measurements a Lakeshore AC 370 Resistance Bridge was used [84], this is an inherently four terminal technique that utilises phase sensitive detection to eliminate noise as in lock in detection. A low excitation frequency is employed (13.7Hz) to avoid the mains frequency and capacitive effects during measurement. Used together with shielding of the sample and 'active noise reduction circuitry' [84] it is possible to make low noise electrical measurements without heating the sample owing to the AC nature of the excitation signal. Both instruments were interfaced through the National Instruments LabView software suite.

A three axis lakeshore Hall probe is used to directly measure the magnetic field. It is placed in between the poles of the magnet as close as possible to the sample. A sample holder was also designed for use in the setup. It was fashioned from aluminium (non-magnetic) and made in house by mechanical workshop staff at Cardiff University. It is a sixteen contact low resistance and low noise sample holder designed for direct use with the AC lakeshore bridge and electromagnet, with a built

in thermometer in thermal contact with the sample. A schematic of the experimental setup is shown in **Figure 4-11**.

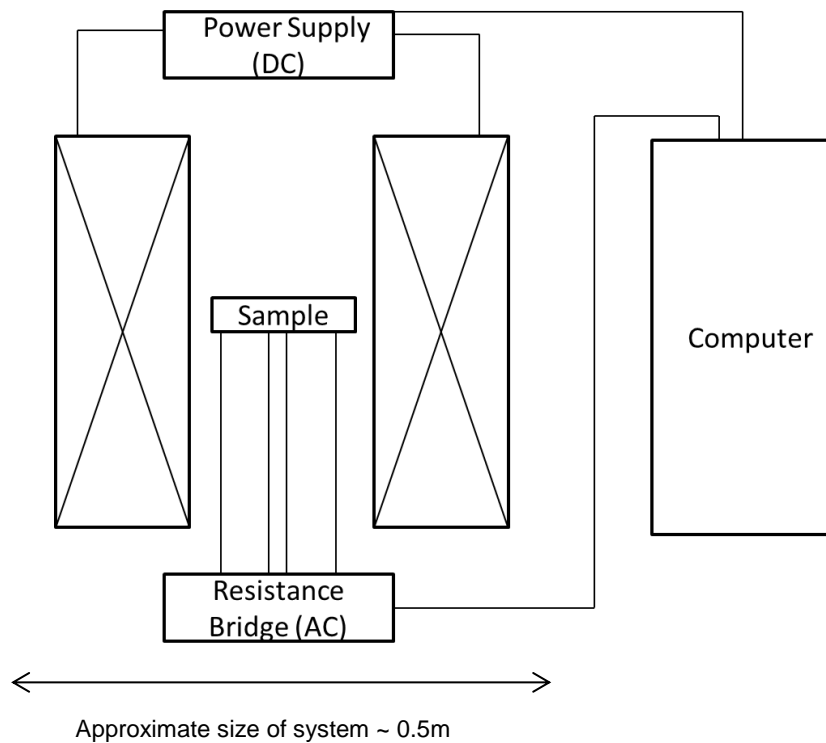


Figure 4-11 Showing the experimental setup that was designed and implemented to measure the anisotropic magnetoresistance of samples used in this thesis. It consists of a magnet connected to a power supply connected to a computer, this is all that is needed for field control. To make electrical measurements a resistance bridge connects to the sample and is in turn connected to the computer for remote control. All Equipment is interfaced through LabView.

4.5.3. Calibration Measurements

After designing and then constructing the experimental setup it needed to be tested and calibrated against known samples. The field uniformity was firstly mapped along with measuring the magnetic field produced by the electromagnet as a function of current. Secondly a GaAs Hall bar was then used to calibrate the system for electrical measurements. It was selected because it was readily available, fairly straightforward to use, and the dependence of resistance on applied magnetic field was well known

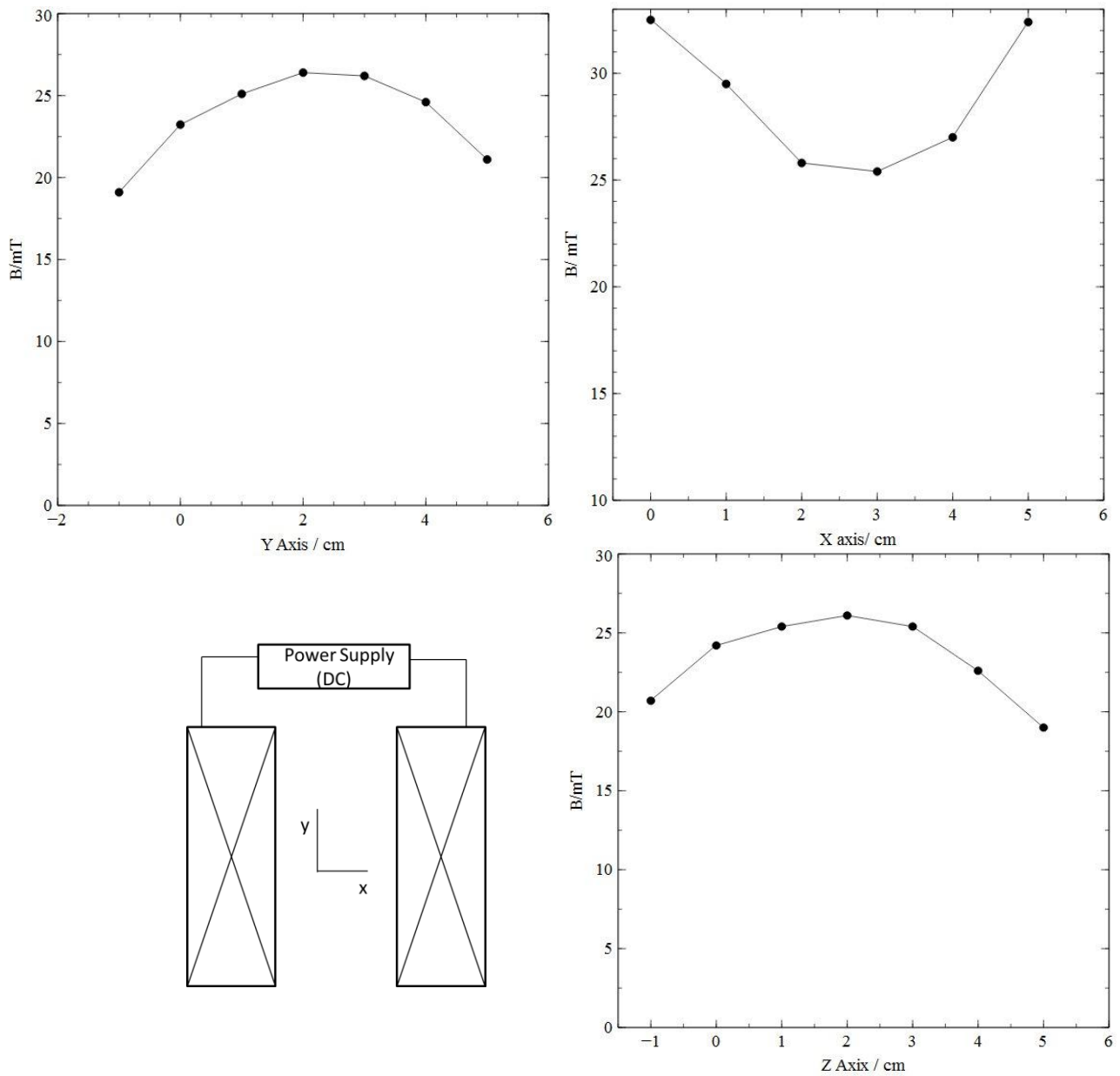


Figure 4-12 Showing the magnetic field distribution for three orthogonal directions. There is a region of uniformity in the centre of the poles of approximately a cm^3 . The measurement axes are defined as shown (z is into the page). Therefore the largest chip size fabricated is 1 cm x 1 cm to ensure it experiences a uniform field.

Figure 4-12 shows the variation in magnetic field when measuring between the poles in different spatial directions (x,y,z). In the x direction the Hall probe gets closer to the poles for extreme measurements and an increase in the field is thus observed. The variation being less than 10mT from centre of the poles to being next to the pole. As expected the other two configurations drop off in field intensity as the Hall probe exits the area between the pole pieces. The effect is less pronounced for these cases with the variation in magnetic field being approximately 5mT. As

expected, the magnetic field is decreasing as you move away from the poles and increasing as you move toward them.

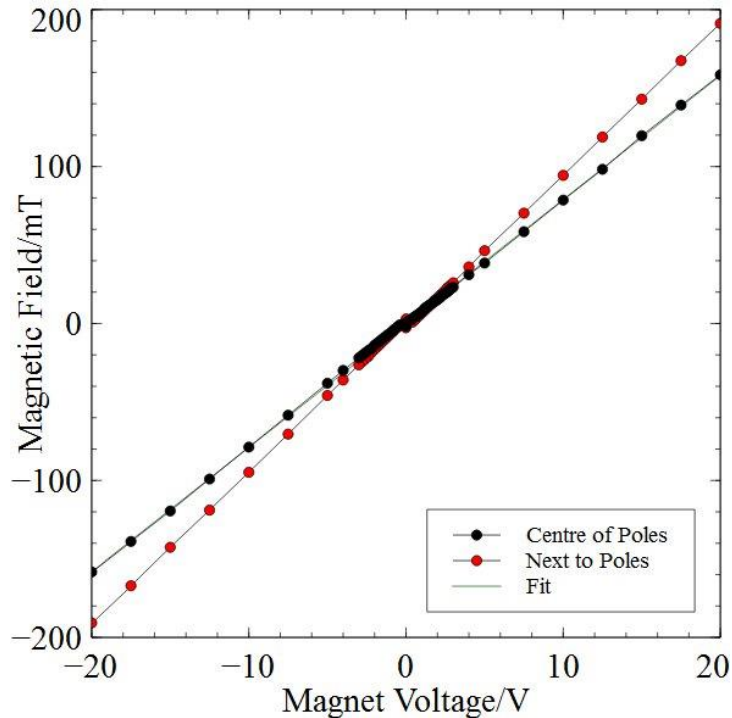


Figure 4-13 Showing the magnetic field as a function of the magnet voltage. A linear dependence is observed with a gradient of 7.4 mT/V for the curve taken in the centre of the poles.

Figure 4-13 shows the variation of magnetic field with respect to the voltage applied to the coils for the electromagnet that is used in the low noise AMR measurement setup. Two plots are shown, one with the Hall probe next to a pole, the other with the Hall probe in the centre of the poles. A linear fit is applied to the curve taken at the centre of the poles. This allows direct conversion between voltage and magnetic field for the given pair of electromagnetic coils. The magnetic field was found to vary according to 7.4 mT/V.

After the field distribution and the magnetic field as a function of the magnet voltage was obtained, measurements were made on a GaAs Hall bar. Two measurement configurations were employed corresponding to a Hall measurement and a magnetoresistance measurement.

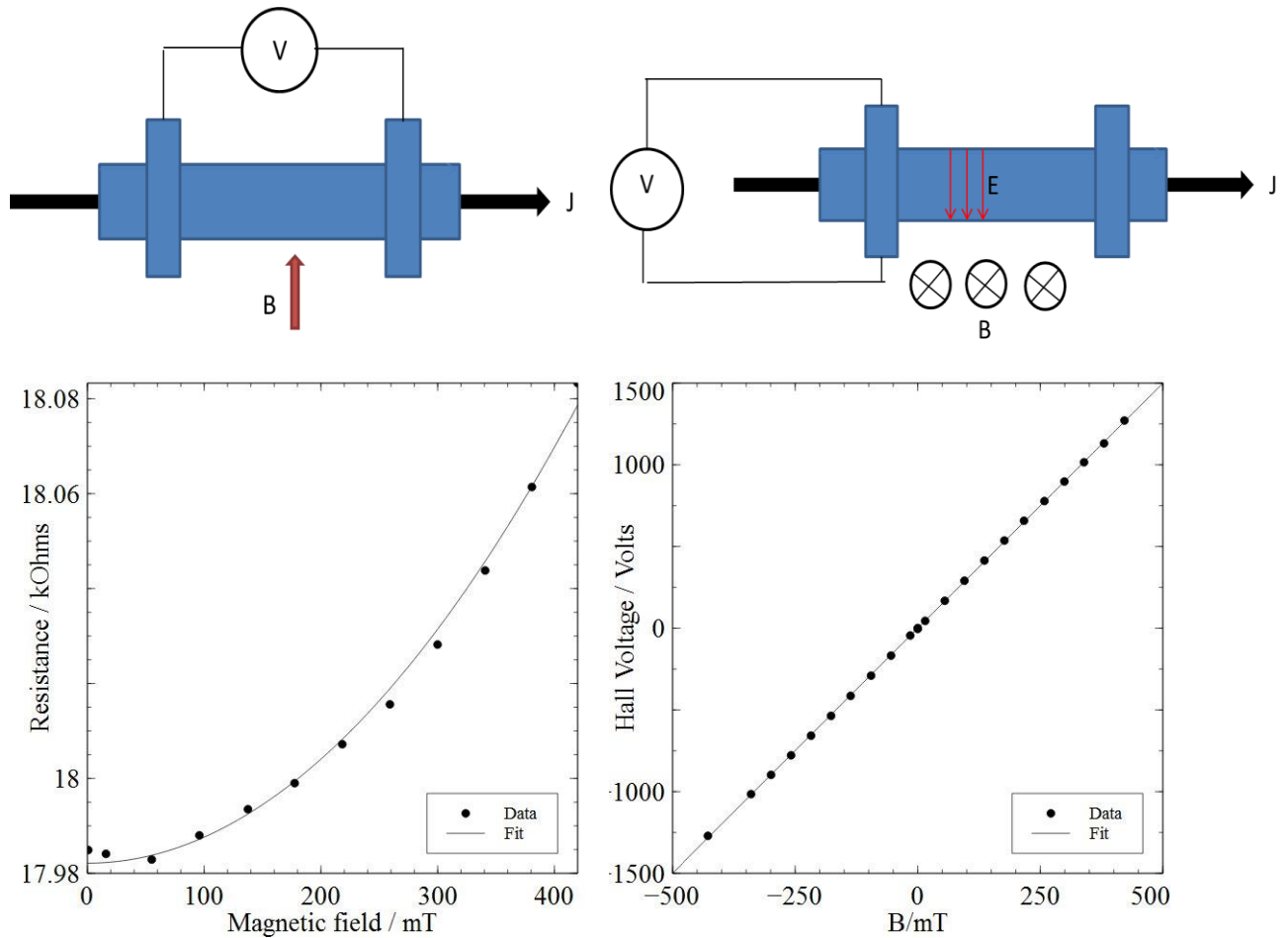


Figure 4-14 Showing the calibration measurements for the homemade magnetoresistance setup. Measurements were performed on a GaAs Hall bar the two shown configurations corresponding to magnetoresistance (top and bottom left images) and a hall measurement (top and bottom right images)

Equation 25 is the relevant equation for the ‘magnetoresistance/parallel’ configuration for a semiconductor. In the magnetoresistance configuration the resistance varies as:

$$R(B) = R_0 \frac{\rho_B}{\rho_0} (1 + C\mu^2 B^2) \quad \text{Equation 25}$$

Where $R(B)$ is the resistance as a function of magnetic field, R_0 the resistance of the sample in zero field, ρ_0 and ρ_B are the resistivity in zero field and in a magnetic field of intensity B respectively. C is a geometrical factor which takes into account that the Hall voltage develops over a distance and is dependent on the sample geometry. This expression predicts a quadratic variation of resistance with magnetic field, and also that the effect is proportional to the mobility squared. It can be understood as an

application of the Lorentz force – where the magnetic field distorts the current path length and as a consequence of this it can alter the resistivity of the sample [85].

As can be seen in **Figure 4-14** (bottom left image) the data in this configuration indeed plots out a quadratic variation, as shown by the fit to the data. There is reasonable agreement between the data and fit.

Regarding the ‘Hall measurement’ (**Figure 4-14** right images) the familiar physics of the Hall effect is responsible for the variation in voltage being directly related to the amount of accumulated charge at one side of the sample due to the out of plane magnetic field. Summarised by the following equations:

$$R_H = \frac{E_y}{j_x B_z} \quad \text{Equation 26}$$

$$R_H = \frac{-1}{ne} \quad \text{Equation 27}$$

Where R_H is the Hall coefficient, E_y is the Hall field in the plane of the sample (shown in **Figure 4-14** top right image), j_x the current density in the plane of the sample but at 90° E_y . B_z the magnetic field induction through the sample plane, n is the carrier density and e is the fundamental electronic charge. These expressions follow directly from the Lorentz law acting on the conducting electrons. For a given field the Hall electric field produced can be measured along with the current density in the x direction. This allows evaluation of the Hall coefficient and thus the mobility of the sample.

Figure 4-14 (bottom right image) displays the Hall Effect for the GaAs Hall bar sample. It shows a positive linear correlation as expected from theoretical considerations (**Equation 26**). From evaluating the gradient the polarity of charged carriers can be inferred and the carrier density calculated. The carrier density calculation requires the thickness of the sample to be measured and due to the sample housing this was not possible. If the carrier density was obtained, the mobility could be calculated using the magnetoresistance data and **Equation 27**.

Noise measurements were also carried out with and without shielding of the sample. It was found the AC resistance bridge performs as expected according to the manual specifications with a shielded measurement. These calibration measurements show

the magnet is operational and the AC resistance bridge is operating up to the specified standards.

5. USING AFM TO MODIFY PERMALLOY NANOWIRES

5.1. Introduction

Nanofabrication in industry relies upon photo and electron beam lithographic techniques for making modern nanoscale devices. Typically as in the case of an integrated chip it is processed layer by layer and the techniques that have been developed for the semi-conductor industry are designed for parallel production (making many chips at once). To fabricate prototype devices it is not cost effective to use the same technologies as for parallel production. Excluding the cost of making a semi-conductor fabrication lab, it can cost up to a half a million pound Sterling to fabricate a single photomask with nanoscale features [86]. This combined with the need for several iterations for prototyping devices leaves researchers and companies seeking cheaper alternative ways to fabricate prototype devices. AFM provides a cheap, easy to use and maintain system for prototyping nanoscale devices [87]. The use of an AFM tip to modify structures is a natural extension of the technique first developed for obtaining topographical information. Allowing control of features down to the sub-nanometre [88], 3D nanomachining [86], and a variety of ways the tip and sample can interact for modification means AFM nanomachining although in its infancy is a versatile and promising technique for device prototyping and in its own right. For example how to incorporate multiple tips of various diameters (nano and micro) and increasing the machining speed are heavily researched topics to enable AFM to compete with the existing nanofabrication tools used for parallel processing [86]. In this thesis AFM nanomachining has been used to influence domain wall dynamics by modifying Permalloy nanowires.

5.2. Literature Review of AFM Machining

A seminal research paper published in 2009 opened the doorway to AFM nanolithography [81]. It looked at establishing the parameters relevant for the machining of NiFe and Silicon thin films with emphasis on the applied force of the AFM tip, the scratch speed and the number of scratches. A logarithmic increase in the scratch size (width and depth) was observed for increasing force for both NiFe and Silicon. Little dependence on the scratch speed was found and with regards to multiple scratches the research was inconclusive.

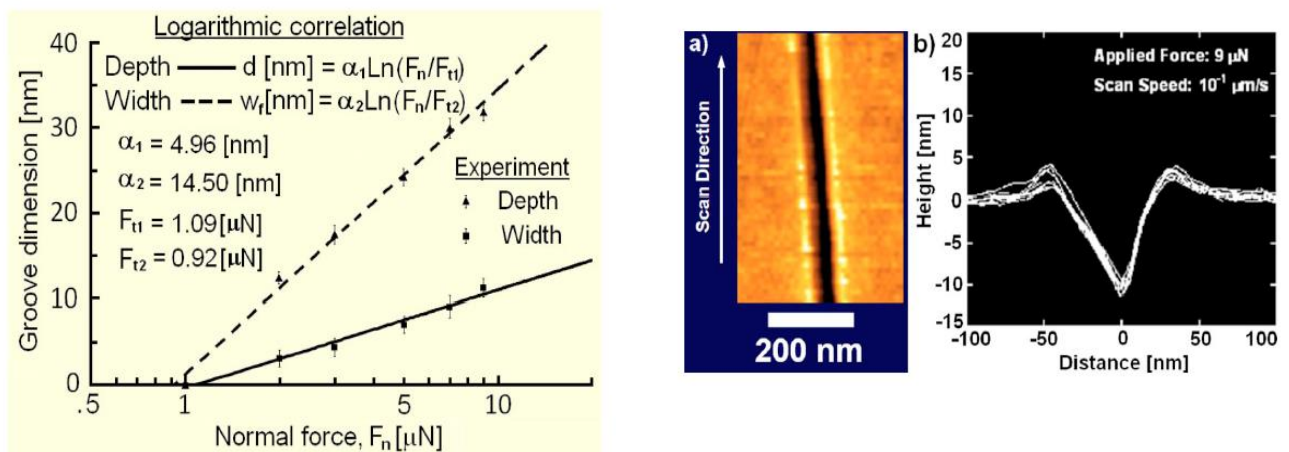


Figure 5-1 Showing a scratch in a NiFe thin film (middle image). AFM profile of the scratch (right image) and the correlation between force and depth/width. The graph (left image) shows the threshold force and the logarithmic trend after overcoming the threshold force for scratching. Images adapted from [81].

Figure 5-1 shows the logarithmic trend for scratching a Permalloy 32nm thick film (left image), a topographical image of a scratch in NiFe (middle image), ten AFM line scans for determining mean and standard deviation (right image). Scratches were performed at 100mm/s in the force range 1 μ N to 9 μ N. Each point on the graph is formed from the average of ten measurements, the standard deviation is reflected with an error bar. The graph (left image) shows the threshold force required to remove material, there is a small difference between the two values for depth and width but the theory and experiment match up well with respect to the threshold force. The equation for predicting the scratch depth/width as a function of the force has the same functional form as the Beer-Lambert law, with α being similar to the reciprocal of the absorption coefficient. It shows a logarithmic trend with the depth

and width depending solely on the applied force, threshold force and α_n which relates to scratch penetration depth or width. This research shows that one can reproducibly produce nanoscale scratches and model the results accurately, it also used the technique to break a NiFe nanowire [81],[89].

The scratch direction with respect to the diamond tip has been researched and due to the pyramidal shape of the AFM tip a dependence on the scratch direction is observed.

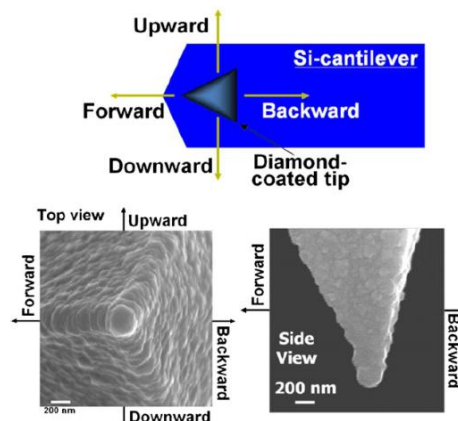
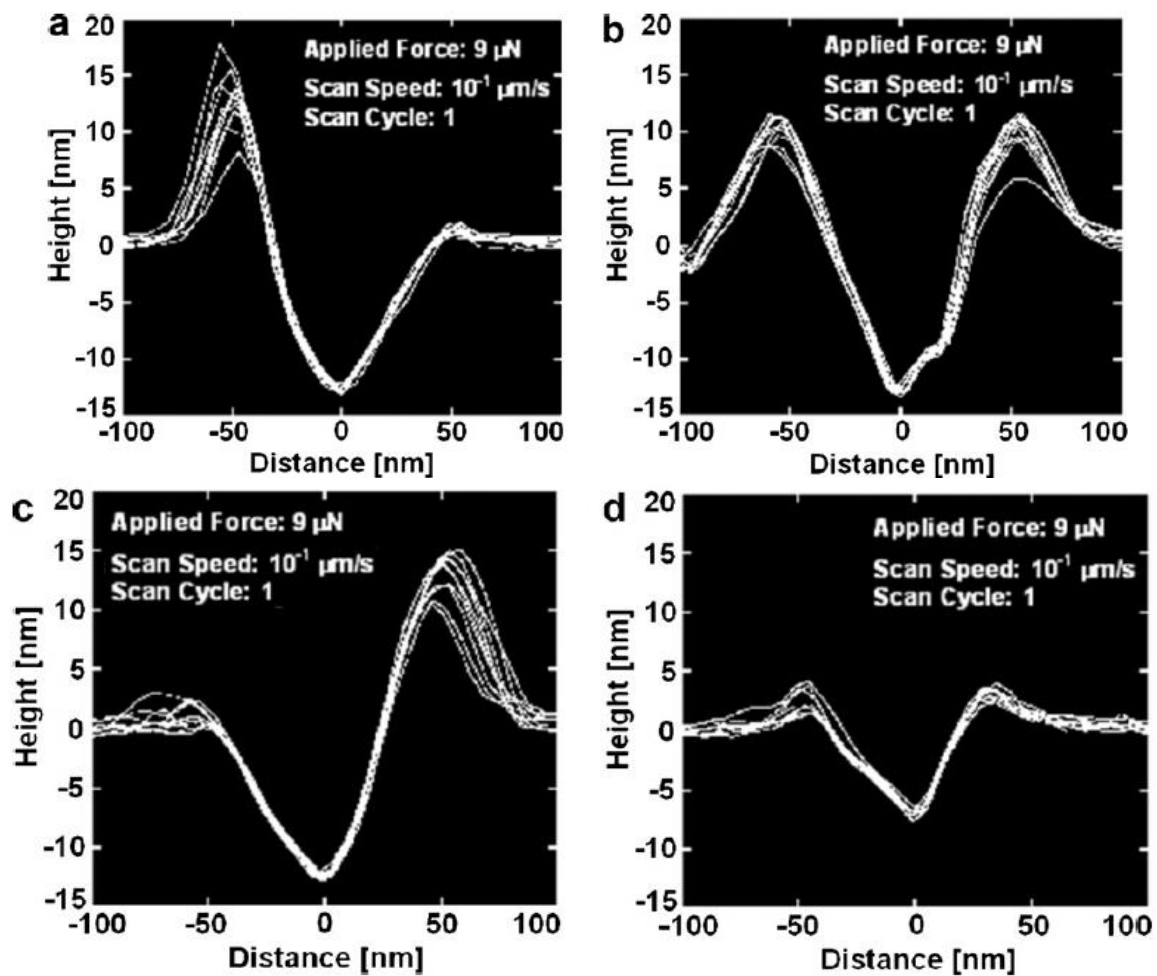


Figure 5-2 Showing multiple line scans taken at random locations along a groove. The four line scans correspond to four different scratching directions. Image (a) is an upward direction, (b) is a forward direction, (c) is a downward direction (d) is a backward direction. All grooves were scratched with a load force of 9 μ N and at a tip speed of 100nm/s on a 30nm thick NiFe thin film. The small image to right defines the different directions. Images adapted from [80].

Figure 5-2 shows four different sets of line scans relating to the different cutting directions, as defined in the smaller image at the bottom of **Figure 5-2**. Image (a) corresponds to the upward cutting direction and all the debris piling up at one side of the diamond tip, which is consistent with what would be expected considering the orientation of the diamond tip with respect to the thin film. The upward cutting direction should be contrasted against the downward direction (c) where the debris is now piled on the opposite side of the groove due to this direction being a mirror image the upward cutting direction. The two faces of the diamond tip are not at equal angles and so debris favours the smallest angle, there is some small debris at the opposite side supporting this argument. Considering (b) there is approximately equivalent amounts of debris built up on both sides now and looking back at the orientation of the tip with respect to the cutting direction shows there are approximately equal angles (30 degrees) either side of the cutting tip. The amount of debris deposited is approximately half that which was deposited on one side in the upward and downward directions, again adding weight to it being a geometrical effect. Considering (d) there is very little debris built up now around the groove this is correlated with the large angle of the cutting face with respect to the cutting direction (90 degrees). Physically this means debris pile up is more favourable for small angles between the cutting face and cutting direction. For the least debris pile up, the backward cutting direction should be used [80] .

In another paper [90] in 2014 It was shown that the use of high aspect ratio diamond single crystal tips and the indentation method can produce high aspect ratio grooves in hard materials such as Silicon and NiFe. The indentation method involves pressing the tip into the material only and no lateral motion when in contact with the material. Multiple indentations are used to create a groove. This pressing into the material can produce large indentations provided the indenting material is harder than that which is being indented. Historically this technique is used for evaluating the hardness of material and has been adapted to modify nanostructures using an AFM high aspect ratio tip. The aspect ratio of the fabricated grooves using this method was as high as 2.1 whereas previous work yielded aspect ratios of 0.1-0.3 [81] which is a significant improvement.

Other groups have looked at the wear of the tip [89], computer modelling the process [91], using cheaper Silicon Nitride tips [92], direction independent scratching [93] and

vibration assisted scratching for improved resolution[88]. The use of AFM machining to modify magnetic nanostructures has not been carefully studied.

A research paper by Narayanapillai and Yang using focussed ion beam milling to modify a magnetic nanostructure from the top [67] is one of the few examples of this geometry. A different technique is used to AFM but the end goal is similar, the formation of a nanotrench as shown in **Figure 5-3**. **Figure 5-3** shows a schematic of a nanowire which has had a nanotrench defined by Ar ion milling (image (a)), (b) shows a micromagnetic simulation of a transverse domain wall positioned at such a nanotrench, (c) shows a micromagnetic simulation of a vortex domain wall positioned at the nanotrench.

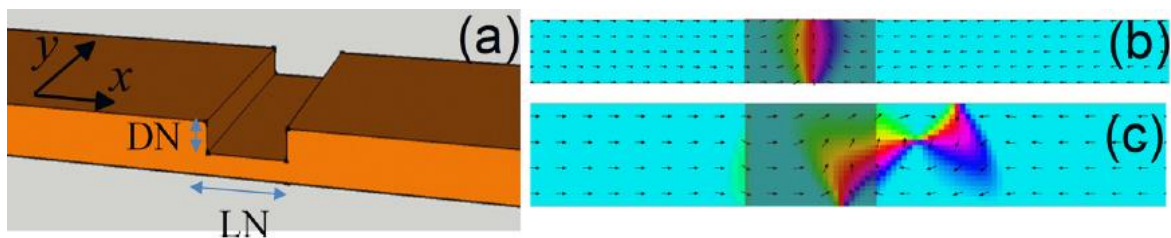


Figure 5-3 Showing vertical modification of a nanostructure (a), Simulations of a transverse (b) and vortex (c) domain wall propagating through such a vertical modification [67].

For simulating transverse walls a width of a 100nm and thickness of 10nm was used for the nanowire dimensions. For simulating vortex walls a width of 200nm and a thickness of 40nm were used as the nanowire dimensions. In both cases the length (LN) of the nanotrench is 240nm and the depth (DN) is 6nm and 20nm respectively for transverse and vortex domain wall types. The transverse wall is stable at the centre of the nanotrench whereas the vortex wall is stabilised outside of the nanotrench. The group made extensive simulations varying the length and depth of the nanotrench for both vortex and transverse domain wall types in a Permalloy nanowire.

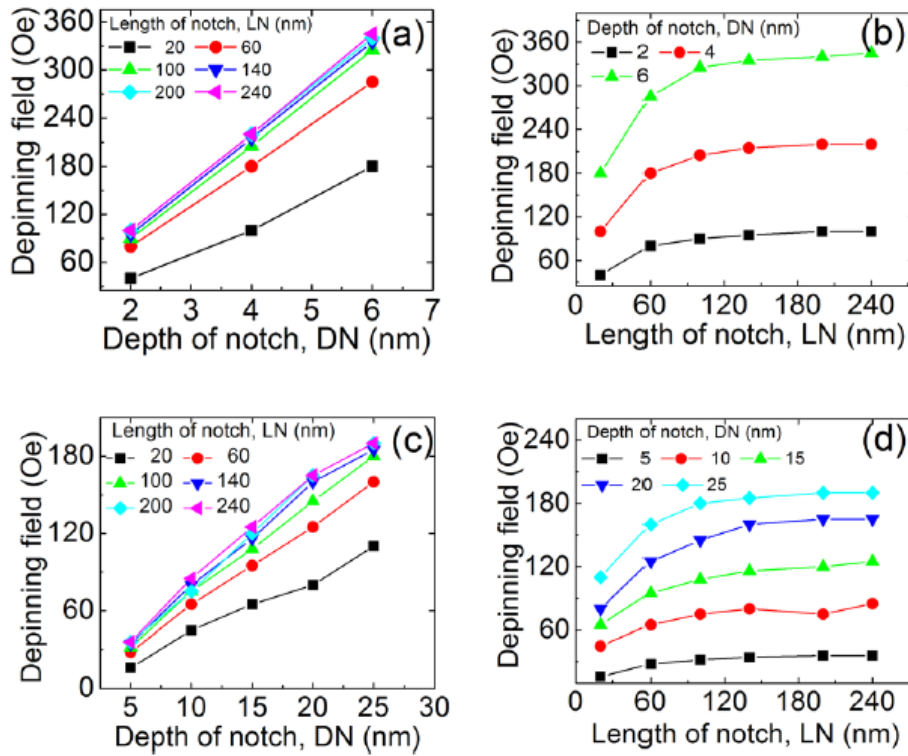


Figure 5-4 Showing the results of the micromagnetic simulations performed. Considering a transverse wall image (a) shows the depth dependence at a fixed length, Image (b) shows the length dependence for a fixed depth. Considering the vortex wall image (c) shows the depth dependence at a fixed length, image (d) shows the length dependence for a fixed depth. From reference [67].

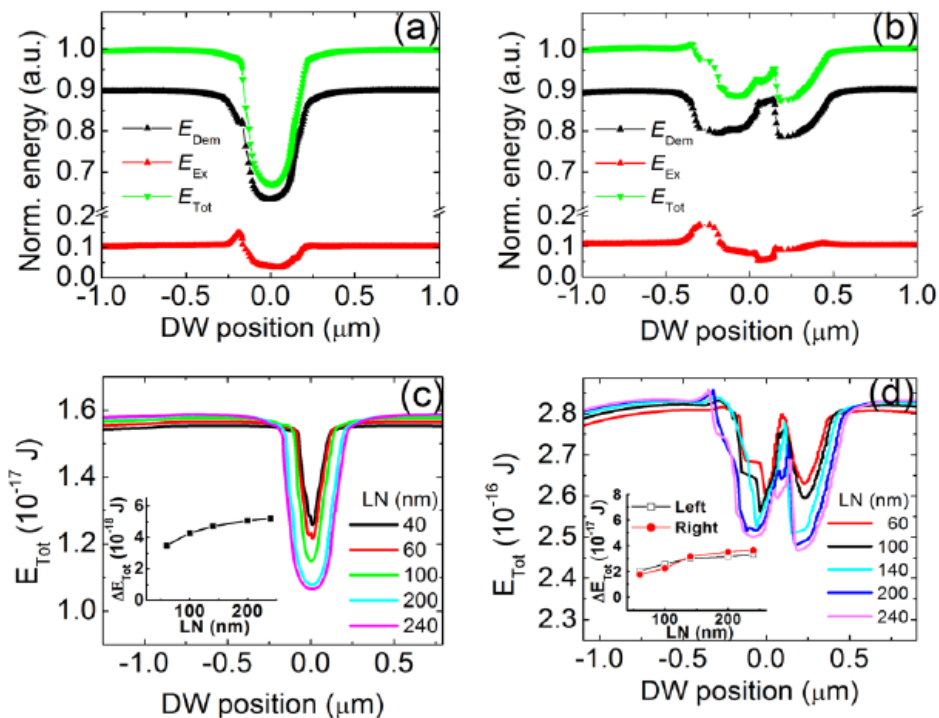


Figure 5-5 Showing the energy profiles with respect to the domain wall position for a transverse wall (a) and a vortex wall (b). Images (c) and (d) show the energy profile for a range of nanotrench lengths for transverse and vortex walls respectively. The change in energy profile as a function of the length of the nanotrench is shown as inset. From reference [67].

Figure 5-4 shows the dependence of the depinning field on the length and depth of the nanotrench for both domain wall types. Firstly considering the transverse wall case, images (a) and (b) of **Figure 5-4**. As the depth increase for a given length (image (a)), a linear increase in the depinning field is observed, the dependence on length saturates at around 100nm. As the length of the nanotrench increases for a fixed depth a linear increase is seen up until saturation which depends on the depth of the nanotrench. For a 6nm deep nanotrench the depinning field saturates when the nanotrench is around 100nm in length. Similar behaviour is observed for the vortex wall. **Figure 5-5** is used to get a gain further understanding, it is the potential profile as calculated from a micromagnetic point of view, minimising the demagnetisation and exchange energy terms. It describes the potential landscape seen by a domain wall travelling through the nanowire. It is calculated for both domain wall types, image (a) and (c) relating to transverse walls and images (b) and (d) relating to vortex domain walls. The centre of the plots correspond to the centre of the nanotrench. Images (a) and (b) show all the individual energy terms and their sums. For transverse walls (a) the nanotrench presents a symmetrical pinning site where the domain wall sits in the centre of the pinning site. For vortex walls (b) a dual dip profile is calculated where the domain wall sits either side of the centre of the nanotrench, it is repelled away from the centre. This is shown graphically in **Figure 5-5** images (b) and (c).

5.3. Experimental Data Prior to Machining a 10nm Thick, 10um Long, 674nm Wide Nanowire

A 10nm thick NiFe nanowire was processed and fabricated using the outlined methods in the chapter 3 (EBL and thermal evaporation). On the fabricated chip were 8 devices of differing widths, two designs were used. In one design the voltage contacts connect to the nanostructure and in the other they connect a little further out than the nanostructure. This is shown in **Figure 5-6**.

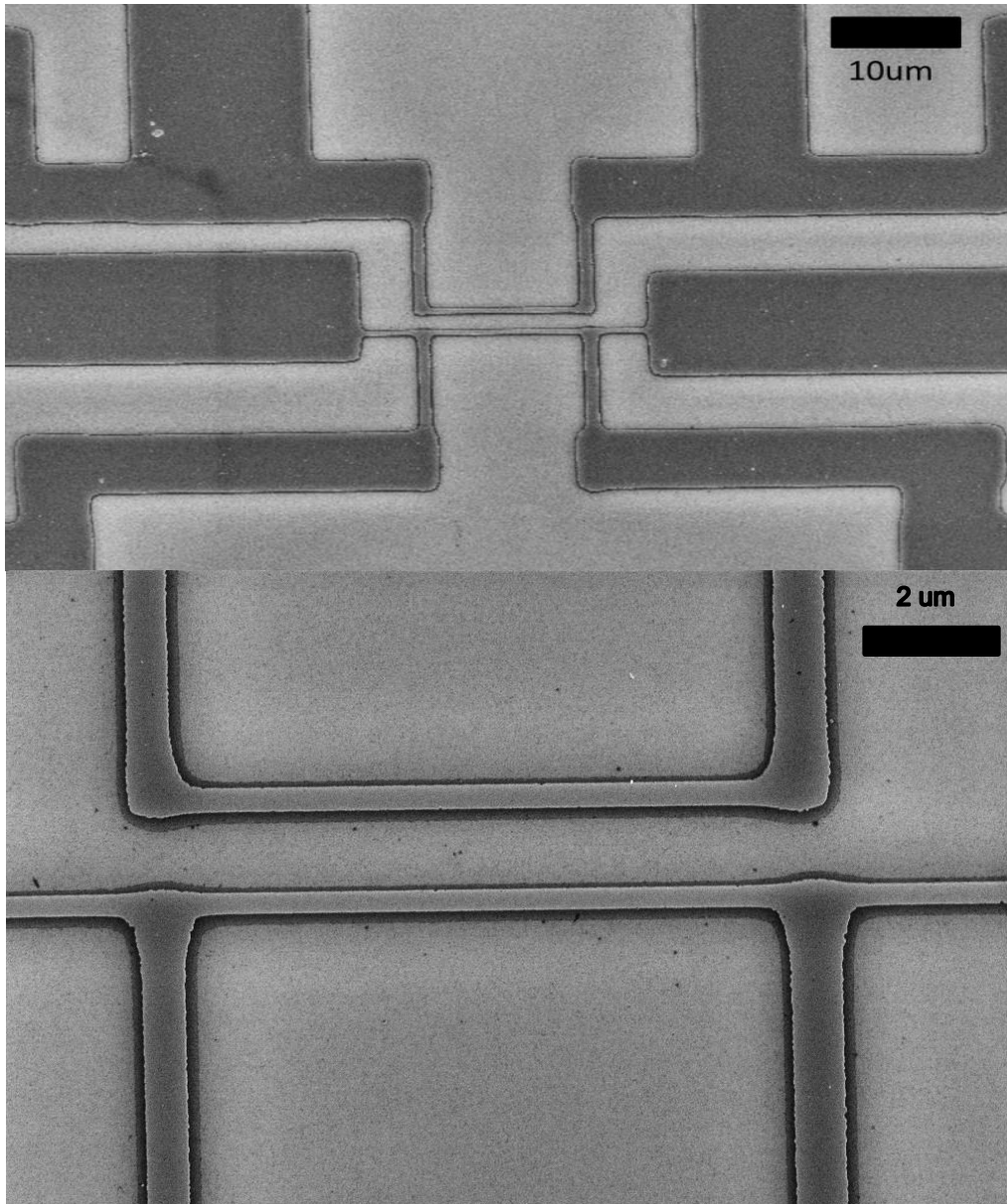


Figure 5-6 Showing different magnification SEM images to show the two different designs employed. The bottom image shows a high magnification image of a fabricated 10nm thick, 400nm wide Permalloy nanowire used for AFM nanomachining.

Figure 5-6 shows a series of SEM images to show the two different designs employed on this chip. The design that connects to the sample a little further out than the nanowire was done so as to gain information on the reversal of the wider sections of the nanowire, it is not expected that machining should affect their reversal in anyway. The eight devices were all examined in detail using an electron microscope prior to any measurement, to look for any defects and to measure the widths of the nanowires.

Out of the eight devices fabricated only one will be studied further after the machining phase and this is the only nanowire that shall be discussed further in this section. Some devices were unmeasurable due to high resistance and thus the noise being too high, this is a direct consequence of the two different designs, one design samples more Permalloy and is thus less resolved, the other devices (another two devices were measured and looked promising) that give reliable data were destroyed in the first machining session. Let us call the nanowire that made it passed the first machining phase, *nanowire 1 (10nm thick)*.

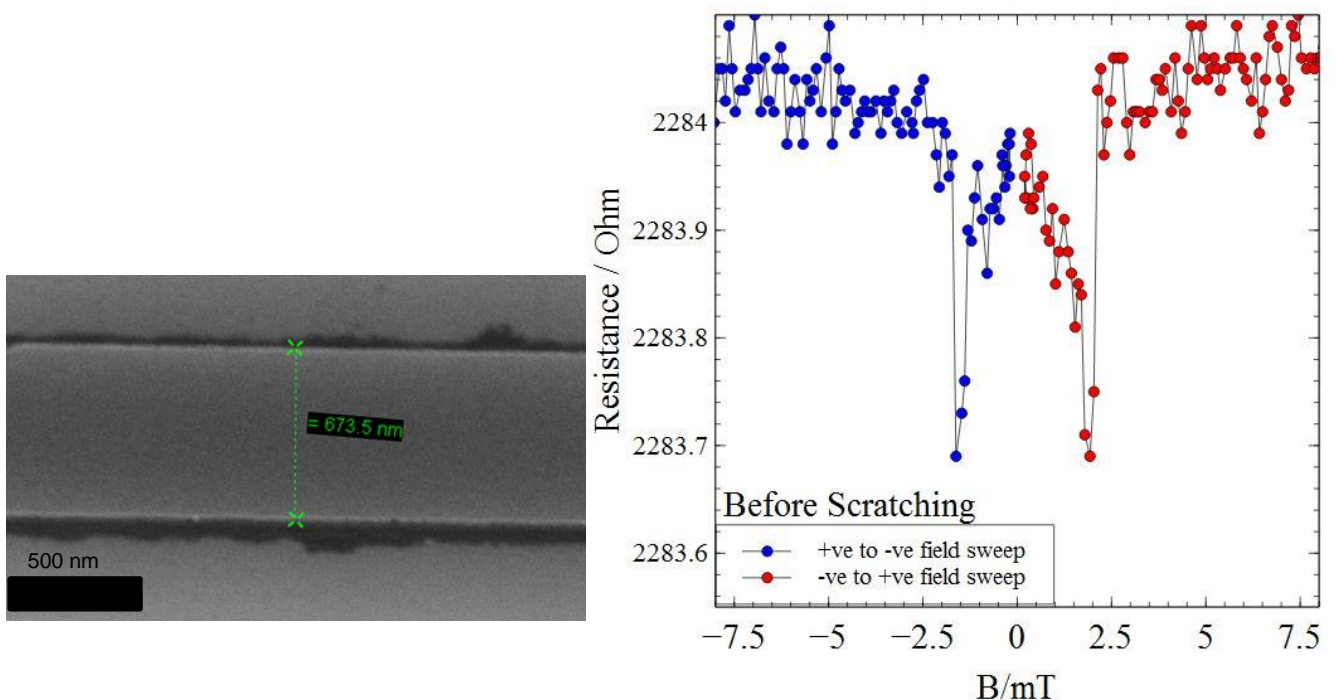


Figure 5-7 Showing a typical AMR curve for a 674nm wide, 10nm thick, 2um in length nanowire. The image to the right shows both field sweep directions. In both cases a discontinuous jump in the resistance is associated with the depinning of a domain wall and rapid reversal via domain wall propagation.

Figure 5-7 shows the transverse AMR response of *nanowire 1 (10nm thick)* a high aspect ratio rectangle of Permalloy, specifically 10nm thick, 674nm wide and approximately 20 μm in length before it was subjected to AFM nanomachining. The field is applied along the nanowire easy axis. A sharp decrease in the resistance is observed followed by a sharp increase in resistance at around 2mT, corresponding to pinning and then depinning of a domain wall initiating the rapid reversal of the magnetisation [72]. The domain wall is presumed to be pinned at the corner of the

contact following from simulations and depinned when a sufficient amount of energy is transferred to the domain wall via the magnetic field to overcome the potential barrier presented by a reduction in width. The change in resistance associated with the domain wall motion is $\sim 0.3\Omega$. This resistance corresponds to a resistance change induced by the presence of a domain wall its effect manifest through AMR. In other words the magnetic structure of a domain wall interacting with the current as it reversing the nanowire produces this change of resistance.

Combining all the measurements made for *nanowire 1 (10nm thick)*, each measurement being a switching event/magnetic reversal event, it is possible to assign an error and calculate an average value for the coercive field and DW AMR for *nanowire 1 (10nm thick)*.

Coercive Field – (1.96 ± 0.11) mT -

DW AMR – (0.32 ± 0.0096) Ω for *nanowire 1 (10nm thick)*

5.4. Experimental Data Post-Machining (1st Scratch)

After measurements were made to characterise the sample before any machining took place, a diamond coated Silicon Nitride AFM tip was used to scratch the surface of *nanowire 1 (10nm thick)*. It was loaded with a mechanical force of $2\mu\text{N}$, and the upward or downward lateral cutting direction was used. The machining was done in contact with the sample (contact mode in the AFM). The machining was carried out in collaboration with the engineering department in Cardiff University with assistance from Mr. Josh Jones under the supervision of Dr. Emmanuel Brousseau.

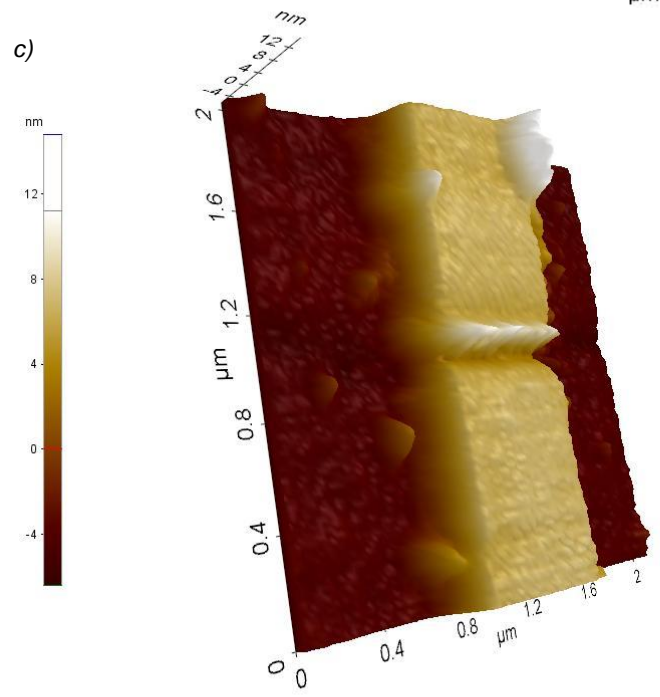
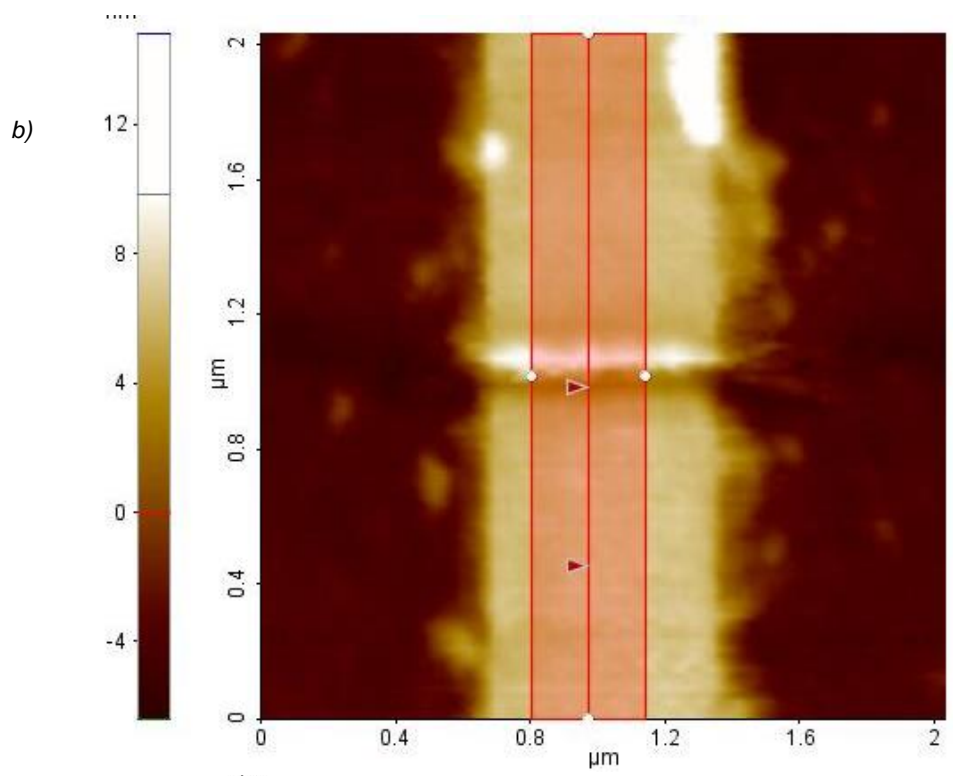
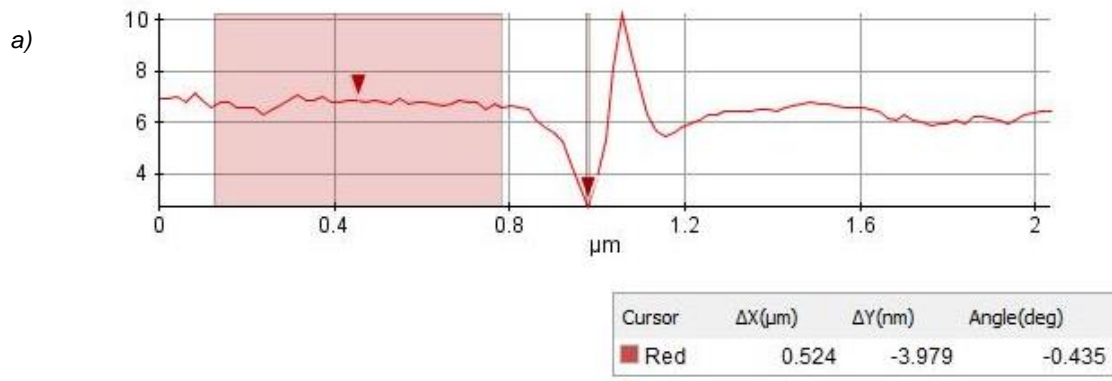
The machining resulted in the removal of material as visible in the images presented in **Figure 5-8**. Debris can be seen at one side of the nanotrench in **Figure 5-8** as a result of using the upward or downward cutting direction, as described earlier. The piled debris being around 5nm in height. It was unknown if this debris would affect the magnetic reversal of *nanowire 1 (10nm thick)*. The debris is visible in the 2D plot of **Figure 5-8** (image b) as a bright spot relating to higher topography. In 3D (image c) it is clearer as it is visualised using park systems XEI software [94], the scratch

and the debris can be seen clearly. AFM was used to ascertain the scratch depth (3.9nm) and width (520nm), again multiple line scans (image a) being used to estimate the values of the errors. In order to investigate the pinning of domain walls at the newly fabricated nanotrench magnetotransport measurements were carried out on the sample at room temperature in the low noise experimental setup.

It was hoped that the modification would influence the pinning and depinning of domain walls in *nanowire 1 (10nm thick)*.

Figure 5-9 shows data taken after machining of *nanowire 1 (10nm thick)*, for the transverse AMR configuration, current and magnetic field are parallel in the nanowire section of the device. **Figure 5-9** shows data for both field sweep directions measured after *nanowire 1 (10nm thick)* was machined using a diamond coated Silicon Nitride AFM tip along with the data taken prior to machining for a visual comparison. At first glance the data taken after machining (blue dataset) looks similar to the data obtained prior to machining (red dataset) although with a larger gap between the pinning and depinning fields. This shows clearly that scratching has affected the AMR response of *nanowire 1 (10nm thick)*, the depinning field is clearly higher, and that is for both field sweep directions (see **Figure 5-9**). There is no notable asymmetry in the data which might be expected from the piled up debris at one side of the scratch. For the positive to negative field sweep directions the DW AMR is $-320\text{m}\Omega$ and for the negative to positive field sweep direction the DW AMR is $-350\text{m}\Omega$. Micromagnetically the same process is taking place as in the un-scratched case, pinning at the corner of the nanowire after the wider section has reversed its magnetisation, except the domain wall is now pinned at the scratch until a higher field is reached, the scratch presenting a pinning site for domain walls.

Considering the change of the resistance after machining, the un-machined data in **Figure 5-9** was offset to overlay with the machined data for comparison. The resistance has gone up after machining and removing material from the nanowire.



File Name	Device 3 – scratch 1
Head Mode	C-AFM
Source	Topography
Data Width	104 (pxl)
Data Height	104 (pxl)
X Scan Size	2.03 (μm)
Y Scan Size	2.03 (μm)
Scan Rate	0.5 (Hz)
Z Servo Gain	1
Set Point	40 (nN)

Figure 5-8 Image a) shows the results of the linescan which is shown in the 2D AFM image (image b)). Image b) shows the a 2D AFM image. Image c) shows a 3D AFM image. The results of the linescan show the depth (3.9nm) and width (524nm) and the debris to one side of the nanotrench. Image c) shows the scratch can clearly be seen along with debris at one side (due to the cutting direction used)

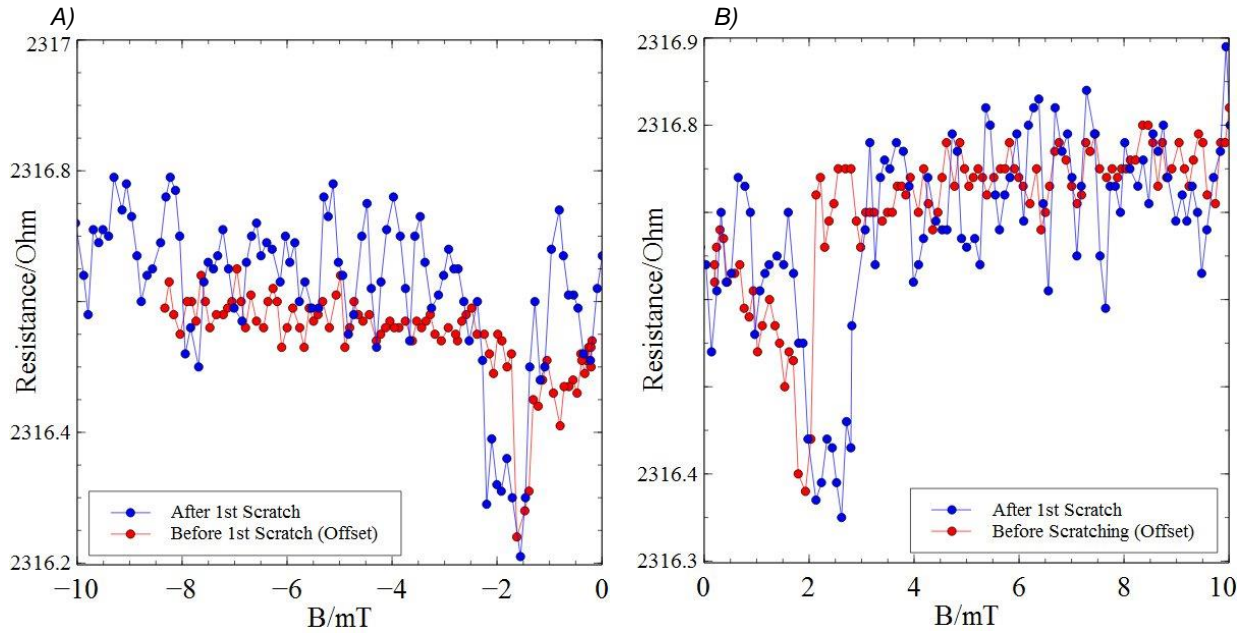


Figure 5-9 Shows a comparison of the data taken before and after the first machining session. Image a) shows the positive to negative field sweep direction. Image b) shows the negative to positive field sweep. Both sets of data taken after the machining, show a small increase in depinning field, the pinning field remaining similar to the non-scratched data. Un-scratched data is offset to overlay with the scratch data.

Specifically it has increased by 32.8Ω (see **Figure 5-9** and **Figure 5-7**), an increase is expected as material has been removed and for a thinner conductor one would expect a higher resistance. An attempt to get a numerical value for this resistance change was undertaken using the standard equation for resistivity and the dimensions of the nanowire along with its measured resistivity. The nanowire was deconstructed into three sections, two of 10nm in height and one central section of 6nm height corresponding to the removal of 4nm of material, the central section was given a length of 100nm and along with the other two sections summed to $20\mu\text{m}$. The resistance was calculated individually for each section and these were all summed in series to give the total resistance. A change of +5 Ohms was predicted, the fact that the experimental determined resistance is higher than the theoretical prediction could be due to an additional effect of surface scattering in a thin film not considered theoretically. Therefore the modelled value for the change in resistance could fall short of the experimentally determined value. Multiple field sweeps were taken to improve statistics, in order to determine errors and to evaluate repeatability.

The stochastic behaviour of domain wall pinning and depinning can be observed by making multiple measurements. Micromagnetically it is possible for different domain wall types to be generated, distinguished by differing coercive fields and DW AMR.

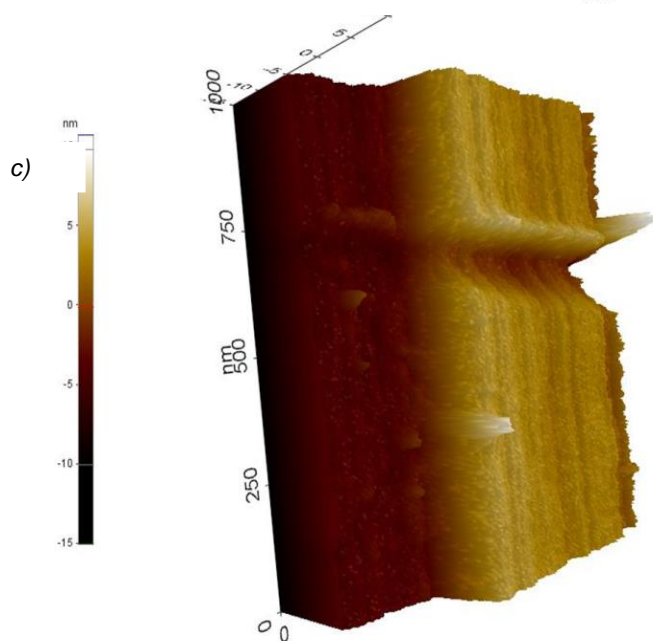
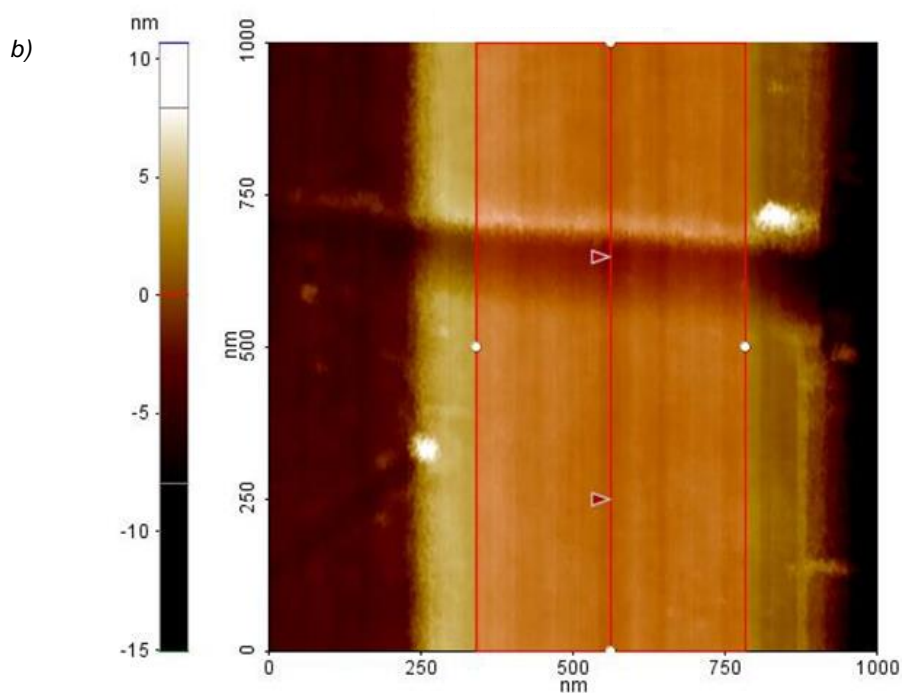
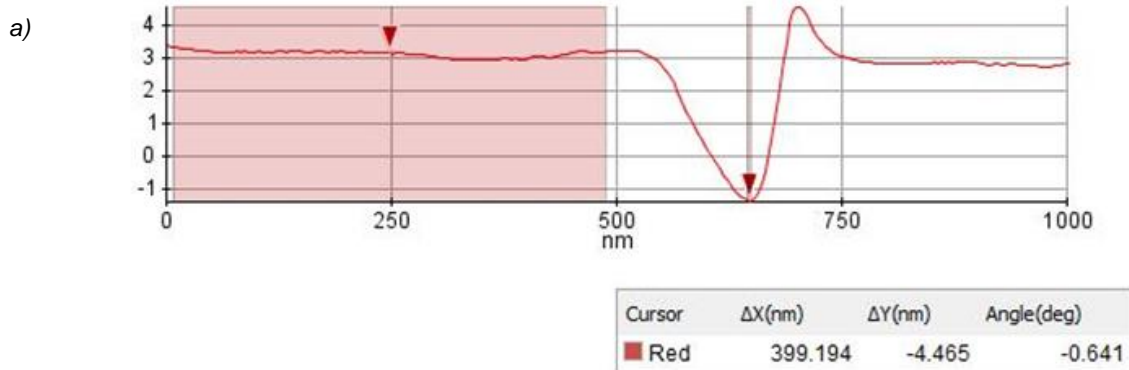
	Coercive field (mT) (pinning)	Coercive field (mT) (depinning)	DW AMR (Ohms) (pinning)	DW AMR (Ohms) (depinning)
Before Scratching	1.47±0.097	1.96±0.11	0.32±0.0096	0.32±0.0096
After Scratching	1.45±0.31	2.27±0.25	0.39±0.08	0.39±0.08
Difference	-0.012	+0.31	+0.07	+0.070

Table 4 Showing the results of multiple field sweeps for before (up) and after (below) nanowire 1 (10nm thick) was machined. The results show the pinning field to remain very similar although the depinning field has increased by 0.3mT after being scratched (depth 3.9nm, length 100nm).

5.5. Experimental Data Post-Machining (2nd Scratch)

The second machining of *nanowire 1 (10nm thick)* was carried out with the same diamond coated Silicon Nitride tip, this time it was loaded with a mechanical force of 1µN. Again contact mode was used where the tip and sample were actually in contact with each. A smaller force was applied hoping to remove less material than previous. i.e. .2µN removed 4nm. It was hoped that 1µN would remove 2nm, leaving 4nm of material in height in the machined section.

After machining of the nanowire the AFM was used to image the machined area as in the previous section. **Figure 5-10** image a) shows a linescan, the depth of the scratch having increased from 4.0nm to 4.5nm, the width of the scratch decreasing from 520nm to 400nm. The piled debris to one side of the scratch as a result of using the upward or downward motion of the tip, has decreased from around 5nm to around 2nm and is clearly visualised in image c) of **Figure 5-10** along with the scratch. This reduction in the height of the debris is most likely a result of cleaning the sample prior to the second scratch using an ultra-sonic agitation and Acetone.



File Name	Device 3 – scratch 2
Head Mode	NC-AFM
Source	Topography
Data Width	256 (pxl)
Data Height	256 (pxl)
X Scan Size	1 (μm)
Y Scan Size	1 (μm)
Scan Rate	0.5 (Hz)
Z Servo Gain	1
Set Point	509 (nm)
Amplitude	1.9555×10^3 (nm)
Sel. Frequency	285.2×10^3 (Hz)

Figure 5-10 Image a) showing the results of a linescan (the linescan is shown in the 2D plot, image b)). The results of the linescan show the depth (4.5nm) and width (400nm) and the debris to one side of the nanotrench. Image c) shows a 3D image produced from AFM, the scratch can clearly be seen along with debris at one side (due to the cutting direction used). The second scratch served to marginally increase the depth of the scratch.

After the second machining session was complete, the device was again measured in the low noise magnetoresistance setup.

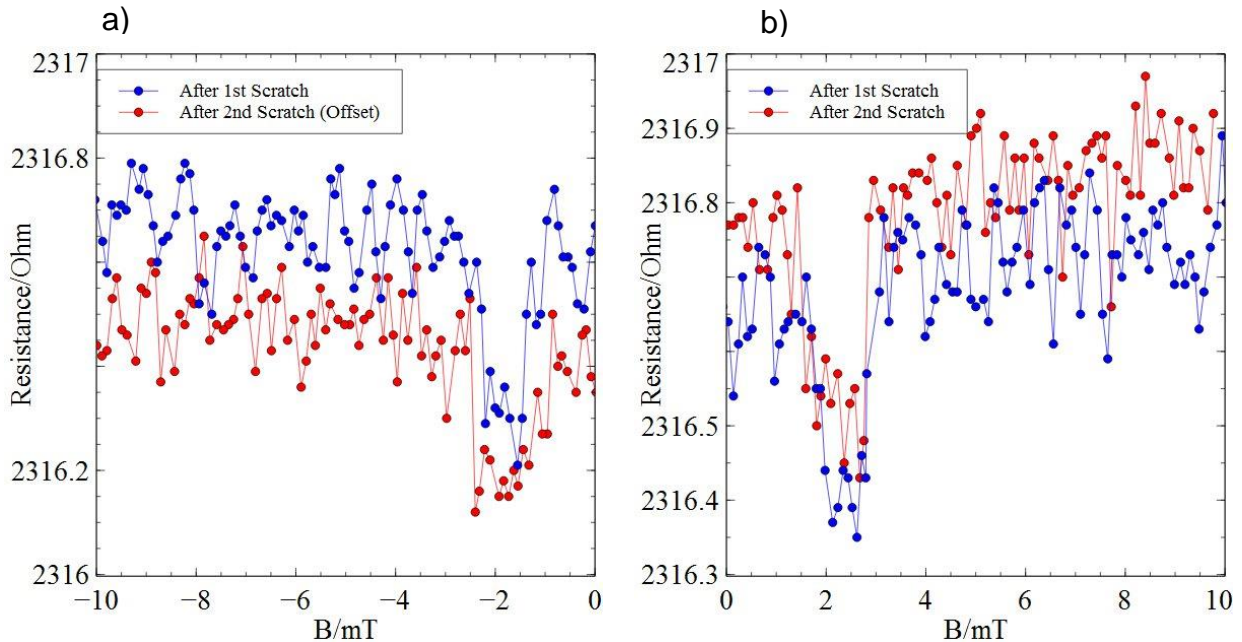


Figure 5-11 Showing a comparison of data taken before and after the second machining session. Image a) compares the positive to negative field data and image b) compares the negative to positive field data.

Figure 5-11 compares the data taken before and after the second scratching session. Image a) shows a clear difference in the depinning fields although there is a great deal of overlap in the depinning data of image b). It is possible to use all the field sweeps and assign an error and mean value to the dataset. This was done and is shown in **Table 5**, it summarises the means and standard deviations of all the data thus far considered i.e. no scratch, 1st scratch and 2nd scratch.

Again let us initially consider the resistance change. The resistance seems to have increased by around 5 Ohms. This was deemed insignificant due to the fact that is on the order of the thermal drift and subsequent field sweeps gave values above and below the value shown for the first scratch within a range of ± 5 Ohms. Also considering the small amount of material that was removed during the second scratching session it is unlikely to have drastically altered the resistance, it certainly would not have reduced it.

<i>Nanowire 1</i> (10nm thick)	Coercive field (mT) (pinning)	Coercive field (mT) (depinning)	DW AMR (Ohms) (pinning)	DW AMR (Ohms) (depinning)
Before Scratching		1.96±0.11		0.32±0.0096
After 1st Scratching (3.9nm)	1.45±0.30	2.27±0.25	0.39±0.082	0.39±0.082
Difference		+0.31		+0.070
After 2 nd Scratch (4.5nm)	1.50±0.36	2.61±0.32	0.31±0.068	0.35±0.049
Difference	+0.047	+0.34	-0.079	-0.038

Table 5 Showing the results for all three datasets (before scratching, 1st scratch and 2nd scratch). These numbers are obtained by evaluating all the points shown in Figure 5.11 and previous plots of this nature. An increase of 0.3mT is measured for scratch one compared to no scratch and for scratch 2 compared to scratch 1.

It is clear by looking at the images of **Figure 5-11** that the depinning datasets for 1st and 2nd scratches do not overlay perfectly. The error and average values are calculated from the data and shown in **Table 5**. There is an increase of depinning field of 0.34mT for the second scratch with respect to the first scratch depinning field. With respect to the no scratch dataset an increase of 0.65mT was measured after the second scratching.

5.6. Destruction of Nanowire 1 (10nm thick)

Nanowire 1 (10nm thick) was machined further in an attempt to deepen and widen the nanotrench. *Nanowire 1 (10nm thick)* proved difficult to machine after the second machining session. **Table 6** shows the scratch force history for *nanowire 1 (10nm thick)*, it shows a gradual increase in the force used to machine *nanowire 1 (10nm thick)* up until it is destroyed.

Scratch no.	Force used (μN)	Depth (nm)	Length (nm)
1	2	3.9	400
2	1	4.5	520
3	2 x 1	No change	No change
4	2	No change	No change
5	1	No change	No change
6	2 x 1.5	No change	No change
7	2 x 1.5	No change	No change
8	2 x 3	Nanowire destroyed	Nanowire destroyed

Table 6 Showing the complete force history of nanowire 1 (10nm thick), the force applied was gradually increased until the nanowire broke.



Figure 5-12 Showing an SEM image of nanowire 1 (10nm thick), after the final machining attempt which destroyed the wire.

Figure 5-12 shows a SEM image of the broken nanowire, the full break being visible. Immediately apparent is the size of the rupture in the nanowire, it is approximately 600nm wide. When one considers that the AFM tip used for machining the nanowire was less than 20nm in diameter, how does a 600nm rupture result? It is thought that the mismatched lattice parameters of Silicon and Permalloy mean there is a lot of strain in the nanowire which is more prevalent the closer to the interface one is. There is possible evidence for this in the complete force history shown in **Table 6**, material was removed in the second machining session using 2 μ N of force, the same force used to machine the nanowire didn't result in any more material being removed, it is getting harder to machine as the nanowire gets thinner and closer to the Permalloy/Silicon interface. Upon inspecting **Figure 5-12**, it shows that almost a micron of material (in length) has been removed. Again if a lot of strain is contained within the Permalloy then a large amount of energy could be released as soon as *nanowire 1 (10nm thick)* was ruptured, taking a 20nm rupture to several hundred nanometres.

Nanowire 1 (10nm thick) served as a prototype device to see if AFM nanomachining was plausible. An increase of over 0.5mT was observed for a machining depth of 5nm on a 10nm thick nanowire. This preliminary experiment was deemed a success and a twenty nanometre thick sample was fabricated in hope to give more material to remove and more data-points to measure via magneto-transport.

5.7. 20nm Thick Permalloy nanowires of Various Widths Machined Using AFM

A set of nanowires with varying widths and a nominal thickness of 20nm was fabricated in the manner outlined in chapter 3 (EBL and thermal evaporation, followed by a lift-off process) for AFM nanomachining studies. The same two designs were employed as for the 10 nm chip, see **Figure 5-6** for clarity. After machining the 10nm chip and observing a small change in the coercive field as a result of the machining, it was decided that another chip would be fabricated with a greater thickness giving essentially more material to remove. The width dependence was also investigated using the 20nm thick devices. All the devices were measured in the

same manner as the 10nm thick devices, using the low noise AMR setup that was assembled during the course of this PhD.

On the 20nm thick sample, six out of the eight fabricated devices were machined and gave meaningful results, this resulted in considerably more data than the previous section detailing the machining of a 10nm thick chip (only one device was machined). Therefore it is not time or space efficient to show all of the data taken, for each scratch iteration and for each device. Example data will be shown for a single device and then datasets of interest will be shown only. Finally all the data will be reviewed as a whole as opposed to individually.

5.7.1. Experimental Data: Prior to Machining a 20nm Thick, 2 μ m Long, 211nm Wide Nanowire

Before machining any devices took place, SEM, AFM and magneto-transport measurements were made on all devices. This was to check the overall integrity of the fabricated devices, to obtain values for the width (SEM) and thickness (AFM) of the fabricated devices. Let us refer to the next nanowire discussed as *nanowire 2* (211nm wide, 20nm thick). Only the nanowires discussed in the results section shall receive a name, in the discussion section nanowires will be differentiated in terms of their differing widths.

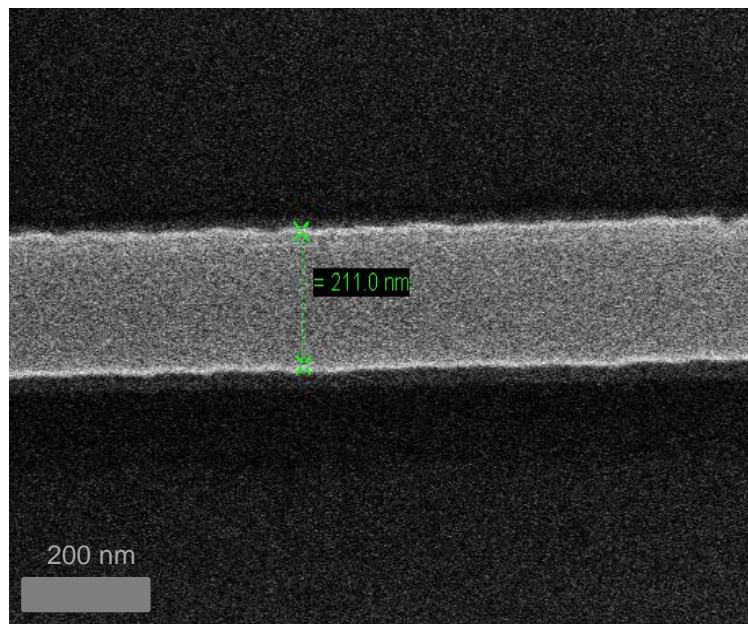


Figure 5-13 Showing a SEM image of a 20nm thick, 211nm wide nanowire, prior to being machined. It shows the clean edge profiles and overall good quality of the fabricated nanowire.

Figure 5-13 shows an SEM image of the narrowest wire fabricated on the 20nm thick set of devices. This was used to assign a width to this nanowire, multiple measurements were made to estimate an error. The fabricated device (*nanowire 2* (211nm wide, 20nm thick)) has a width of (211±2) nm. Clean edge profiles were observed for all nanowires fabricated on the same chip with a 20nm thickness. After checking the quality, thickness and width of the nanowire, it was then measured in the low noise AMR setup for measuring the magnetoresistance. The magnetic field is applied parallel to the long axis of the nanowire.

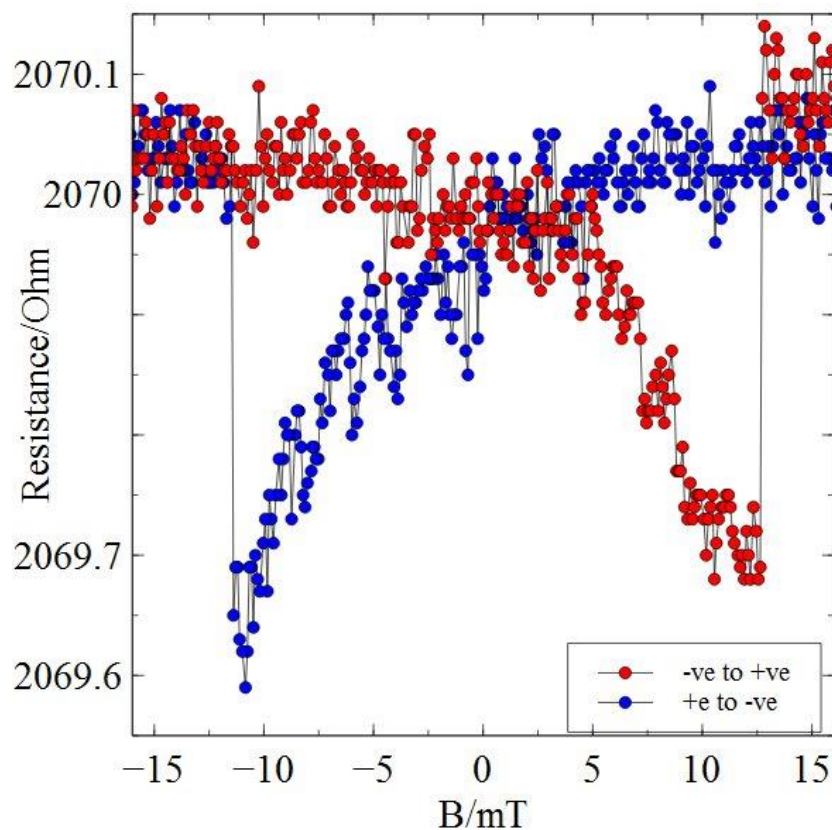


Figure 5-14 Showing a typical AMR curve as measured for a 211nm wide 20nm thick and 2µm long nanowire of Permalloy (SEM shown in figure 5.13). The magnetic field applied along the easy axis of the nanowire. In both sweep directions there is a clear abrupt change in the resistance around 11mT corresponding to the rapid reversal of the nanowire facilitated by domain wall motion.

Figure 5-14 shows the transverse AMR response from a 211nm wide and 20nm thick nanowire of Permalloy of a few microns of length. An abrupt change in the nanowires resistance is observable for both field sweep directions corresponding to

a domain wall propagating through the structure and reversing its magnetisation. As discussed previously the domain wall is pinned at the point where it enters the narrowest section of the nanowire, a higher magnetic field is required to propagate the domain wall through the narrower section and so the domain wall will be pinned at this point until the potential barrier has been overcome, which is the narrowest section of the wire. The narrower the wire the greater the field required to reverse the nanowires magnetisation by virtue of its increased shape anisotropy.

Multiple measurements are carried out in order to assign an error and assess the stochastic behaviour of the magnetic reversal in magnetic nanowires. As discussed previously it is possible for more than one domain wall type to be responsible for the magnetisation reversal and so multiple measurements are essential to fully understand how the nanowire is reversing its magnetisation.

Coercive Field – (11.8 ± 0.5) mT

Magneto-resistance – (0.37 ± 0.03) Ohm, for *nanowire 2 (20nm thick, 211nm wide)*

Errors were assigned by calculating the standard deviation of the coercive fields and the DW AMR measured. However, the variation in coercive field is less than one mT (0.5mT), as discussed in the literature review for this section, one might expect changes as high as 5mT for differing domain wall configurations. The experimental variation in the DW AMR was very small also being only (0.030Ω) whereas for differing domain wall types variations on the order of 0.5Ω are expected [13]. For *nanowire 2 (20nm thick, 211nm wide)* it is accepted that a single domain wall type or possibly two are responsible for reversing the nanowires magnetisation, given its dimensions and experimentally determined errors. A technique providing magnetic contrast on the nanoscale would provide the ultimate proof of the number and type of domain walls that are responsible for reversing the nanowires magnetisation.

5.7.2. Experimental Data: Post Machining of a 20nm Thick, 2µm Long, 211nm Wide Nanowire (1st Scratch)

A diamond coated Silicon Nitride AFM tip was used to machine the surface of *nanowire 2 (20nm thick, 211 nm wide)*. It was loaded with a mechanical force of $2\mu\text{N}$ as in the previous section assuming similar results, and the upward or downward

cutting direction was used again also. The machining was done with the tip in contact with the sample (contact mode).

The machining according to **Figure 5-15** had not altered the structure drastically. There looks like there could be some modification to the nanowire although from the image shown in the figure it is not obvious. There are a few bright spots corresponding to an increase in height, and considering the cutting direction used one would expect a collection of material at one side of the nanotrench, considering this, the highest peak is most likely closet to the scratch. It was decided that magneto-transport measurements would provide another independent way of probing to see if a pinning site for domain walls was created.

It was hoped that the modification would influence the pinning and depinning of domain walls in *nanowire 2* (20nm thick, 211nm wide).

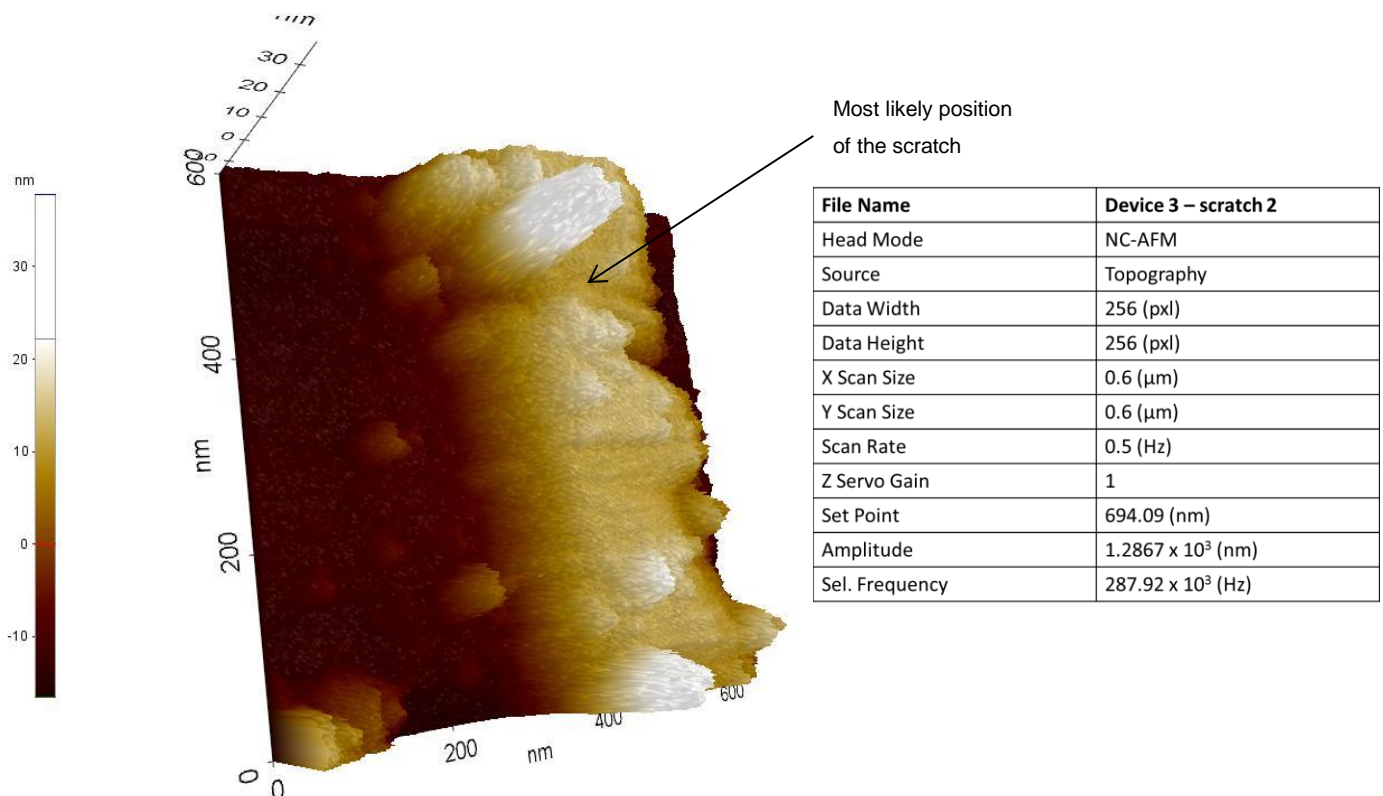


Figure 5-15 Showing the modification to nanowire 2 (20nm thick, 211nm wide), there is no clear indication that the machining has been successful here although it was decided to measure the AMR response of the nanowire as another independent way to investigate if any changes have occurred. The most likely position of the scratch is shown with an arrow.

The sample was again loaded into the low noise AMR measurement setup for magneto-transport measurements. The magnetic field was again applied along the long axis of the nanowire.

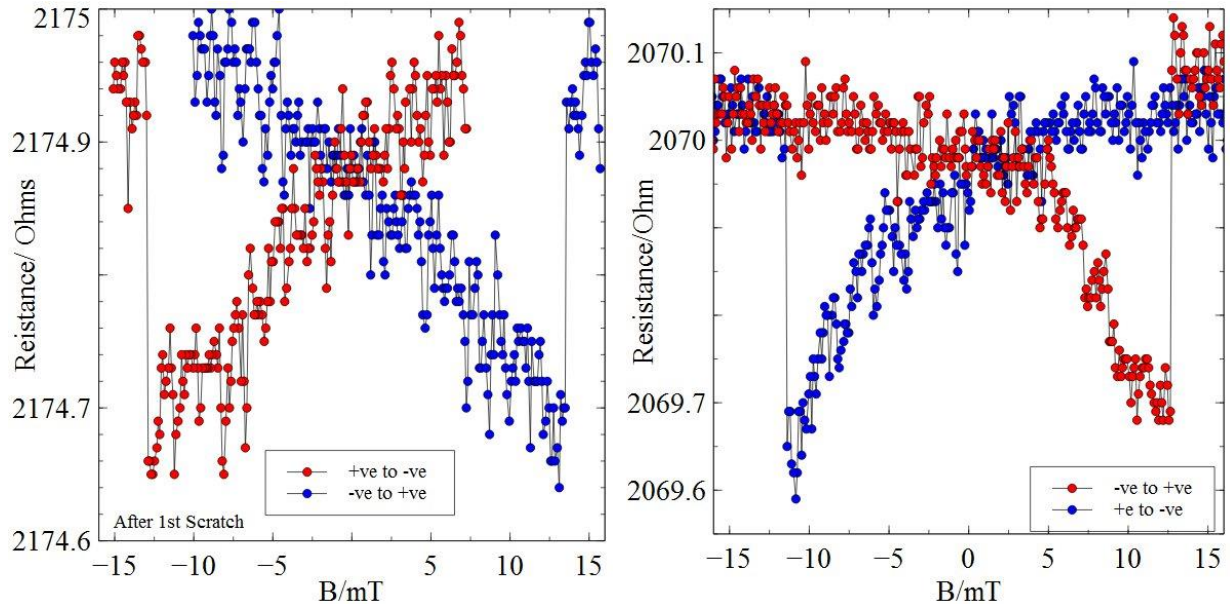


Figure 5-16 Showing a comparison of the data taken before and after scratching nanowire 2. It is clear the coercive field has increased and it looks like the change in resistance has reduced. The total resistance has increased due to the scratch removing some NiFe. This is evidence to suggest a scratch took place and has formed a pinning site for domain walls in nanowire 2.

Figure 5-16 shows transverse AMR data for *nanowire 2* (211nm wide, 20nm thick), taken before and after machining. Notable changes are: the increase in coercive field and the resistance increase. Both of these facts imply that the scratch has formed a pinning site for domain walls in *nanowire 2* (211nm wide, 20nm thick).

Figure 5-17 presents data taken before nanowire 2 was scratched and after the scratch. The datasets are overlaid to highlight the increase in coercive field and the reduction of the DW AMR, this is clear for both field sweep directions.

Firstly, let us consider the resistance change before and after machining, it is close to a 100Ω increase in the resistance which should be associated with the removal of material. It is not easy to calculate the resistance change in the case of this particular nanowire given the ambiguity in exact position of the scratch and thus the depth and width. The increase in total resistance of the wire is further evidence that scratching of *nanowire 2* (20nm thick, 211nm wide) was successful i.e. material was removed.

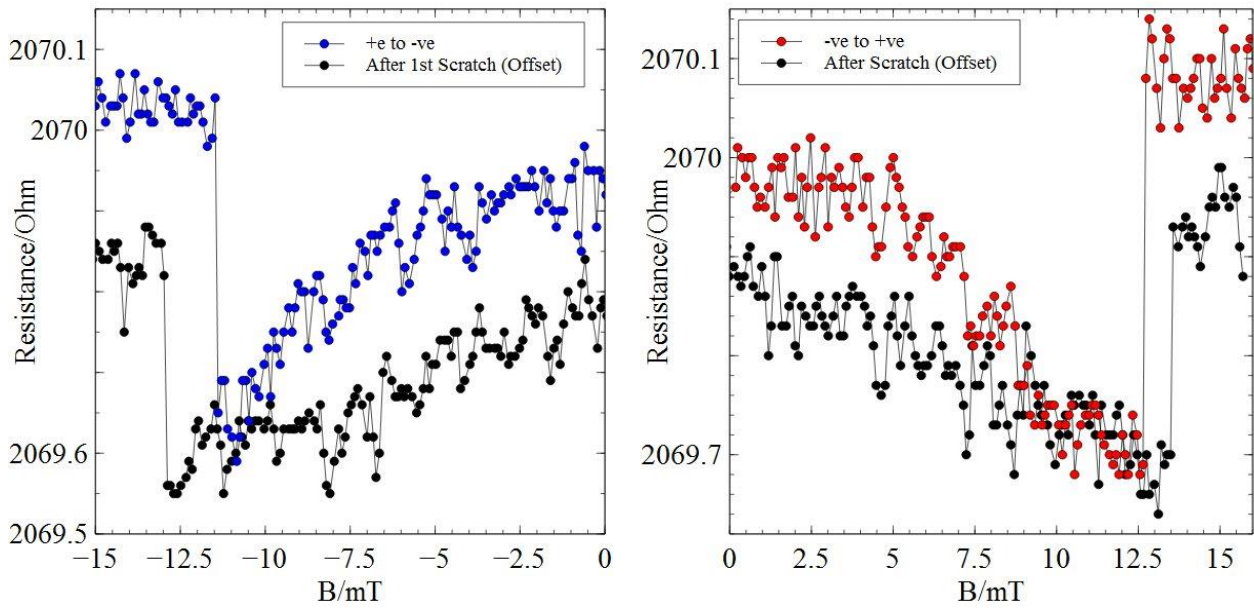


Figure 5-17 A comparison of data taken before and after the scratching of nanowire 2. It is clear that the coercive field has increased and the size of the magneto-resistance has reduced. The dataset taken after the scratch was offset to overlay the datasets.

Considering the magnetotransport measurements presented in **Figure 5-16** and **Figure 5-17** it is apparent that the scratch has modified the coercive field. It has increased by 1.4mT when averaging all the measurements taken after the sample was machined, when considering the error ($\sim 0.5\text{mT}$) associated with measurements made before and after scratching it is reasonable to assume that scratching the nanowire is responsible for the measured change in coercive field. It is expected that a scratch in the nanowire would result in a pinning site for a domain wall and potentially a larger field would be required to de-pin the domain wall and reverse the magnetisation as a result, this was observed experimentally for nanowire 2. Regarding DW AMR it seems to have decreased, analysing all the measurements taken to calculate an average and error it was found that the DW AMR had decreased by 0.06 Ohms. This is significant as shown in **Figure 5-17**, the AMR has almost halved in size. According to both the 1D model of Neel walls in planar nanowires and also the conduction channel model [12] [95], an increase in the DW AMR is predicted for a reduction in thickness. This will be discussed further in the discussion section for 20nm, section 5.9.

Given the error on the coercive field for *nanowire 2* (20nm thick, 211nm wide) after being machined it is assumed that a single domain wall type is responsible for reversing the magnetisation as prior to being scratched.

Device 1 no pads / <i>nanowire</i> 2 (20nm thick, 211nm wide)	Coercive field (mT) (depinning)	DW AMR (Ohms) (depinning)
Before Scratching	11.77±0.52	0.32±0.01
After Scratching	13.17±0.50	0.25±0.03
Difference	+1.41	-0.064

Table 7 Summarising the results obtained for *nanowire 2* (20nm thick, 211nm wide). The results show an increase in the coercive field and a decrease in the AMR.

Table 7 summarises the data obtained for *nanowire 2* (20nm thick, 211nm wide). See the discussion (Section 5.9) for an in-depth analysis of the data.

5.7.1. Experimental Data: Prior to Machining a 20nm Thick, 2µm Long, 403nm Wide Nanowire

The second 20nm thick nanowire to be presented is *nanowire 3* (403nm wide, 20nm thick). This nanowire was machined twice and a decrease in the coercive field was observed after both machining sessions. This nanowire was chosen to be presented due to the fact it responded in an unexpected way to machining i.e. an increase in coercive field is theoretically predicted but a decrease was observed for this nanowire.

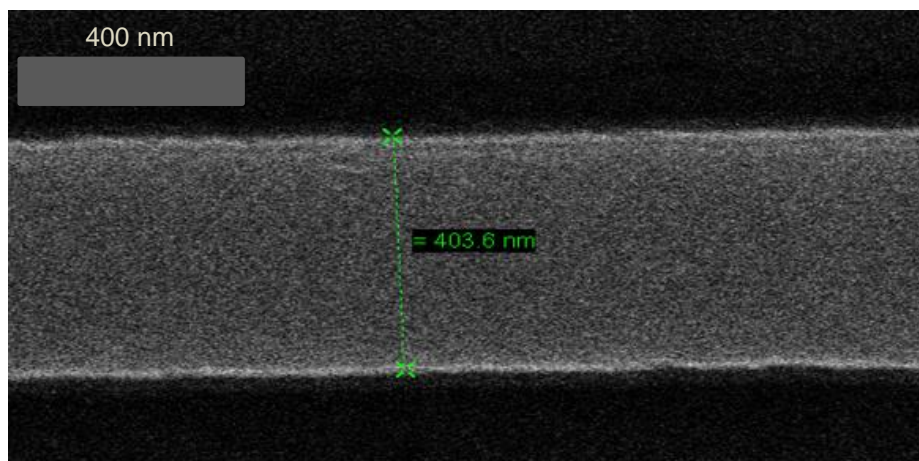


Figure 5-18 High magnification SEM image of *nanowire 3* (20nm thick, 403nm wide). Showing clean edge profiles and overall good integrity of the fabricated nanowire.

Figure 5-18 shows the width of *nanowire 3* (20nm thick, 403nm wide) and the quality of the fabrication i.e. there are no major defects present and a good edge profile has been achieved. SEM was used to assess the quality of the whole device not just the nanowire section. *Nanowire 3* (403nm wide, 20nm thick) has a width of (403 ± 2) nm

After imaging *nanowire 3* (20nm thick, 403nm wide), it was measured in the low noise AMR setup with the magnetic field applied along the long axis of the nanowire. This nanowire utilised the second design shown earlier in **Figure 5-6**. The nanostructure is not directly connected to the voltage contacts it connects to a larger pad a little way out from the nanowire. This meant that information on the wider parts of the device was obtained as well as that relating to the nanowire section of the device.

Figure 5-19 image a) shows a typical AMR dataset obtained for *nanowire 3* (20nm thick, 403nm wide) prior to any machining. An inset is included to show the full AMR dataset, when viewing the inset it is not possible to see the smaller features which relate to reversal of the nanostructure, the inset shows an AMR curve typical of a thin film exhibiting coherent rotation. This is a consequence of connecting to a wider section of Permalloy of dimensions $10\mu\text{m} \times 10\mu\text{m}$, which is behaving as a thin film (see image b). The effects associated with the reversal of the nanowire are superimposed on top of the bell curve produced by the effectively thin film section of the nanowire and are shown in the larger graph in **Figure 5-19** image a).

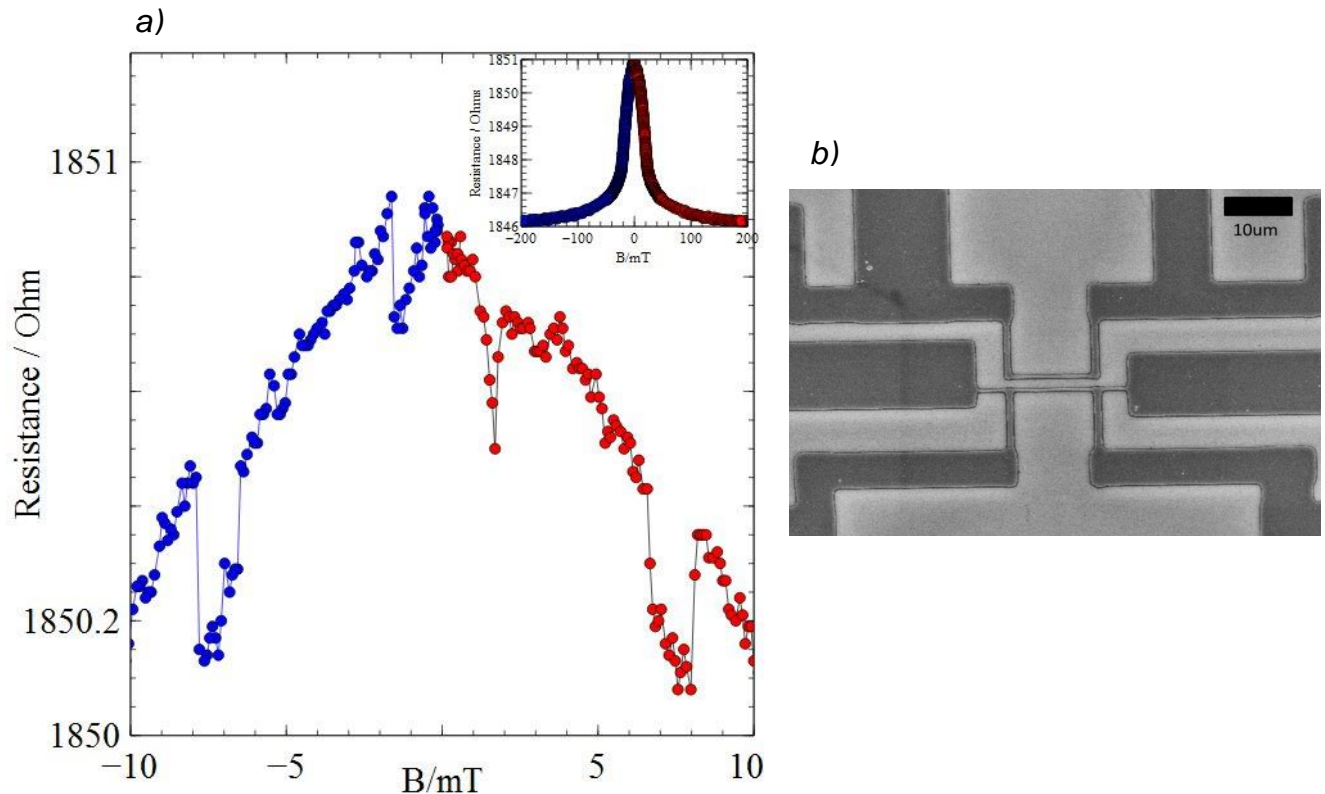


Figure 5-19 Image a) showing a typical measurement in the transverse AMR configuration for nanowire 3. This nanowire was fabricated and utilised a device design that allowed simultaneous measurement of the nanowire and other larger sections of magnetic material that the nanowire is connected to. See figure 5.6 for clarity (shows and SEM of both designs employed). The highest field effects correspond to pinning and depinning of a domain wall corresponding to reversal of the nanostructure. The inset image shows the AMR curve plotted to higher magnetic fields to show the full trend measured for this nanowire. Image b) showing the design used for nanowire 3, it has been added to aid description of the data presented in image a).

The main graph in **Figure 5-19** image a) is a zoom in on the central section of the inset. It shows fine details not visible in the inset. Firstly there is the bell shaped curve which is a result of the 10 μ m by 10 μ m size pad the voltage contacts connect to shown in **Figure 5-19** image b). Secondly there are features around +/-2mT attributed to a micron size contact pad leading to the nanostructure whose easy/long axis is ninety degrees to the applied field direction. There are two features at around 6mT and 8mT in both field directions, the resistance rapidly decreases and rapidly increases shortly thereafter. This is attributed to a domain wall being pinned at the corner before entering the nanostructure and then being depinned and reversing the entire nanowire. As for the nanowire 1 error values are calculated from multiple measurements.

5.7.1. Experimental Data: Post Machining of a 20nm Thick, 2µm Long and 403nm Wide Permalloy Nanowire

A diamond coated Silicon Nitride AFM tip was used to scratch the surface of *nanowire 3* (20nm thick, 403 nm wide,) the upward or downwards cutting direction was again used. Multiple attempts of increasing force were used to modify *nanowire 3* (20nm thick, 403nm wide) as summarised in **Table 8**.

Scratch No.	Force (µN)	Length (nm)	Depth (nm)
1	2x1 (two 1µN attempts)	0	0
2	3	280	1.1

Table 8 Showing the machining history of nanowire 3 (20nm thick, 403 nm wide)

After scratching the nanowire it was imaged using AFM to observe the result of scratching. It is used to measure the width and depth of the scratch made by AFM nanomachining. Multiple measurements are used to assign errors.

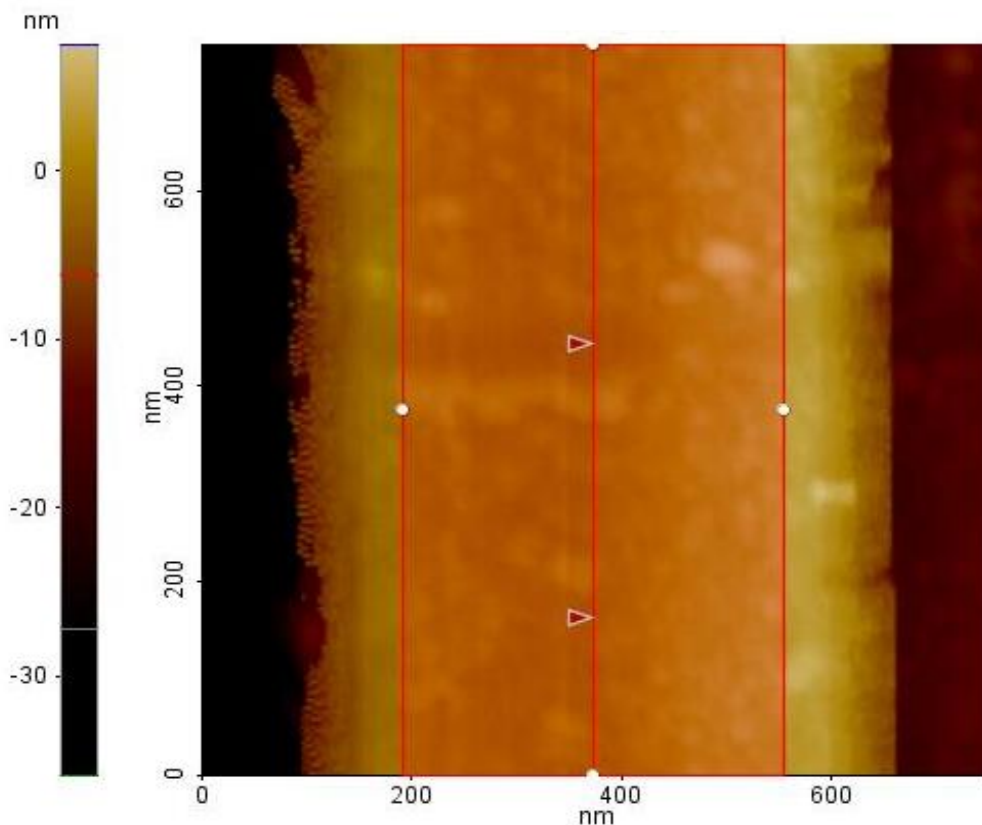


Figure 5-20 Showing a 2D AFM image of the nanowire 3 (20nm thick, 403nm wide) after being scratched. The red box denotes a line scan. Depth of scratch is approximately 1nm.

Figure 5-20 shows a 2D AFM image used to assess the scratch in terms of depth and width. The scratch is not clear in the 2D image presented, 3D images were also generated for this nanowire although none of which showed a clear and obvious scratch. The linescan shown in **Figure 5-21** shows the clearest evidence that a scratch was made, it shows a clear drop in thickness of around 1nm corresponding to the scratch and a piling of debris at one side of the scratch resulting from the cutting direction used.

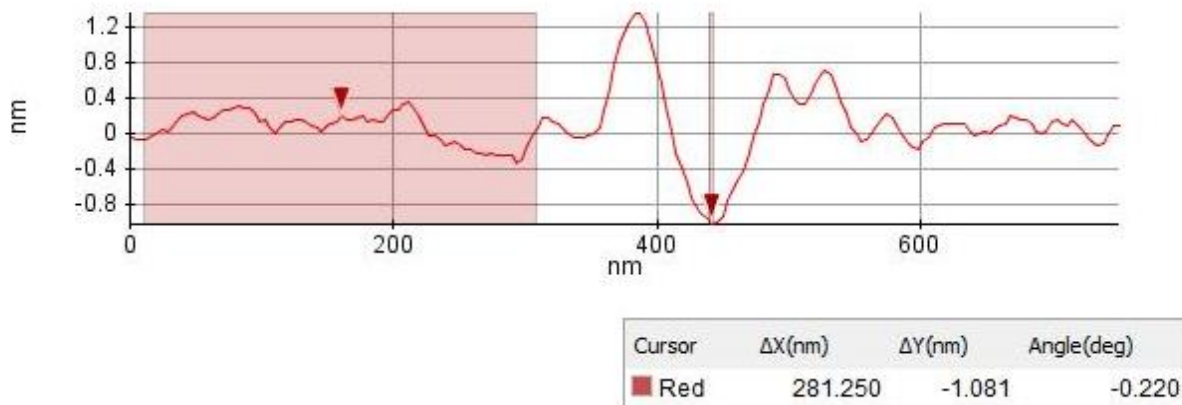


Figure 5-21 Results of the linescan shown in figure 5.20. It shows a depth of 1nm and a small pile up of debris, at one side, due to the cutting direction used.

It is not known whether such a small modification would alter the domain wall pinning/depinning process so it was decided to measure the sample after this scratch to see if it had affected the magneto-transport properties of *nanowire 3* (20nm thick, 403nm wide).

Figure 5-22 shows the AMR of *nanowire 3* (20nm thick, 403nm wide) after it was machined. It displays a very similar AMR curve to the data taken prior to machining the nanowire (**Figure 5-19**). A bell shaped curve corresponding to the wider section of the Permalloy, with the effects attributed to the nanostructure superimposed on top of this curve. The resistance has increased by 40 Ω after machining the nanowire, this increase in resistance is consistent with the removal of material. The DW AMR has reduced compared to the data taken prior machining, this is clearly seen in **Figure 5-23** showing a comparison of data taken before and after machining for a single field sweep. Also in **Figure 5-23** a small increase in the pinning and depinning fields is presented. This is an isolated event for this device, most pinning and

depinning fields had a lower coercive field when compared to the dataset measured prior to machining. It is necessary to analyse all the field sweeps taken in order to calculate a mean and standard deviation. The error given for the dataset prior to machining with respect to the coercive field is 0.3mT, as suggested earlier within this chapter it is unlikely that multiple domain wall types are responsible for reversing this nanowire. After *nanowire 3* (20nm thick, 403nm wide) was machined the error on the coercive field was 0.4mT, given the size of the error the same argument applies as for the pre-scratch data, a single domain wall type is therefore likely to be responsible for reversing this nanowires magnetisation.

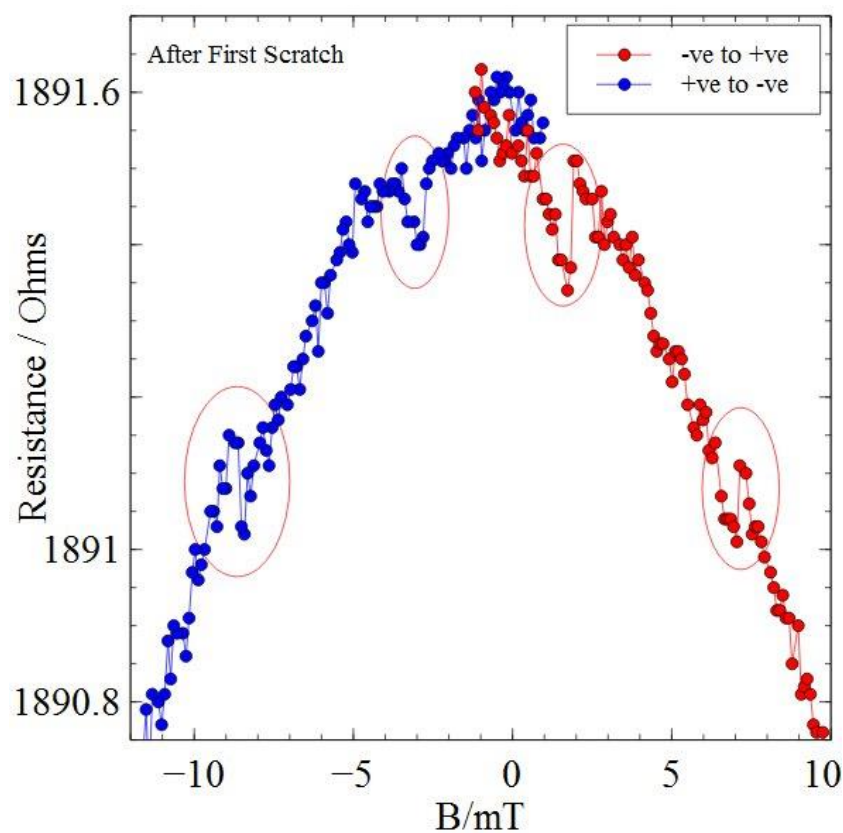


Figure 5-22 Showing a typical AMR response from nanowire 4 (20nm thick, 403nm wide). The red data points show a feature corresponding to reversal of the nanowire via domain wall reversal at around 8mT. The blue data points contain a feature associated with the nanowire reversal at around 5mT. Such a large difference between the two depinning fields implies that it may be two different domain wall types for each field direction shown in the above graph.

Multiple field sweeps are taken in order to evaluate the distribution of coercive fields and the associated DW AMRs.

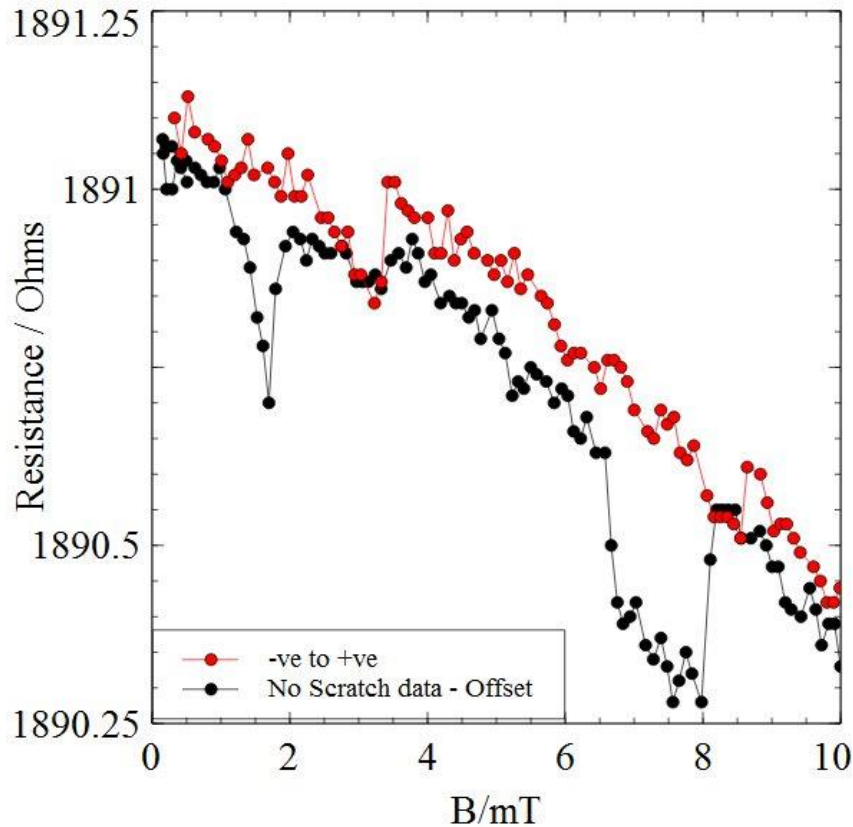


Figure 5-23 Showing a comparison between datasets taken before and after the first scratching session for a single field sweep, the data corresponding to no scratch was offset to allow comparison. Immediately obvious is the reduction in the size of the AMR. In the above figures it is difficult to see the effect in the scratched dataset, it is easier to view in figure 5.23 without the superimposed unscratched datasets.

5.7.2. Experimental Data: Post Machining of a 20nm Thick, 2 μ m Long and 403nm Wide Permalloy Nanowire second scratch

A diamond coated Silicon Nitride AFM tip was again used to scratch the surface of *nanowire 3* (403 nm wide, 20nm thick) for a second time. The machining history is summarised in **Table 9**.

Scratch No.	Force (μ N)	Length (nm)	Depth (nm)
1	2x1	403	1.
2	3	403	1
3	5	403	6

Table 9 Showing the machining history of nanowire 4 (20nm thick, 403 nm wide). Three scratches have been made.

Table 9 summarises the machining history for the second machining session undertaken on *nanowire 3* (403nm wide, 20nm thick), the force that was used to machine the nanowire in the first machining session (3 μ N) had no noticeable effect on the nanowire. A greater force was required (5 μ N) and removed a substantial amount of material. AFM was then used to assess the amount of material removed and assign a width and length of the modification.

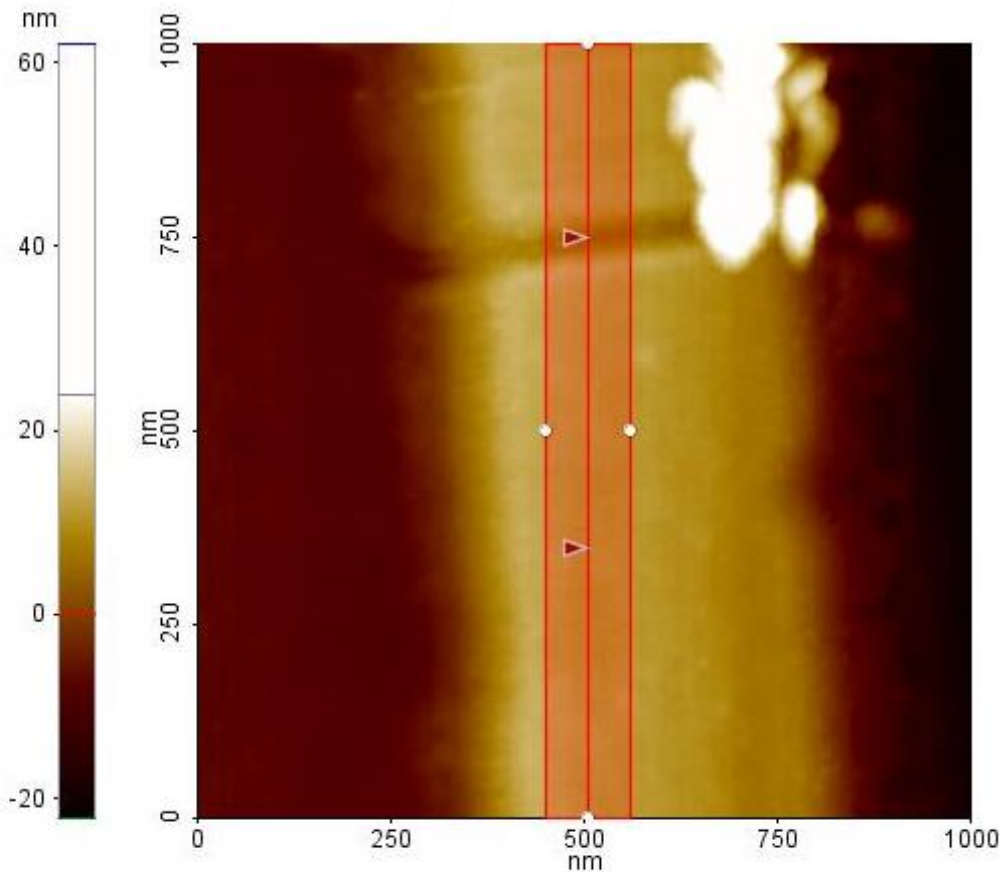


Figure 5-24 Showing a 2D AFM image of the second scratch made on the surface of nanowire 3 (20nm thick, 403nm wide). The red box shows a linescan. There is a clear scratch now in this nanowire. There is also debris shown by the white spots.

Figure 5-24 shows a 2D AFM image of *nanowire 3* (20nm thick, 403nm wide) after the second scratch. A clear scratch is shown in the image along with some material which registers as high as 60nm, the source of this large deviation in height is unknown. **Figure 5-24** also shows a linescan the results of which are displayed in the **Figure 5-25**.

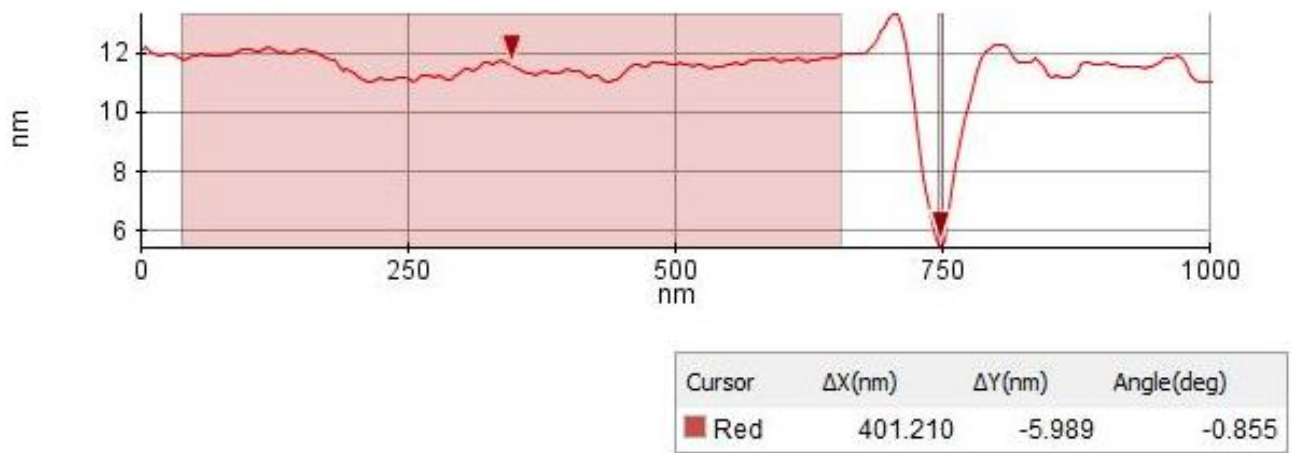


Figure 5-25 Showing the results of the linescan shown in figure 5.25. There is clear modification of the nanowire, maximum depth being 6nm. There is debris pile up at one side as a result of the cutting direction used. The length of the scratch is now approximately 400nm.

Figure 5-25 shows a scratch in the nanowire with a maximum depth of 6nm and a length of 401nm. The line profile shows a pile up of debris at one side of the scratch which is a direct result of the scratching direction used. Finally a 3d image is presented to show the clear formation of a scratch in *nanowire 3* (20nm thick, 403nm wide) after the second machining session.

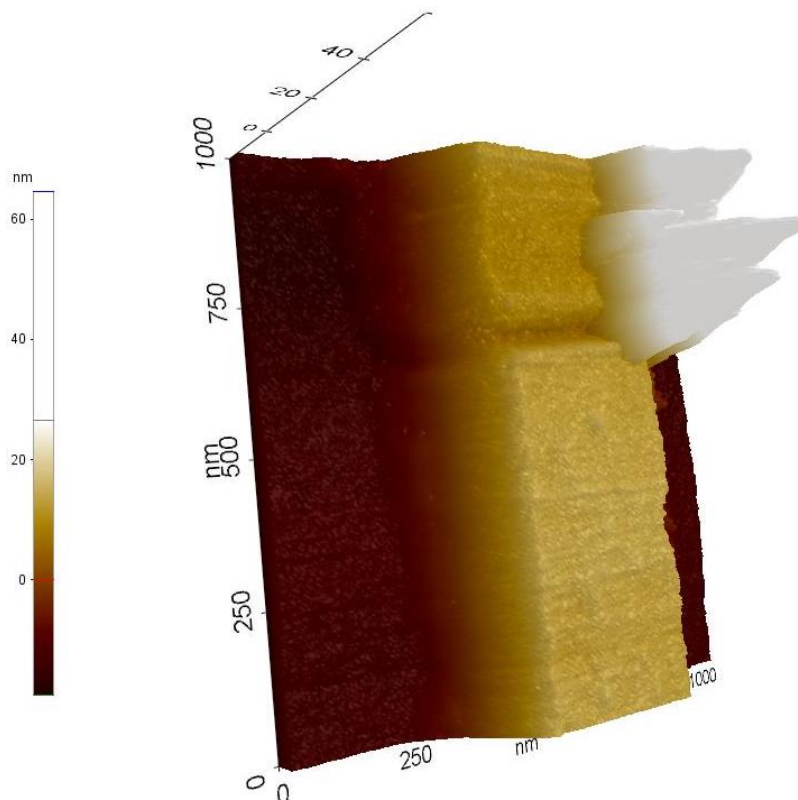


Figure 5-26 Showing a 3D AFM image taken after nanowire 3 was machined for a second time. A clear scratch is visible in the 3D image.

Figure 5-26 shows a 3D AFM image taken after *nanowire 3* (20nm thick, 403nm wide) was machined for a second time. A scratch is clearly shown in this image and the debris is just about visible also to one side of the scratch. An anomalously high pile up of material is observed in this image although it's origin is not yet known.

After imaging the nanowire using AFM it was measured using the low noise AMR setup with the magnetic field oriented along the long axis of the nanowire to probe the effect the scratch had on domain wall pinning using magneto-transport measurements.

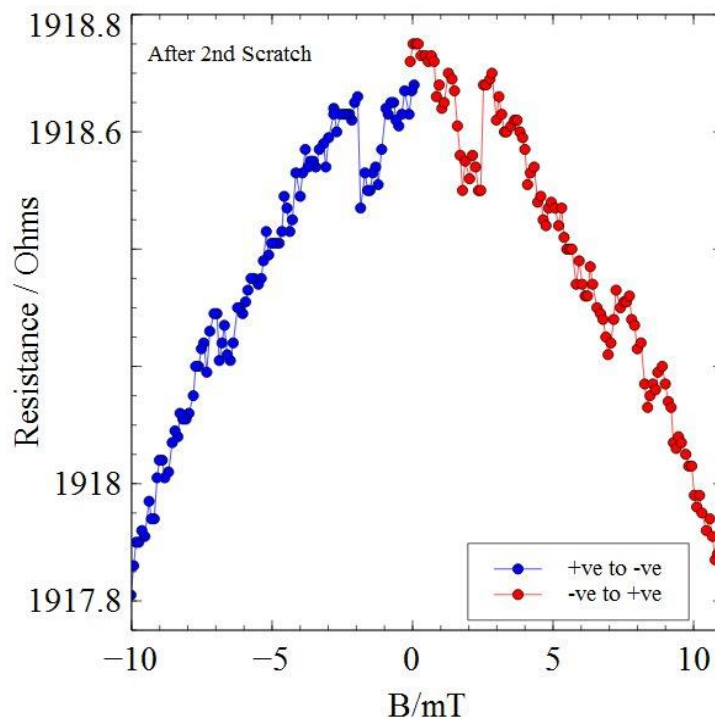


Figure 5-27 Showing the AMR transverse response measured after the 2nd scratch. The resistance has increased due to material being removed. Coercive fields associated with the reversal of the nanowire are similar. The size of the AMR has also decreased further.

Figure 5-27 presents a complete field sweep from the data gathered after the second machining session. A similar trend and features are observed as for the previous datasets obtained for this nanowire (prior to scratching, and after the 1st scratch). The bell-shaped curve is present and is a result of measuring a large section of Permalloy approximately 10 μ m by 10 μ m resulting in a response akin to a thin film, other features are superimposed on this bell curve background. Considering the higher field features that are around 2-3mT, as discussed earlier these are due to a micron sized wire leading to the nanowire at ninety degrees to the

applied magnetic field. To allow clear determination of the AMR (it was close to the noise threshold level) multiple field sweeps were compared to each other to ensure the field range was repeatable and consistent, it was possible to extract a value for the domain wall depinning in the post second scratch data for most field sweeps (red data in **Figure 5-27**), some it was not possible (blue dataset **Figure 5-27**).

Device 2 with pads	Coercive field (mT) (depinning)	DW AMR (Ω) (depinning)
Before Scratching	7.82 ± 0.26	0.30 ± 0.046
After Scratching	6.73 ± 0.37	0.11 ± 0.026
After 2 nd Scratch	6.60 ± 0.46	0.11 ± 0.034

Table 10 Showing the results of all three machining session on nanowire 3 (403nm wide, 20nm thick). The average and standard deviation were calculated for each dataset shown.

Table 10 shows the results after calculating an average coercive field and DW AMR, from all the field sweeps taken and an error based on the standard deviation for each dataset and scratch iteration. The results show an initial decrease in both coercive field and DW AMR after the first scratching session but both these values remain approximately constant after the second machining session. This is unexpected in two ways, an increase in coercive field is predicted and a decrease is observed experimentally. Also after the second machining session, taking the depth of the scratch from ~ 1 nm to ~ 6 nm, no change in coercive field or DW AMR was observed.

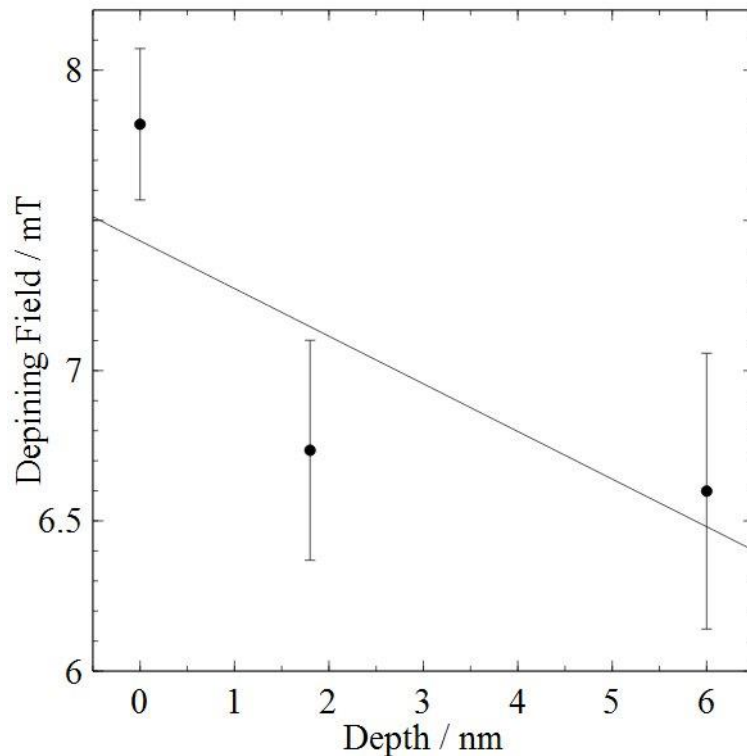


Figure 5-28 Showing the domain wall depinning field as a function of the depth of the scratch for nanowire 3. A clear decrease in the depinning field is observed for this nanowire.

Figure 5-28 shows the variation in domain wall depinning field as a function of the maximum depth of the scratches made to *nanowire 3* (20nm thick, 403nm wide). A clear reduction is observed after both machining sessions. Considering the data prior to the scratch and after the first scratch data there is no overlap in error in depinning field giving extra weight that the coercive field has definitively decreased. There is considerable overlap between the pre-scratch and post second scratch datasets, one might expect the second modification to affect the depinning field to a greater extent than the first scratch given the greater increase in the depth of the scratch.

Figure 5-29 shows the variation of domain wall depinning field as a function of the length of the scratch. A decrease is observed with a straight line fitted to the data for comparison with theory. There is no overlap between the pre-scratch and post first scratch data, there is considerable overlap between the post first scratch and post second scratch datasets. Ideally only one of these parameters would be varied (length or depth), the length would be varied whilst keeping the depth constant or vice versa. This has proved difficult to achieve as subsequent machining tends to

increase both the length and depth, this is essentially the first attempt to modify a nanowire in this way so it is not surprising that certain aspects of the machining will likely be improved with time.

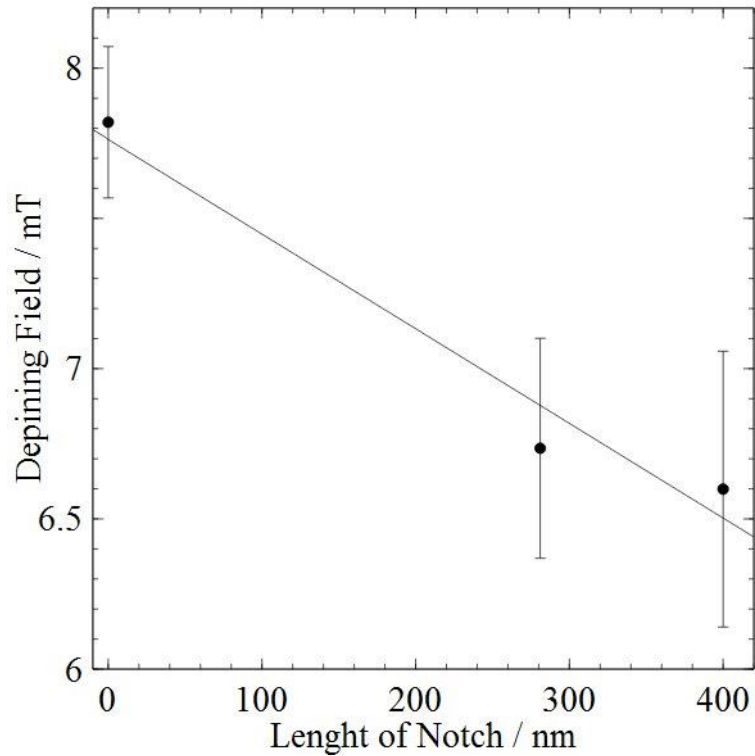


Figure 5-29 Showing the change in domain wall depinning field as a function of the length of the scratch. A clear decrease is observed. It is not clear what produce a decrease in the depinning field.

5.7.1. Data Prior to Machining a 20nm Thick, 2 μ m Long and 323nm Wide Permalloy Nanowire

The fourth nanowire to be presented is *nanowire 4* (323nm wide, 20nm thick). This nanowire was machined once and an increase in coercive field was observed although there was some overlap given the size of the error value.

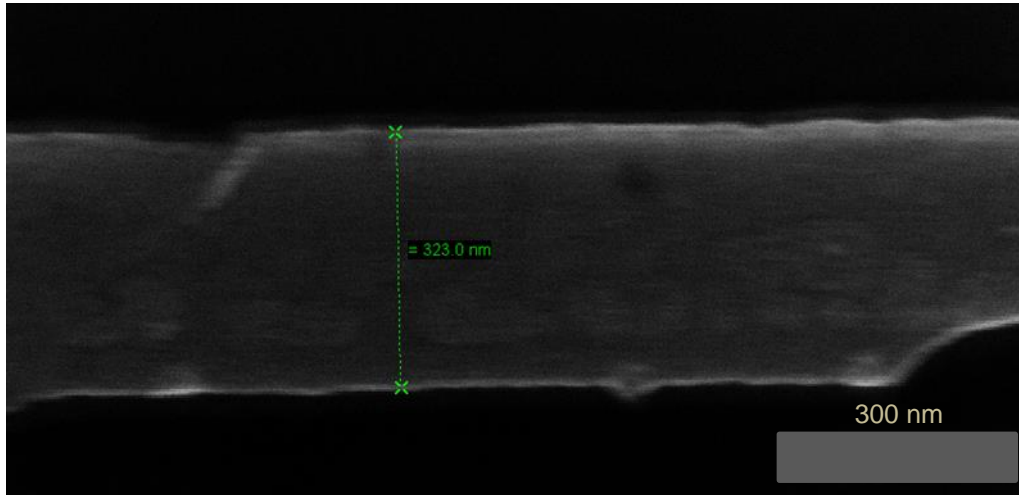


Figure 5-30 High magnification image of nanowire 4 (20nm thick, 323nm wide), this nanowire had a rougher edge profile than all other 20nm thick nanowires, it is not known why, as all 20nm thick nanowires were fabricated with nominally identical conditions.

Figure 5-30 shows a high magnification SEM image of nanowire 4. This image shows this nanowire has rougher edges than previously presented nanowires in this chapter. This nanowire also has the largest error presented for the coercive field, it is believed the former leads to the latter i.e. a domain wall is pinned at different defects in the nanowire and a larger variation in the coercive field increases results. The width of this nanowire was calculated to be (323 ± 2) nm.

After reviewing the overall structure of the nanowire using SEM it was then loaded into the low noise AMR setup to make magneto-transport measurements prior to AFM nanomachining.

Figure 5-31 shows the AMR response for *nanowire 4* (20nm thick, 323nm wide) with the magnetic field applied along the long axis of the nanowire. The blue dataset shows a clear domain wall depinning event at ~ 10 mT, an abrupt change in the resistance corresponding to domain wall depinning and leaving the nanowire thus reversing its magnetization. The red dataset shows another field sweep for the same nanowire, this field sweep does not show a single clear abrupt change in resistance as in the blue dataset, the magnetisation has fully reversed by 11.5mT however. It is thought that the domain wall that is responsible for reversing the nanowires magnetisation is being pinned and the depinned at multiple defects as it transverses the nanowires length. The variation in DW AMR could be explained by either

distortion or transformation of the domain wall responsible for reversing the nanowire in the red dataset.

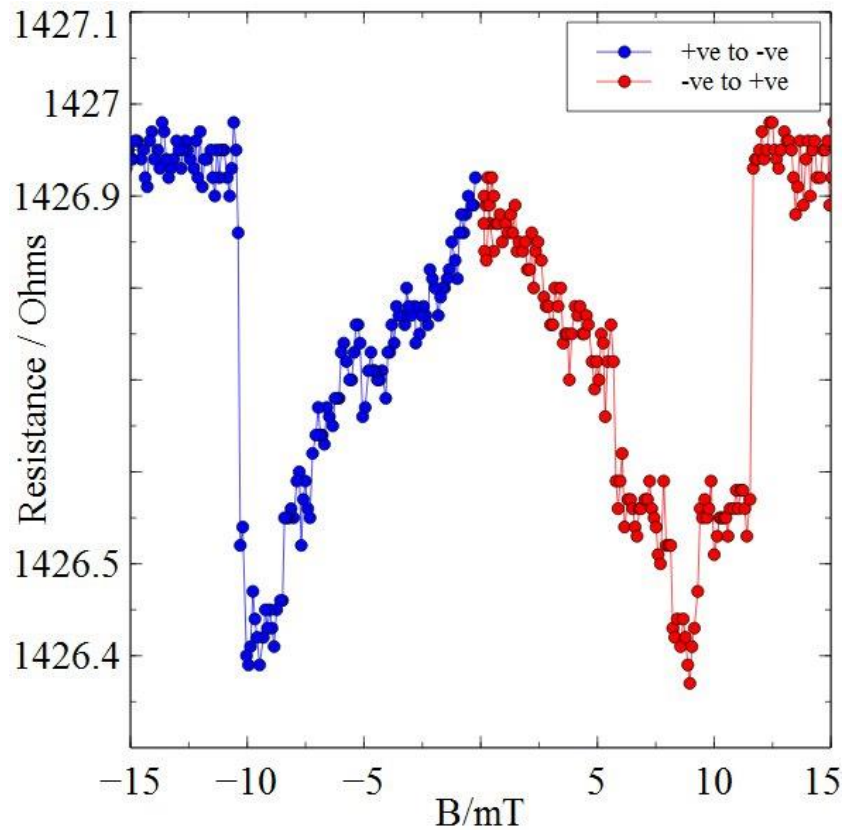


Figure 5-31 Showing the transverse AMR response of nanowire 4 (20nm thick, 323nm wide). The blue dataset shows an abrupt change in the resistance at a single field value corresponding to the nanowire being reversed via domain wall propagation. The red dataset has more than one feature attributed to the domain wall being pinned at defects within the nanowire due to its rougher edges.

5.7.2. Experimental Data: Post Machining of a 20nm Thick, 2 μ m Long and 323nm Wide Permalloy Nanowire

A diamond coated Silicon Nitride AFM tip was used to scratch the surface of *nanowire 4* (323 nm wide, 20nm thick). The machining history is summarised in **Table 11**.

Scratch No.	Force (uN)	Length (nm)	Depth (nm)
1	2x1	0	0
2	2	323	1.1

Table 11 Showing the machining history for nanowire 4 (20nm thick, 323nm wide)

After the machining was completed AFM images were taken and analysed to assess the results of AFM nanomachining.

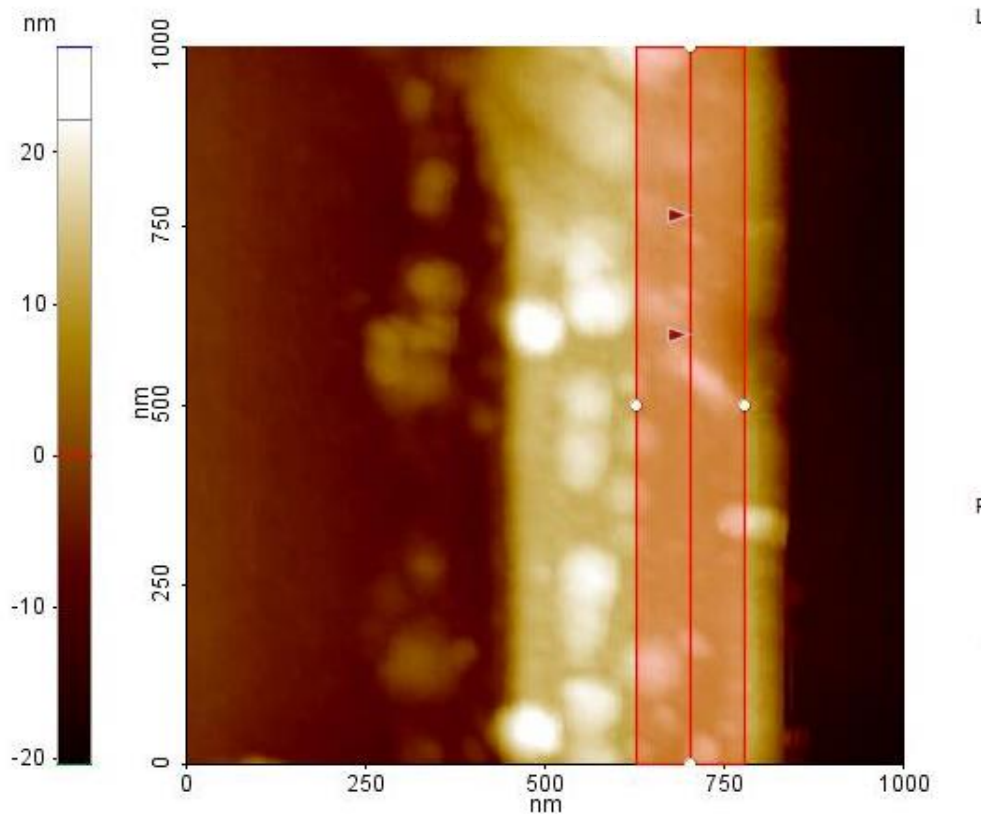


Figure 5-32 Showing a 2D AFM image and a linescan. The scratch not clearly visible in this image and the linescan needs to be reviewed to assess the scratch further.

Figure 5-32 shows a 2D AFM image of *nanowire 4* (323 nm wide, 20nm thick) taken after being machined. The scratch is not clearly visible in the image. There is a lot of material registering heights >20nm, it is not clear why there is much debris on and around this nanowire although as noted earlier this nanowire seemed to be of an overall lower quality in terms of fabrication than all other 20nm thick nanowires presented in this chapter. .

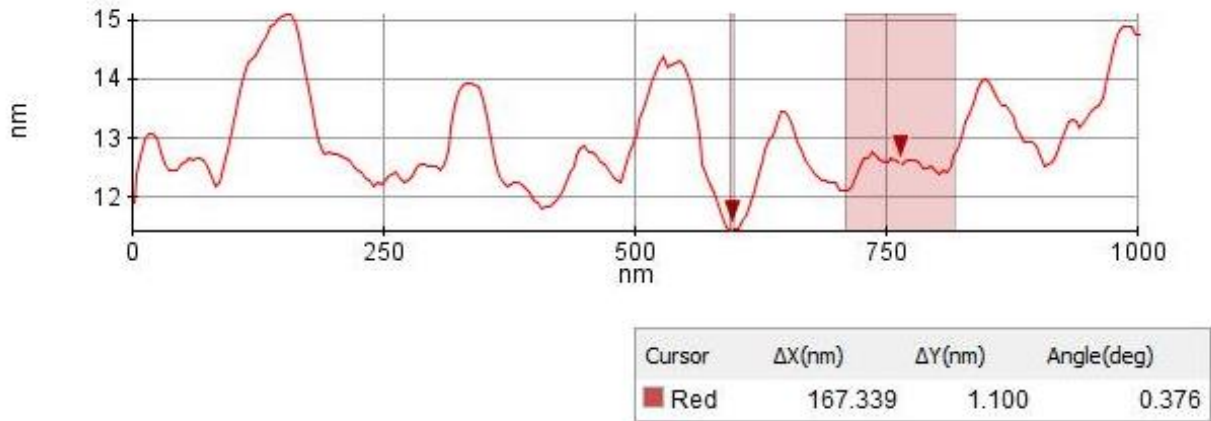


Figure 5-33 Showing the results of the linescan shown in Figure 5-32. This is an unclear linescan, the scratch is nearly obstructed entirely by the material littering the nanowire surface.

Figure 5-33 shows the results of a linescan shown in **Figure 5-32**. The results of the linescan are not clear, there is so much debris littering the nanowire surface and surrounding area it makes extracting the thickness more difficult due to not knowing the exact position. The linescan was evaluated in the following way:

The linescan only scans the surface of the nanowire, the 3D AFM images showed that all the debris located on the nanowire should register as an increase in height rather than a decrease, only the scratch should show a decrease in height. The linescan is scanned solely for a decrease rather than an increase. There is only one small decrease in the linescan attributed to the scratch made to *nanowire 4* (20nm thick, 323nm wide). The position where the scratch was made was also known. 3D AFM images revealed little extra information.

After the machining of *nanowire 4* (323nm wide, 20nm thick) it was then loaded again into the low noise AMR setup with the magnetic field applied along the long axis of the nanowire for magnetotransport studies.

Figure 5-34 shows a typical AMR curve measured with the magnetic field applied along the long axis of the nanowire, taken after *nanowire 4* (323nm wide, 20nm thick) was machined. Both field directions show a clear abrupt change to the resistance at around 10mT. The AMR data taken for this nanowire showed the greatest variation in DW AMR and coercive field. It is believed that this is due to the rough edge profile and also potentially the debris of an unknown origin situated on top of this nanowire.

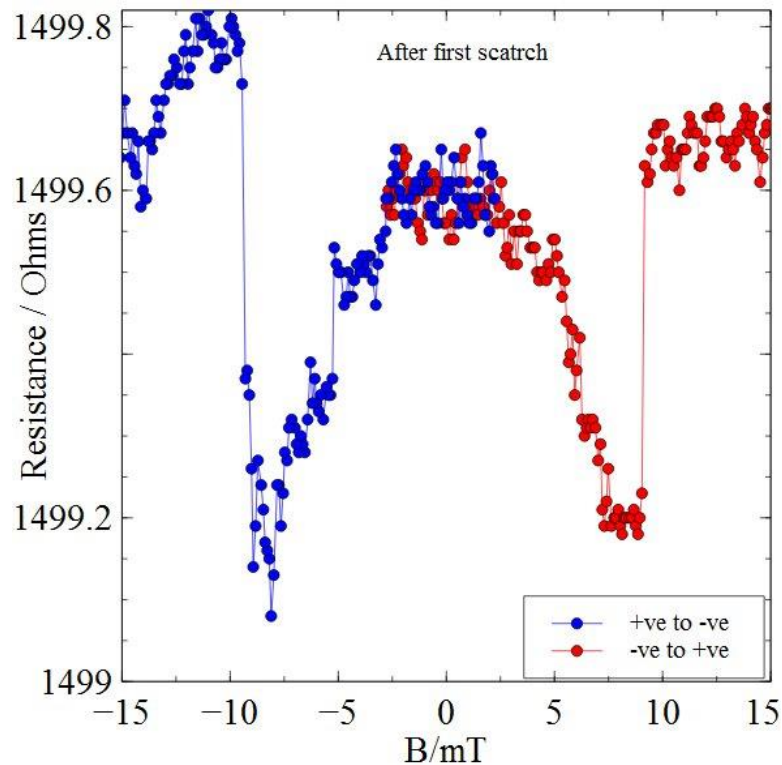


Figure 5-34 Showing a typical AMR curve taken after nanowire 4 was machined. The red dataset shows a abrupt change at a single field value corresponding to a domain wall reversing the nanostructures magnetisation. The blue dataset has a more fine structure in the curve than in the red dataset, this is believed to be due to a domain wall being pinned at different points throughout the nanowire during reversal.

Figure 5-35 shows a comparison of data taken before and after machining *nanowire 4* (323nm wide, 20nm thick). Note the data presented in **Figure 5-34** is not the same data presented in **Figure 5-35**. The data presented in **Figure 5-34** show the most abrupt changes in resistance as a function of field for *nanowire 4* (323nm wide, 20nm thick). Data in **Figure 5-35** displays changes that are less abrupt and cover a larger range of field values to shows the stochastic nature of domain wall pinning and depinning for *nanowire 4* (323nm wide, 20nm thick).

Table 12 shows the results after making multiple field sweeps and then evaluating an average for the depinning fields and DW AMR. There is an increase of 0.6mT after machining due to the formation of a scratch in the nanowire. The magnitude of the DW AMR is effectively the same before and after machining when considering the size of the error.

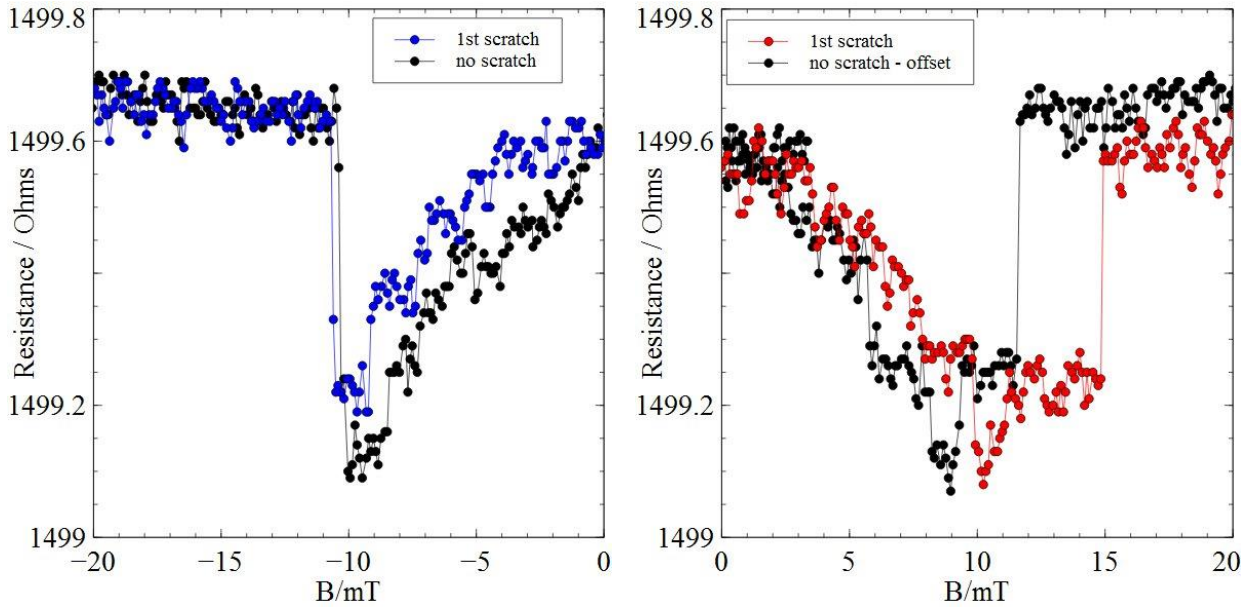


Figure 5-35 Comparing data taken before and after nanowire 4 was machined, the scratched datasets have coercive fields at a value higher than the unscratched data.

Device 3 no pads	Coercive field (mT) (depinning)	DW AMR (Ω) (depinning)
Before Scratching	10.7 ± 0.88	0.48 ± 0.064
After Scratching	11.3 ± 0.82	0.41 ± 0.074
Difference	+0.6	-0.073

Table 12 Showing the results of multiple measurements taken before and after nanowire 4 (20nm thick, 323nm wide) was machined. The depinning field has increased whilst the size of the effect has decreased.

This concludes the presentation of 20nm thick nanowires used for AFM nanomachining in the results section. Three more nanowires underwent machining and will be discussed in the following discussion section.

5.8. Discussion of AFM Machined NiFe Nanowires

Two samples were fabricated for AFM nanomachining studies. A 10nm thick chip with 8 devices with different widths, the same design was employed for a 20nm chip also resulting in another 8 devices at 20nm thickness and again of varying widths. In total 16 devices were fabricated for AFM nanomachining studies. Regarding the 10nm chip only one device was successfully machined. Regarding the 20nm thick chip, six out of the eight fabricated devices were machined using AFM.

5.8.1. 10 nm Chip Discussion: Coercive field analysis.

<i>Nanowire 1</i> (10nm thick)	Coercive field (mT) (pinning)	Coercive field (mT) (depinning)	DW AMR (Ω) (pinning)	DW AMR (Ω) (depinning)
Before Scratching		1.96 \pm 0.11		0.32 \pm 0.0096
After 1st Scratching (3.9nm)	1.45 \pm 0.31	2.27 \pm 0.25	0.39 \pm 0.082	0.39 \pm 0.082
Difference		+0.31		+0.070
After 2 nd Scratch (4.5nm)	1.50 \pm 0.36	2.61 \pm 0.32	0.31 \pm 0.068	0.35 \pm 0.049
Difference	+0.05	+0.34	-0.079	-0.038

Table 13 Summarising the data obtained for nanowire 1 (10nm thick), data is shown for prior to any machining and for after two machining sessions.

Table 13 summarises the data obtained during machining of *nanowire 1* (10nm thick), it shows the increase in depinning field after subsequent scratches, the pinning field remaining constant and the size of the AMR decreasing. The above values (coercive fields) all have reasonably low error values, the largest being less than 20% of the average value, comparing the absolute values to the literature a much larger variation in the coercive field is seen for differing domain wall types. For example a research paper from the year 2006 [13] from Stuart Parkin's group showed definitively that variations in the coercive field combined with variations in the DW resistance were due to different DW types (vortex and transverse) and of

two different chiralities. The variation in coercive field was over 5mT and in DW AMR it was 0.3Ω , comparing to the uncertainties in the measurement for *nanowire 1* (10nm thick) it would imply that a single domain wall of a single chirality is responsible for the nanowire magnetisation reversal, this is true also for the DW AMR measured. In the research paper from Stuart Parkins group [13] MFM was used to provide the ultimate proof of the different domain wall types and chiralities allowing one to image directly the domain walls and ascertain the domain wall type and chirality. It is assumed if this technique was used for *nanowire 1* (10nm thick) a single domain wall type and chirality would be observed consistently.

Referring back to **Figure 5-4**, a plot that showed the change in coercive field with respect to both depth and length of a nanotrench, for both vortex and transverse domain wall types is presented. For a 4nm deep and 100nm long nanotrench in the vortex wall regime a change in the coercive field of around 1mT is to be expected, for a 4nm deep and 100nm long nanotrench in the transverse wall regime a change in the coercive field of around 1.8mT is to be expected, a change of 0.3mT was measured experimentally. This shows reasonable agreement between theory and experiment for both regimes. It is closer to the vortex wall theoretical prediction. Let us consider the phase diagram of domain walls in Permalloy nanowires [96] and attempt to pin down what type of domain wall (vortex or transverse) are most likely responsible for magnetic reversal in *nanowire 1* (10nm thick).

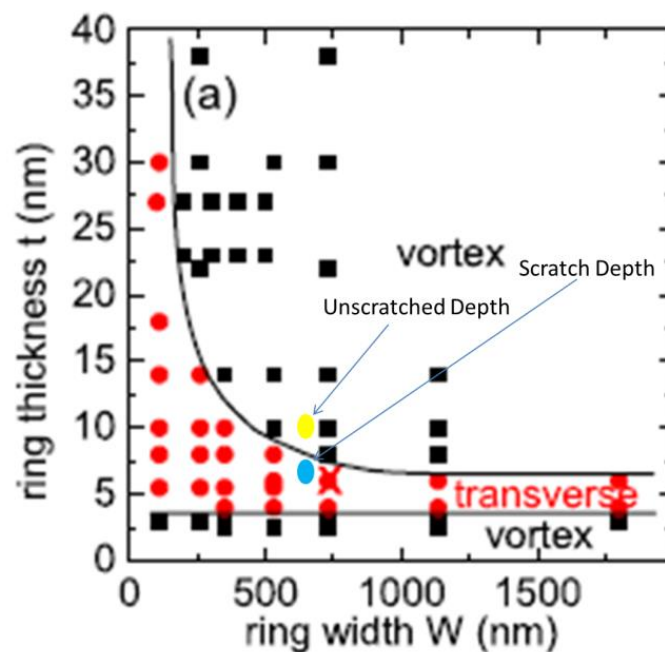


Figure 5-36 Showing the phase diagram for domain walls in Permalloy. Two extra points are added corresponding to the thickness of the nanowire before and after scratching. Image adapted from [96].

Figure 5-36 shows the phase diagram for Permalloy nanowires as a function of both the parameters width and thickness. The unscratched wire sits in the vortex wall regime although the thickness of the scratched section is less, sitting in the transverse wall regime but close to the boundary. It is important to know where the domain wall is nucleated. Let us consider the nucleation of domain walls in a nanowire of Permalloy where the nanometre section is connected to a larger pad as is the case for *nanowire 1* (10nm thick).

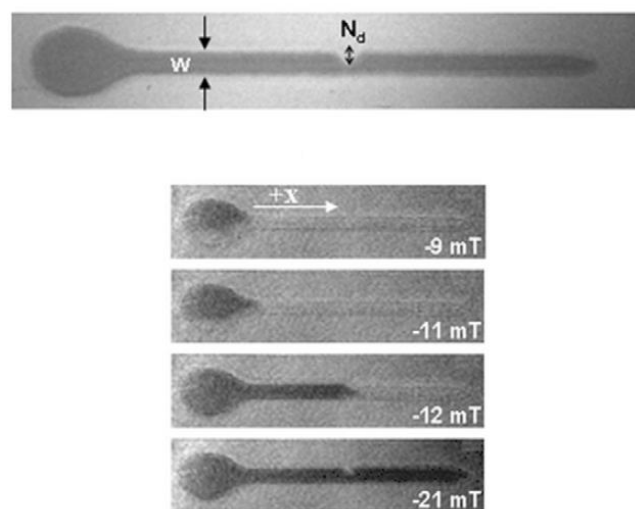


Figure 5-37 Showing how a domain wall is nucleated in the pad before propagating and being pinned at the notch. Wire dimensions are 50nm thick, 450nm wide and a few microns long. The term nucleation pad is widely used in the literature. Images adapted from [115].

Figure 5-37 shows full field x-ray microscope (with XMCD contrast) measurements made whilst applying a magnetic field (in steps) along the easy axis of the nanowire. It is clear looking at **Figure 5-37** that the magnetisation of the pads switches/ reverses direction prior to the nanowire, due to its shape anisotropy. This is significant because it shows where the domain wall is formed and for *nanowire 1* (10nm thick) it means a vortex wall is most likely formed (given the dimensions, yellow point **Figure 5-36**) even after it has been scratched, the point corresponding to the scratch thickness (blue point) shown in **Figure 5-36** is misleading because the domain wall will not be formed at this point, it will be formed where the wire width is greater. This means that the change in coercive field should be compared to the vortex wall theoretical predictions as opposed predictions for a transverse wall. For

the dimensions of the nanotrench a coercive field of change of around 1mT is predicted and 0.3mT is measured. When one recalls that the simulations were performed using OOMMF which is a zero temperature simulation, the absolute value of the simulated field values are often higher than those measured experimentally. However, good agreement is obtained between theory and experiment, differing by only a factor of 0.3.

Referring back to **Figure 5-4** which showed a theoretical prediction for the change in depinning field as a function of both length and depth of the nanotrench/notch, let us compare the experimental data taken with this. Initially let us compare the width and thickness of the experimental data and theoretical and ensure that a comparison is valid.

Vortex Domain Walls	Thickness (nm)	Width (nm)
Simulations	40	200
Experiment (<i>nanowire 1 (10nm thick)</i>)	10	674

Table 14 Showing a comparison of the thickness and width for the nanowire1 (10nm thick) with the parameters that were used to create the vortex wall simulations in reference [67].

The above parameters in both cases ensure that a vortex wall is nucleated and is responsible for the reversing of the nanostructure. In the simulation case the extra thickness facilitates the vortex wall and in the experimental case the extra width, even given the substantially reduced thickness, the width ensures a vortex domain wall is nucleated for reversal. See **Figure 5-36** which shows the phase diagram for domain walls in Permalloy and offers support to this argument. It is likely that the dynamics would differ for vortex walls in such different dimensions, but this is the closest theoretical description available and will therefore be used for comparison. The width dependence is investigated later for 20nm thick devices.

Figure 5-38 shows the experimentally obtained data before and after nanomachining *nanowire 1 (10nm thick)* and a comparison to theory. The dataset corresponding to theory was taken from reference [67] and was discussed in the literature review

section 5.2. Image a) shows both theory and experiment together for comparison, image b) shows only the experimentally obtained data with a linear fit along with the line of best fit for the theoretical data for clarity.

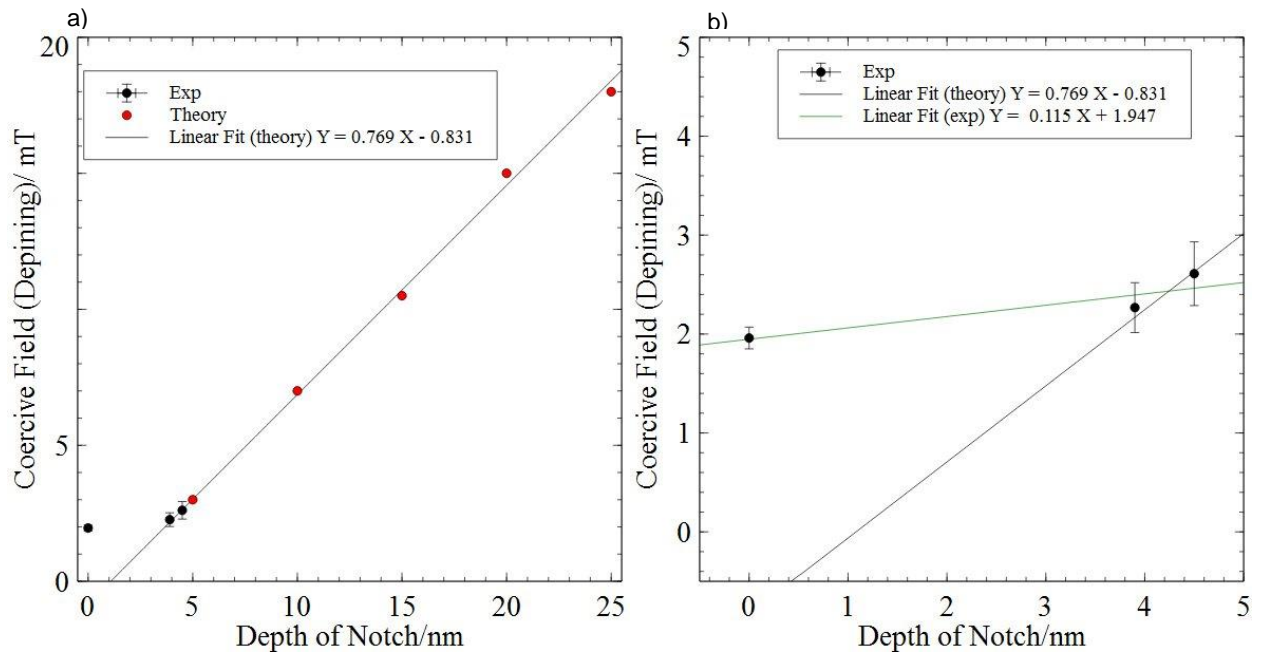


Figure 5-38 Showing the change in depinning field as a function of the depth of the nanotrench/notch. Left image shows both theory and experiment. Right image shows only the experimental data with the theoretical linear gradient taken from fitting the theory dataset. Theoretical data taken and adapted from [67]

Theoretical data prior to machining a trench was not presented and therefore cannot be compared to experiment. It is possible to estimate the coercive field for the given dimensions by extrapolating the linear fit to the zero depth region, this gives an unphysical value of a zero depinning field. Alternatively, it is possible to simulate the zero scratch depth coercive field of the dimensions used in the simulation i.e. run the simulations with no scratch present. Due to the nature of the simulation, OOMMF being a zero temperature simulation the field values are not directly comparable, it is the overall distribution of data that one is interested in so this has not been carried out. Although the first experimental data point doesn't fall close to the linear trend plotted out by the theoretical data set, there is nothing to compare it too and so no conclusions may be drawn. The next two experimental data points generated via machining *nanowire 1 (10nm thick)* twice, agree closely with the simulated data line

plotted out by the theoretical data points. It is possible to calculate a gradient composed of all three experimental data points yielding 0.16 mT/nm which differs considerably to the theoretical linear fit yielding 0.77 mT/nm, this is shown in image b) of **Figure 5-38**. They differ by a factor of approximately 5, the theoretical gradient being higher than experimentally determined gradient. Overall, reasonable agreement between the theory and experimental data is obtained, a linear increase in the coercive field with respect to deepening the scratch is predicted and shown experimentally.

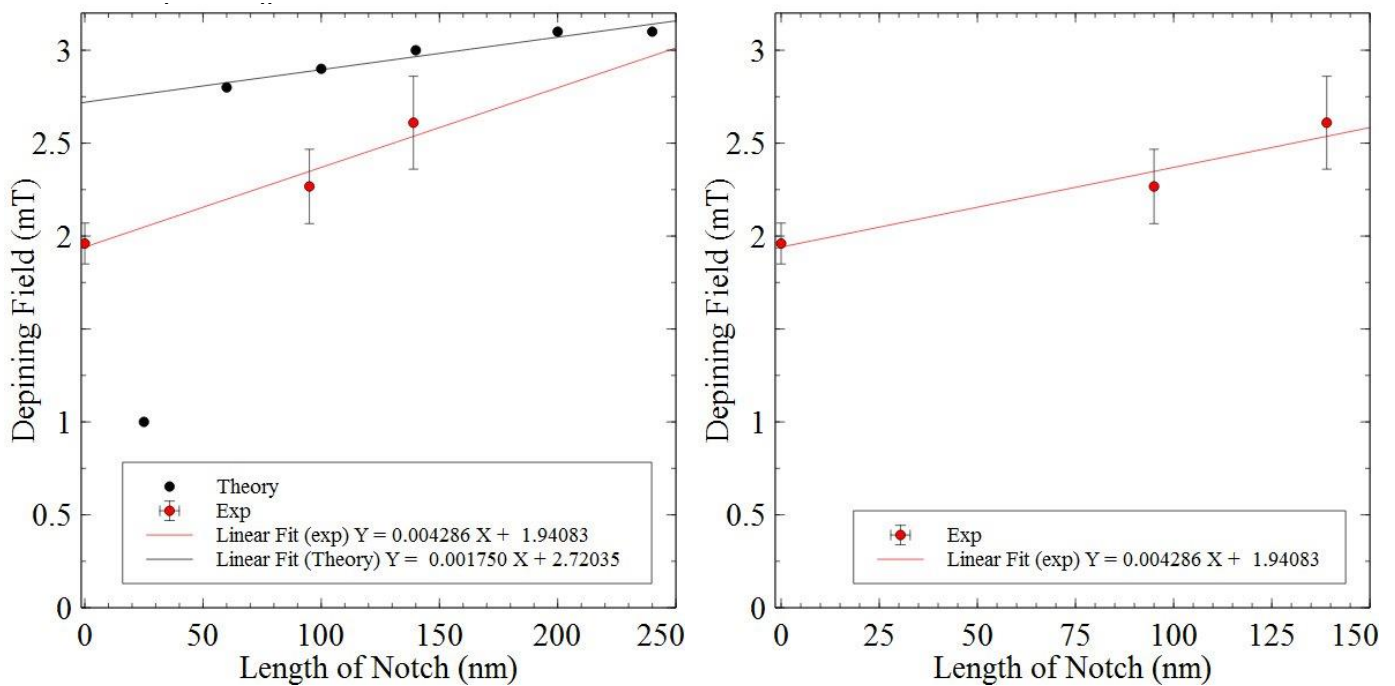


Figure 5-39 Showing the dependence on the depinning field as a function of the length of the nanotrench. Left image shows both experimental data and theory both with fitted with a linear fit. The right image shows only the experimental data and the linear fit (included for clarity). Theoretical data adapted from reference [67].

Figure 5-39 shows a comparison of the experimental data and theoretical data taken from reference [67] for the change in coercive field as a function of the length of scratch. It is worth noting that in the research paper the data is taken when simulating either the depth increasing or the length increasing with the other parameter held constant. That is, when the depth was being increased the trench was kept at a fixed length, this was not achieved experimentally. Image a) of **Figure 5-39** shows the experimental data along with the theoretical data. A line of best fit was calculated for both datasets, in the case of the theoretical dataset, the first point was excluded from the linear fit, this was done to give the best fit to theory as it

seems to increase linearly after the first data point, hence the exclusion. Comparing the absolute field values with theory and OOMMF can often be misleading due to OOMMF being a zero kelvin simulation, therefore the overall distribution of the data should be compared, in this case the gradients. The gradients differ by approximately a factor of 2.5, showing the experimental data matches up with the simulations only qualitatively.

5.8.2. Discussion: Domain Wall Resistance Compared With 1D Model

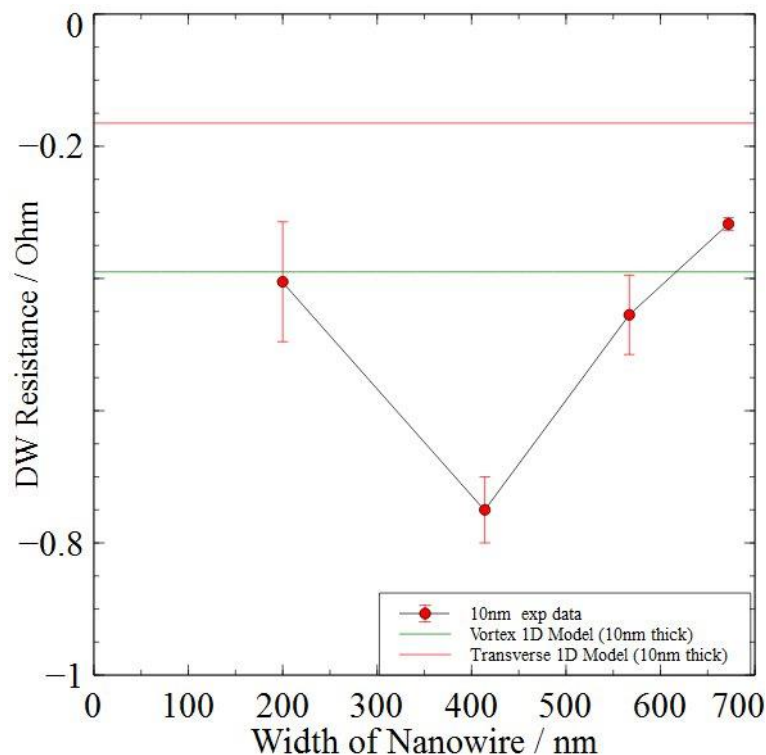


Figure 5-40 Showing the variation in domain wall resistance as a function of the width for a 10nm thick nanowire only the widest device underwent successful machining. Two straight lines have been added to the plot to showing the theoretical prediction by the 1D model for vortex and transverse domain walls [14].

Figure 5-40 shows the domain wall resistance as a function of the width for 10nm thick devices. It is compared with the 1D model for Neel walls in planar nanowires as introduced in the theory section. To make the theoretical prediction only two parameters are required to be determined experimentally, $\Delta\rho$ relating to the AMR response of the device and the thickness of the nanowire. The thickness of the nanowire is probed directly using AFM, $\Delta\rho$ is ideally obtained from measurements made on a thin film in two configurations. There is no theoretical framework to

extract $\Delta\rho$ from measurements made on a nanowire. A thin film was fabricated at the same time as the 10nm thick nanowires were processed although it was machined in order to calibrate the force required to modify 10nm thick Permalloy, no magneto-transport measurements were made on the thin film. To get a value for $\Delta\rho$ the literature was used. In reference [95] plots are generated showing $\Delta\rho/\rho$ as a function of thickness from the work of three separate authors and also a corresponding plot of ρ (average resistivity) as a function of thickness. A value of 1.25% was estimated for $\Delta\rho/\rho$ of a ten nanometre thick film and a value of $40 \mu\Omega\text{cm}$ was also obtained for 10nm thick Permalloy. The 1D model can then be used to determine the domain wall resistance of a 10nm thick nanowire exhibiting a vortex or transverse wall domain configuration. A value of -0.39Ω is theoretically predicted by the 1D model for vortex walls for all widths of 10nm thick nanowires. A value of -0.17Ω is predicted for transverse domain walls for all widths 10nm thick nanowires. As can be seen in **Figure 5-40** there is variation in the domain wall resistance as a function of nanowire width for a set of 10nm thick nanowires. The theoretically predicted value for the vortex domain wall is of the correct order and is close in numerical value to three of the widths presented. Deviating by only a factor of two for the approximately 400nm wide nanowire. This shows reasonable agreement between theory and experiment in terms of the average value of domain wall resistance for a 10nm thick nanowire, although clearly there is variation in the size of the domain wall resistance as a function of width which is not theoretically predicted by the 1D model. The transverse domain wall resistance predicted by the 1D model doesn't overlay with any of the experimentally measured domain wall resistances. According to the phase diagram of domain walls in 10nm thick nanowires, a transition from transverse to vortex domain wall is predicted to occur at around 470nm. This would imply that the narrowest width of approximately 200nm should exhibit a transverse domain wall and be compared with the theoretical prediction for transverse domain walls. The theory (transverse domain walls) and experiment for the narrowest width differ by a factor of 2.5. A value for $\Delta\rho$ and ρ was estimated using the literature, it would be possible to get a more accurate prediction of the domain wall resistance by measuring $\Delta\rho$ and ρ using a thin film (processed in the same conditions as the measured nanowires) to directly measure these parameters. However, this would only change the absolute value of the domain wall resistance and have no effect on the width dependence. Clearly the 1D model is

applicable for an order of magnitude calculation, but it is inappropriate for predicting the variation in domain wall resistance as a function of width, as seen experimentally. The drawbacks of the model were highlighted in the theory section and are most notably the underestimation of the width of the domain wall and the detailed spin structure of the domain wall is not included in the theory. Comparison to another model will be made in hope to get better agreement between theory and experiment, particularly the variation in the domain wall resistance as a function of width.

5.8.3. Discussion: Domain Wall Resistance Compared With Conduction Channel Model

As introduced in the theory section 2.6.2, a model was developed [12] that incorporated the detailed spin structure of a domain wall into the calculation of the domain wall resistance, called the conduction channel model. Full details are included in the theory section.

Figure 5-41 compares the experimentally determined domain wall anisotropic magnetoresistance (DW AMR) with predictions made using the conduction channel model for determining the DW AMR. It is important to note why there is overlap in the transverse and vortex wall theoretical predictions i.e. for widths less than 400nm there is a prediction for both the transverse and vortex wall types. This is due to the nature of domain wall formation, it is an energy minimising process and it is possible for both domain wall types to nucleated for widths <400nm as they are metastable states separated by a small energetic barrier. It has been shown experimentally that ambient thermal energy at room temperature is sufficient to overcome this energetic barrier and induce changes between transverse and vortex domain wall types for certain dimensions.

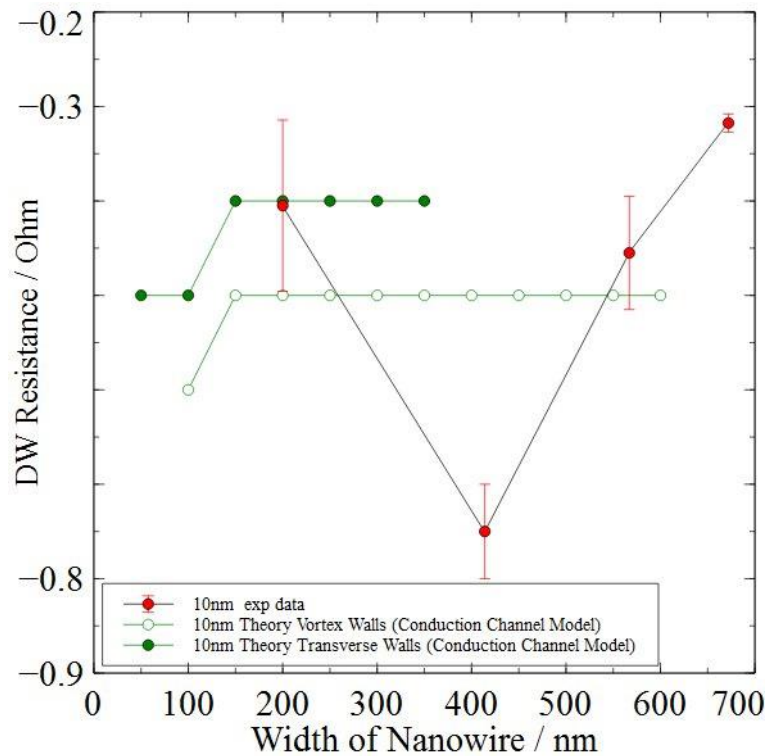


Figure 5-41 Showing the experimentally determined domain wall anisotropic magnetoresistance for 10nm thick nanowires, as a function of width, along with the theoretical prediction made by the conduction model [12].

As shown by the phase diagram (**Figure 5-36**) vortex wall types become more dominant in wider nanowires and hence the exclusion of the both types if they differed in energy by more than 10%. The DW AMR theoretical prediction shows a dependence on the width of the nanowire that was not predicted by the 1D model, the DW AMR increases for both domain wall types by $+0.1\Omega$ at a width of 150nm. The data point corresponding to the narrowest nanowire measured experimentally overlays with the theoretical prediction for the transverse domain wall type, in terms of the average value of DW AMR (not considering the error). Upon considering the error, the error bar extends to the prediction for vortex wall domain wall types, this implies that measurements made on the narrowest wire could consist of both vortex and transverse wall types to some degree. Considering the experimental data point for the approximately 400nm wide nanowire, it doesn't agree with the theoretical predictions for either domain wall type. The DW AMR becomes significantly more negative with respect to the narrowest nanowire. This general trend is also present in the data presented for 20nm thick nanowires (**Figure 5-45**), adding weight in approximating the results obtained. The next two data points corresponding to

550nm and 650nm in width, show the DW AMR becoming more positive with respect to the experimental data point at around 400nm, again this is unexpected because the theoretical prediction for vortex domain walls is more negative than the transverse wall type. Therefore, as the nanowire becomes wider and vortex walls become more favourable, the DW AMR should become more negative. Recalling how the model was created, there is only one answer for how the theory and experiment may differ, the detailed spin structure. The type of domain wall formed is dependent on minimising the overall energy for this reason multiple domain wall types are possible. It is also well known that defects, edge roughness of the nanowire and the ambient thermal energy can influence domain wall formations and even cause transformations from one domain wall type to another. Therefore, the simulated case even though it takes the detailed spin structure into account, still requires incorporation of the outlined effects (defects, thermal energy and nanowire roughness). Clearly these effects will influence how domains form and the DW AMR.

5.8.4. DW AMR as a Function of Scratch depth

Regarding the size of the DW AMR, it remains essentially constant throughout the whole AFM nanomachining studies made on *nanowire 1 (10nm thick, 672 wide)*. This makes sense when one attempts to understand where the domain wall is pinned with respect to the scratch. The 1D model predicts an increase in domain wall resistance for a reduced thickness. If the domain wall was pinned at the scratch and was effectively pinned at a point of reduced thickness, one might expect the DW AMR to increase. In practice it is found that the DW AMR remained constant, implying that the thickness also remained constant. The answer lies with how domain walls pin at an artificially defined defect and to get an idea of how they will pin, it is necessary to look at the energy profile of the domain walls in the scratch region. The simulated energy profiles were presented and discussed in the literature review section relative to this chapter, section 5.2. It was noted that for transverse walls a symmetrical potential well situated at the centre of the scratch results, causing the domain wall to sit inside of the scratch. Regarding the vortex wall energy profile, it is centred around the scratch again, although less symmetric and the

energy peaks at the centre rather than dipping, presenting a potential barrier with a very low likelihood of the DW equilibrating at such an unstable potential. This means for *nanowire 1 (10nm thick)* recalling that the vortex wall configuration is the most likely and the low noise AMR measurement is not sensitive to the DW dynamics (the measurements made are quasi-static), no change in the size of the signal would be predicted and that is observed in the experiment.

5.9. 20nm Thick Chip Discussion

Six devices were machined using a diamond coated Silicon Nitride tip and studied to observe the effect machining had on domain wall pinning and depinning. A variety of effects were observed with the coercive field increasing, decreasing or remaining constant. **Figure 4-42** shows the coercive field as a function of width for all devices machined on the 20nm thick chip that was fabricated for AFM nanomachining studies. The majority of measured DW AMRs remained either constant or decreased after undergoing machining. All the devices presented were fabricated on a single chip under nominally identical conditions using the methods outlined in chapter 3, Sample Fabrication. **Figure 4-42** shows the coercive field as a function of width for all devices and all scratch iterations. It provides a clear way to visualise all the data taken for the 20m thick devices.

As is shown in **Figure 4-42**, the narrowest device (width~ 211nm) shows an obvious and significant increase in coercive field with no overlap in error, this applies to the second narrowest device (width ~ 323nm) also, although there is overlap between the errors this time. The third narrowest device (width ~ 400nm) shows a decrease in the coercive field after the first initial scratch and then very little change after the second scratching session (with respect to the 1st scratch data-point), this result is unexpected, as mentioned previously the formation of a scratch in the nanowire is expected to form a pinning site and cause the coercive field to increase.

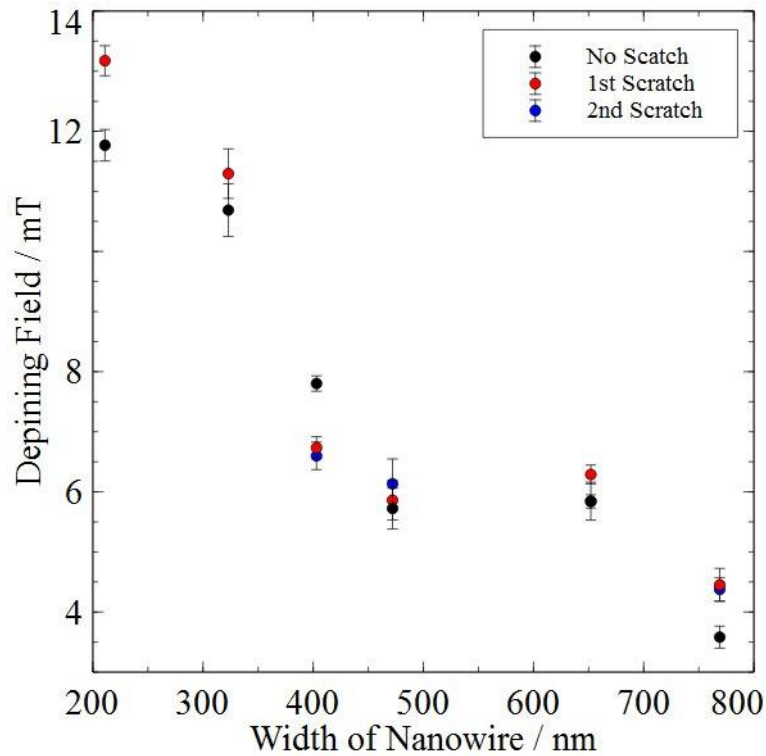


Figure 5-42 Showing the coercive fields obtained, for each (20nm thick) device and scratch iteration, as a function of width.

The next widest device (width ~ 470nm) shows overlap in error for all coercive fields measured, implying little if any modification to the coercive field has resulted from machining this device. The last but one widest device (width ~ 650nm) shows an increase with overlap between errors, and then a decrease to the approximate value prior to any machining (it is not possible to see the second scratch coercive field as it is behind the coercive field measured prior to any scratching). The widest device (width ~ 770nm) shows a clear increase in coercive field after the first scratch with respect to the unscratched data point, the second machined data point is essentially the same as the first machined data-point, showing little change after a second scratch to a deeper thickness. The results are summarised in the following table:-

Device Width (nm)	1st Scratch Compared to No Scratch	2 nd scratch Compared to 1 st Scratch
211	Increase – no overlap in error	N/A
323	Increase – overlap in error	N/A
403	Decrease – no overlap in error	No change
472	No change	No change
652	Increase – no overlap in error	Decrease – no overlap in error
707	Increase – overlap in error	No change

Table 15 Showing the range of effects observed in nanomachining nanowires of different widths and whether there is overlap in error.

Table 15 shows a summary of the results presented in **Figure 4-42** strictly in terms of an increase or decrease in the coercive field and whether this change is significant or not given the calculated value of the error on these measurements. Where there is significant overlap in error it is not possible to say whether any change has resulted from machining the nanowire. This shows that for only three devices out of the six a change was observed in coercive field that was above the error threshold after the first scratch iteration and no device underwent significant changes to the coercive field after in the second machining session.

5.9.1. 20nm Thick Chip Discussion: Experimentally Determined Change in Coercive Field Compared With Theoretical Predications.

Figure 5-43 shows the measured coercive fields as a function of the depth of the scratch for nanowires that showed a decrease in coercive field after being machined. The data shown is for nanowires of width 403 nm (dark red dataset) and 652 nm (purple dataset), the theoretical lines were evaluated from data presented in reference [67], the gradient of the linear fit corresponding to transverse domain walls has a value of 6.52 mT/nm and for the vortex domain wall type a gradient of 0.86 mT/nm is obtained. Linear fits were also made to the experimental data to allow

comparison with the theoretical datasets. Regarding the 403nm wide nanowire a gradient of -0.13 mT/nm was evaluated and for the 652nm wide nanowire a gradient of -0.03 mT/nm. In terms of theory, the theoretical datasets are simulated using the following dimensions:

Transverse Walls (Theory) – 10nm thick, 100nm wide

Vortex Walls (Theory) – 40 nm thick, 200 nm wide

Which differ considerably to the presented experimental datasets with the following dimensions:

Experimental dimensions – 20nm thick, (403, 652) nm wide.

According to the phase diagram of Permalloy nanowires presented in reference [96] (see **Figure 5-36**) the theoretical dataset for transverse walls is approximately, 400nm in terms of width, away from the boundary for vortex walls. The theoretical dataset corresponding to vortex walls is very close to the phase boundary between transverse and vortex walls. With respect to the experimental datasets, both widths sit firmly in the vortex wall phase. This means domain walls in the 20nm thick nanowires presented in **Figure 5-43** should be vortex domain wall structures, and a comparison should be made with the prediction for vortex walls. Comparing to the vortex wall theoretical predictions, the gradients are of different polarities, and differ by a maximum factor (comparing with the 652nm wide nanowire) of ~ 30. Clearly comparing a decrease in coercive field with a predicted increase is inappropriate.

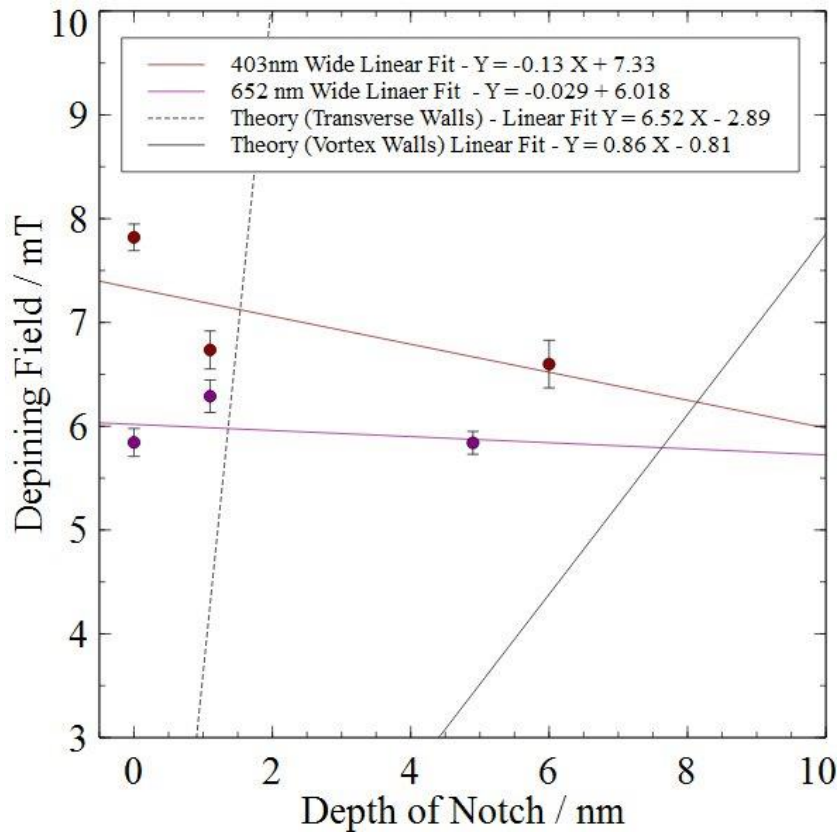


Figure 5-43 Showing the depinning field as a function of the depth of the scratch, for the cases where the coercive field decreased. Linear fits were made to the experimental datasets. Theoretical data was adapted from [67].

Figure 5-44 shows the depinning field as a function of the scratch depth for all nanowires that showed an increase in coercive field after machining. Theoretical data was adapted from reference [67], it was discussed in the literature review section relevant for this chapter and used to create the linear fits to compare the experimental data with.

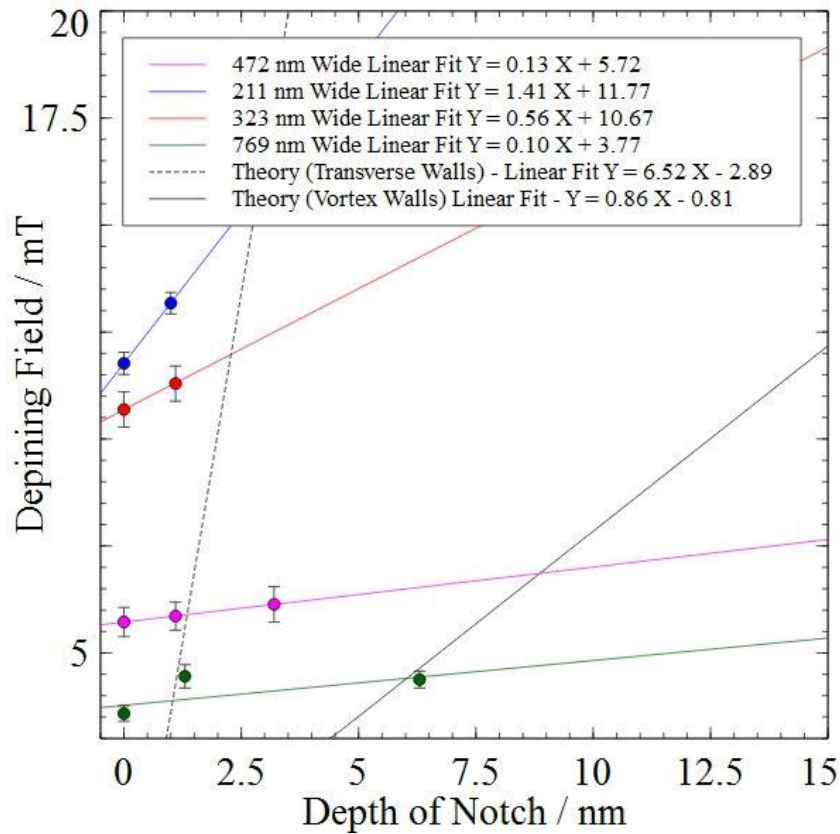


Figure 5-44 Showing the depinning field as a function of depth of the scratch, for all nanowires that showed an increase in coercive field due to machining. Linear Fits were created from theoretical data presented in reference [67]

Initially let us compare the dimensions of the experimental datasets and the theoretical datasets:

Transverse Walls (Theory) – 10nm thick, 100nm wide

Vortex Walls (Theory) – 40 nm thick, 200 nm wide

Experimental dimensions – 20nm thick, (211, 323, 472, 769) nm wide.

In terms of dimensions there is not exact agreement but in both cases the dimensions were used to ensure a specific type of domain wall was nucleated (transverse or vortex). According to the phase diagram of Permalloy nanowires presented in reference [96], the theoretical dataset for transverse walls is not near the phase boundary and the theoretical dataset corresponding to vortex walls is very close to the phase boundary between transverse and vortex walls. Regarding the experimental datasets, for 20nm thick Permalloy the phase boundary is predicted to be at approximately 200nm. This means that the experimental datasets should all be compared with the vortex wall predictions, except for the narrowest nanowire at

211nm wide (this nanowire is close to the phase boundary). For completeness comparison has been made to both domain wall types for all four nanowires presented in **Figure 5-44**. **Table 16** presents the gradients obtained by fitting a linear equation to each experimental data set. Also presented are the ratios of the experimentally determined gradients with respect to the theoretically predicated gradients to quantify how well they agree. The gradient theoretically predicted for transverse domain wall types is 6.52 mT/nm and for the vortex domain wall type a gradient of 0.86 mT/nm is predicted.

Nanowire Width	Experimentally Determined Gradient [mT/nm]	Ratio between experimentally determined gradient (Transverse Walls)	Ratio between experimentally determined gradient (Vortex Walls)
211	1.41	4.5	0.6
323	0.56	11.5	1.5
472	0.13	50.2	6.6
769	0.10	65.2	8.6

Table 16 Showing the experimentally determined gradients for all nanowires that showed an increase in coercive field. A comparison is made with theory in terms of the ratio of gradients.

Table 16 shows for increasing nanowire width, scratching the nanowire has a lesser effect on the coercive field represented by a reduced gradient. Regarding comparison with the theoretical datasets, for increasing nanowire width an increase in deviation from the theoretically predicted gradients was observed for both domain wall types, the deviation being more pronounced for the transverse domain wall type. The best agreement is obtained for the nanowire of width 323 nm compared to the vortex wall theoretical predications, having gradients within a factor of 1.5 of each other. A range of ratios is obtained when evaluating all widths presented with respect to the theoretical predictions. Comparing with the transverse wall type a range of 4.5 to 65.2 is obtained. With respect to comparing with the vortex domain wall type the range is 1.5 to 8.6. As discussed in the analysis of data taken for 10nm thick devices, the numerical field values output by OOMMF are not comparable for our measurements due to simulations using the OOMMF software being a zero

temperature simulation. A comparison of the gradients is more appropriate, the gradient capturing the overall trend of the data.

Agreement is obtained between theory and experiment although it is believed that the difference in the dimensions would alter the domain wall depinning as a function of scratch depth, therefore for a better theoretical predication, the simulations presented in reference [67] should be re-simulated with the appropriate dimensions or the experimental nanowire dimensions changed.

5.9.2. 20nm Thick Chip Discussion: DW AMR Compared with the 1D model and the conduction channel model.

As in the previous section of this chapter analysing the results obtained for 10nm thick Permalloy nanowire devices, a comparison with the 1D model for DW AMR for planar nanowires will be made and also a comparison with the conduction channel model, both were discussed in detail in the theory section 2.6.

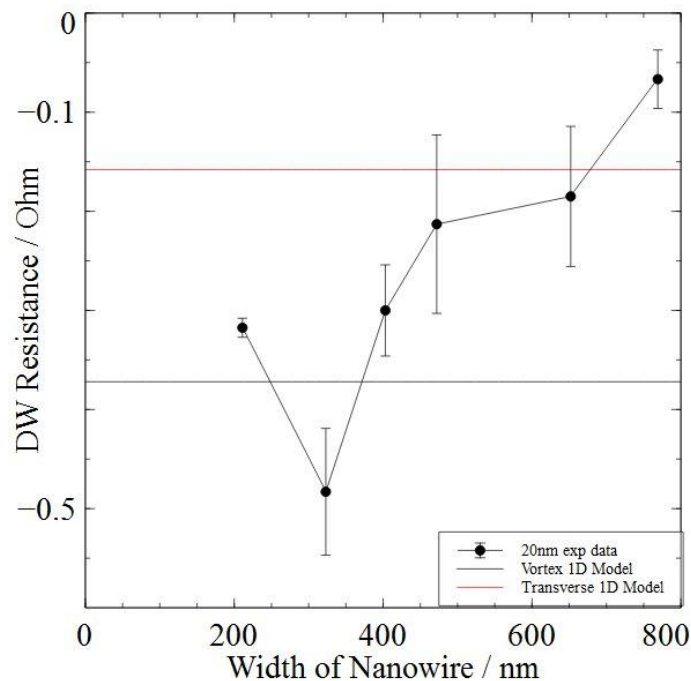


Figure 5-45 Showing the experimentally measured DW AMR as a function of width for 20nm thick nanowires along with the predictions of the DW AMR for vortex and transverse walls using the 1D model.

Figure 5-45 displays the DW AMR as a function of width for 20nm thick devices used for AFM nanomachining studies within this thesis. Presented also are predictions of the DW AMR generated using the 1D model which depends on thickness only and neglects the width of the nanowire. To estimate the values of the DW AMR using the 1D model, the same process was used as for the 10nm thick devices i.e. an estimation of the AMR ratio was made using the literature and also for the resistivity of 20nm thick Permalloy. The graph presented in **Figure 5-45** shows that the predictions made by the 1D model are insufficient to accurately predict the exact value of the DW AMR, as an order of magnitude calculation they are sufficient. Firstly a clear dependence on width is seen which is not predicted, secondly the theory predicts the transverse wall type DW AMR is less negative than the vortex wall configuration, experimentally the opposite is hinted at, the vortex wall DW AMR is less negative than that of the transverse wall type. The widest nanowires are expected to have vortex walls and the narrowest nanowires are expected to have transverse walls. The width dependence shown by 20nm thick Permalloy nanowires is very similar to the dependence seen in the 10nm thick nanowires, see **Figure 5-46**. The DW AMR initially becomes more negative when increasing the width, for both thickness presented and the DW AMR gradually increases at the approximate value for the phase boundary between transverse and vortex walls for each corresponding dataset. The measured decrease in resistance is within a factor of 0.3 for the 10nm phase boundary predicted by theory and the decreases in the 20nm experimental dataset is within a factor of 0.15 for the 20nm predicted by theory. The closeness of these values requires further investigation, there is no theoretical prediction regarding a decrease in DW AMR at the phase boundary between transverse and vortex wall. If the DW AMR shows a dependence on the phase boundary, this is unaccounted for in theoretical models. Further study in both experiment and theory would be required to unambiguously show the dependence is definite and incorporate this dependence into to existing models for DW AMR. In short, these experiments need to be repeated for a variety of thickness (all varying in width) which cause the position of the predicated phase boundary to move and if the decrease in DW AMR is attributed to this, it should also move its position in accordance with the phase boundary and a correlation would be possible.

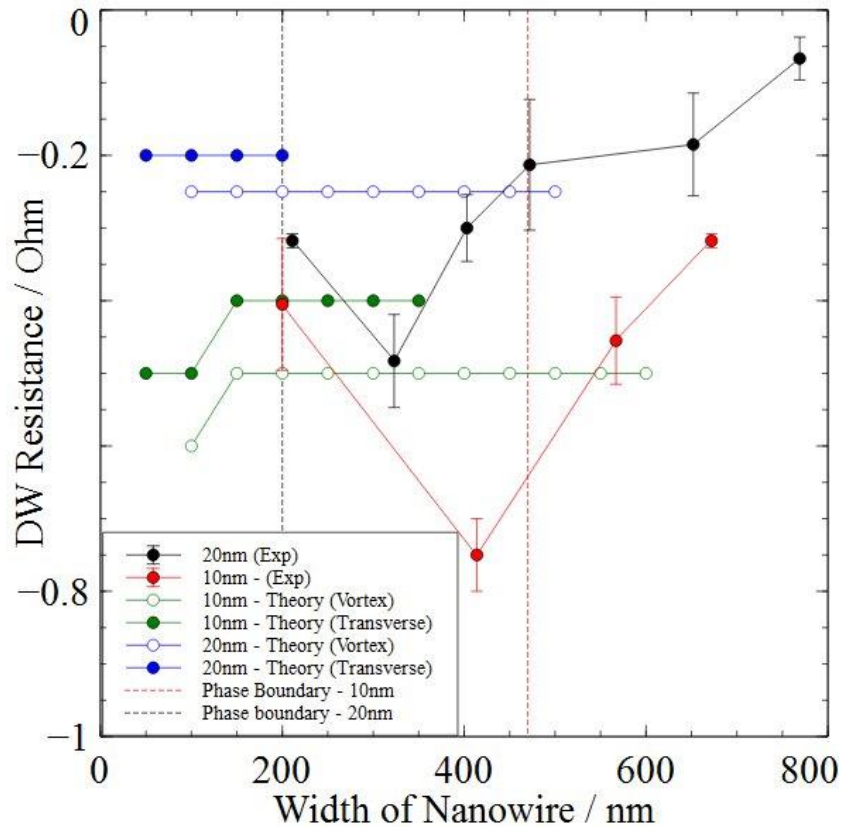


Figure 5-46 Comparing the experimentally measured DW AMR with the theoretical predications of the conduction channel model [12]. Theory is shown for 10nm and 20nm thick nanowires for both domain wall types (vortex and transverse) and a line has been added to show the expected phase boundary for transverse and vortex wall for both thicknesses.

5.9.3. 20nm Thick Chip Discussion : DW AMR reduction due to machining / reduced thickness

It was shown in the discussion that the DW AMR of a 10nm wide nanowire at constant width, showed no change to DW AMR due to machining. Shown in **Figure 5-47** is the experimentally measured change in DW AMR produced via machining the 20nm thick wires, a range of widths (~200nm to ~750nm) were machined for 20nm thick nanowires. Comparing the nanowire at ~650nm (this corresponds to the same width presented in the 10nm section) no change is observable due to machining, there is overlap in error between the prior and post machining DW AMR data. The DW AMR associated with the first machined data point of the nanowire at a thickness of ~770nm is anomalous in the sense that an increase (in absolute

value) of 0.38Ω was measured for this data point only. It is believed this data point is anomalous and should be excluded from the discussion. Considering all the data less than 770nm in width, the decrease in DW AMR is a maximum for the 403nm wide nanowire which is the closest to the phase boundary between transverse and vortex walls, a decrease (in absolute value) of 0.20Ω was measured. The phase boundary seems to coincide with a decrease in DW AMR for constant thickness and when the nanowire is machined the largest reduction in DW AMR is observed close to the phase boundary. Considering all the data corresponding to the 2nd machining session (red data points), all DW AMRs are around the same value (-0.1Ω) implying that machining has the effect of reducing the DW AMR for all widths to a constant value. These two phenomena (the dip in DW AMR prior to machining close to phase boundary and a constant value of DW AMR when devices are machined for all widths) are not reported in the existing literature at the time of writing this thesis. Detailed modelling of the scratch (exact dimensions) and domain wall propagation through such a modification would be desirable.

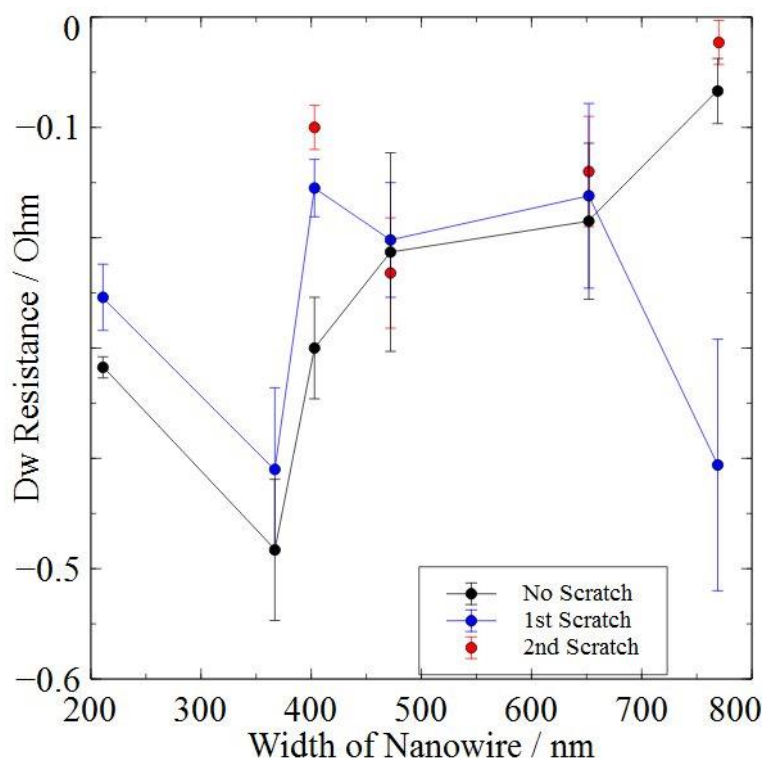


Figure 5-47 Showing the DW AMR for 20nm thick Permalloy nanowires as a function of wire width. The data suggests a decrease in DW AMR after machining.

5.9.4. Conclusion

AFM nanomachining studies were carried out on seven nanowires. A 10nm thick, 674nm wide nanowire was machined twice and successful modification to the domain wall pinning and depinning process was shown, an increase of 0.5mT in the nanowires coercive field was shown after machining the nanowire twice. The results were compared to theoretical predictions in terms of change in coercive field, the experiment and theory were found to differ by a factor of 0.3.

Six nanowires 20nm thick having a range of widths were machined and the machining was found to influence the domain wall pinning and depinning in these structures. Some structures exhibited a decrease in coercive field but the majority of machined nanowires showed an increase in the pinning and depinning of a domain wall. When compared to theory it was found that narrower wires were closer to theoretical predications.

For all fabricated nanowires the DW AMR was compared with theory and deviation from theory was found in that the DW AMR was observed to decrease experimentally but not theoretically predicted. The regions where a decrease in the DW AMR was observed seemed to correspond with the phase boundary for transverse to vortex domain walls.

6. *In-situ* AMR Measurements of a Thin Film of NiFe as a Function of Thickness

6.1. Introduction

There are few measurement systems in existence that allow the simultaneous electrical and optical probing of a thin film or patterned media during the deposition/growth stage i.e. *in situ* electrical and optical characterisation during the deposition process. Considering that thermal evaporation implies a vacuum to carry out the deposition, removal of the sample from vacuum can result in changes to the electrical, optical and magnetic properties of the sample by virtue of the samples interaction with air. One of the most obvious mechanisms for altering a samples properties by interaction with air is the formation of an oxidised surface layer. In the case of a thin film of NiFe, on exposure to air, the surface is initially covered with Nickel oxide (NiO), Nickel Hydroxide (Ni(OH)₂), and Iron oxides (Fe_xO_y) with no preferential oxidation [97]. The result is a nano oxide of typically less than 2nm, consisting of anti-ferromagnetic Nickel and Iron oxides and the ferrimagnetic Fe₃O₄ phase [97]. These nano oxide layers can couple to the ferromagnetic NiFe thin film underneath via exchange bias.

6.2. Literature Review

There are not many research papers relating to the *in situ* monitoring of magnetic material during deposition. One paper recently published [98] grew NiFe and at different thickness halted the deposition and measured the AMR of the sample. The results identified two regions of AMR, tunnelling AMR at low thicknesses, measured before the film coalesces and becomes continuous. This makes sense at low thicknesses because microscopically there will be isolated islands of magnetic material that are not electrically connected, attempting to electrically measure such a system will inevitably involve tunnelling currents, combined with the material being magnetic, tunnelling MR results. As the film coalesces and becomes continuous,

separated islands becoming inter-connected grains, there will be no more need for tunnelling and so the tunnelling MR will cease to be measured and the conventional AMR will be measured. This paper also investigated the effect of using different substrates and this was found to alter the thickness at which the film coalesces and the thickness scale over which the transition would take place. A SiO₂ substrate providing the sharpest transition at the lowest thickness, the other investigated substrates were Al₂O₃ and MgO.

Another research paper from the year 2007 [99] looked at the effect of applying a magnetic field in a variety of ways during the deposition process. They monitored the changes in sheet resistance of the films as they were growing and attempted to correlate changes in the sheet resistance for different applied fields with the different microstructures resulting from the different applied fields. To elucidate, just before coalescence of the film (approximately 2nm thick) the deposition was stopped and the thin films grown were imaged using AFM and TEM. When applying a constant field in a constant direction, they found the grains aligned with the field. When applying a rotating magnetic field they observed in the microstructure much less pronounced preferential alignment with a single direction and the grain-grain gap size was less also. In **Figure 6-1** the microstructure resulting for the two different applied fields is shown. The parameter Δd_x is defined as the major gap length between two adjacent lines/grains. It is measured at 90 degrees to the applied field (x direction in **Figure 6-1**) and is a measure of how packed adjacent grains are in the direction 90 degrees to the applied field. The parameter δd_x is defined as the minor gap length between two neighbouring lines, measured in the direction of the applied field (as a result it should be smaller than the major gap length), it is a measure of how densely packed the lines/grains are in the direction of the applied field.

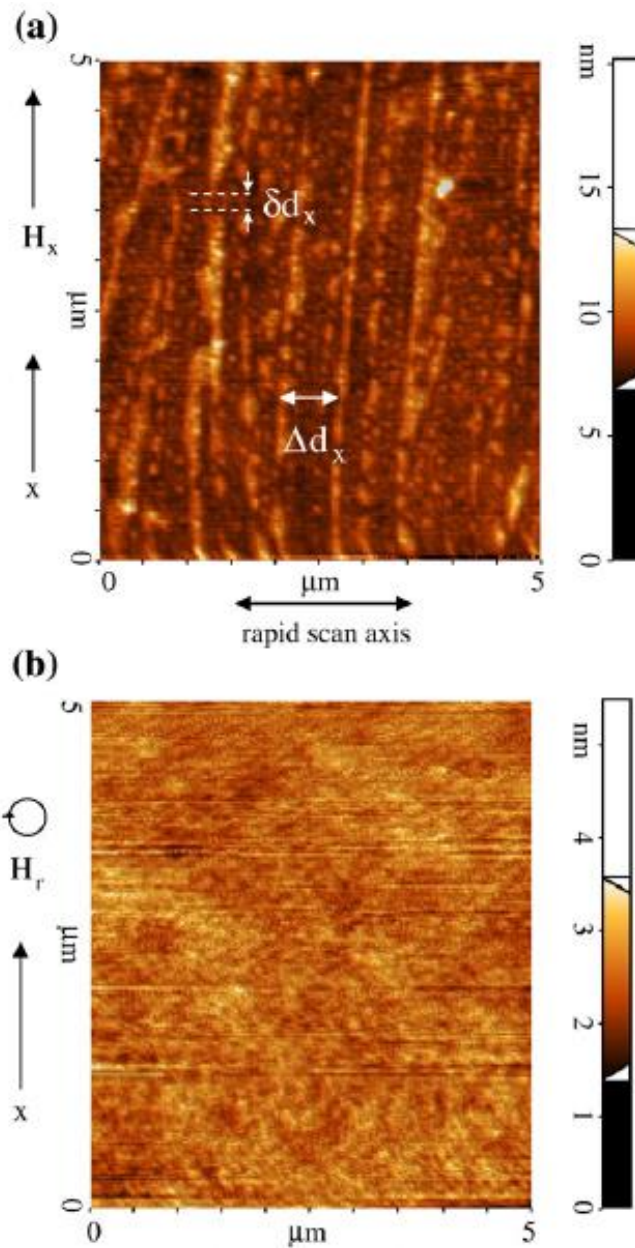


Figure 6-1 Showing how different magnetic fields applied during the deposition directly affect the microstructure of the film. The different microstructures are distinguishable by their sheet resistance as a function of thickness in the low thickness regime, images adapted from [99].

Figure 6-2 shows the *in-situ* electrical measurements made for a variety of different applied magnetic field conditions namely no field, a range of static applied fields and a range of rotating magnetic fields. The results of **Figure 6-2** show how the different microstructures resulting for the different applied field conditions have different behaviours in the resistance as a function of thickness curves, particularly in the low thickness regime. At 1nm thick for the different applied fields there is a variation in resistance of around 312 k Ω for the differing microstructures.

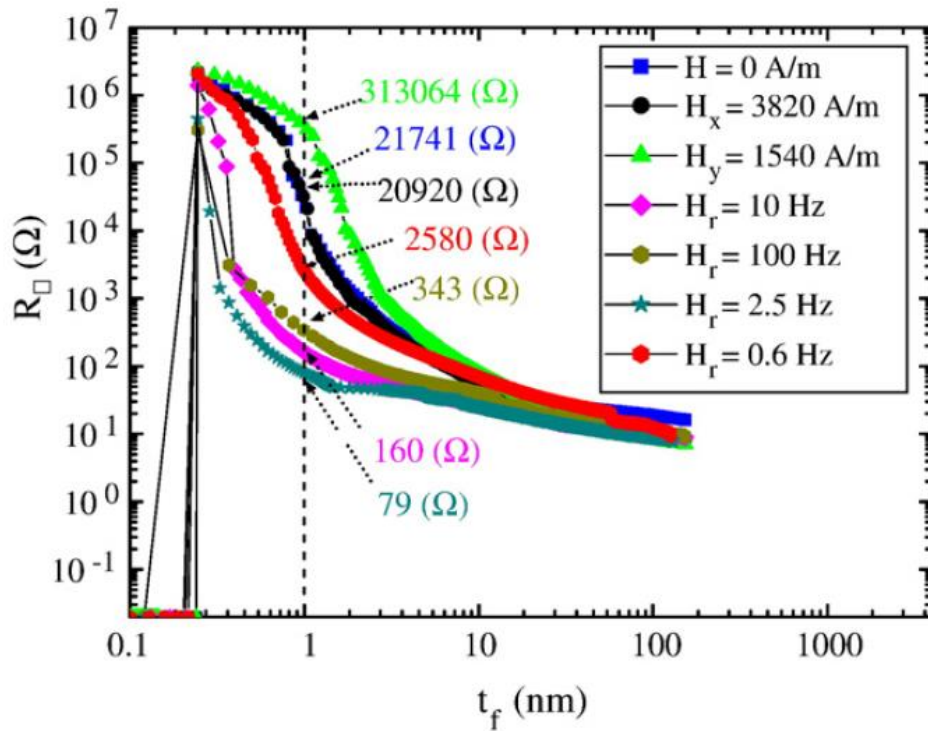


Figure 6-2 Showing the sheet resistance as a function of thickness from reference [99], of particular interest is the difference in behaviour in the low thickness limit for different applied fields i.e. each different applied field is resulting in microstructure changes that are measurable. There is a sharp increase in resistance during the initial stages of the deposition and then the resistance tends to the bulk value for all curves beyond 10nm thick.

6.1. In-situ Experiments

Initially after the *in situ* setup was complete (thorough details are included in section 3.1) an experiment was carried out to ensure the system was functioning as expected. A thin film of NiFe was grown up to 20nm in thickness and then AMR measurements were carried out to probe the sample *in situ*. The sample was then removed from the vacuum chamber and transported to the AMR low noise measurement rig as described in section 4.5.

A sample was prepared and loaded into the custom built evaporator, the system was pumped down until a suitable pressure ($\times 10^{-8}$ mbar) was reached, after which the evaporation was begun.

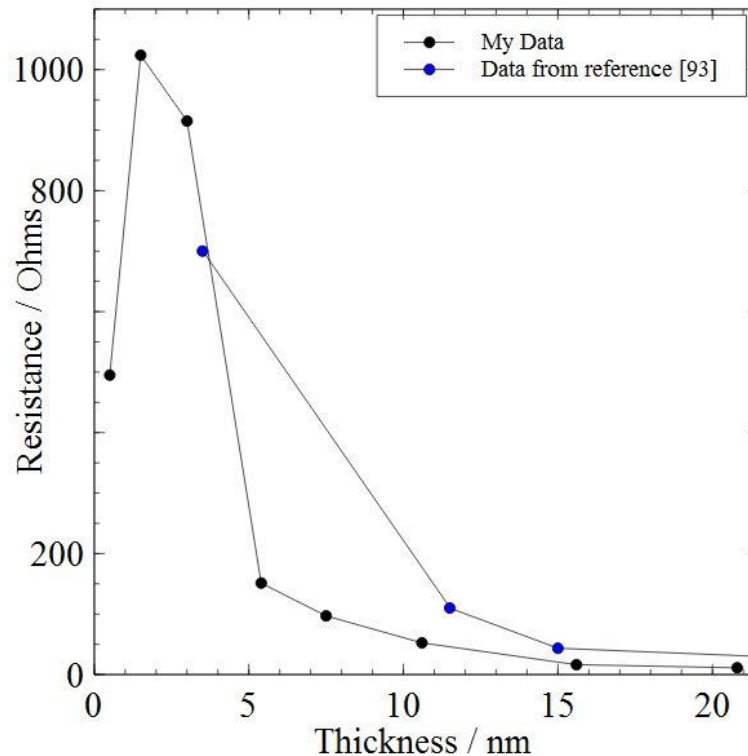


Figure 6-3 Showing how the resistance varies with increasing thickness, measured *in situ*. For comparison data has been taken from a relevant dataset [95].

Figure 6-3 shows the resistance as a function of the thickness of the film. As soon as the deposition starts a sharp increase in resistance is observed followed by a decrease of the resistance with increasing thickness. Also shown is data taken from the literature [95] for comparison, there is general agreement between the two datasets. The initial increase upon deposition is absent within the data taken from reference [95], although this is to be expected given that very low thickness measurements are not presented.

Figure 6-4 shows the AMR effect in a 20nm thin film measured *in situ* in the transverse configuration and **Figure 6-5** shows the same sample measured *ex situ* in the low noise AMR setup. The thin film corresponds to the sample *in situ* 3 and was a single deposition up to 20nm. The AMR effect in absolute value is (2.63 ± 0.35) mOhms and is centred around ± 0.5 mT for the *in situ* dataset. The percentage change is 0.025% of the maximum resistance. For the *ex situ* data the size of the AMR effect is (9.94 ± 0.51) mOhms and the percentage change is 0.087%, this is an increase by a factor of 3.5 from the *in-situ* dataset for both percentage and absolute value.

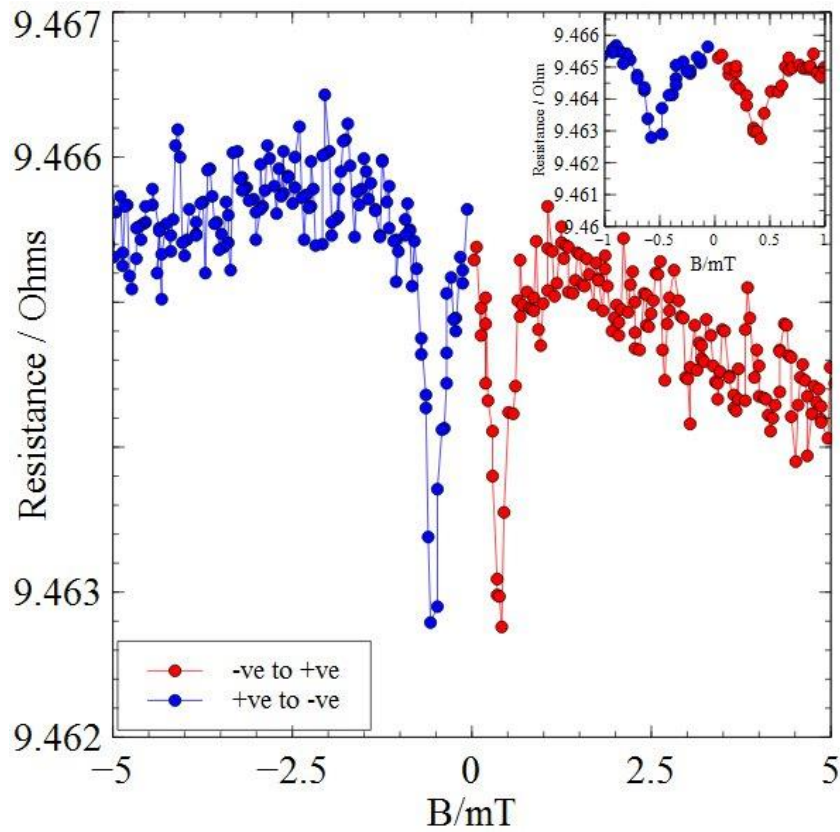


Figure 6-4 Showing the AMR data obtained for *in situ* run 3, the current and magnetic field are in the same direction (transverse configuration). To be compared with measurements made *ex situ* in the same configuration, Figure 6-5).

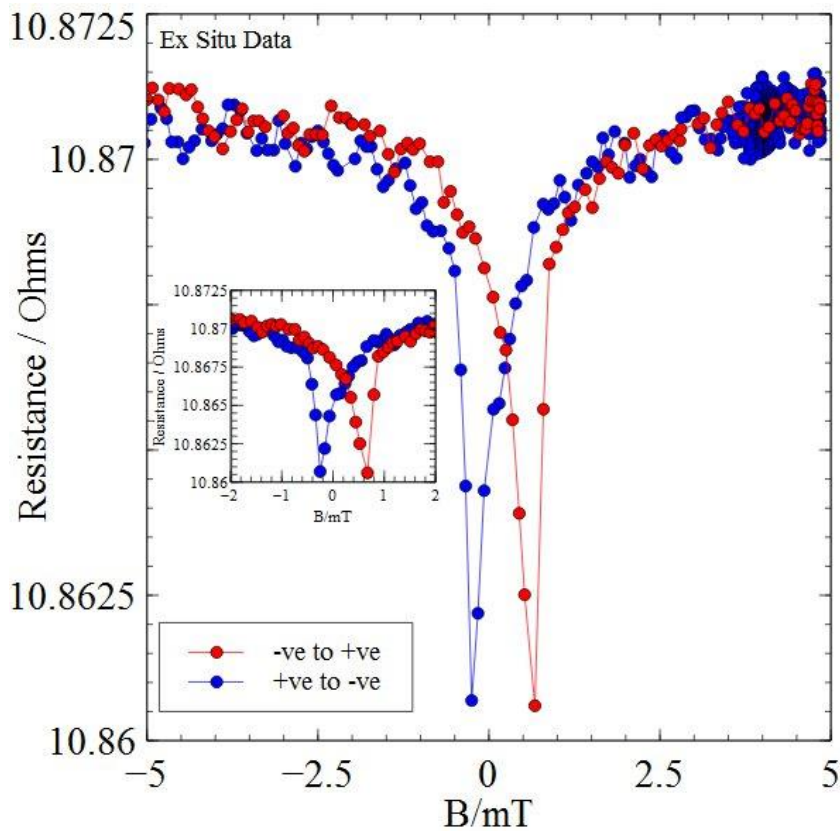


Figure 6-5 Presenting *ex situ* measurements made for the sample (*in situ* run 3) in the transverse configuration. There is agreement between the *in situ* data (Figure 6-4) and the *ex situ* data apart from the sample undergoing oxidation upon exposure to air.

The measured data both *in situ* and *ex situ* show similar features, namely, peaks in both field directions for both datasets that occur at externally applied magnetic fields less than approximately 0.5mT. The coercive fields for the *ex situ* data occur at fields of 0.7mT and -0.29mT. The variation in the two field values is attributed to the Hall probe used to measure the applied field directly being closer to one pole rather than in the exact centre of the electromagnet. Half the sum of the modulus of each value gives a coercive field value of +/- 0.5mT. This value for the coercive field value is typical of a thin film of NiFe [100].

The *in situ* and *ex situ* AMR are very small in terms of absolute value and percentage change, typical values in other studies are the order of a few percent [100]. It is speculated that the reason for the reduced signal is either some form of contamination present in the chamber or the ratio of NiFe has moved away from Ni ~81% and Fe~ 19%, the AMR ratio is sensitively dependent on concentration showing a maximum value for the quoted percentages above.

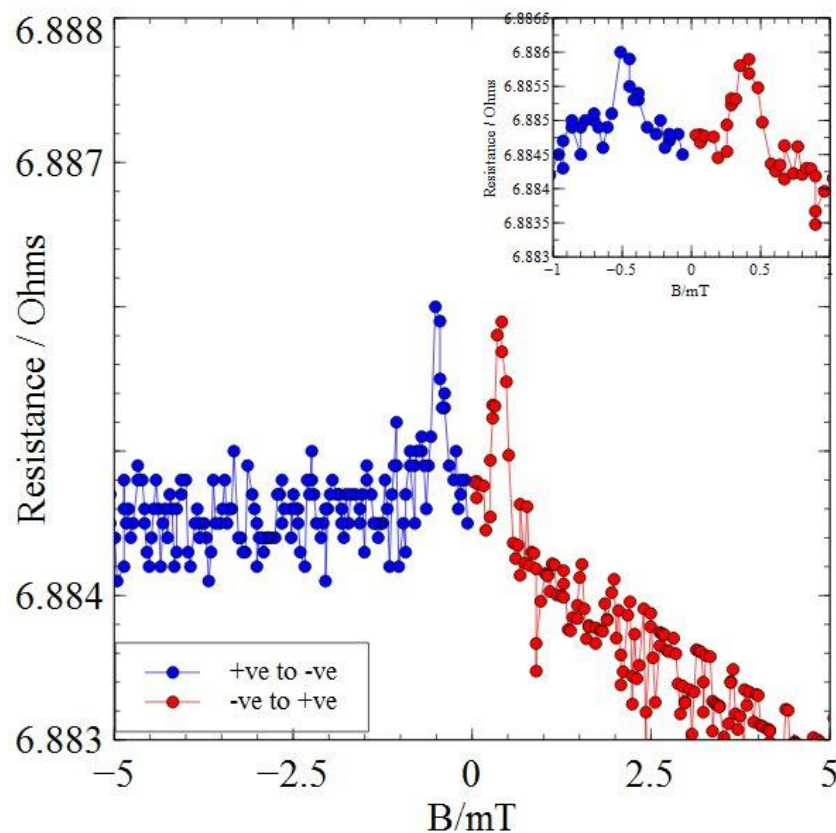


Figure 6-6 Presenting the AMR data for sample *in situ* run 3 with the magnetic field and current perpendicular to one another (longitudinal configuration). This image is to be compared with the data measured *ex situ* for the same sample and configuration shown in Figure 6-7.

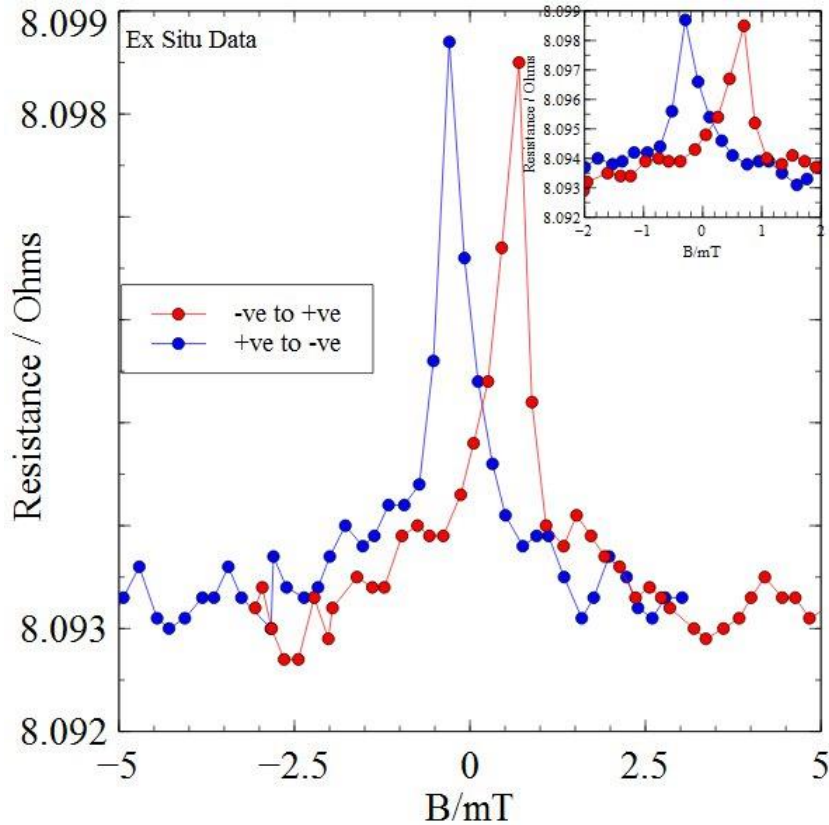


Figure 6-7 Presenting the *ex situ* data for sample *in situ* run 3, measured in the low noise AMR setup (*ex situ*) with the current and applied magnetic field perpendicular to one another. There is agreement between the *in situ* (Figure 6-6) and the *ex situ* data although the *ex situ* data may have undergone some degree of oxidation.

Figure 6-6 shows the longitudinal (current and field perpendicular) configuration for *in situ* run 3 and **Figure 6-7** presents the *ex situ* data for the same sample. The *in situ* data shows clear peaks of size (2.62 ± 0.25) mOhms and occurs at a value of ± 0.5 mT, the size of the AMR is the same as in the transverse configuration. There is consistency between the two *in situ* measured configurations in terms of magnitude of the peaks and their position in field, which is expected for a thin isotropic film of NiFe measured in these two configurations. The change of resistance between maximum positive and maximum negative fields shown in **Figure 6-6** is likely due to heating of the sample, this small heating of the sample is probably caused by the magnet within in the vacuum chamber heating as it is energised. Ignoring the absolute change due to heating, the *ex situ* dataset behaves in a similar way to the *in situ* dataset, two clear peaks relating to the reversal of the magnetisation of the thin film. The *ex situ* and *in situ* datasets agree qualitatively. The AMR measured *ex situ* is (5.52 ± 0.51) m Ω corresponding to an increase of 2.89 m Ω or in terms of a multiplicative factor, the *ex situ* AMR is 2.1 times larger than the *in situ* AMR, with respect to the AMR data in the longitudinal configuration. The field values at which

the peaks occur are 0.67mT and -0.25mT, applying the same analysis as for the previous configuration for the field values yields a coercive field of 0.46mT. This yields a reasonable value for the coercive field as discussed earlier [100].

	Resistance (Ohms)	AMR – absolute value (mOhms)	AMR – percentage change (%)	Measured Coercive Fields (mT)	
<i>In situ</i> Longitudinal	6.88	2.62±0.25	0.040	0.50±0.11	-0.47±0.09
<i>Ex situ</i> Longitudinal	8.09	5.52±0.51	0.068	0.70±0.10	-0.29±0.08
<i>In situ</i> Transverse	9.46	2.63±0.35	0.025	0.55±0.13	-0.49±0.11
<i>Ex situ</i> Transverse	10.87	9.94±0.51	0.087	0.67±0.08	-0.25±0.09

Table 17 Showing a comparison of resistances, AMR magnitude and percentage change, and coercive fields for tow configurations for both *ex situ* and *in situ* data.

Table 17 shows a comparison of the coercive fields and AMR (percentage and absolute) for ease of comparison. For both *ex situ* configurations the four terminal resistances are higher than in the *in situ* case. For each configuration, it was found that the resistance had increased by a factor of 1.25 upon removal from the vacuum chamber, this is consistent for both configurations, in other words the resistance change is the same in both configurations. One possible explanation for the increase in resistance is due to the formation of an oxide layer upon removing the sample from the vacuum chamber and exposing it to air. It is possible to attempt to estimate this change simply by using the standard resistivity equation, $\rho = RA/L$, and calculating what thickness the resistance change corresponds to. Using this method a thickness reduction of 5 Å gives the observed resistance change, which compares reasonably well with the thickness of the oxide expected for a thin film of NiFe [97]. A recent research paper [97] used x ray photoelectron spectroscopy (XPS) and work function measurements to investigate the initial steps in the oxidation process of a thin film of NiFe, they found that a self-limiting nano-oxide of 8 Å was formed upon exposure to air with no preference for oxidising the Fe or Ni species. Given that the

calculated value for the observed resistance changes returns 5 Å it is very likely that the resistance change due to removing the sample from the vacuum chamber was due to the formation of a nano-oxide of ~ 5 Å.

Regarding the resistance measured *in situ* and *ex situ*, the resistance increased by a constant factor applicable to both configurations. This is not true in terms of the absolute value of the AMR for both configurations i.e. the AMR has not increased by the same factor for both configurations presented. The AMR increased upon removal from the vacuum chamber by the factors 3.8 and 2.1 for the transverse and longitudinal configurations respectively. This is evaluated by taking the ratio of the *in situ* and *ex situ* AMR for both configurations. The fact that both have increased is consistent however.

These measurements show that the two systems (*in situ* and *ex situ*) are in agreement apart from the sample undergoing some presumed oxidation when the chamber is opened resulting in a small increase in both the resistance and AMR. A simple experiment was devised to confirm oxidation was producing the increase in resistance seen when comparing *ex situ* data to *in situ* data. Another *in situ* sample was prepared, it was decided after growing a 20nm film, the vacuum chamber would be opened (to allow air in) and then the pumps turned back on (to remove any air from the chamber) to attempt to correlate and change in resistance with air being in the chamber and thus oxidation.

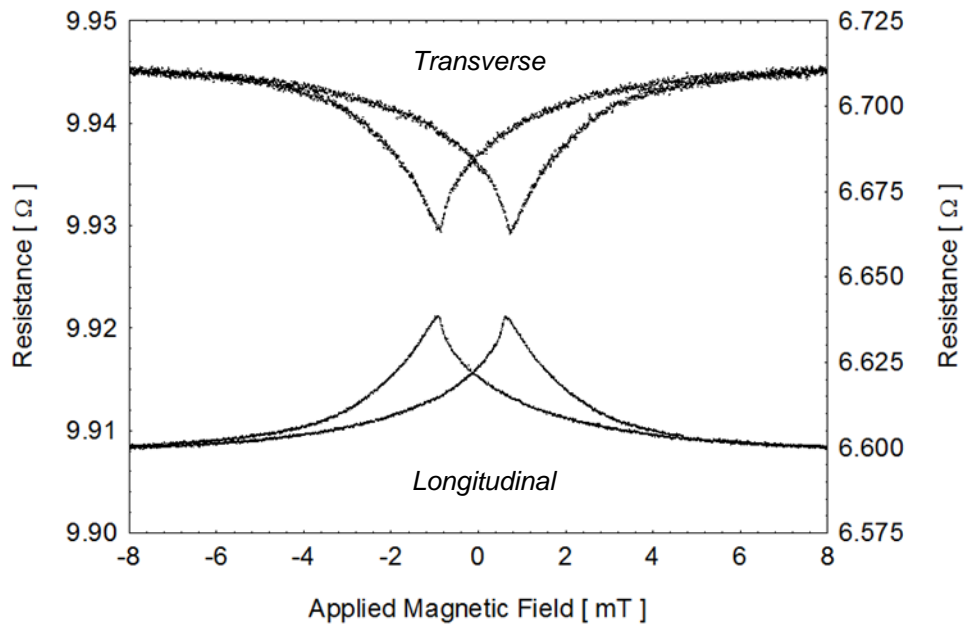


Figure 6-8 Showing the AMR for both field and current configurations for the sample used to investigate oxidation. Upper graph corresponds to the transverse configuration measurement and the lower graph corresponds to the longitudinal configuration measurement.

Figure 6-8 shows the AMR in the two measurement configurations used throughout this section, the upper graph corresponds to the transverse configuration and the left hand scale and the bottom graph corresponds to longitudinal configuration and the right hand scale. The percentage AMR is calculated to be 0.2%, which is a small increase from the previous experiment but still considerably smaller than the typical film displaying an effect as large as 1.5%, presented later in this section. As mentioned above after growing the thin film the chamber was opened to allow air in. Upon exposure to air a steady increase in the resistance was observed tending to a fixed value of resistance, this is assumed to be due to oxidation of the sample in air and the fixed value it tends to is indicative of a self-limiting oxide as predicted for thin films of NiFe [97].

Figure 6-9 shows the opening of the vacuum chamber to air and the increase in resistance associated with the thin film becoming oxidised, the chamber is then closed and the pumps turned back on in an attempt to remove the air and stop the oxidation taking place. This was observed in practice as shown by the inset in **Figure 6-9** (the full time scale shown in the inset is approximately 10 minutes), it is clear then, that the exposure of the thin film to air results in oxidation of the thin film. The resistance reached a plateau after approximately 4 hours of exposure to air.

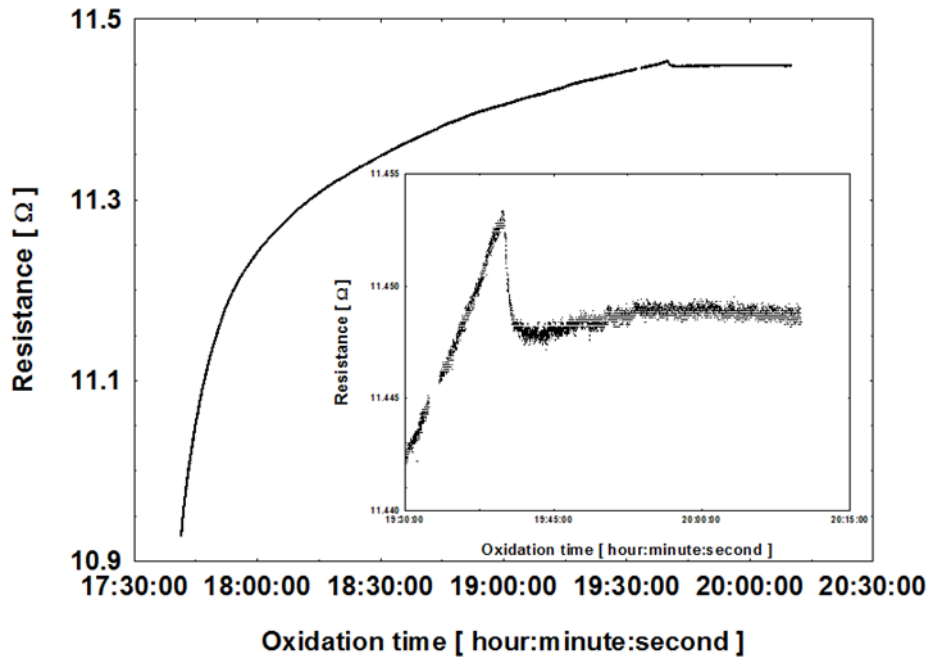


Figure 6-9 Showing the change in resistance upon exposing the sample to air. The inset shows the chamber closed and pumped removing the air. The increase in resistance attributed to oxidisation was absent with the sample held under vacuum.

After the *in situ* measurement setup was shown to be working and giving meaningful and reliable results a more involved and challenging project was undertaken. The idea was to grow a thin NiFe film as previously, except this time to interrupt the deposition at fixed thickness and measure the AMR response of the thin film *in situ*, to observe how the AMR signal evolves with thickness. This was supposed to serve as a prelude to investigating spin valve based effects and nanostructures *in situ* and during deposition. However, this experiment yielded an unexpected result.

A recent research paper (discussed in section 6.2) showed in brief, that considering a thin film there are two different regimes of magneto-transport, tunnelling magnetoresistance in the low thickness limit physically corresponding to isolated islands. After the percolation limit the film exhibited anisotropic magnetoresistance. The research also investigated the use of different substrates which resulted in the transition from tunnelling to anisotropic varying for each substrate used [98].

The substrate was loaded into the chamber in the same manner as the previous experiment conducted *in situ*, the deposition began again as before when a suitable pressure was reached, the only experimental difference the second time is that deposition was interrupted at fixed thickness intervals (every 2nm) and magnetoresistance measurements attempted. From surveying the literature it is

expected that a signal can be measured for an ultrathin film of NiFe as small as 8 Å [98].

Due to a reduced signal size of the AMR that was below the noise threshold obtained for *in situ* measurements, no reliable data relating magnetic field to resistance was obtained *in situ*. It is believed that growing the film in steps of around 2nm in thickness and then stopping to attempt magnetoresistance measurements (sometimes for as long as an hour) reduced the signal due to oxidation taking place within the vacuum chamber at each thickness step, this is one plausible argument put forward to explain the reduced signal size obtained for a 20nm film grown in 2nm steps the other being that the ratio of Nickel to Iron had changed considerably, the AMR ratio is a maximum for the composition corresponding to Permalloy ($\text{Ni}_{81}\text{Fe}_{19}$) [101]. The final possibility is contamination of the sample in some way, although after extensively attempting to identify this contamination through trial and error and examining every item used within the vacuum chamber no obvious contaminants were found to be present. Only after the sample was removed from the vacuum chamber and measured *ex situ* where a lower noise level was found, was any reliable magneto-transport data taken for this sample. **Figure 6-10** shows the data taken for this sample measured *ex situ* in the low noise AMR measurement system and a typical thin film displaying a larger AMR for comparison.

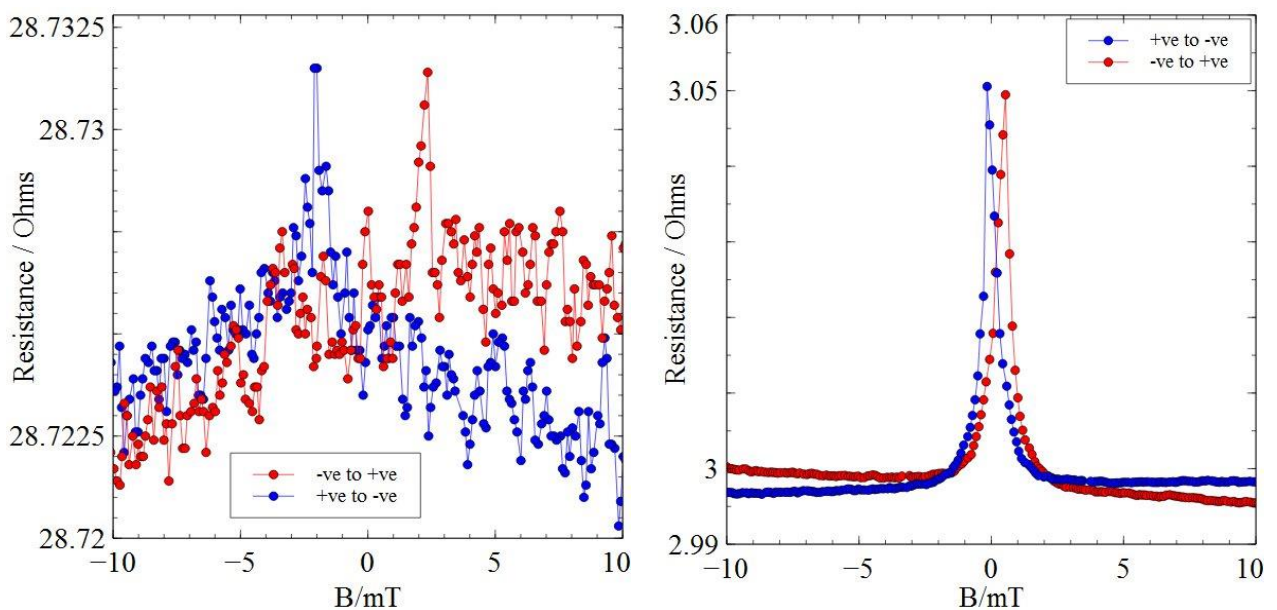


Figure 6-10 Comparing a thin film grown in a single step (right image) with a thin film grown in 2nm steps (left image). Both films are 20nm thick and measured *ex situ*. Clearly the sample shown in the graph on the right has a lower resistance and larger AMR effect.

Name	Size of AMR / mOhms	AMR Percentage Change / %	Resistance / Ohms	Coercive Field / mT
Film grown in a single step (evap 88)	50 ± 0.18	1.63	3.05	0.3± 0.11
Film Grown in 2nm Steps (<i>in situ</i> 1)	6.5 ± 0.2	0.024	28.73	2.2 ± 0.15

Table 18 Summarising the results obtained for the thin film grown in 2nm steps up to a thickness of 20nm and a typical thin film grown in a single deposition up to 20nm.

Figure 6-10 shows magnetoresistance measurements made in the longitudinal configuration (current and magnetic field parallel), measured *ex situ* for the thin film grown in 2nm steps (left image) and for a typical thin film (right image) i.e. grown in normal conditions not utilising the *in situ* setup. Both show two peaks for each field sweep direction relating to the reversal of the thin films magnetisation, the field value at which the peak occurs is the coercive field of each film. The AMR is very small for the film grown in steps, the effect being in absolute value (6.52 ± 0.21) mΩ and 0.024% in terms of percentage change, for the typical film presented an AMR as large as 50mΩ was observed with a percentage change of 1.63%. There is approximately an order of magnitude difference between these two absolute values relating to the AMR. Comparing the percentage changes a similar difference is observed although the percentage change is two orders of magnitude greater for the single step grown thin film. Considering the coercive fields, the typical (single step grown) thin film coercive field is what is expected for a magnetically soft material like NiFe fabricated as a thin film i.e. a coercive field less than 1 mT [100]. Regarding the film grown in steps a coercive field over 2mT was measured implying the magnetisation is more difficult to rotate for the film grown in steps i.e. it costs more energy to reverse the magnetisation of the film grown in steps as opposed to the single step grown thin film. Finally considering the resistances of the samples in the longitudinal configuration, they differ considerably with respect to this also, the thin film grown in steps being ten times more resistive approximately. All these parameters considered the film grown in steps is atypical, displaying a very small

AMR, having a slightly higher coercive field and a resistance ten times higher than that of a typical (single step grown) thin film of similar dimensions. These results were not highlighted in reference [98] where a similar experiment was carried out.

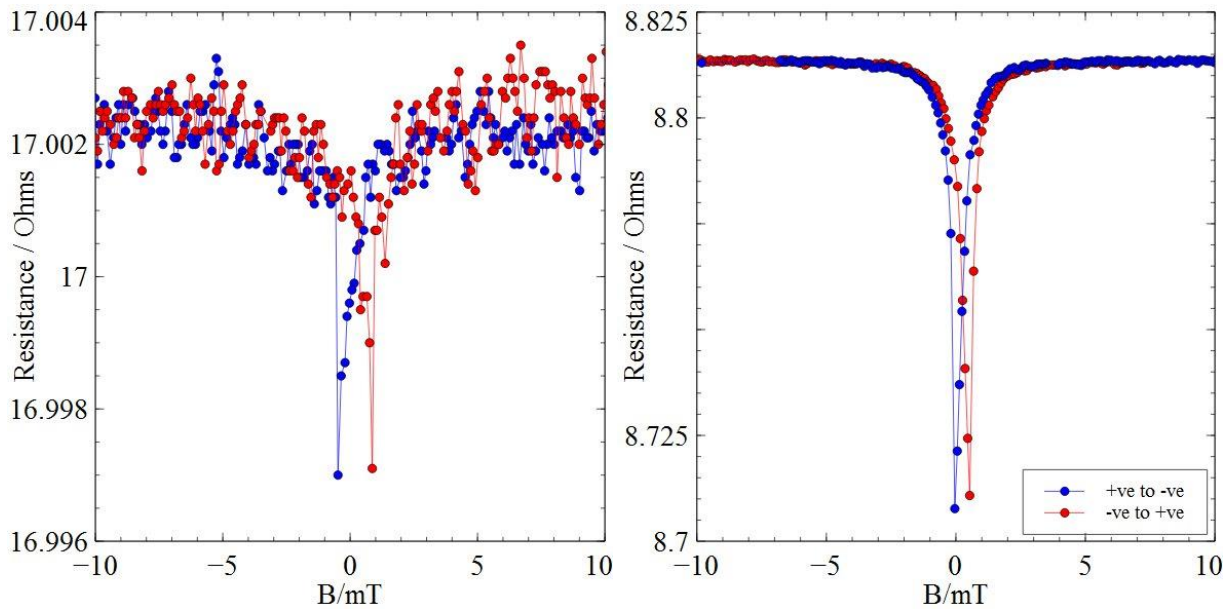


Figure 6-11 Showing a comparison between a thin film grown in a single step (right image) and a thin film grown in 2nm steps (left image). Both are 20nm thick and measured in the transverse configuration.

Sample Name	Size of AMR / mOhms	AMR Percentage Change / %	Resistance / Ohms	Coercive Field / mT
Film grown in a single step (evap 88)	90.15 ± 0.13	1.021	8.82	0.21 ± 0.11
Film Grown in 2nm steps (<i>in situ</i> 1)	5.12 ± 0.18	0.031	17.00	0.63 ± 0.23

Figure 6-11 shows the results after taking magnetoresistance measurements in the transverse configuration (current and magnetic field parallel) for a thin film grown in a single step and the film grown in 2nm steps. Again two clear peaks are visible for both films relating to the magnetisation reversing direction at the coercive field of the sample. A very small AMR effect is observed again for the film grown in steps being

(5.12 ± 0.18) m Ω with the percentage deviation from the baseline resistance being 0.031%. For the single step grown film the effect is (90.15 ± 0.13) m Ω and the percentage change is 1.021%, both values considerably more than that of the film grown in steps. Considering the coercive fields a value of 0.2 ± 0.1 mT is obtained for the film grown in one step and a value of 0.63 ± 0.23 mT is obtained for the film grown in multiple steps. The coercive field for this configuration has yielded a more expected result in terms of coercive fields of both films giving values around the expected value of 0.5 mT although the film grown in steps does give the higher result again. Considering the resistances in this configuration again the film grown in steps is approximately ten times more resistive than the single step film.

6.2. Discussion

It has been shown in the preceding section that a thermal evaporation chamber complete with magnetic and optical probes has been successfully assembled and calibrated. Specifically, anisotropic magnetoresistance (AMR) is the chosen probe for electrical and magnetic characterisation allowing one to determine the reversal mechanism, coercive field and attempt to quantify the quality of a magnetic thin film by comparing the AMR response to known samples and theory. The chosen optical probe is the magneto optical Kerr effect (MOKE) allowing determination of the coercive field, reversal mechanism and again an attempt can be made to quantify the quality of a magnetic film by comparing the obtained parameters with known sources. In this thesis only the AMR effect has been used to characterise thin magnetic films *in situ* and *ex situ*.

After the chamber and probes were setup and found to be functional a simple 20 nm thick NiFe thin film was grown and measured *in situ*, it was then removed from the vacuum chamber and measured *ex situ* in the low noise AMR setup. Good agreement was found between the *in situ* and *ex situ* datasets in terms of size of the AMR effect and resistances. Both were seen to increase when removed from the vacuum chamber due to the formation of an approximately 5 Å thick nano-oxide.

Another experiment was then devised to show that the resistance change going from *in situ* to *ex situ* was due to oxidation. A clear correlation was seen between the resistance increase and air being admitted into the growth chamber.

Finally a more involved experiment was undertaken where a thin NiFe film was grown up to 20nm in steps to see how the AMR signal evolved with film thickness. At each step an attempt to measure the AMR of the thin film was undertaken although due to a small signal size no meaningful measurements were obtained *in situ*. The sample was removed from the chamber and then measured *ex situ* where a small signal was obtained owing to a lower noise level obtainable in the low noise AMR setup compared with the *in situ* measurements. This sample (*in situ* in steps) was then compared with a film grown in a single step in normal conditions (not the *in situ* setup) to attempt to understand why the signal was so small in comparison. In theory growing a film in 2nm steps should give the same results as growing a 20nm film in a single step however, this was not observed in practice. The AMR signal was found to be an order of magnitude smaller and the resistance was an order of magnitude larger, considering that the size of the AMR effect is proportional to the thickness of the film [100] this makes sense. The argument resulting in a reduced 'effective' thickness for the sample grown in 2nm steps is as follows:

The sample grown in 2nm steps underwent some amount of oxidation at each 2nm step, a calculation was made that gave a self-limiting oxide nano layer of approximately 5 Å for a 20nm thick film calculated earlier, this value is essentially independent of the thickness of the film. It is reasonable to assume that after every deposition the sample underwent oxidation to a thickness of 5Å measured from the surface. Summing this oxide thickness over all depositions yields a total oxide thickness of around 4nm, for the total oxide thickness for a 16nm thin film grown in 2nm steps. The final deposition was for this sample was from 16nm to 20nm (partially an attempt to see if the 2nm steps were too small) this leaves approximately 15nm of material that is involved in producing the AMR effect, accounting for the final oxide layer (16- 20 nm deposition). But for a 15nm thick Permalloy layer a larger value than 5mΩ is to be expected for the AMR. Considering each oxide is insulating and the fact that current will follow the path of least resistance, this implies a very small amount of Permalloy (3.5nm – final deposition

thickness with the oxide thickness subtracted) is responsible for the majority of the AMR signal as it will be generated by the top layer with little conduction between layers deeper within the film. Using a value of 3.5nm for the thickness to attempt to estimate the expected AMR percentage change, the AMR rapidly approaches zero for thickness less than 5nm and a very small AMR is experimentally measured. This gives additional weight to the argument put forward for why the AMR is so low for a thin film grown in steps. To definitively confirm the formation of oxides at the surface of each deposited layer, other techniques would need to be used. X-ray absorption spectra could reveal if any oxides are present. The intensity of the peak (corresponding to the oxide) would be a first indication as to how much oxide material was contained within the thin film (grown in steps). Transmission electron microscopy is routinely used to analyse the thickness of layers in the sub nanometre region and would give a cross section of the film allowing one to directly image each layer and any corresponding oxides.

6.3. Conclusion

An high vacuum experimental setup was constructed that allowed for magnetic field dependent electrical measurement monitoring and thermal evaporations of magnetic thin films *in situ*. The selected probes for magnetic characterisation were anisotropic magnetoresistance (electrical) and magneto optical Kerr effect (optical).

It was explicitly verified that results obtained from AMR *in situ* were comparable to results obtained *ex situ* in the low noise AMR experimental setup. Oxidisation of a thin surface layer of magnetic thin films was shown to be the cause of the small resistance increases observed between the *in situ* and *ex situ* datasets.

A thin film of NiFe was grown up to 20nm in 2nm steps (final deposition 16nm – 20nm) and was found to have an AMR signal (in absolute size) of $\sim 5\text{m}\Omega$ and a resistance an order of magnitude above a typical (single step grown) thin film of the same dimensions. It was postulated that this was due to the sample undergoing oxidation at each growth step, resulting in a thin film where the AMR signal was only being measured in the top most layers due to the insulating oxide layers formed at each thickness deposition step.

Preliminary tests of the *in situ* setup utilising an ion pump to replace the currently employed turbo-molecular pump are underway. Operating this system at a lower pressure is expected to reduce the oxidation currently taking place within the growth chamber.

7. EXPERIMENTS WITH METAL SPIN VALVES

7.1. Introduction

Spintronics is the area of physics that investigates the effect of electron spin on conduction. Since the first application of electronics, the spin of the electron has mostly been ignored [18]. When an electrical current was first generated the spin of the electron was an unknown concept. Electron spin has been extensively studied since its discovery for over a hundred years now [15] although its effect on electronic conduction has only been studied in detail since the 1970s. It is a natural evolution of electronics due to the ever reducing size of electronic components. At reduced dimensions it is impossible to neglect the effect of spin on conduction. If one considers Moore's law, a plot which shows the number of transistors on a chip plotted against year, it can be shown that by 2020 the projected size of a transistor is atomic.

It is clear then that to reach such dimensions the effect of spin on conduction needs to not only be understood, but incorporated into device architecture. To this end experiments have been carried out investigating spin polarised currents and the transmission of such currents through different types of materials and interfaces.

7.2. Spin injection From Nickel Electrodes into A Gold Spin Channel

After an initial review of the literature it was found that successful spin injection from Nickel in a lateral spin valve structure had not yet been shown experimentally (this was true when Nickel spin valves were being fabricated for this thesis (2012), although successful injection from Nickel electrodes in lateral structures was shown in 2014 [37]). One research paper reported measurements made on a Nickel/Copper/Nickel lateral spin valve with an electrode spacing of 500nm [21], they observed no signal due to spin accumulation and placed an upper limit on the spin

valve effect in their devices ($<20\mu\Omega$). The low signal was attributed to the low spin polarisation of Nickel (0.06) and possible uncontrolled oxidation of the Copper. A calculation of the spin signal using the 1D equation for Nickel injector and detector electrodes (200nm separation) and a Gold spin channel was made and an estimation of the spin signal was obtained as approximately $0.4\text{m}\Omega$. It was thus decided that a Nickel/Gold/Nickel lateral spin valve would be fabricated and measured to investigate spin accumulation from a Nickel injection electrode into a Gold non-magnetic spin medium, as the low noise AMR setup had an experimentally verified noise level below $0.4\text{m}\Omega$ for the expected resistance range of the device.

The device was fabricated in the manner outlined in the section 3. Before attempting to measure the spin valve effect, locally and non-locally, the magnetic electrodes and spin channel are electrically probed to ensure there is continuity of all the circuits to be used.

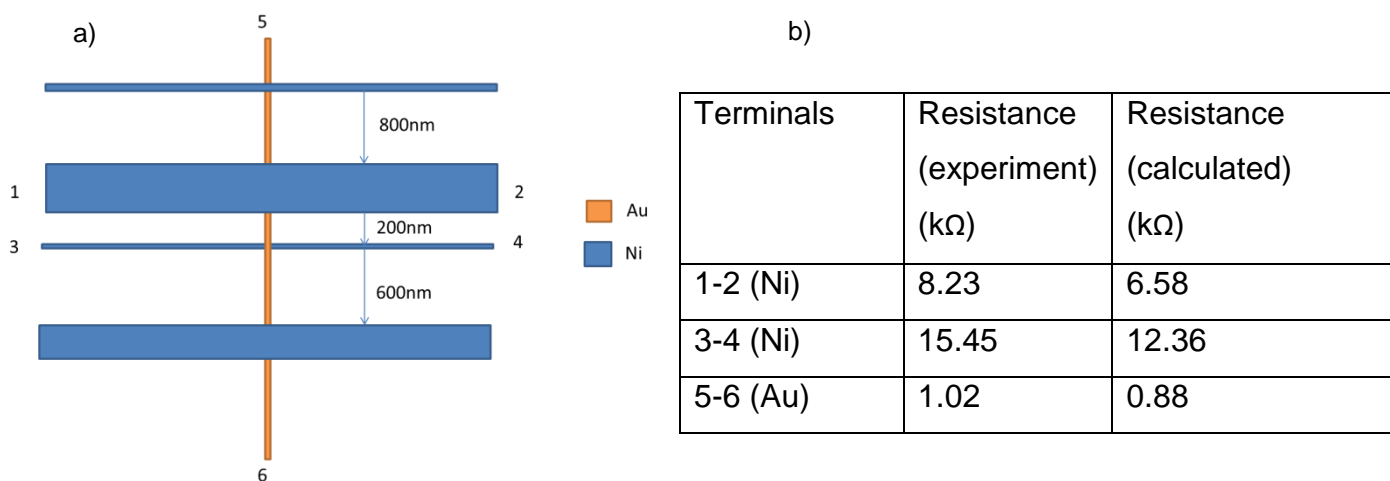


Figure 7-1 Showing a schematic of a fabricated spin valve device (a) for highlighting how different measurements are carried to ensure the device is performing as expected prior to measuring the spin valve effect. Image (b) shows example resistances obtained using two terminal electrical measurements.

Figure 7-1 shows a schematic of a fabricated Nickel/Gold/Nickel spin valve device and a table summarising the two terminal electrical measurements made on such a structure. All the measurements shown in the table of **Figure 7-1** are two terminal electrical measurements including the contacts into the measurement. This was purposely done to ensure the wires and contacts were all behaving as expected. The

resistance of the spin channel (Au) is less than that of the Nickel structures, due to Gold having a smaller resistivity than Nickel. Gold has a resistivity ($2.88 \times 10^{-8} \Omega\text{m}$) approximately an order of magnitude smaller than Nickel ($10.5 \times 10^{-8} \Omega\text{m}$). Gold is approximately an order of magnitude smaller in terms of two terminal resistance as a result. The exact value for the measured resistance depends on the dimensions of the different nanowires and the corresponding resistivity. Calculations were made to estimate the resistance of every fabricated nanowire using the standard resistivity equation and the nanowire dimensions. All estimates were within a factor of 15 of the measured resistances, the deviation (measured was always greater the calculated) was assumed to be due to not accounting for surface scattering in the estimations, the thinner structures become, the more prominent surface scattering becomes. After measuring the two terminal resistances in all configurations, provided the device is behaving as expected, the magnetic electrodes are then probed using AMR to determine the coercive fields using electrical measurements.

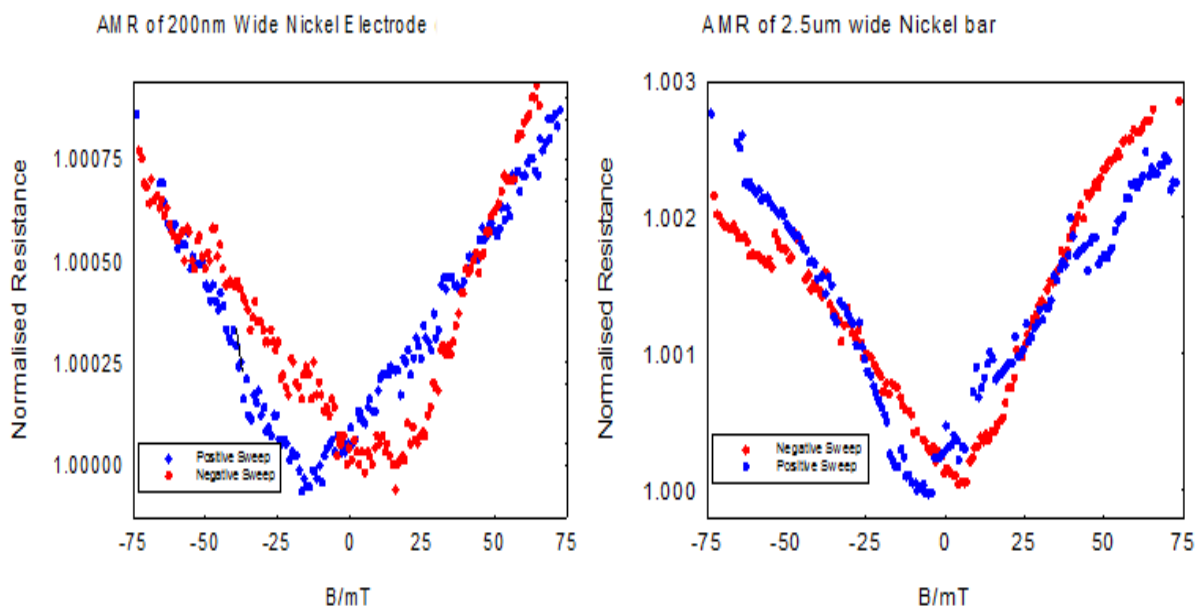


Figure 7-2 Showing AMR curves for the injecting and detecting Ni electrodes shown in Figure 7-3. Allows evaluation of coercive fields.

Figure 7-2 shows AMR curves measured in the transverse configuration for two Nickel magnetic electrodes of different widths. The left image corresponds to 200nm wide Nickel and the right image corresponds to 2500nm wide Nickel. The bell shape

of the curves results from the measurements being two terminal and sampling larger section of Nickel that behave like a thin film. The dip in the bell curves correspond to reversal of the nanowire. For the 200nm wide nanowire a coercive of $\sim 20\text{mT}$ is measured and for the 2500nm wide nanowire a coercive field of $\sim 8\text{mT}$ is measured. AMR measurements used in this chapter are solely used to ensure distinct coercive fields are obtained. Simply by varying the width of a ferromagnetic nanowire it is possible to access a range of coercive fields, this was experimentally verified for Nickel using AMR measurements prior to carrying out spin valve measurements. Many Nickel/Gold/Nickel devices were fabricated and measured in an attempt to optimise and improve on both the design and fabrication of these devices, ultimately to achieve a separation of injector and detector electrodes of 200nm in width and with distinct coercive fields. This was a non-trivial task as highlighted by the various parameters and steps involved in electron beam lithography and thermal evaporation in the chapter Sample Fabrication.

After some number of attempts a lateral spin valve composed of Nickel/Gold/Nickel was fabricated that displayed two distinct coercive fields for the injector and detector electrodes along with an injector-detector separation close to 200nm.

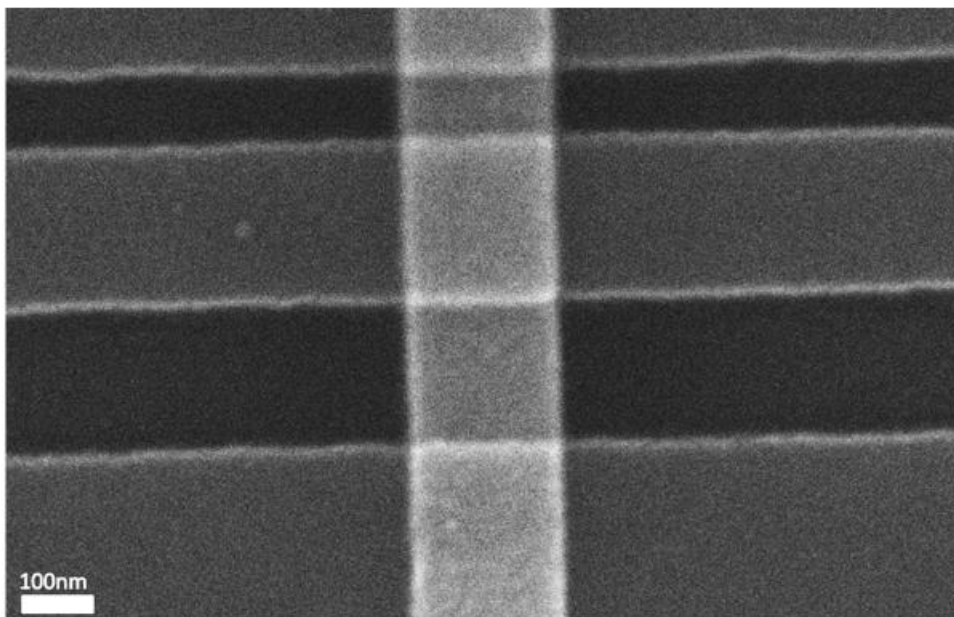


Figure 7-3 Showing a high magnification SEM image of a fabricated Nickel/Gold/Nickel lateral spin valve structure with a 200nm separation between injecting and detecting electrodes.

Figure 7-3 presents an SEM image of a fabricated Nickel/Gold/Nickel lateral spin valve device with an electrode separation of approximately 200nm. The electrode separation of 200nm is shown in the centre of the image and a separation of less than 100nm is shown between electrodes at the top of the image. The electrodes with a separation of less than 100nm merged into a single electrode a little further out, this is not visible in the presented SEM image i.e. the smaller separation was unmeasurable.

The device presented in **Figure 7-3** was used to measure the spin valve effect in the local and non-local configurations, the details of local and non-local measurements were discussed in the theory section.

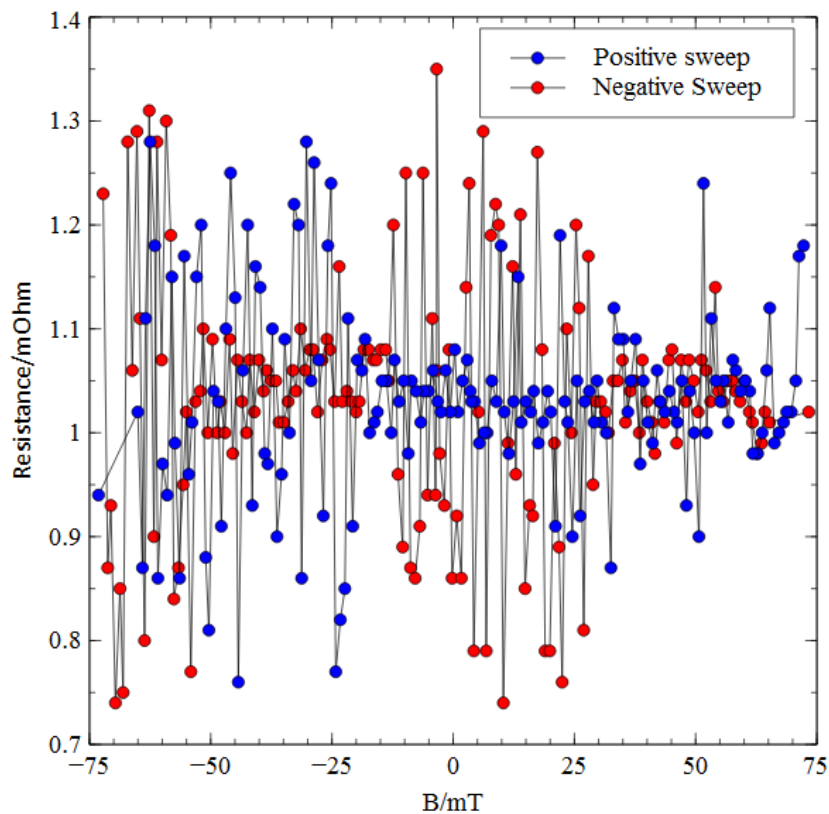


Figure 7-4 Presenting the non-local spin valve effect measured for a Nickel/Gold/Nickel lateral spin valve with an injector –detector separation of 200nm. The spin valve effect was not observed for this device.

Firstly the local spin valve effect is attempted, where the injection and detection circuits are setup such that both a net polarisation of charge and spin are injected

and a voltage is setup relating to both these parameters. Theory predicts this configuration is twice the size of the voltage induced in non-local spin valve effect [21]. No field dependant effects were obtained in the local configuration for any of the Nickel/Gold/Nickel spin valve samples. An upper limit can be placed on the spin signal in the local configuration of $<2\text{m}\Omega$ for a Nickel/Gold/Nickel interface with an injector-detector spacing of 200nm, predictions for the voltage change induced by spin accumulation in the local measurement configuration corresponded to a resistance of $2\text{m}\Omega$. The four terminal resistance corresponding to the local measurement configuration, over a range of devices, was measured to be in the range (10-300) Ω , comparing to other local measurements made over a range of devices [102]-[103] a smaller variation was observed (1-10) Ω , this was assumed due to a lack of any interface control, ion milling was used in the presented references [102]-[103] for interface control. After measuring the local spin valve effect attempts were made to measure the spin valve effect in the non-local configuration (**Figure 7-4**), no signal was observed in this configuration for any fabricated Nickel/Gold/Nickel lateral spin valve structures. An upper limit can be placed on the non-local spin valve effect for a Nickel/Gold/Nickel systems of $<0.2\text{m}\Omega$. It was assumed that the lack of interface control combined with the low spin polarisation of Nickel (0.06 from [4]) and low spin diffusion length of Gold ($\sim 50\text{nm}$ from [104]) resulted in induced voltages due to spin accumulation that were below the noise threshold achieved for these devices.

7.3. Spin Injection from NiFe Electrodes into A Gold Spin Channel

Permalloy (NiFe) was investigated as a spin injector and detector and was found to have a larger spin polarisation (0.45) than that of Nickel (0.06), it was thus decided that Nickel would be replaced with Permalloy for spin transport investigations. The 1D model was used to re-estimate the size of the induced voltage due to spin accumulation in a NiFe/Gold/NiFe lateral spin valve structure using the relevant dimensions, converting this voltage to a resistance gives an estimated spin valve effect of $1.5\text{m}\Omega$. Many NiFe/Gold/NiFe lateral spin valves were thus fabricated and measured.

As discussed in the theory section 2.7 it was found that interface control is key to constructing reproducible devices [33][105][106][107]. Oxide layers can serve as scattering sites for spin polarised electrons and in the case of NiFe, an anti-ferromagnetic oxide layer can form which is detrimental to spin polarised current passing through such a layer [97] [32]. Control of the interface comes generally in the form of two separate processes, multi-angle evaporation to avoid oxides or ion beam milling to remove them. One can also form a variety of tunnel barriers to attempt to control the interface. A tunnel barrier will increase the spin signal because there is reduced spin diffusion back through a tunnel contact as opposed to a metallic contact [32]. It is not possible to use the two-angle deposition technique in the custom built evaporator (not without a rotational stage) and there is no ion beam mill in the vacuum chamber to clean interface before deposition, so it was decided that the interface would be controlled in the following manner.

To avoid oxide layers gold was used as a spin channel, it does have a low spin diffusion length (~50nm from reference [104]) but does not oxidise upon contact with air. Gold was fabricated as the first step in the fabrication process, secondly then NiFe was deposited as the injector and detector electrodes avoiding any oxide layer due to the NiFe, as it was deposited in a vacuum directly onto the clean gold surface free from any oxide layers.

Initially after full fabrication of NiFe/Gold/NiFe spin valve the same procedure was followed as outlined in the previous section, after imaging the sample with a scanning electron microscope (**Figure 7-5**) to ensure the sample was intact and extracting the widths and spacing of the injector and detector electrodes, simple electrical measurements were then employed to ensure all circuits are operational and giving the expected resistances.

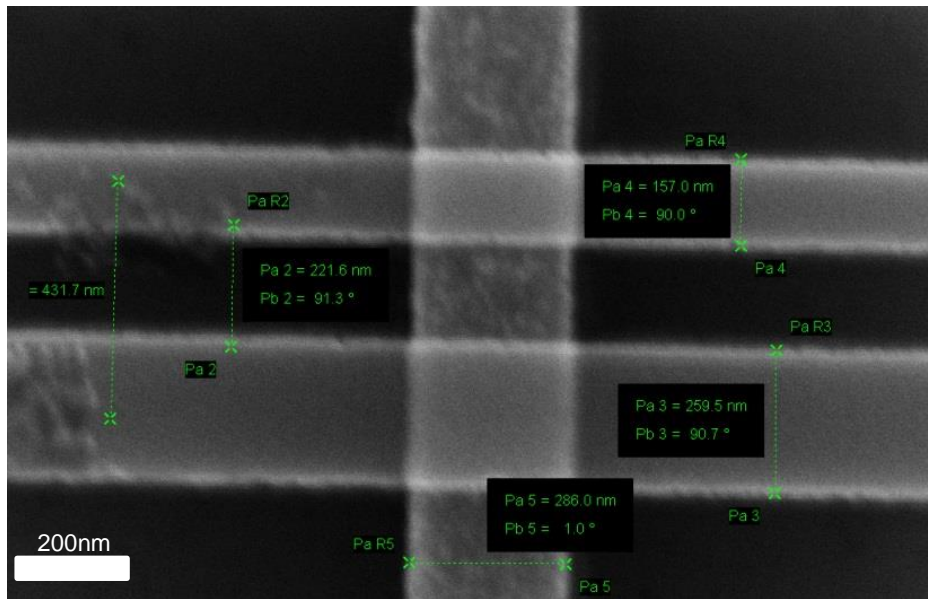


Figure 7-5 Presenting an SEM image of a measured NiFe/Gold/NiFe lateral spin valve. SEM was employed to determine the widths of fabricated nanowires and injector-detector spacing.

After this the coercive fields were measured via the AMR effect and attainment of an anti-parallel state was explicitly verified, example curves are shown in **Figure 7-6**. **Figure 7-6** shows two complete example AMR datasets (both field directions) for 300nm wide and 400nm wide nanowires. As discussed extensively in the theory section 4.3.2 it was shown how a domain wall is responsible for reversing the magnetisation of a nanowire and how AMR can be used to determine the coercive field of such a reversal event – a discontinuity in the resistance at the field value at which a domain wall reverses the nanowires magnetisation. Coercive fields were measured to be 5.1mT for a 300nm wide Permalloy nanowire and 3mT for a 400nm wide Permalloy nanowire as shown in **Figure 7-6**.

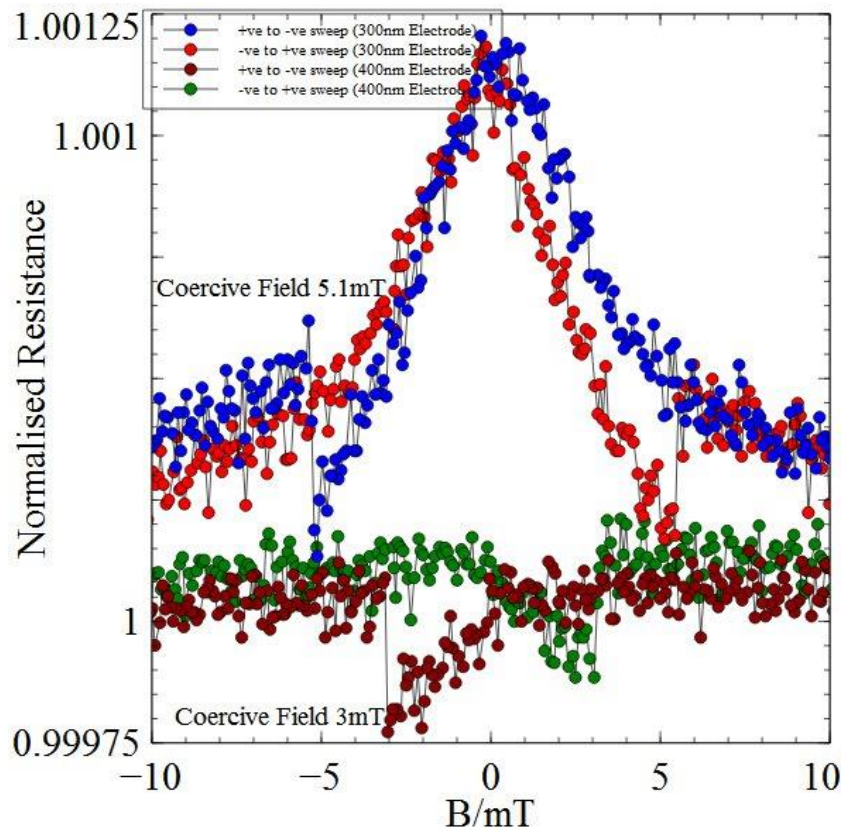


Figure 7-6 Showing two distinct coercive fields measured with the AMR effect. Two distinct coercive fields are shown at approximately 5mT and 3mT for the 300nm wide and 400nm wide nanowires respectively.

The difference in coercive fields here stems from solely the different widths of the nanowires, this is the only parameter that differs for these nanowires. A narrower nanowire has a larger contribution to its shape anisotropy from the reduced size and so requires more energy to reverse its magnetisation. After explicitly verifying the distinct coercive fields, the local spin valve effect was then measured where the detecting circuit is sensitive to the effects of both spin and charge. **Figure 7-7** presents the local spin valve effect measured in a NiFe/Gold/NiFe lateral spin valve at room temperature. For a single field sweep direction, considering the red data points of **Figure 7-7**, starting at maximum negative field (-20mT) the device is in a low resistance state corresponding to parallel alignment of the magnetisation of the injecting and detecting magnetic electrodes. As the field crosses zero and reaches the coercive field of the wider electrode (approximately 4mT) the device enters into a high resistance state corresponding to anti-parallel alignment of the magnetisation of

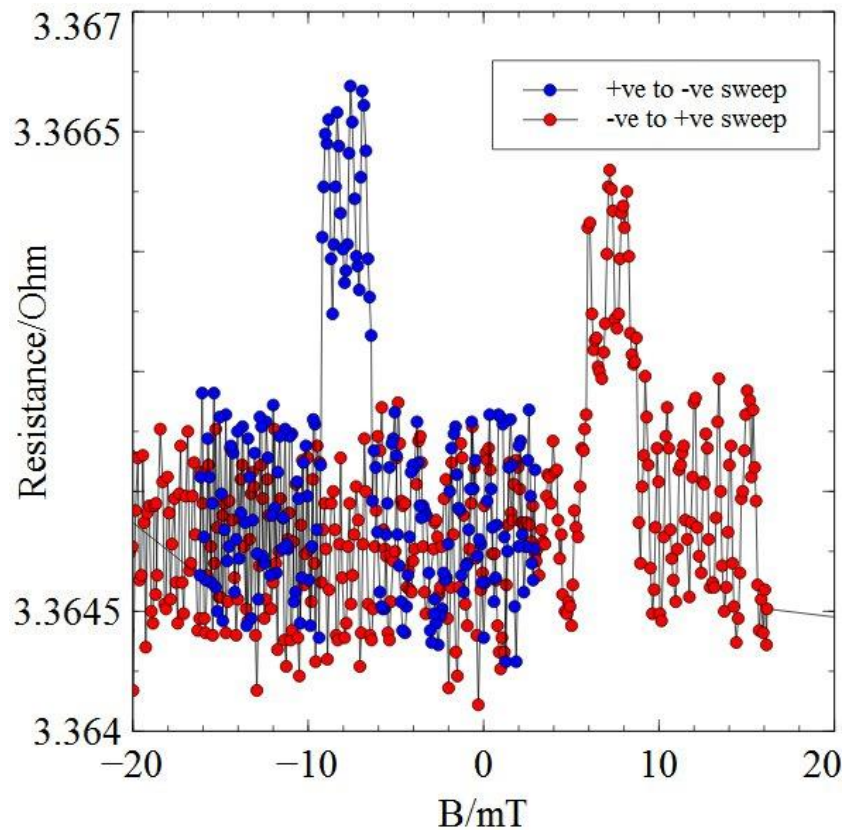


Figure 7-7 Presenting the local spin valve effect measured at room temperature using a NiFe/Gold/NiFe lateral spin valve.

the injecting and detecting magnetic electrodes. Further increasing the magnetic field until the coercive field of the narrower magnetic electrode is reached (approximately 8mT) and then the device enters back into its low resistance state corresponding to parallel alignment of the magnetisation of the injecting and detecting magnetic electrodes. The same analysis applies to the opposite field sweep direction (blue dataset of **Figure 7-7**). A signal size of 1.5 mΩ was expected from the literature [102], [108], [109], [110] and a signal size of (1.38 ± 0.08) mΩ was experimentally measured.

Finally the non-local signal was measured, shown in **Figure 7-8**. No spin based effects were observed, the expected signal size was at the noise level threshold and so presumably lost to the noise, it is possible to set an upper limit on the non-local spin valve effect as < 0.1 mΩ.

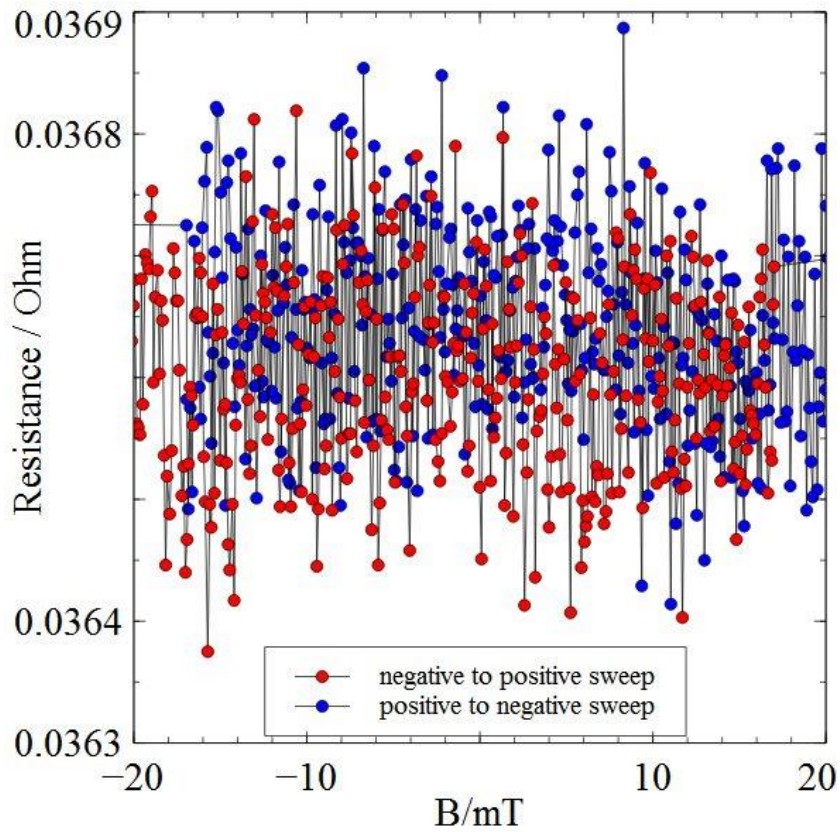


Figure 7-8 Showing the non-local spin valve effect in a NiFe/Au/NiFe lateral spin valve. No effect was observed and only and upper limit was placed on the effect ($<0.1 \text{ m}\Omega$).

7.4. Spin Injection from NiFe into Au as a Function of the Injection Length

In terms of NiFe/Gold/NiFe lateral spin valves, three devices repeatedly produced the spin valve effect in the local configuration, all these measured spin valves differed in terms of injector-detector spacing only. This allows calculation of the spin diffusion length of Gold and spin polarisation of NiFe by plotting out the signal size as a function of electrode separation and fitting to the 1D model for spin transport (**Equation 23**) as presented in section 2.7.7.

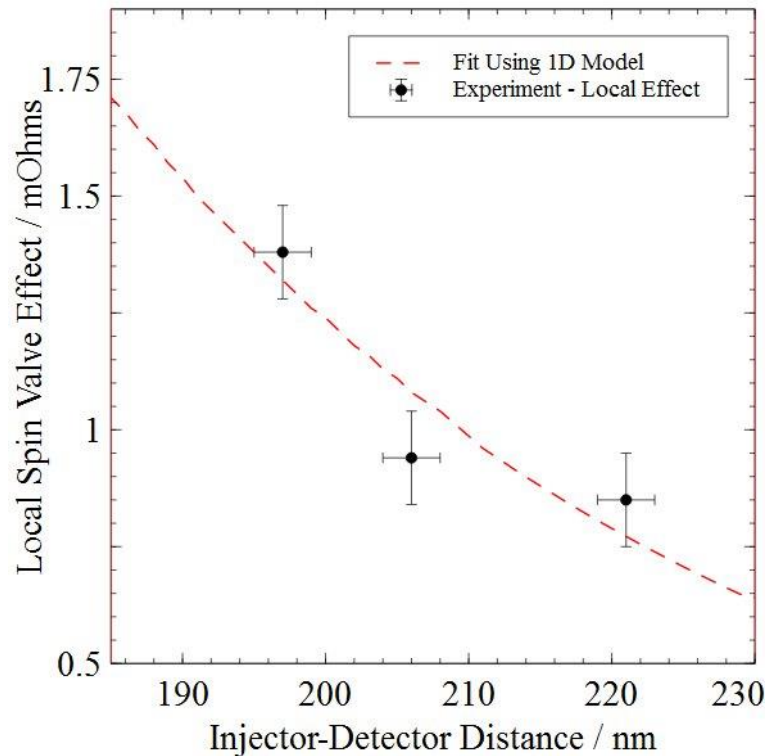


Figure 7-9 Presenting the local spin valve effect as a function of the injector-detector separation. The data was fitted with a 1D model describing spin transport.

Figure 7-9 presents the local spin valve effect as a function of the injector-detector separation. The data was fitted using the python software, the parameters spin diffusion length, injection efficiency and spin polarisation of the NiFe were allowed to vary to achieve the best fit. The parameters resistivity, cross sectional area of spin channel and injector-detector spacing were set by experimentally measured values. The fit shows agreement with the experimentally determined values, the two extreme data points intersect the fit although the middle data-point doesn't intersect the fit at all, it is about 0.1mΩ away from intersecting the fit, the dependence on injector-detector spacing of the experimental data matches with the theoretically generated dataset. The outputs of the fit are summarised in **Table 19** along with data from a relevant research paper.

<i>Parameters Obtained for NiFe/Au/NiFe Lateral Spin Valves</i>	<i>Numerical Value Extracted From Fit – (300K Measurements)</i>	<i>Values Presented in Reference [111] – (15K Measurements)</i>
Spin Diffusion Length in Gold (nm)	(46±8)	63 ± 15
Injection efficiency of NiFe/Au Interface	(0.35±0.15)	N/A
Spin Polarisation of NiFe	(7±1.5)%	3%

Table 19 Presenting numerical values obtained through fitting the experimentally measured data with the relevant theory (1D model for spin transport).

The above parameters were generated from the theoretical data presented in **Figure 7-9**. All values are of the expected orders of magnitude and close to values obtained in other experiments [103], [109], [110] These parameters will be discussed at length in context of the existing literature and further analysis will be carried out in the discussion section.

7.5. Spin Injection from NiFe Electrodes into An Aluminium Spin Channel Through an Aluminium Oxide Tunnel Barrier

After successful fabrication of a NiFe/Au/NiFe lateral spin valve displaying the local spin valve effect. It was decided that Aluminium would be used to replace the Gold as the non-magnetic spin medium. Aluminium was chosen for the spin channel for several reasons, it has one of the longest spin diffusion lengths of the metals (~700nm according to reference [112]) which increases the induced voltage due to spin accumulation and allows detection at greater injector-detector separations. Aluminium has been shown to have a native oxide that forms a tunnel barrier and enhances the spin injection efficiency [45]. A new recipe was concocted to fabricate NiFe/AIO_x/Al/AIO_x/NiFe, where the AIO_x corresponds to a tunnel barrier at the interface between the NiFe and Aluminium. These devices were fabricated as follows:

NiFe was deposited first and then to avoid the need for cleaning the interface a thin Aluminium layer (2nm) was deposited on top of the NiFe electrodes (without breaking vacuum/in the same deposition process) and then allowed to oxidise in air forming an oxide layer and thus tunnel barrier. This increases the spin signal by reducing the backflow of spin polarised electrons and removed the need for cleaning the interface or multi-angle evaporation techniques. The deposition of Aluminium in a controllable manner to a thickness of 2nm was a non-trivial task requiring a lot of practice and research. As with the previous samples, SEM was used first to assess the overall integrity of the devices, electrical measurements are then used to ensure all circuits are behaving normally. Provided the sample passed these tests (many samples did not presumably due to the formation of a poor oxide layer and thus interface) the coercive fields of the magnetic electrodes were first measured using AMR. Image a) of **Figure 7-10** shows a typical AMR curve measured for an electrode in a NiFe/AIO_x/Al/NiFe lateral spin valve device. A clear abrupt change in resistance is observable close to 5mT for each field direction, the dip close to zero in the data corresponds to reversal of a wider magnetic element connecting to the nanowire, contained in the measurement. Only one magnetic electrode was measurable in terms of AMR. The local spin signal was then measured in which a voltage depending on both charge and spin injection is measured (**Figure 7-10** image b). There was a repeatable effect in the local spin valve configuration shown in the right image of **Figure 7-10** image b). The measurement resembled the spin valve effect and matches up with the one measured electrode switching field as shown in image a) of **Figure 7-10**, a line was added to show the coercive field of the one electrode on the graph presenting the local measurements. The unmeasured electrode is the narrower than the measured magnetic electrode and so is anticipated to have a higher coercive field. The difficulty in interpreting this as an entirely spin dependent signal comes from the charge dependent effects being superimposed on top of the spin dependent effects. In previously fabricated samples electrodes with similar dimensions had coercive fields of approximately 10mT, this matches up with the device entering back into the low resistance state in **Figure 7-10** b) close to 10mT. The non-local spin valve effect was unmeasurable in this sample due to a merged contact during the fabrication process.

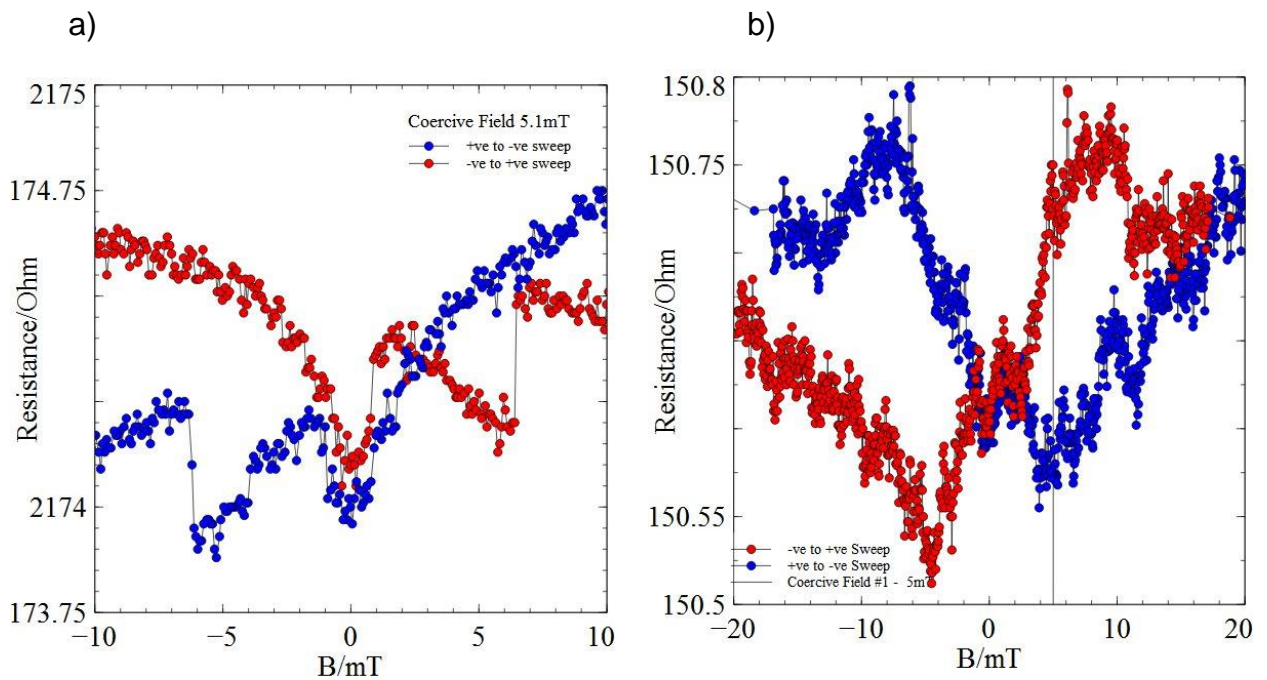


Figure 7-10 Presenting an AMR measurement of a magnetic electrode used in the spin valve measurement for a NiFe/AIO_x/Al/AIO_x/NiFe lateral spin valve, coercive field is close to 5mT for both field directions. Image b) presents the local spin valve effect measured for a NiFe/AIO_x/Al/AIO_x/NiFe lateral spin valve, the coercive field of the measured magnetic electrode is also plotted to aid interpretation.

After successful fabrication and injection from a tunnel barrier in the local configuration but not in the non-local configuration, as the expected signal was bordering on the noise level threshold. It was decided that to increase the spin signal a dual injection scheme would be used (discussed in section 2.7.8) as a potential increase in the induced voltage due to spin accumulation by a factor of 2.4 is possible [33]. The only necessity for operating a dual injection lateral spin valve in the non-local configuration is three electrodes, two for forming the injection circuit and a third for acting as a detector (details in section 2.7.8).

The dual injection sample was fabricated in the same manner as all previously fabricated samples, the same designs and fabrication process was followed as for creating lateral spin valves with a tunnel barrier (details in section 7.5) with fabrication of an additional ferromagnetic injection electrode added. A separation close to 200nm between all electrodes was achieved. The same procedure was followed as to assess the quality of the sample and ensure that it was behaving normal as in the previous results sections of this chapter.

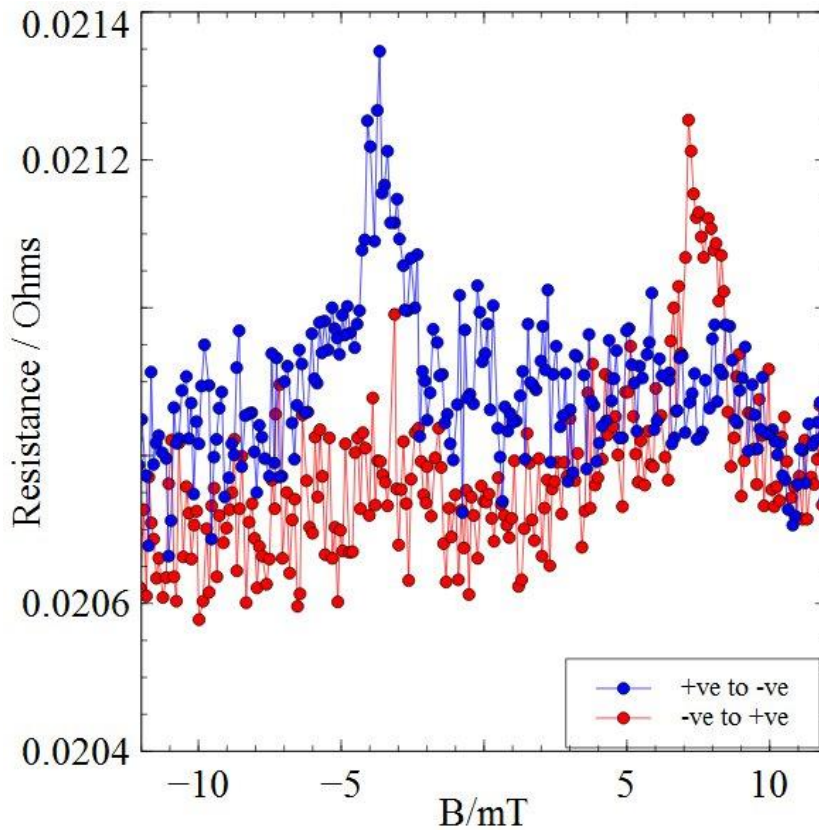


Figure 7-11 Presents the non-local signal in a NiFe/AlO_x/Al/AlO_x/NiFe dual injection lateral spin valve, measured in the dual injection configuration. The datasets are not typical of a non-local spin valve effect in a dual injection lateral spin valve, but were repeatable. In this configuration the measured voltage is only sensitive to spin dependent effects.

Figure 7-11 presents the non-local detection of a spin dependent voltage in a dual injection NiFe/AlO_x/Al/AlO_x/NiFe lateral spin valve. In the non-local measurement configuration, the charge is isolated from the spin current at the detection point (no voltage drop) and hence no signal is detected from a flow of charge. The only thing that is detected in the non-local configuration is the voltage produced due to spin accumulation diffusing in to the non-magnetic medium. Hence the data presented in **Figure 7-11** is attributed to spin dependent transport solely. A clear high resistance state and low resistance state is observed for both field sweep directions. There is an offset in field between the two datasets (blue and red datasets) due to positioning of the Hall probe used to measure the applied magnetic field. The absolute size of the effect measured in this device is (0.4 ± 0.04) m Ω . This will be discussed further in the discussion section of this chapter where a comparison with relevant devices will also be carried out.

7.6. Discussion

7.6.1. Spin Injection from Nickel Electrodes

No successful spin injection was achieved using a Nickel/Gold/Nickel lateral spin valve structure in experiments undertaken within this thesis. There have been reports [37] of using Nickel as the injector and detector magnetic electrodes in lateral spin devices to successfully inject spin current, although the spin channel used had longer spin diffusion lengths than gold i.e. Copper and Aluminium. There have been no reports of successful spin injection from Nickel into Gold for a lateral spin valve structure. It is possible to place an upper limit on the size of the spin valve effect in the non-local configuration for Nickel/Gold/Nickel lateral spin valves based on measurements undertaken in this thesis, the effect is $<0.2\text{m}\Omega$. Predictions made using the 1D model for spin transport in a lateral spin valve of the appropriate dimensions and materials gave values of the order of a single $\text{m}\Omega$. Comparing with the lower limit obtained for Nickel/Aluminium/Nickel spin valves from reference [21] of $<0.02\text{m}\Omega$ it is likely that the spin valve effect for a Nickel/Gold/Nickel lateral spin valve is below this value also, due to Gold having a smaller spin diffusion length than Aluminium. This demonstrates that Nickel does not inject spin efficiently at a Nickel/Gold interface and other magnetic electrodes should be employed.

7.6.2. Spin Injection In NiFe/Gold/NiFe Lateral Spin Valves

Successful spin injection from NiFe into Gold was achieved at room temperature using lateral spin valve devices in the local measurement configuration for varying injector-detector spacing. **Equation 23** was used to fit the data to and the spin diffusion length, polarisation of the ferromagnets and injection efficiency were extracted. The extracted parameters will now be compared with other measurements made on NiFe/Gold/NiFe lateral spin valves. All other work referenced here has applied the same theory to obtain the values of their parameters. There is discrepancy within the literature regarding definition of the injector-detector spacing and difficulty can be found when attempting to compare with results that have defined parameters in different ways. It was decided that the injector-detector

spacing would be defined as the edge to edge distance of the injector and detector electrodes, this potentially underestimates the size of the derived parameters if the spin injection takes place across the whole area of the interface. It is believed that spin injection occurs at the formation of point contact for Ohmic junctions [104] and it has been shown that the injection area directly affects spin injection [113].

Spin Diffusion Length (nm)	Polarisation of Injecting Ferromagnet (%)	Injection efficiency (UNITS)	Thickness Of Au layer	Temp	Reference
46 ± 8	7 ± 1.5	0.35 ± 0.18	20	300K	This Work
63 ± 15	3		20	15K	[111]
85	9.3		60	15K	[103]
168 ± 10		0.26	60	15K	[110]

Table 20 Presenting a summary of spin diffusion lengths and associated parameters from the literature. This work has a spin diffusion length comparable with the work of other authors.

Table 20 presents spin diffusion lengths, spin polarisation of the ferromagnetic electrodes and injection efficiency of the interface from this work and the work of other authors. Immediately obvious is the spin diffusion length obtained in this work is comparable to the spin diffusion length of other works carried out at 15K, a minimum factor of 1.3 differing for the smallest referenced spin diffusion length and factor of 3.5 away from the longest referenced spin diffusion length. The largest presented spin diffusion length is 168nm which has a calculated efficiency less than that calculated for this work, it is not possible to estimate the change in diffusion length as a function of temperature but it might be expected that this work would be similar if not larger than 168nm at 15K given the room temperature spin diffusion length and the injection efficiency. It is worth noting the differing thickness presented in **Table 20** as there has been research to show that the thickness of the spin channel layer affects spin transport properties [114], displaying an increase in spin diffusion length for increasing thickness. This is confirmed by the data presented in **Table 20**. The 60nm thick referenced devices presented in **Table 20** were fabricated in the same manner as devices in this thesis with the addition of an ion mill of the

spin channel before magnetic electrode deposition and the data corresponding to 20nm thick devices referenced in **Table 20** were made using a two angle deposition.

The results presented from reference [111] are of the same thickness as the devices presented in this work but with reduced polarisation of the ferromagnetic layer. Considering how samples were fabricated in reference [111], a two angle deposition technique was used, which involves depositing material with the substrate at an angle. This technique avoids oxide layers as the vacuum is not broken when depositing both materials (ferromagnets and non-magnetic spin channel) so it is not likely that the interface is of higher resistance than results presented in this thesis. In the theoretical framework for calculating the voltage change due to spin accumulation in lateral spin valves no interface resistance is taken into account and it is postulated that a small interfacial resistance may enhance the spin accumulation akin to a tunnel barrier.

7.6.3. Spin Injection Using AlO_x Tunnel barriers

A Traditional lateral spin valve utilising NiFe as the injecting and detecting electrodes, Aluminium oxide as a tunnel barrier and Aluminium as the spin channel displayed the local spin valve effect. The absolute size of the effect was $(150 \pm 5 \text{m}\Omega)$. This is larger than presented in [32] as shown in **Table 21**, although the injector-detector distance differs considerably along with the temperature. The lower temperature would increase the spin diffusion length and the greater injector-detector distance would decrease the signal. Varying the injector-detector distance along with variable temperature measurements would be the natural extension to these measurements although reproducibility in these devices was an issue due to the uncontrolled formation of the Aluminium oxide tunnel barrier. It is not possible to estimate the size of the effect at greater injector-detector distances given a single measurement at a single injector-detector distance or the temperature dependence of the signal. It is presumed the fabricated device is of good quality in the sense that it produces the spin valve effect reproducibly with a signal size greater than was achieved for the NiFe/Au/NiFe devices which is an improvement. To carry out a full comparison with the literature the formation of the tunnel barrier needs to be

Parameters	This Work	Reference [32]
Spin Valve Effect (Local)	150±5mΩ (local) (Measured)	1 mΩ (Estimated)
Spin Valve Effect (Non-Local)	75 mΩ (Estimated)	0.5 mΩ (Measured)
Injector-detector distance	200 nm	820 nm
Tunnel Barrier	Aluminium Oxide	Aluminium Oxide
Temperature	300K	2K

Table 21 Presenting the spin valve effect measured using tunnel barriers incorporated into the device design for this work and a similar device from the literature for comparison. Estimates were made by using a factor of two as the non-local and local measurements are theoretically predicated to differ by this factor.

controlled (utilising the *in situ* setup for example) to allow devices with reproducible effects to be fabricated and then investigated.

7.6.4. Spin Injection Using AlO_x Tunnel barriers And a Dual Injection Scheme

A series of dual injection spin valves were fabricated in an attempt to increase the spin valve effect by injecting more spin carriers and reducing the volume available for spin relaxation as discussed in the relevant literature review (section 2.7.8). Only one device displayed the non-local spin valve effect, demonstrating pure spin current injection and detection. It is believed these devices suffered from irreproducibility due to the uncontrolled formation of the tunnel barrier and as such, a series of devices varying the injector-detector spacing was not possible. This device will be compared with the most similar device in the literature, another dual lateral spin valve with Permalloy injecting and detecting magnetic electrodes, a Silver spin channel and a Magnesium oxide tunnel barrier. The devices are compared in **Table 22**.

Parameters	Magnetic Electrodes	Injector – detector distance	Tunnel Barrier	Spin Channel	Size of Effect	Temp
This Work	NiFe	200 nm	AlO _x	Al	0.4±0.04 mΩ	300K
Reference [33]	NiFe	500 nm	MgO	Ag	200 mΩ	10K

Table 22 Showing a comparison of between a dual lateral spin valve presented in this thesis and a relevant dual lateral spin valve from the literature.

Table 22 summarises the parameters for a dual lateral spin valve presented in this thesis and a relevant device from the literature. Immediately obvious is the lower signal size measured for a dual lateral spin valve in this thesis as compared to the literature [33]. The devices are not exactly the same, how they differ and whether it renders the comparison useless will now be discussed. The same magnetic material was used for spin injection and detection (NiFe) of similar dimensions (~200nm wide and ~ 20nm thick). The different injector-detector distances will affect the size of the spin signal, an exponential dependence on spin channel length is observed in these devices. Comparing the distances, the device presented in this thesis is a factor of 0.4 smaller than the device presented from the literature. This should mean a larger signal should be measured considering distance solely. Considering the tunnel barriers, they are of different materials, but in essence they both do the same thing, change the interface from an Ohmic contact to a tunnelling contact. It is possible however to quantify a tunnel barrier in terms of a tunnel conductance, a dependence of the spin signal on the tunnel conductance is known to exist [32], although these measurements were not carried out in this thesis or for the device presented from the literature. The spin channels differ although the spin diffusion lengths in both materials are similar. The temperature differs considerably, with a difference of 290K being substantial. An exponential dependence of the spin signal on temperature is known to exist and would affect the signal size in dual lateral spin valves. They are two parameters then (injector-detector distance and temperature) that differ considerably and will affect the signal size. The fact that the device presented in this thesis has a smaller injector-detector distance should make the signal larger but the fact that the temperature is much higher when measuring this device would also

push the spin valve signal down. Ultimately the signal measured in my device is 500 times smaller than the device presented from the literature which would imply the tunnel barrier formed is of poor quality, specifically having a low tunnel conductance. This is supported by the discussion in section 7.6.2 which showed my devices without the inclusion of a tunnel barrier were comparable to if not better than the existing literature. Clearly the formation of the tunnel barrier needs to be a controlled process potentially using the *in situ* setup.

7.7. Conclusion

Metallic lateral spin valves were fabricated and studied over a range of materials. The spin diffusion length of gold was measured using a NiFe/Au/NiFe lateral spin valve. It was found to be of an order comparable to similar systems. Pure spin current was demonstrated using a tunnel barrier of AlO_x in a dual injection lateral spin valve.

8. Further Experiments and Outlook

Regarding AFM machining given more time a comparison with theoretical data of the same dimensions would have been carried out, therefore it is proposed that either the simulations compared to be re-run or the fabricated and machined nanowires be chosen to match the specifications of the simulations. An attempt to make a spin valve using a break in a ferromagnetic nanowire using AFM nanomachining is to be further investigated. Consideration of how to best deposit the subsequent non-magnetic medium in the broken nanowire is as of yet unknown and would require further work. Some interesting 3D structures resulting from machining thin films were observed and it could be interesting to investigate their magnetic properties using magneto-transport measurements, an example of an interesting structure is shown in **Figure 8-1**.

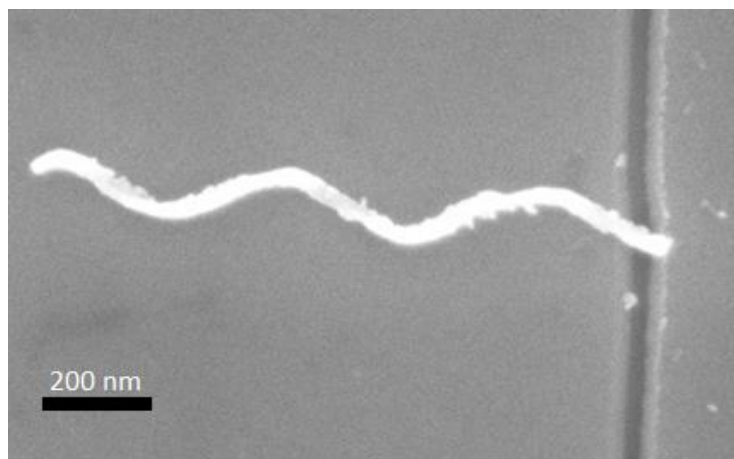


Figure 8-1 Showing an interesting 3D magnetic nanostructure produced as a side product of machining a NiFe thin film.

Relating to the *in situ* experiments, reduction of the pressure in the chamber would allow more reliable characterisation to be obtained *in situ*. A variety of experiments are envisioned after investigating the AMR of a thin film as a function of thickness. The same experiment is envisioned for a nanowire although the DW AMR being measured as a function of thickness this time. *In situ* measurement and characterisation of spin valves, specifically monitoring the formation of tunnel barriers used for spin injection is also imagined.

9. Conclusion

The studying of magnetisation reversal using anisotropic magnetoresistance (AMR) was carried out at many points throughout this thesis to study NiFe thin films and nanowires. In order to study thin films a custom built thermal evaporator was used to grow and monitor thin films *in situ*. In terms of nanowires AFM nanomachining was used to modify NiFe nanowires and the resulting effects probed using AMR. Lateral spin valve structures were also fabricated and measured but *in situ* modification of these structures has not yet been realised.

In chapter 5, AFM nanomachining was used to modify NiFe nanowires, a diamond coated SiN tip was used to machine and remove material away from the nanowires. 10nm thick and 20nm thick nanowires were machined and magnetoresistance measurements were employed to see the effect it had on domain wall pinning and depinning. It was found that for the majority of nanowires the machined section of the nanowire presented itself as a pinning site to domain walls and increased the depinning field of the machined nanowires. A comparison was made with a theoretical study where it was found that the change in depinning field depended linearly on the depth of the machined section and theory overestimated this dependence. Domain wall anisotropic magnetoresistance (DW AMR) was investigated as a function of width for 10nm and 20nm thick nanowires. Comparisons were made with two theoretical models for DW AMR, a 1D model which is used routinely in the literature - 1D model for DW AMR in planar nanowires containing Néel walls. This model gave an accurate prediction of the average DW AMR value of a nanowire of any width, although failed to predict any width dependence (the model only depends on thickness). Another model that incorporated the detailed spin structure of a domain wall into the simulations of a DW AMR and predicted width dependence was compared with the experimental data. Close agreement between calculations and experimental results were found for the average value of DW AMR, the individual DW AMR experimentally became more negative close to the phase boundary between domain wall types and this was not predicted theoretically.

In chapter six *in situ* electrical measurements were used to probe the AMR of thin films grown in a custom built thermal evaporator. It was shown initially that the

system was operational and *in situ* results were compared with *ex situ* results, it was found that both regimes agreed in terms of the magneto-transport measurements, the only difference noted was that data measured *ex situ* had a marginally increased resistance which was later attributed to oxidation. Another thin film was grown and oxidised within the chamber, it was shown that there was a correlation between the chamber being open to air and the resistance increasing due to oxidation. Finally, a 20nm thick film was grown in two nanometre steps and magnetoresistance measurements were used to each thickness interval to investigate the AMR as a function of thickness *in situ*. No reliable data was obtained *in situ* and it was attributed to oxidation taking place within the vacuum chamber and postulated that the experiment should be run with a lower base pressure in the future.

In chapter 7 lateral spin valve structures are investigated using a variety of magnetic injector and detector electrodes (Ni and NiFe) and non-magnetic mediums (Au and Al) through Ohmic junctions and tunnel barriers. No reliable spin injection was shown using Nickel/Gold/Nickel lateral spin valves, this was presumed to be due to the low spin polarisation of Nickel coupled with the small spin diffusion length of gold. Successful spin injection was demonstrated using a NiFe/Gold/NiFe lateral spin valve in the local configuration. The injector-detector distance was varied and a fit was made using a 1D model for spin transport to extract the spin diffusion length of Gold, the polarisation of NiFe and the injecting efficiency at room temperature. Comparing to other NiFe/Gold/NiFe lateral spin valves, devices presented in this thesis were found to have similar parameters to those extracted from measurements made by other groups. NiFe/ AlO_x /Al/ AlO_x /NiFe lateral spin valves were then presented, where tunnel barriers were fabricated at the NiFe/Al interface by growing two nanometres of Aluminium on top of the magnetic electrodes and allowing it to oxidise in air. Signals were obtained in the non-local configuration for some devices where the voltage induced by spin accumulation was 500 times smaller than similar devices found in the literature. This was thought to be due to the lack of control regarding oxidation of the 2nm Aluminium layer to form a tunnel barrier.

10. References

- [1] S. S. P. Parkin, M. Hayashi, and L. Thomas, "Magnetic Racetrack Memory," *Science* (80-.), vol. 320, no. 5873, pp. 190–194, 2008.
- [2] D. A. Allwood, G. Xiong, C. C. Faulkner, D. Atkinson, D. Petit, and R. P. Cowburn, "Magnetic domain-wall logic.," *Science*, vol. 309, no. 5741, pp. 1688–1692, 2005.
- [3] B. D. Cullity and C. D. Graham, *Introduction to Magnetic Materials, Second Edition*. John Wiley & Sons, Inc., 2008.
- [4] J. M. D. Coey, *Magnetism and Magnetic Materials*, 1st ed. Cambridge: Cambridge University Press, 2010.
- [5] L. Landau and E. Lifshits, "On the Theory of the Dispersion of Magnetic Permeability in Ferromagnetic Bodies," *Phys. Zeitsch. der Sow.*, vol. 169, no. 14, pp. 14–22, 1935.
- [6] W. F. Brown, "Some Magnetostatic and Micromagnetic Properties Of The Infinite Rectangular Bar," *J. Appl. Phys.*, vol. 35, no. 7, pp. 2102–2106, 1964.
- [7] K. H. and F. M, *Micromagnetisation and the Microstructure of Ferromagnetic Solids*. Cambridge: Pres, Cambridge University, 2003.
- [8] G. Nahrwold, J. M. Scholtyssek, S. Motl-Ziegler, O. Albrecht, U. Merkt, and G. Meier, "Structural, magnetic, and transport properties of Permalloy for spintronic experiments," *J. Appl. Phys.*, vol. 108, no. 1, 2010.
- [9] A. Hurbert, *Magnetic Domains: The Analysis of Magnetic Nanostructures*. Springer, 1998.
- [10] G. Catalan, J. Seidel, R. Ramesh, and J. F. Scott, "Domain wall nanoelectronics," *Rev. Mod. Phys.*, vol. 84, no. 1, pp. 119–156, 2012.
- [11] A. D. West, T. J. Hayward, K. J. Weatherill, T. Schrefl, D. a Allwood, and I. G. Hughes, "A simple model for calculating magnetic nanowire domain wall fringing fields," *J. Phys. D. Appl. Phys.*, vol. 45, no. 9, p. 95002, 2012.
- [12] L. K. Bogart and D. Atkinson, "Domain wall anisotropic magnetoresistance in planar nanowires," *Appl. Phys. Lett.*, vol. 94, no. 4, 2009.
- [13] M. Hayashi, L. Thomas, C. Rettner, R. Moriya, X. Jiang, and S. S. P. Parkin, "Dependence of current and field driven depinning of domain walls on their structure and chirality in permalloy nanowires," *Phys. Rev. Lett.*, vol. 97, no. 20, pp. 1–4, 2006.
- [14] Y. Nakatani, A. Thiaville, and J. Miltat, "Head-to-head domain walls in soft nano-strips: A refined phase diagram," *J. Magn. Magn. Mater.*, vol. 290–291 PA, pp. 750–753, 2005.
- [15] P. A. M. Dirac, "The Quantum Theory of the Electron," *Proc. R. Soc. A Math. Phys. Eng. Sci.*, vol. 117, no. 778, pp. 610–624, 1928.
- [16] J. J. Thomson, "Charge carried by the Cathode Rays .," *Discourse*, vol. IX, pp. 1–24, 1897.
- [17] N. Mott, "The electrical conductivity of transition metals," *Proc. R. Soc. London*.

- Ser. A*, ..., vol. 153, no. 880, pp. 699–717, 1936.
- [18] J. F. Gregg, I. Petej, E. Jouguelet, and C. Dennis, “Spin electronics a review,” *J. Phys. D. Appl. Phys.*, vol. 35, no. 18, pp. R121–R155, 2002.
- [19] R. Farshchi and M. Ramsteiner, “Spin injection from Heusler alloys into semiconductors: A materials perspective,” *J. Appl. Phys.*, vol. 113, no. 19, 2013.
- [20] T. Kimura and Y. Otani, “Large spin accumulation in a permalloy-silver lateral spin valve,” *Phys. Rev. Lett.*, vol. 99, no. 19, pp. 1–4, 2007.
- [21] F. J. Jedema, M. S. Nijboer, a. T. Filip, and B. J. van Wees, “Spin injection and spin accumulation in all-metal mesoscopic spin valves,” p. 16, 2002.
- [22] T. V. A. Fert, “Valet, Fert - 1993 - Theory of the perpendicular magnetoresistance in magnetic multilayers.pdf.” *PHYSICAL REVIEW B*, pp. 7099–7113, 1993.
- [23] M. Johnson and R. H. Silsbee, “Interfacial charge-spin coupling: Injection and detection of spin magnetization in metals,” *Phys. Rev. Lett.*, vol. 55, no. 17, pp. 1790–1793, 1985.
- [24] K. Takanashi, “Creation and control of spin current in solids,” *Jpn. J. Appl. Phys.*, vol. 49, no. 11, 2010.
- [25] M. N. Baibich and J. M. Broto, “Giant Magnetoresistance of (001)Fe/(001)Cr Magnetic Superlattices,” *Phys. Rev. Lett.*, vol. 61, no. 1, pp. 2472–2475, 1988.
- [26] A. Fert and P. Grunberg, “Nobel Prizes,” 2007. [Online]. Available: http://www.nobelprize.org/nobel_prizes/physics/laureates/2007/. [Accessed: 01-Aug-2016].
- [27] J. M. Daughton, “GMR applications,” *J. Magn. Magn. Mater.*, vol. 192, no. 2, pp. 334–342, 1999.
- [28] F. J. Jedema, A. T. Filip, and B. J. van Wees, “Electrical spin injection and accumulation at room temperature in an all-metal mesoscopic spin valve,” *Nature*, vol. 410, no. 6826, pp. 345–348, 2001.
- [29] F. J. Jedema, “Electrical spin injection in all metallic spin valve- number of Citations,” 2016. [Online]. Available: <https://www.scopus.com/results/citedbyresults.uri?sort=plf-f&cite=2-s2.0-0035868698&src=s&imp=t&sid=472F449597F7EBD5D4146C09A3329CFA.Vdktg6RVtMfaQJ4pNTCQ%3A30&sot=cite&sdt=a&sl=0&origin=inward&editSaveSearch=&txGid=0>. [Accessed: 04-Aug-2016].
- [30] Times Higher Education, “Citation Averages.” [Online]. Available: <https://www.timeshighereducation.com/news/citation-averages-2000-2010-by-fields-and-years/415643.article>. [Accessed: 04-Aug-2016].
- [31] S. R. Boona, R. C. Myers, and J. P. Heremans, “Spin caloritronics,” *Energy Environ. Sci.*, vol. 7, no. 3, p. 885, 2014.
- [32] A. Vogel, J. Wulfhorst, and G. Meier, “Enhanced spin injection and detection in spin valves with integrated tunnel barriers,” *Appl. Phys. Lett.*, vol. 94, no. 12, pp. 4–7, 2009.
- [33] H. Idzuchi, S. Karube, Y. Fukuma, T. Aoki, and Y. Otani, “Impact of interface properties on spin accumulation in dual-injection lateral spin valves,” *Appl.*

- Phys. Lett.*, vol. 103, no. 16, pp. 1–5, 2013.
- [34] H. Idzuchi, Y. Fukuma, S. Takahashi, S. Maekawa, and Y. Otani, “Effect of anisotropic spin absorption on the Hanle effect in lateral spin valves,” *Phys. Rev. B - Condens. Matter Mater. Phys.*, vol. 89, no. 8, pp. 1–5, 2014.
- [35] S. Nonoguchi, T. Nomura, and T. Kimura, “Longitudinal and transverse spin current absorptions in a lateral spin-valve structure,” *Phys. Rev. B - Condens. Matter Mater. Phys.*, vol. 86, no. 10, pp. 1–5, 2012.
- [36] F. J. Jedema, H. B. Heersche, a T. Filip, J. J. a Baselmans, and B. J. van Wees, “Electrical detection of spin precession in a metallic mesoscopic spin valve.,” *Nature*, vol. 416, no. 6882, pp. 713–716, 2002.
- [37] L. O’Brien, M. J. Erickson, D. Spivak, H. Ambaye, R. J. Goyette, V. Lauter, P. a Crowell, and C. Leighton, “Kondo physics in non-local metallic spin transport devices.,” *Nat. Commun.*, vol. 5, no. May, p. 3927, 2014.
- [38] Y. Fukuma, L. Wang, H. Idzuchi, S. Takahashi, S. Maekawa, and Y. Otani, “Giant enhancement of spin accumulation and long-distance spin precession in metallic lateral spin valves.,” *Nat. Mater.*, vol. 10, no. 7, pp. 527–531, 2011.
- [39] S. A. Crooker, M. Furis, X. Lou, C. Adelman, D. L. Smith, C. J. Palmstrøm, and P. a Crowell, “Imaging spin transport in lateral ferromagnet/semiconductor structures.,” *Science*, vol. 309, no. 5744, pp. 2191–2195, 2005.
- [40] M. W. Wu, J. H. Jiang, and M. Q. Weng, “Spin dynamics in semiconductors,” *Phys. Rep.*, vol. 493, no. 2–4, pp. 61–236, 2010.
- [41] R. Geng, T. T. Daugherty, K. Do, H. M. Luong, and T. D. Nguyen, “A review on organic spintronic materials and devices: I. Magnetic field effect on organic light emitting diodes,” *J. Sci. Adv. Mater. Devices*, vol. 1, no. 2, pp. 128–140, 2016.
- [42] V. N. Prigodin, J. W. Yoo, H. W. Jang, C. Kao, C. B. Eom, and A. J. Epstein, “New advances in organic spintronics,” *Int. Conf. Trends Spintron. Nanomagnetism (Tsn 2010)*, vol. 292, no. 1, p. 12001, 2011.
- [43] B. Dlubak, M.-B. Martin, C. Deranlot, B. Servet, S. Xavier, R. Mattana, M. Sprinkle, C. Berger, W. a. De Heer, F. Petroff, A. Anane, P. Seneor, and A. Fert, “Highly efficient spin transport in epitaxial graphene on SiC,” *Nat. Phys.*, vol. 8, no. 7, pp. 557–561, 2012.
- [44] Y. Cho, Y. C. Choi, and K. S. Kim, “Graphene spin-valve device grown epitaxially on the Ni(111) substrate: A first principles study,” *J. Phys. Chem. C*, vol. 115, no. 13, pp. 6019–6023, 2011.
- [45] T. Yamaguchi, S. Masubuchi, K. Iguchi, R. Moriya, and T. MacHida, “Tunnel spin injection into graphene using Al₂O₃ barrier grown by atomic layer deposition on functionalized graphene surface,” *J. Magn. Magn. Mater.*, vol. 324, no. 5, pp. 849–852, 2012.
- [46] X. J. Wang, H. Zou, L. E. Ocola, and Y. Ji, “High spin injection polarization at an elevated dc bias in tunnel-junction-based lateral spin valves,” *Appl. Phys. Lett.*, vol. 95, no. 2, pp. 131–134, 2009.
- [47] W. Han, K. Pi, K. McCreary, Y. Li, J. Wong, a. Swartz, and R. Kawakami, “Tunneling Spin Injection into Single Layer Graphene,” *Phys. Rev. Lett.*, vol. 105, no. 16, 2010.

- [48] H. Liu, D. Bedau, J. Z. Sun, S. Mangin, E. E. Fullerton, J. A. Katine, and A. D. Kent, "Dynamics of spin torque switching in all-perpendicular spin valve nanopillars," *J. Magn. Magn. Mater.*, vol. 358–359, pp. 233–258, 2014.
- [49] P. Laczkowski, L. Vila, V. D. Nguyen, a. Marty, J. P. Attané, H. Jaffrès, J. M. George, and a. Fert, "Enhancement of the spin signal in permalloy/gold multiterminal nanodevices by lateral confinement," *Phys. Rev. B - Condens. Matter Mater. Phys.*, vol. 85, no. 22, pp. 2–5, 2012.
- [50] R. M. Abdullah, A. J. Vick, B. a Murphy, and A. Hirohata, "Spin-current signal amplification by a geometrical ratchet," vol. 482001, pp. 1–6.
- [51] S. Franssila, *Microfabrication*. West Sussex: Wiley, 2004.
- [52] L. R. Harriott, "SCALPEL: projection electron beam lithography," *Proc. 1999 Part. Accel. Conf. (Cat. No.99CH36366)*, vol. 1, pp. 595–599, 1999.
- [53] Y. Fu, N. Kok, and A. Bryan, "Focused ion beam direct fabrication of micro-optical elements : features compared with laser beam and electron beam direct writing," *Precis. Eng.*, vol. 639798, no. 1, pp. 1–7, 2004.
- [54] A. a. Tseng, K. Chen, C. D. Chen, and K. J. Ma, "Electron beam lithography in nanoscale fabrication: Recent development," *IEEE Trans. Electron. Packag. Manuf.*, vol. 26, no. 2, pp. 141–149, 2003.
- [55] Raith, "Raith Products Web Page." [Online]. Available: m.raith.com/products/eline-plus.html. [Accessed: 19-Apr-2016].
- [56] D. Constancias, C., Landis, S., Manakli, S., Martin, L., Pain, L., and Rio, "Lithography," Hoboken, NJ, USA: John Wiley and Sons, 2013.
- [57] M. A. Mohammad, M. Muhammad, and S. K. Dew, *Nanofabrication*. 2012.
- [58] K.-S. Lee, R. H. Kim, D.-Y. Yang, and S. H. Park, "Advances in 3D nano/microfabrication using two-photon initiated polymerization," *Prog. Polym. Sci.*, vol. 33, no. 6, pp. 631–681, 2008.
- [59] L. J. van der Pauw, "A method of measuring the resistivity and Hall coefficient on lamellae of arbitrary shape," *Philips Tech. Rev.*, vol. 20, pp. 220–224, 1958.
- [60] D. Brandon, D., Kaplan, "Scanning Electron Microscopy," in *Microstructural Characterization of Materials*, 2nd ed., D. Brandon, D., Kaplan, Ed. John Wiley & Sons, 2008, pp. 261–331.
- [61] N. Bell, C., Erdman, *Introduction to the Theory and Advantages of Low Voltage Electron Microscopy*. Chichester, UK: John Wiley & Sons, 2012.
- [62] W. Thomson, "On the Electro-Dynamic Qualities of Metals:--Effects of Magnetization on the Electric Conductivity of Nickel and of Iron," *Proc. R. Soc. London*, vol. 8, pp. 546–550, 1856.
- [63] C.-J. Zhao, L. Ding, J.-S. HuangFu, J.-Y. Zhang, and G.-H. Yu, "Research progress in anisotropic magnetoresistance," *Rare Met.*, vol. 32, no. 3, pp. 213–224, 2013.
- [64] G. Vieira, A. Chen, T. Henighan, J. Lucy, F. Y. Yang, and R. Sooryakumar, "Transport of magnetic microparticles via tunable stationary magnetic traps in patterned wires," *Phys. Rev. B - Condens. Matter Mater. Phys.*, vol. 85, no. 17, pp. 1–8, 2012.
- [65] M. Donolato, M. Gobbi, P. Vavassori, M. Leone, M. Cantoni, V. Metlushko, B.

- Ilic, M. Zhang, S. X. Wang, and R. Bertacco, "Nanosized corners for trapping and detecting magnetic nanoparticles.," *Nanotechnology*, vol. 20, no. 38, p. 385501, 2009.
- [66] S. Krzyk, A. Schmidfeld, M. Kl??ui, and W. R??diger, "Magnetotransport effects of ultrathin Ni₈₀Fe₂₀ films probed in situ," *New J. Phys.*, vol. 12, 2010.
- [67] K. Narayanapillai and H. Yang, "Control of domain wall motion at vertically etched nanotrench in ferromagnetic nanowires," *Appl. Phys. Lett.*, vol. 103, no. 25, pp. 2011–2015, 2013.
- [68] V. D. Nguyen, L. Vila, P. Laczkowski, a. Marty, T. Faivre, and J. P. Attané, "Detection of domain-wall position and magnetization reversal in nanostructures using the magnon contribution to the resistivity," *Phys. Rev. Lett.*, vol. 107, no. 13, pp. 1–4, 2011.
- [69] A. Manzin, V. Nabaei, H. Corte-león, O. Kazakova, P. Krzysteczko, H. W. Schumacher, R. Metrologica, T. I-, P. Bundesanstalt, B. D-, and I. I. N. U. M. Odel, "Modeling of Anisotropic Magnetoresistance Properties of Permalloy Nanostructures," *IEEE Trans. Magn.*, vol. 50, no. 4, pp. 10–13, 2014.
- [70] H. Corte-León, V. Nabaei, A. Manzin, J. Fletcher, P. Krzysteczko, H. W. Schumacher, and O. Kazakova, "Anisotropic Magnetoresistance State Space of Permalloy Nanowires with Domain Wall Pinning Geometry," *Sci. Rep.*, vol. 4, pp. 1–10, 2014.
- [71] A. B. De Oliveira, G. L. Da Silva, S. M. Rezende, and A. Azevedo, "Magnetization reversal in single ferromagnetic rectangular nanowires," *J. Phys. Conf. Ser.*, vol. 200, no. 7, p. 72023, 2010.
- [72] A. B. Oliveira, S. M. Rezende, and A. Azevedo, "Magnetization reversal in permalloy ferromagnetic nanowires investigated with magnetoresistance measurements," *Phys. Rev. B - Condens. Matter Mater. Phys.*, vol. 78, no. 2, pp. 1–6, 2008.
- [73] A. Beguivin, H. Corte-León, A. Manzin, V. Nabaei, P. Krzysteczko, H. W. Schumacher, D. Petit, R. P. Cowburn, and O. Kazakova, "Simultaneous magnetoresistance and magneto-optical measurements of domain wall properties in nanodevices," *J. Appl. Phys.*, vol. 115, no. 17, pp. 251–254, 2014.
- [74] V. D. Nguyen, C. Naylor, L. Vila, a. Marty, P. Laczkowski, C. Beigné, L. Notin, Z. Ishaque, and J. P. Attané, "Magnon magnetoresistance of NiFe nanowires: Size dependence and domain wall detection," *Appl. Phys. Lett.*, vol. 99, no. 26, pp. 2011–2014, 2011.
- [75] G. Binnig, C. Quate, and C. Gerber, "Atomic Force Microscope," *Physical Review Letters*, vol. 56, no. 9, pp. 930–933, 1986.
- [76] G. Binnig, H. Rohrer, C. Gerber, and E. Weibel, "Surface Studies by Scanning Tunneling Microscopy," *Physical Review Letters*, vol. 49, no. 1, pp. 57–61, 1982.
- [77] J. DiNardo, N, "Nanoscale Characterization of Surfaces and Interfaces," in *Atomic Force Microscopy*, Wiley, 2007, pp. 118–137.
- [78] I.B.M, "'IBM' atoms." [Online]. Available: http://www-03.ibm.com/ibm/history/exhibits/vintage/vintage_4506VV1003.html. [Accessed:

- 01-May-2016].
- [79] I.B.M, "A Boy And His Atom: The World's Smallest Movie," 2013. [Online]. Available: <http://www.research.ibm.com/articles/madewithatoms.shtml#fbid=gAN3KVoGEXm>. [Accessed: 01-May-2016].
- [80] A. a. Tseng, C. F. J. Kuo, S. Jou, S. Nishimura, and J. I. Shirakashi, "Scratch direction and threshold force in nanoscale scratching using atomic force microscopes," *Appl. Surf. Sci.*, vol. 257, no. 22, pp. 9243–9250, 2011.
- [81] A. a. Tseng, J. Shirakashi, S. Nishimura, K. Miyashita, and A. Notargiacomo, "Scratching properties of nickel-iron thin film and silicon using atomic force microscopy," *J. Appl. Phys.*, vol. 106, no. 4, p. 44314, 2009.
- [82] G. Watanabe, S. Koizumi, T. Yamada, Y. Takemura, and J. Shirakashi, "Magnetoresistance of patterned NiFe thin films with structures modified by atomic force microscope nanolithography," *J. Vac. Sci. Technol. B Microelectron. Nanom. Struct.*, vol. 23, no. 6, p. 2390, 2005.
- [83] A. a Tseng, J. Shirakashi, S. Nishimura, K. Miyashita, and Z. Li, "Nanomachining of permalloy for fabricating nanoscale ferromagnetic structures using atomic force microscopy.," *J. Nanosci. Nanotechnol.*, vol. 10, no. 1, pp. 456–466, 2010.
- [84] L. S. Cryotronics, "Model 370 AC Resistance Bridge." [Online]. Available: <http://www.lakeshore.com/products/AC-Resistance-Bridges/Model-370/Pages/Overview.aspx>. [Accessed: 01-May-2016].
- [85] S. Tumanski, *Thin Film Magnetoresistive Sensors*. Bristol: IOP Publishing, 2001.
- [86] A. a. Tseng, "Three-dimensional patterning of nanostructures using atomic force microscopes," *J. Vac. Sci. Technol. B Microelectron. Nanom. Struct.*, vol. 29, no. 4, p. 40801, 2011.
- [87] A. Bergmann, D. Feigl, D. Kuhn, M. Schaupp, G. Quast, K. Busch, L. Eichner, and J. Schumacher, "A low-cost AFM setup with an interferometer for undergraduates and secondary-school students," *Eur. J. Phys.*, vol. 901, 2013.
- [88] J. Shi, L. Liu, P. Zhou, F. Wang, and Y. Wang, "Subnanomachining by Ultrasonic-Vibration-Assisted Atomic Force Microscopy," vol. 14, no. 4, pp. 735–741, 2015.
- [89] A. A. Tseng, "A comparison study of scratch and wear properties using atomic force microscopy," *Appl. Surf. Sci.*, vol. 256, no. 13, pp. 4246–4252, 2010.
- [90] A. Temiryazev, "Pulse force nanolithography on hard surfaces using atomic force microscopy with a sharp single-crystal diamond tip," *Diam. Relat. Mater.*, vol. 48, pp. 60–64, 2014.
- [91] Z. C. Lin and Y. C. Hsu, "A study of estimating cutting depth for multi-pass nanoscale cutting by using atomic force microscopy," *Appl. Surf. Sci.*, vol. 258, no. 10, pp. 4513–4522, 2012.
- [92] T. Konnig, T. Papke, A. Kopyshv, and S. Santer, "Atomic force microscopy nanolithography: Fabrication of metallic nano-slits using silicon nitride tips," *J. Mater. Sci.*, vol. 48, no. 10, pp. 3863–3869, 2013.
- [93] A. Brataas, A. D. Kent, and H. Ohno, "Current-induced torques in magnetic

- materials," *Nat. Mater.*, vol. 11, no. 5, pp. 372–381, 2012.
- [94] P. Systems, "AFM Software." [Online]. Available: <http://www.parkafm.com/index.php/products/research-afm/park-ae15/specifications>. [Accessed: 22-May-2016].
- [95] L. K. Bogart, "An Investigation of the Structure, Pinning and Magnetoresistance of Domain Walls in Permalloy Planar Nanowires," Durham University, 2010.
- [96] M. Kläui, "Head-to-head domain walls in magnetic nanostructures," *J. Phys. Condens. Matter*, vol. 20, no. 31, p. 313001, 2008.
- [97] M. Salou, B. Lescop, S. Rioual, A. Lebon, J. Ben Youssef, and B. Rouvellou, "Initial oxidation of polycrystalline Permalloy surface," *Surf. Sci.*, vol. 602, no. 17, pp. 2901–2906, 2008.
- [98] S. Krzyk, a. Schmidfeld, M. Kläui, and W. Rüdiger, "Magnetotransport effects of ultrathin Ni80Fe20 films probed in situ," *New J. Phys.*, vol. 12, 2010.
- [99] S. U. Jen, T. C. Wu, C. M. Wong, Y. T. Chen, and H. P. Chiang, "In-situ magnetic deposition field effect on sheet resistance of Permalloy films," *Thin Solid Films*, vol. 515, no. 18, pp. 7382–7386, 2007.
- [100] T. G. S. M. Rijks, S. K. J. Lenczowski, R. Coehoorn, and W. J. M. de Jonge, "In-plane and out-of-plane anisotropic magnetoresistance in Ni80Fe20 thin films," *Phys. Rev. B*, vol. 56, no. 1, p. 362, 1997.
- [101] T. R. McGuire and R. I. Potter, "Anisotropic Magnetoresistance," *IEEE Trans. Magn.*, vol. 11, pp. 1018–1038, 1975.
- [102] J. Ku, J. Chang, S. Han, J. Ha, and J. Eom, "Electrical spin injection and accumulation in ferromagnetic/Au/ferromagnetic lateral spin valves," *J. Appl. Phys.*, vol. 99, no. 8, pp. 2004–2007, 2006.
- [103] J. Ku, J. Chang, S. H. Han, J. Geun Ha, and J. Eom, "Spin injection in NiFe/Au/NiFe spin valves," *J. Magn. Magn. Mater.*, vol. 304, no. 1, pp. 273–275, 2006.
- [104] J. H. Ku, H. C. Koo, S. H. Han, J. Eom, G. Kim, and J. Chang, "Large spatial distribution of spin accumulation in wide Au channel," *Solid. State. Electron.*, vol. 89, pp. 72–75, 2013.
- [105] Y. Fukuma, L. Wang, H. Idzuchi, and Y. Otani, "Enhanced spin accumulation obtained by inserting low-resistance MgO interface in metallic lateral spin valves," *Appl. Phys. Lett.*, vol. 97, no. 1, pp. 109–112, 2010.
- [106] S. Yakata, Y. Ando, and T. Kimura, "Optimization of interface condition for efficient spin injection in Permalloy/Cu lateral spin valve," *IEEE Reg. 10 Annu. Int. Conf. Proceedings/TENCON*, pp. 126–128, 2010.
- [107] P. Łączkowski, L. Vila, S. Ferry, A. Marty, J. M. George, H. Jaffrès, A. Fert, T. Kimura, T. Yang, Y. Otani, and J. P. Attané, "Spin signal in metallic lateral spin valves made by a multiple angle evaporation technique," *Appl. Phys. Express*, vol. 4, no. 6, pp. 3–5, 2011.
- [108] Y. Ji, a. Hoffmann, J. S. Jiang, and S. D. Bader, "Spin injection, diffusion, and detection in lateral spin-valves," *Appl. Phys. Lett.*, vol. 85, no. 25, pp. 6218–6220, 2004.

- [109] G. T. K. J. Ku, J. Chang, H. C. Koo, J. Eom, S. H. Han, "Spin Valve Effect in Laterl Py/Au/Py Devices," *Journal of magnetics*, vol. 12, no. 4. pp. 152–155, 2007.
- [110] J. H. Ku, J. Chang, H. Kim, and J. Eom, "Effective spin injection in Au film from Permalloy," *Appl. Phys. Lett.*, vol. 88, no. 17, pp. 131–134, 2006.
- [111] Y. Ji, a Hoffmann, J. S. Jiang, J. E. Pearson, and S. D. Bader, "Non-local spin injection in lateral spin valves," *J. Phys. D. Appl. Phys.*, vol. 40, no. 5, pp. 1280–1284, 2007.
- [112] N. Motzko, N. Richter, B. Burkhardt, R. Reeve, P. Laczkowski, L. Vila, J. P. Attané, and M. Kläui, "Spin relaxation in Cu and Al spin conduits," *Phys. Status Solidi Appl. Mater. Sci.*, vol. 211, no. 5, pp. 986–990, 2014.
- [113] Y. Otani and T. Kimura, "Manipulation of spin currents in metallic systems.," *Philos. Trans. A. Math. Phys. Eng. Sci.*, vol. 369, no. 1948, pp. 3136–3149, 2011.
- [114] M. Erekhinsky, A. Sharoni, F. Casanova, and I. K. Schuller, "Surface enhanced spin-flip scattering in lateral spin valves," *Appl. Phys. Lett.*, vol. 96, no. 2, 2010.
- [115] M.-Y. Im, L. Bocklage, G. Meier, and P. Fischer, "Magnetic soft x-ray microscopy of the domain wall depinning process in permalloy magnetic nanowires," *J. Phys. Condens. Matter*, vol. 24, no. 2, p. 24203, 2011.